NANO-MODIFIED CEMENTITIOUS COMPOSITES REINFORCED WITH BASALT FIBER PELLETS AND THEIR POTENTIAL FOR REPAIR/OVERLAY APPLICATIONS

by

Ahmed Mohamed Hisham Ibrahim Azzam

A Thesis Submitted to the Faculty of Graduate Studies of
The University of Manitoba
in partial fulfillment of the requirements for the degree of

Doctor of Philosophy

Department of Civil Engineering
University of Manitoba
Winnipeg

September 2021

ABSTRACT

Under loading and environmental conditions, the brittle nature of conventional concrete flatwork infrastructure (e.g. pavements/bridge decks) may negatively affect its performance due to susceptibility to excessive cracking, requiring costly rehabilitation or replacement of damaged sections. Thus, this thesis aimed at developing and testing a novel type of high-performance cementitious composites. Nano-modified cementitious composites comprising 50% fly ash or slag and reinforced with an innovative type of macro-fibers [basalt fiber pellets (BFP)] were developed and extensively studied. The consistency and flowability/flowability retention of the composites as well as setting times were investigated. The mechanical performance of the composites was tested under static and dynamic (Split Hopkinson Pressure Bar) loading schemes. Moreover, the performance of the cementitious composites under aggravated (alkaline and salt-frost) exposures was comprehensively explored. To investigate the potential of these composites for repair and overlay applications in concrete flatwork, thermal, elastic, and mechanical compatibility of the cementitious composites with conventional concrete paving mixture as well as their suitability for bonded overlay systems were experimentally and numerically studied.

The results showed that the nano-modified composites with 6% nano-silica exhibited enhanced mechanical performance at both early- and late-ages. Moreover, they revealed the efficacy of BFP in reinforcing the cementitious composites and highlighted their role at enhancing the post-cracking performance in terms of energy absorption capacity and strain at failure. While the alkaline exposure provided favorable conditions for the binders' reactivity, this was accompanied by reduction of ductility of composites due to pellets' degradation. The matrix of the composites deteriorated physically and/or chemically under the salt-frost exposure, albeit to different extents according to the binder

type. The composites showed high thermal, elastic, and mechanical compatibility with concrete substrate even after aggravated exposures. In addition, the cementitious composites showed significant efficacy in bonded overlay systems, even with pre-cracked substrate concrete layer.

The synoptic outcomes of this thesis highlighted the promising fresh, mechanical, and durability properties of the nano-modified cementitious composites, particularly the slag-based composites, as well as their compatibility with normal concrete paving mixture. Thus, they may present a viable option for high-performance repair/overlay applications at critical and heavy-duty locations in concrete pavements and bridge decks.

CO-AUTHORSHIP

This thesis has been prepared in accordance with the regulation of integrated-article format stipulated by the Faculty of Graduate Studies at the University of Manitoba. Substantial parts of this thesis were either published in or submitted for publication to peer-reviewed technical journals and international conferences as shown below:

Journal Papers

1. **Azzam, A.**, Bassuoni, M.T. and Shalaby, A., 2021. Flexural Performance of Nano-Modified Cementitious Composites with BFP as a Bonded Overlay. *Journal of Materials in Civil Engineering, ASCE,* (Submitted in July 2021; under revision).

2. **Azzam, A.**, Bassuoni, M.T. and Shalaby, A., 2021. Nano-Modified Cementitious Composites with BFP: Repair/Overlay Option. *ACI Materials Journal, ACI* (Submitted in May 2021; under revision).

3. **Azzam, A.**, Bassuoni, M.T. and Shalaby, A., 2021. Performance of Nano-Modified Cementitious Composites Reinforced with Basalt Fiber Pellets under Alkaline and Salt-Frost Exposures. *Cement and Concrete Composites, ELSEVIER* (Submitted in March 2021; under revision).

4. **Azzam, A.**, Bassuoni, M.T. and Shalaby, A., 2021. Nanomodified Cementitious Composites Incorporating Basalt Fiber Pellets under Tensile and Impact Loads. *Journal of Materials in Civil Engineering*, *ASCE,* 33(10), p.04021260.

5. **Azzam, A.**, Bassuoni, M.T. and Shalaby, A., 2019. Properties of High-Volume Fly Ash and Slag Cementitious Composites Incorporating Nanosilica and Basalt Fiber Pellets. *Advances in Civil Engineering Materials*, *ASTM* 8(3), pp.255-274.

Conference Proceedings

1. **Azzam, A.**, Bassuoni, M.T. and Shalaby, A., May 2020. Durability of Nano-modified Cementitious Composites Reinforced with Basalt Fiber Pellets. *In 2nd International Conference on Nanotechnology of Cement and Concrete (TRB) (2NCC20)*, California, US. (Accepted in February 2020). (Conference sessions suspended due to COVID-19 situation).

2. **Azzam, A.**, Bassuoni, M.T. and Shalaby, A., Jul. 2019. Nano-modified Cementitious Composites with High Volume Supplementary Cementitious Materials Incorporating Basalt Fiber Pellets. *In Fifth International Conference on Sustainable Construction Materials and Technologies (SCMT5)*, London, UK. (Accepted in Jan. 2019).

Dedication

Working hard is crucial, yet, I would have achieved nothing without the support and love of my family

This work is dedicated to:

My Parents, Hisham and Azza,

My Two Siblings, Sief and Nour,

My Beloved Wife, Riham, and Son, Hisham,

My whole family that has a great influence in my life,

All my heart to you for your support to achieve every success, if any, in my life.

Acknowledgements

First and above all, all praises, thanks, and gratitude to Almighty Allah for the benevolence he has bestowed upon me and the guidance to complete this work.

Finally, I can express my deep sense of gratitude and heartfelt respect to my advisor Dr. Mohamed Bassuoni, for his mentorship, immense knowledge, patience, and enthusiasm throughout this work. I appreciate his treatment as a supportive older brother to me. I am mainly attributing the quality of this work to his compassion, knowledge, and endless enthusiasm, without holding back any tiny amount of effort.

I would like to also express my sincere gratitude to my co-advisor Dr. Ahmed Shalaby, for his continuous support throughout this research. I ascribe the level of this work to his encouragement, enthusiasm, and knowledge as well as insightful comments, deep discussions and significant suggestions that added a lot to the value of this work.

In addition, I would like to greatly thank my colleagues for their support during my work stages; particularly Ahmed Ghazy, Ahmed Yasien, Mohamed Sakr and Anis Abayou as well as the assistance of the McQuade Heavy Structures Laboratory staff, Dr. Chad Klowak and Mr. Samuel Abraha for the valuable technical support during the preparation and testing stages.

I highly appreciate the financial support from Natural Sciences and Engineering Research Council of Canada, City of Winnipeg as well as the IKO Construction Materials Testing Facility and Manitoba Institute for Materials at the University of Manitoba at which these experiments were conducted.

I would like to express my deepest gratitude to my parents (Hisham Azzam and Azza Salem) for their moral support and inspiration throughout my entire life. I am grateful for their endless love, patience, encouragement, and prayers. Also, I acknowledge my two brothers (Sief and Nour) for their continuous emotional and spiritual support.

I want to express my appreciation to Riham, my wonderful wife, who supported me with all love, and stood with me side by side in finding our path. I also express my

gratitude to Hisham, my little young man, who is a spontaneous motivator for a better future for us all.

TABLE OF CONTENTS

LIST OF TABLES

LIST OF FIGURES

NOTATIONS

ANOVA	Analysis of Variance
A_s	Steel Bar Cross Sectional Area
a	Crack length.
a/b	Geometry factor
BSEM	Backscattered Scanning Electron Microscopy
BFP	Basalt fiber pellets
c	Cohesion sliding resistance between two layers
C/S	Calcium-to-Silicate Ratio
Ca^{++}	Calcium Ion
$CaCl_2$	Calcium Chloride
$CaCO_3$	Calcium Carbonate
CH	Calcium Hydroxide (Portlandite)
COW	City of Winnipeg
C-S-H	Calcium-Silicate-Hydrate
DF	Durability Factor
dl	Relative Displacement
E	Modulus of Elasticity
EDX	Energy Dispersive X-Ray Analysis
ESEM	Environmental Scanning Electron Microscopy
f'c 28d	28 Days Compressive Strength
f'c 3d	3 Days Compressive Strength
f'c 7d	7 Days Compressive Strength

F	Fly Ash
FRCC	Fiber reinforced cementitious composite
GU	General Use Cement
G	Slag
G	Rate of strain energy release
G_{IC}	Critical rate of strain energy release
HRWRA	High-Range Water Reducing Admixture
HPFRCC	High performance fiber reinforced cementitious composite
ITZ	Interfacial Transition Zone
K_I	Stress intensity factor for crack opening mode
L_f	Fiber length
MIP	Mercury Intrusion Porosimetry
NaCl	Sodium Chloride
NS	Nano-Silica
OH^-	Hydroxyl Ion
p	Normal contact pressure
pH	Potential of Hydrogen
RH	Relative Humidity
r	Distance to the crack tip
S	Steel fibers
SCMs	Supplementary Cementitious Materials
SEM	Scanning Electron Microscopy
t	Time
TG	Thermogravimetry

TGA	Thermogravimetry analysis
w/b	Water-To-Binder Ratio
w/c	Water-To-Cement Ratio
x	Experimental Value
XRD	X-ray Diffraction
ρ	Density
σ	applied stress on the structure
τ	Horizontal shear stresses acting at the interface between the concrete layers
τ_b	Bond Strength
θ	Angle of inclination
$\mathcal{U}$	Poisson's ratio
σ_{cu}	Maximum bridging stresses that can be supported by the fibers
δ_p	Crack opening after which a decline in the stress may take place
δ	Crack opening
μ	Friction coefficient

CHAPTER 1: INTRODUCTION

1.1 Overview

Service life of concrete elements (e.g. pavements, bridge decks, runways, etc.) is linked to multiple factors including the rheological, mechanical and durability characteristics of the materials used, exposure conditions and loading configurations. These interrelated parameters may provoke the initiation and propagation of cracks in concrete, and negatively influence its overall performance and longevity, especially in vulnerable locations such as heavy-duty locations and joints in pavements and bridges [Jones *et al*., 2013]. Exposed concrete elements customarily suffer from different aging factors of loading and environmental schemes, especially in the presence of moisture and salts, which require periodic maintenance with high performance materials. Different rehabilitation and repair techniques such as full-depth and partial depth repairs, overlays, joints and cracks resealing, etc. as well as speciality materials such as high-performance cementitious composites have been recommended to restore the performance and serviceability of aging concrete infrastructure [Smith and Eng, 2010; Lepech and Li, 2010].

One of the most viable options to improve the ductility of cement-based materials is using fibers to reinforce the matrix. Different types of fibers, including steel, synthetic and organic fibers have been applied in cementitious composites (FRCC) to improve their flexural performance and ability to arrest cracks [e.g. Bentur *et al*., 2006]. Addition of fibers in cementitious composites imparts positive effects on their fresh and hardened states such as reduction of bleeding and plastic settlement, controlling plastic and drying shrinkage cracks and improving impact resistance. The key advantages of high-performance FRCC [HPFRCC] are their increased deformability, residual strength beyond first cracking and toughness [Benture *et al*., 2006]. Homogenously distributed fibers can

bridge and arrest cracks in the cementitious matrix, which are the key mechanisms for improving the energy absorption capacity of HPFRCC. This behavior depends on the type, dosage, engineering properties and geometry of the fibers, which affect the post-cracking stage through deformation, fiber de-bonding and pullout processes [Mehta and Monteiro, 2014; ACI 544.1R, 2010].

Many studies have been conducted in the area of HPFRCC, including the advent of engineered cementitious composites (ECC) [e.g. Yu *et al*., 2015]. In addition, high-performance FRCC, comprising cement, supplementary cementitious materials (SCM) and nanoparticles (less than 100 nm) have been recently developed targeting various flatwork applications including pavements and bridge decks [e.g. Salemi and Behfarnia, 2013; Kim and Bordelon, 2017; Zhu *et al*., 2012]. The use of SCMs, such as fly ash and slag, as a part of the binder is one of the techniques towards sustainable construction materials and it improves the properties of mortar/concrete, by refining the pore structure as they react with calcium hydroxide/portlandite (CH) to produce calcium-silicate-hydrate (C-S-H) gel [Neville, 2011]. However, the use of high volumes of SCM in mortar/concrete brings about some technical limitations, including delay of hardening, strength and microstructural development [Mehta and Monteiro, 2014]. Nevertheless, these limitations can be mitigated by adding nano-silica to such binders, as it speeds up the kinetics of cement hydration at early ages by creating nucleation sites for early precipitation of hydration products as well as imparting very rapid pozzolanic activity [Kong *et al*., 2012].

Basalt fibers are a relatively new type of fibers, which are gaining momentum in the construction market owing to its balanced mechanical properties and cost, compared to other types of fibers (e.g. glass). Basalt fibers have high tensile strength (3000-4000 MPa), reasonable modulus of elasticity (93-110 GPa) as well as high thermal and corrosion

resistance. Hence, they may present an attractive candidate for FRCC, as shown by previous studies [e.g. Ghazy *et al*., 2016]. However, basalt fibers were reported to have low alkaline resistance that made them vulnerable to degradation when used in alkaline media with typical pH values of 11-13 [Lee *et al*., 2014; Rabinovich *et al*., 2001]. Good bonding between basalt fibers and cementitious systems was observed at early-age (7 days); however, this bond diminished within 90 days due to degradation of fibers [Jiang *et al*., 2014]. Basalt fibers are susceptible to similar mechanisms of dissolution as glass fibers in concrete, due to reactions between the silicate component in the fibers and alkaline pore solution, resulting in loss of strength and durability of the reinforced composite [Branston *et al*., 2016]. The vulnerability of basalt fibers to alkaline media can be mitigated by encapsulating them with polymeric resins, e.g. epoxy or polyamide, forming basalt fiber pellets (BFP). In a recent study at the University of Manitoba, 25 and 36 mm long BFP were used at a single dosage of 2.5% by volume to develop high performance FRCC comprising 54% cement, 40% slag and 6% nano-silica [Mahmoud *et al*., 2017]. The FRCC with 36 mm BFP had high compressive strength and improved flexural post-cracking performance and toughness, suggesting promising potential for a suite of infrastructural applications.

1.2 Need for Research

Concrete flatwork (pavements, bridge decks, industrial floors, runways, etc.) may suffer different types of distress due to the actions of loading (static, dynamic, or impact) and environmental conditions, especially temperature and moisture fluctuations. These include longitudinal cracking, corner fracture, curling, D-cracking, thermal cracking, fatigue cracking, transverse slab cracking, faulting, etc. [Lenz, 2011; Griffiths *et al*., 2007; T.I.C., 2002; FAA, 2004]. Therefore, patch repairs (full or partial depth) and protective overlays

are being employed as corrective rehabilitation and protection strategies for concrete flatwork. For a durable and functional repair system, the repair material should be sufficiently bonded to the base concrete, resistant to cracking, and have low permeability to prevent the ingression of moisture, salts, or aggressive chemicals that may result in aggravated deterioration. Repair systems include high performance materials such as latex modified concrete, micro-silica concrete and epoxy toppings. Current studies dealing with high performance FRCC for flatwork applications is growing due to its promising potential.

Over the last three decades, significant research on HPFRCC has been performed to address the brittleness of plain concrete. Multiple types and geometries of fibers (e.g. steel, polyvinyl alcohol) have been used with different binders' formulations (GU cement, silica fume, fly ash, slag, etc.) and range (0.14 to 0.35) of water-to-binder ratios (w/b). Such composites have a wide range of compressive strength (40 to 150 MPa) and different ductile behavior (strain softening or hardening) when subjected to tensile stresses [e.g. Douglas and Billington, 2005; Mechtcherine et al., 2012; Yang and Li, 2014]. For example, after first-cracking, these composites may develop high tensile ductility, within the range of 3 to 7% [Zhou et al., 2012], compared to conventional concrete which fractures at approximately 0.01% tensile strain [Wang, 2005]. With the advent of nano-materials and new types of fibers in FRCC, it is imperative to understand its fundamental behavior with respect to flowability, mechanical strength, volume stability, and durability to aggressive conditions. Various types of fibers (e.g. steel, glass, polyvinyl alcohol) have been used in HPFCC with different binders (plain cement, or cement blended with supplementary cementitious materials (SCM): fly ash, slag, silica fume, etc.) at a content of (350-1250 kg/m3) and water-to-binder ratios (w/b) (0.14 to 0.35) [e.g. Jiang *et al*., 2018; Curosu *et al*., 2016]. Nano-modified binders have been used to produce cement-based materials with

high-volume SCM, to mitigate the technical limitations associated with slowly reactive SCM (e.g. fly ash, slag) on early-age properties. For example, the incorporation of nano-silica with fly ash or slag significantly reduces the initial and final setting times and improves the early-age strength of concrete, due the accelerated hydration and pozzolanic reactivity of the nano-modified binder [e.g. Ghazy *et al*., 2016; Zhang and Islam, 2012].

The selection of the fiber types in HPFRCC depends on the fibers' quality, dispersibility and interfacial properties with the cementitious matrix. Basalt fibers are a relatively new type of fibers, presenting a feasible option for the concrete industry, owing to their favorable mechanical properties and cost relative to other types of fibers (e.g. glass). Basalt fibers have high mechanical properties, together with high corrosion and thermal resistance [e.g. Jiang et al., 2014], accordingly, basalt fibers have been used to reinforce cement-based materials in many studies to test their physical and mechanical properties. For example, the use of basalt fibers with different dosages (0.05% to 1% by volume) and aspect ratios (15 to 925) in cement-based materials were found to improve their tensile performance as well as control the initiation and propagation of cracks under static loading configurations [Ghazy et al., 2016; Zhang et al., 2017]. However, the vulnerability of basalt fibers to alkaline environments represent a huge stumble against their employment in cement-based materials (pH of 11-13) [Lee *et al*., 2014]. Sim and Park [2005] investigated the influence of constantly submerging basalt fibers in 1N NaOH solution at 40°C for a duration ranging between 7 and 28 days. Due to significant degradation of the basalt fibers, 50% and 80% reductions in tensile capacity of fibers were observed at 7 and 28 days, respectively.

Few studies reported on the dynamic behavior of cement-based materials reinforced with basalt fibers. For instance, Li and Xu [2008, 2009a] reported that 0.1% basalt fibers

by volume improved the performance of normal concrete (35 MPa) in terms of dynamic compressive strength and energy absorption capacity, where the size of the fracture pieces of the basalt fiber reinforced concrete were larger relative to that of reference concrete. Zhang et al. [2017] studied the impact behavior of concrete (compressive strength of 25, 35 and 45 MPa) reinforced with low contents of basalt fibers (0 to 0.25% by volume) under various high strain rates (30 to 95 s-1) using Split Hopkinson Pressure Bar (SHPB) apparatus. It was found that as the fiber content increased, the toughness of the basalt fiber reinforced concrete was improved, while the fiber content of 0.1% led to the highest compressive strength [Zhang et al., 2017]. However, these studies did not consider other binder formulations (e.g. nano-modified binders), novel basalt fiber types, and linkage of bulk trends to fiber/matrix interaction.

Highly alkaline media represent an aggressive exposure that could affect the microstructure and mechanical properties of cement-based materials incorporating vulnerable types of fibers (e.g. basalt fibers). Along with the high alkalinity of the matrix pore solution, concrete elements can be exposed to the ingress of external alkaline chemicals (e.g. sodium chloride, hydroxide, and carbonate) from soil, groundwater, or de-icing salts. Few studies investigated the effect of alkaline loading on HPFCC. For instance, Sahmaran and Li [2009] studied the effect of 1 N sodium hydroxide solution at 38°C for 30 and 90 days on HPFCC (55% and 70% fly ash replacement by mass of the binder [1250 kg/m^3], *w/b* of 0.26 and 2% polyvinyl alcohol fibers by volume). Slight to intermediate loss of tensile ductility (13% to 21%) were reported according to the state of specimens (un-cracked or pre-cracked). Basalt fibers maybe coated by a polymeric resin (e.g. epoxy, polyamide), termed as mini basalt bars or basalt fiber pellets (BFP) to protect them from

the surrounding environment [Mahmoud *et al*., 2017]. As of yet, whether this form of basalt fibers in HPCC can fully resist alkaline environments has not been investigated.

Furthermore, accelerated deterioration of exposed concrete elements such as highway pavements and bridge decks is a key issue in cold regions, due to recurring freeze-thaw cycles and prevalent use of de-icing salts. This deterioration is linked to physical mechanisms (frost damage, salt crystallization) [Scherer, 1999; Valenza and Scherer, 2006] and/or chemical interaction of high concentration de-icing salts with the hydration products of cement paste resulting in voluminous reaction products and disintegration of the matrix [Peterson *et al*., 2013]. Limited information has been reported on the performance of HPFCC under freezing-thawing cycles with deicing salts of HPFCC [e.g. Şahmaran and Li, 2007; Zhu *et al*., 2012]. For instance, Sahmaran and Li [2007] investigated the mechanical and salt-frost scaling resistance of non-air entrained HPFCC after a typical exposure (25 and 50 cycles subjected to 4% calcium chloride solution), according to ASTM C672. The composites incorporated a total binder content of 1250 kg/m3 (two binder formulations of fly ash/cement ratio 1.2 and 2.2), w/b of 0.26 and 2% fiber content (polyvinyl alcohol fibers). High resistance to surface scaling and high residual tensile capacity of the composites were reported after this exposure. Yet, there is scarce data [e.g. Azzam et al., 2019] on the freeze-thaw resistance (without/with different concentrations of deicing salts) of HPFCC incorporating basalt fibers or BFP.

The overall performance of cementitious rehabilitation systems including FRCC depends on the bonding and compatibility between the repair material and the existing/parent concrete, which is a critical issue for many repair materials. Hence, in order to successfully employ a new repair material in heavy duty and harsh environmental exposed application, the rehabilitation system should be designed to deform monolithically

with substrate concrete to ensure the integrity of the composite section and load transfer between layers of the assembly [ACI PRC-546R-14; ACI PRC-325.13-06].

This doctoral thesis presents a part of an ongoing program led by the Cementitious Materials Research Group at the University of Manitoba. The first phase of this project investigated the behavior of high-strength nano-modified cementitious composites incorporating 6% nano-silica with 40% slag and reinforced with a new type of fibers (BFP) [Mahmoud *et al*., 2017]. The developed composites showed improved mechanical performance, suggesting their suitability for a suite of infrastructural applications such as flatwork systems. However, various aspects still require further investigation in order to fully exploit this innovative composite in infrastructure and flatwork applications and identify performance risks/limitations, if any. These aspects include the inclusion of higher dosages of BFP, and their interaction with other binder formulations (e.g. comprising higher volumes of fly ash or slag), with and without the incorporation of nano-silica, as well as the bond properties of pellets/matrix interaction. In the same context, the durability of these composites under different mechanical, chemical and environmental conditions still needs to be explored, especially concerning the influence of nano-silica on the evolution of the microstructure, BFP vulnerability to degradation, and self-healing potential of these innovative composites. In addition, the volume stability, bonding and compatibility of these composites with substrate concrete are still unknown. Hence, the motive for this doctoral research.

1.3 Objectives of Research

To respond to the aforementioned research needs, the fundamental theme of this research program is to develop high performance cementitious composites reinforced with a novel

basalt fiber form termed as basalt fiber pellets and its suitability for flatwork applications. The specific objectives of this doctoral research are to:

- develop nano-modified cementitious composites containing high-volume fly ash or slag reinforced with innovative BFP and provide fundamental data on their fresh and hardened properties;
- evaluate the performance of the developed composites under different and severe loading configurations, as well as investigate the BFP/matrix interfacial bonding properties and correlate it to the bulk properties of the composites;
- explore the influence of nano-silica, binder configuration and BFP on the durability performance of the developed composites under aggravated exposures for un-cracked and pre-cracked specimens, in addition to evaluating their self-healing potential;
- investigate the thermal and elastic compatibility as well as bonding behavior of the cementitious composites with substrate normal concrete paving mixture, to evaluate their suitability for repair and overlay of flatwork applications under normal and aggravated exposures; and
- examine the mechanical compatibility of the composites with normal concrete substrate through a flexural overlay assembly as well as the influence of reflective cracking on its mechanical performance, and further verify the results through numerical modeling with parametric analysis of selected variables.

1.4 Scope of Research

To achieve the objectives of this research, the research work involves both experimental and numerical studies as described below:

- *Providing fundamental data on nano-modified cementitious composites reinforced with innovative BFP and incorporating 50% SCM (slag or fly ash)*: The effect of varying the binder type and dosage of BFP on the fresh (slump flow, slump retention, air content and setting time), hardened (compressive strength, flexural strength and toughness) and durability (penetrability and frost scaling) properties pertinent to flatwork applications were evaluated. Six different mixtures were cast and tested. Furthermore, thermal and microscopy studies were performed to track the hydration evolution and microstructure of the composites.
- *Exploring the behavior of the developed cementitious composites under low and high strain rates loading configurations:* The cementitious composites were tested in quasi-static (direct tension and compression) and high-speed dynamic (compression splitting configuration) loading scenarios. The dynamic loading in this work was achieved through Hopkinson bar in the splitting configuration. In order to have a deeper insight of the material performance under various loading speeds, micro-scale tests were performed additionally, to study the strain-rate dependency of the bonding behavior between the BFP and the developed matrices. These tests comprise the single fiber pull-out test coupled with scanning electron microscopy analysis.
- *Studying the durability of the developed composites for cracked and un-cracked specimens as well as its self-healing prospect under aggravated exposures:* This was achieved by performing aggravated durability tests. Salt-frost resistance of the composites was investigated according to ASTM C666 exposure cycles protocol except for using high concentration saline solution instead of fresh water, where cracked and un-cracked prisms were tested. In addition, the resistance of the mixtures to a highly alkaline solution at a high temperature were assessed. The assessment criteria for the

resistance of cementitious composites to such exposures was carried out through determining the physical properties as well as residual flexural strength of prismatic specimens after the aggravated exposure regimes. Moreover, the self-healing ability of cracked specimens was studied, with respect to the effects of the high replacement level of SCM with nano-silica. This was performed by monitoring the crack widths through an optical microscope and identifying the hydration deposits in the cracks through scanning electron microscopy coupled with elemental dispersive X-ray analysis; furthermore, the residual flexural strength of cracked concrete prisms were determined after the exposures.

- *Investigating the potential of employing cementitious composites in repair/overlay applications:* The thermal and elastic compatibility between the repair/overlay material (cementitious composites) and substrate concrete were studied. The bond strength of the composites was further investigated through pull-off test (pure tensile stresses at the interface) after normal and aggravated exposures. The experimental program was conducted to evaluate the different variables comprising four types of overlay binders, two BFP dosages, and three interface treatments, where the substrate layer surface was mechanically roughened to improve the interface between the two layers. This was coupled with thermal and microstructure studies to verify the bulk properties' trends.
- *Examining the flexural performance of the cementitious composites as a concrete bonded overlay:* The mechanical compatibility was studied through beam flexural test (combination of shear and compressive stresses at the interface) to evaluate the bond strength between the overlay layer (cementitious composites) and substrate normal concrete paving mixture. Subsequently, a complementary modeling study using the finite element method (FEM) was performed to simulate the bond behavior between

cementitious composites' topping layer and concrete substrate layer using ANSYS software package. The FEM was then calibrated and validated against the experimental data obtained. Thereafter, the model was used to conduct a parametric study on key parameters including substrate compressive strength and overlay thickness.

1.5 Original Contributions

The current Ph.D. thesis introduces an integrated approach for rehabilitation of infrastructure and flatwork applications based on the next generation of high-performance cement-based materials engineered with nano-particles and innovative fiber class, as well as providing systematic knowledge and extensive data on such HPFRCC, and its suitability to be employed in repair/overlay applications. The outcomes of this work will contribute to the scientific and engineering communities as follows:

- Developing novel high performance cementitious composites and providing large pool of data on such composites amalgamating nano-silica particles and innovative form of basalt fibers (BFP), based on key mixture variables (different binder formulations, nano-silica, BFP dosage) and their influence on the composites' performance.
- Providing detailed information about the static and dynamic behavior of the cementitious composites that fits in different heavy-duty flatwork and infrastructure applications, as well as providing deep insight on the BFP/matrix interaction properties and their sensitivity/dependency on the applied loading rates.
- Generating scientific data on the durability potentials of the cementitious composites under aggravated exposures, and their self-healing potential. This helps in the proper design of new construction or rehabilitation of infrastructure usually encountering such harsh conditions;

- Demonstrating the thermal, elastic and mechanical compatibility of the studied cementitious composites with normal concrete paving mixture after normal and severe exposures, as well as presenting the influence of using different interfacial treatments for the substrate layer including misting, commercial bonding agent and nano-silica emulsion on the integrity of the rehabilitation system.
- Developing 3D finite element models and numerical data for simulating the behavior of the nano-modified cementitious composites incorporating the optimum BFP dosage (4.5%), in an overlay system over normal parent concrete, including parametric study on the influence of the substrate layer strength and overlay layer thickness on the performance of the rehabilitation system.
- Offering a high performance cementitious composites alternative with balanced fresh, mechanical and durability properties that suits different repair and overlay applications for infrastructures such as pavements and bridge decks.

1.6 Structure of the Thesis

This thesis consists of eight chapters as described below:

- **Chapter One** contains introduction, problem definition/research significance, objectives, scope of work, and contributions of the proposed research.
- **Chapter Two** presents literature review on basalt fibers, FRCC and their dimensional stability, bond properties of FRCC to cementitious composites/concrete, and repair systems.
- **Chapter Three** presents the results and discussion to evaluate the behavior of the nano-modified cementitious composites reinforced with BFP in terms of the fresh and hardened properties as well as the complementary thermal and microscopy studies.

- **Chapter Four** describes the test results and discussion for the developed composites subjected to quasi-static and high-speed dynamic loading schemes, as well as the pellets/matrix bonding properties.
- **Chapter Five** describes the test results and discussion for the durability characterization of the studied composites after aggravated exposures as well as self-healing potential for cracked specimens of the developed composites.
- **Chapter Six** introduces the test results and discussion for the thermal and elastic compatibility of the studied composites with substrate concrete as well as its bonding strength after normal and aggravated exposures with the parent concrete.
- **Chapter Seven** presents the test results and discussion for the flexural performance of overlay assembly with the studied composites as a topping layer over substrate concrete layer; in addition to the finite element modeling and its validation against test results, as well as the results of a parametric study.
- **Chapter Eight** provides a summary of the research findings, concluding remarks based on the test and modeling results and recommendations for future research.

CHAPTER 2: LITERATURE REVIEW

The demand for long life and sustainable infrastructure these days poses new challenges for developing high performance materials that can be implemented in the civil engineering field. Concrete had a vital role in developing the existing infrastructure, owing to its acceptable performance and relatively low cost besides its flexibility in the production and manufacturing processes, which made it to be among the most commonly used materials around the world. Recently, more comprehensive approaches were used to enhance the material performance, trying to overcome some of the drawbacks and developing concrete of higher performance to meet the requirements, which are generally not available in the traditional concrete. Limited ductility and durability are considered the most important areas of interest in the concrete structures improvements from the materials point of view, where incorporating fibers are considered an interesting approach [Li, 2004].

2.1. Overview on Cementitious Composites

High performance fiber reinforced cementitious composites (HPFRCC) are part of the family of fiber reinforced concrete (FRC). It offers pseudo-tensile strain hardening behavior, multiple cracking, in some cases, and relatively high levels of strain. In the last three decades, a large number of formulations have been reported, to understand the interaction of fiber/matrix and to achieve high performance materials at a competitive cost. The production of high performance cementitious composites, incorporating different types of fibers for better performance and considerable amounts of industrial by-products, yields improved structural performance, reduced energy demand, and limited maintenance cost during its life cycle. In order to develop such composites, the mechanisms that govern the fracture behavior of the matrix incorporating fibers as well as fiber/matrix interaction besides the production process, have to be well understood [Li, 2004]. For example, the

unstable propagation of a material pre-existing crack controls the tensile capacity of a brittle material, which is well known. On this basis, it will be possible to determine the material properties and microstructure, which govern the composite behavior. Therefore, micromechanics serves as a bridge between the composite properties and the material constituents. The resulting information can be utilized in composite design approaches [Li, 1998].

Generally, high-performance cement-based materials, concerning their superior mechanical performance, can be roughly divided into two main categories: high-compressive-strength and high-ductility cementitious composites such as strain hardening cement composites (SHCC) and engineered cementitious composite (ECC), as well as some high-performance cementitious composites reinforced with fiber (HPFRCC). High-compressive strength cement composites can be used effectively to reduce the structural member's size besides providing an additional margin of strength safety for reinforced concrete structures. High ductility cementitious composites, generally, can preserve a portion of its tensile strength under considerable deformation and improve the structure's reliability when extremely loaded occasionally (e.g. earthquakes, impact, blasts, hurricanes, etc…) [Li, 2004].

ECC is a synthetic grade of high-tensile-ductile cement based materials mostly reinforced with fibers, where it has been investigated widely since it was introduced by Li and coworkers in the 1990s [Ma *et al*., 2015]. ECC is also known as high performance fiber reinforced cementitious composites (HPFRCC) and strain hardening cementitious composites (SHCC), where it is designed based on the micromechanics theory. ECCs have a tensile strain capacity of more than 3% while keeping the volume of the used fibers not more than 2% [Li, 2004]. ECCs are characterized by their high ductility which is about

several hundred times that of conventional concrete or even fiber reinforced concrete (FRC). ECCs possess multiple cracking behaviors during the strain-hardening process with limited micro-crack width of less than 100 microns, making it a highly durable material in different environmental conditions [Li, 2004].

2.2. Composition

HPFRCC is considered to be a part of the fiber reinforced concrete (FRC) family. It has a pseudo-tensile strain hardening behavior; relatively high strain levels with multiple cracking formations. In the last 30 years, a huge number of mixtures formulations have been introduced (e.g. **Table 2.1**), to understand fiber-matrix interaction behavior and to achieve a competitive cost material with high performance. These enhancements were attributed to the optimization of the fiber volume, matrix formulation including the use of supplementary cementitious materials (SCMs).

One of the key aspects of this development process is the selection of the right fiber type; where a wide variety of fibers have been adopted in the HPFRCC formulations such as steel, carbon, polypropylene, polyvinyl alcohol, and aramid. Moreover, using SCMs is an essential direction towards developing sustainable materials. HPFRCC mixtures are characterized mainly by the absence of coarse aggregate, besides the high volumes of powder materials especially fly ash and slag [Li, 2004]. Strain hardening cement based composites (SHCCs) is the most common type of high performance cementitious composites (HPCC) besides other types such as textile-reinforced concrete.

Table 2. 1: Exemplar mixtures proportions per cubic meter

Mixture ID.	Cement (kg)	Fly ash (kg)	Slag (kg)	Water* (kg)	Fibers (Volume)	Fine aggregate (kg)	HRWR (l)
1	560	675	---	315	2%	450	3.8
2	381.6	890.4	---	318	2%	462	15.3
3	381.6	763.2	127.2	318	2%	462	15.3
4	381.6	636.0	254.4	318	2%	462	15.3
5	381.6	508.8	381.6	318	2%	462	15.3

1 [Halvaei *et al*., 2014] and 2-5 [Zhu *et al*., 2012]

SHCCs reinforced by short fibers represent relatively a new class of construction material, which possesses pseudo strain hardening behaviour through multiple cracks formation when loaded in tension. The high strain capacity and ductility of SHCC provide this material with a large potential to be used in applications where high, non-elastic deformations are required as shown in **Figure 2.1**. Some of the most suitable applications are concrete structures strengthening and repair. The mechanical performance of SHCC subjected to tension is very unique, where after exceeding the first-crack stress, fibers start to take over the load-bearing function and permit a further tensile strength capacity, the gradual multiple cracks formation result in a decrease in the composite stiffness. SHCC fails due to exceeding the load-bearing capacity of the used fibers or the pullout of the fibers from the matrix at the weakest crack location and softening takes place [Mechtcherine, 2013].

SHCC material design is based on the mechanical behavior of the interaction between the matrix and the fibers through an interface. One of the important aspects in the material design basics is to use fine fibers which are homogeneously distributed through the matrix as well as modifying the matrix strength and the strength of the matrix/fiber interfacial bond in order to achieve a steady-state cracking behavior. When this interfacial zone is weak, there would be a huge risk of early fibers pull out, yet, when the interfacial

bond is significantly enhanced, fibers break which leads to premature composite failure. The required well fiber distribution makes it mandatory to use only aggregates in the form of fine sand. Micro high-density polyethylene and polyvinyl alcohol fibers with relatively high aspect ratios were considered the most suitable fibers for reinforcement of the HPCC. Correspondingly, the mixture consistency is very crucial to guarantee the required homogeneous fibers distribution within the matrix [Mechtcherine, 2013].

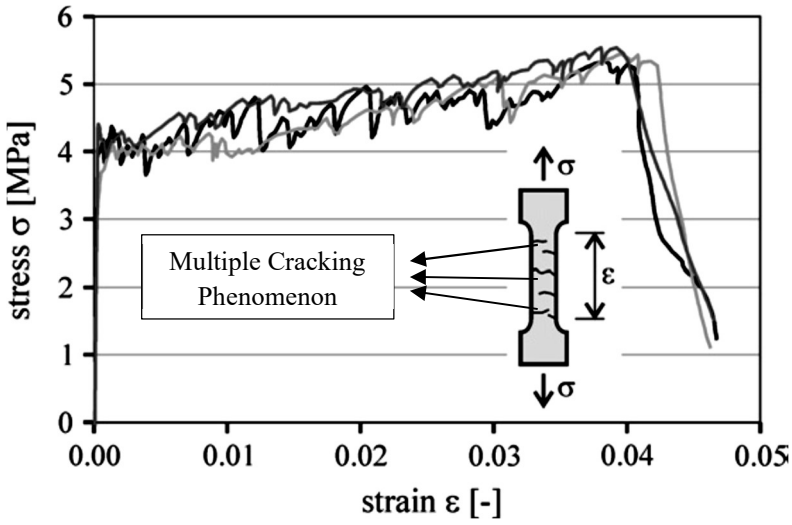

Figure 2.1: Typical stress-strain curve of SHCC subjected to tension [adapted from Mechtcherine, 2013]

2.3. HPCC Properties

The main purpose of using fiber reinforcement in cementitious composites is to enhance its brittle nature through bridging the cracks when subjected to tensile loading besides arresting the cracks growth and coalescence. The use of fibers has proved to enhance the material flexural and shear strengths as well as the ductility, impact resistance, and fatigue, in addition to reducing permeability and controlling shrinkage cracks.

The efficiency of using fibers depends on many factors, including the matrix properties in addition to the fiber type, geometry, volume, size, and dispersion, however, fibers might inversely affect the workability of cementitious materials. In addition, the use

of fibers might make the mixing process more difficult, leading to excessive voids content besides high risk of clumping and fiber clustering. To improve effective utilization of fiber reinforcement, the fresh characteristics of the cementitious composite have to be controlled to improve its fresh state and keep the superior hardened properties unaffected [Kuder *et al*., 2007].

2.3.1. Rheological Properties

Fresh properties of cementitious composites can be identified using the mixture rheological parameters. Regarding cementitious composites, rheological parameters are very useful tool to determine different workability aspects such as pumpability, placeability, compactability and finishability; where each application needs specific rheological properties. Understanding the rheology of cementitious composites enables tailoring the mixture design to fit the desired applications, including advanced concrete systems like FRC. Different models exist describing the rheological properties of cement-based systems. Bingham model is the most commonly used, which is given by **Equation 2.1**:

$$\tau = \tau_0 + \mu_0 \gamma \qquad \textbf{(Equation 2.1)}$$

Where τ_0 is the Bingham yield stress, identifying the stress required to start the flow, μ_0 is the Bingham plastic viscosity representing the material resistance to flow, while γ and τ represent the shear rate and stress, respectively.

Typical shear stresses vs time relation for cement based materials under constant rate deformation is presented in **Figure 2.2**. Peak, as well as equilibrium stress, can be observed because of the material thixotropic nature. When subjected to a constant rate of shear stress, time-dependent viscosity reduction occurs; this is attributed to the material microstructural breakdown. Once removing shear stress, the microstructure rebuilds again.

Generally, protocols of rheological measurement are based on either the value of the equilibrium stress or the peak stress [Kuder *et al*., 2007].

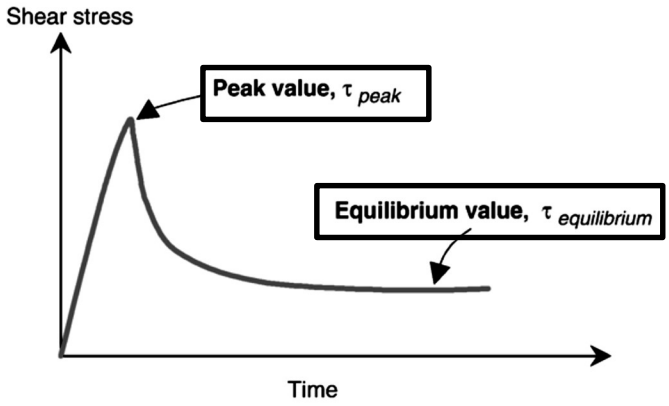

Figure 2. 2: Equilibrium and peak values for shear stress at a constant rate [adapted from Kuder *et al*., 2007]

In the same context, some simple tests were adopted in different studies to determine the workability of cementitious composites such as spread flow test and flow retention test using flow table to provide general insight on the composites rheological properties [e.g. Felekoglu *et al*., 2014; Mahmoud *et al*., 2017]

2.3.2. Mechanical Properties

As previously mentioned, cementitious composites are characterized by their high ductility as well as controlled crack width. Unlike traditional and fiber reinforced concrete, HPCC (such as ECC) exhibits strain-hardening behavior under tension loading beyond the first cracking stage resulting in a high ductility and strain capacity within the range of 3–7%. The crack width is usually controlled optimally at 60 microns without any steel reinforcement [Zhou *et al*., 2012]. The superior mechanical properties of cementitious composite materials, especially when subjected to tensile governing stresses loading like flexural loading, motivated many researchers to work in such direction trying to further

enhance its mechanical behavior through improving the manufacturing process or using different fibers types, or even manipulating with mixing proportions and materials.

Some researchers investigated the influence of modifying the manufacturing procedures on the ECC performance. Zhou *et al*. [2012] studied the effect of modifying the mixing sequence on the fibers distribution and mechanical performance. An innovative approach of mixing sequences was introduced to enhance the fiber distribution. In the standard mixing procedures, fibers were introduced after all liquid and solid materials were mixed, where the plastic viscosity of the mixture before the addition of fibers may result in a poor distribution of fiber and cause limited hardened performance. Thus, in the modified mixing procedures, the solid and liquid materials were divided into two fractions. The first fraction was mixed then fibers were added, subsequently, the second portion of liquid and solid materials was added. Furthermore, the effect of various sequences of water mixing was studied via comparing the fiber distribution analysis and uniaxial tensile test experimental results. The adjusted sequence was reported to improve the maximum tensile strength and the tensile strain capacity of the ECC mixtures as presented in **Figure 2.3**, as well as the distribution of fibers [Zhou *et al*., 2012].

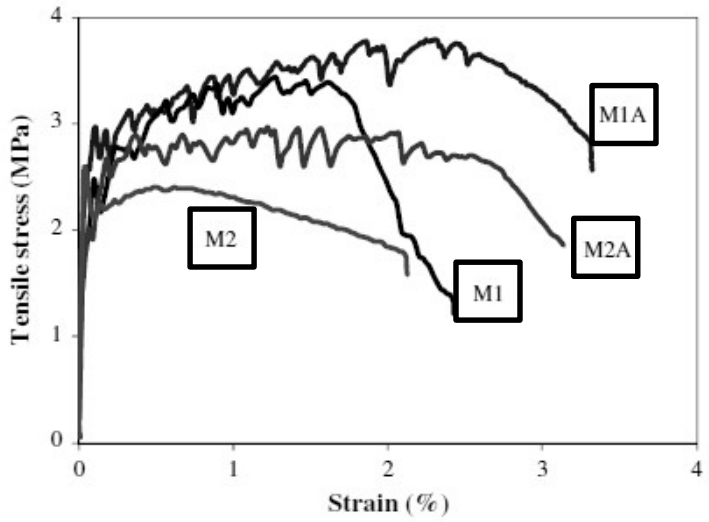

Figure 2. 3: Uniaxial stress–strain curves for four mixtures subjected to tensile load after 28 days from casting, where notation (1, 2) refers to the mixture and (A) refers to the modified mixing sequence [adapted from Zhou *et al*., 2012].

Other researchers investigated the effect of incorporating different minerals in the cementitious composite mixtures to improve the matrix, taking into account that the most common minerals used are fly ash and slag [e.g. Yang *et al*., 2007]. Zhu *et al*. [2012] studied the influence of using 70% of powder content as a combination of mineral admixtures including fly ash and ground granulated blast furnace slag as presented in **Table 2.2**. It was found that ECC using mineral admixtures combination could achieve the required strain-hardening performance as well as tensile strain capacity of more than 2.5% after 90 days. Meanwhile, relative to ECC with only fly ash, the combination of slag and fly ash increased effectively the ECC compressive strength, specifically at early ages. For instance, the compressive strength of the mixture with 40% fly ash and 30% slag was 45% and 60% higher than that of its counterpart with 70% fly ash of the total binder [Zhu *et al*., 2012].

Table 2.2: Mixtures proportions [Zhu *et al*., 2012].

Mixture ID	PC (kg)	FA (kg)	Slag (kg)	Sand (kg)	Water (kg)	HRWR (l)	PVA Fibers (kg)
ECC 70-0	381.6	890.4	0	462	318	15.3	26
ECC 60-10	381.6	763.2	127.2	462	318	15.3	26
ECC 50-20	381.6	636.0	254.4	462	318	15.3	26
ECC 40-30	381.6	508.8	381.6	462	318	15.3	26

One of the attractive trends in this field is studying the influence of using different types of fillers and fine aggregate on the mechanical behavior of cementitious composites such as nano-silica, nano-titanium, nano-carbon tubes, glass cenospheres, and other fillers [e.g. Hanif *et al*., 2017]. Other studies focused on the effect of fiber type on the mechanical performance of cementitious composites like steel fibers, carbon fibers, polypropylene fibers, polyvinyl alcohol fibers and others, where the interfacial zone at the fiber matrix interface is the most effective parameter on the overall performance [e.g. Pan *et al*., 2015; Xu *et al*., 2021].

2.3.3. Durability Properties

Since ECC's main advantage is its excellent tensile ductility, this material would likely be employed in structures expected to experience large deformations. This requires the structure to remain serviceable when the material suffers from multiple micro-cracking accompanied by the tensile strain hardening. Accordingly, the durability examination of ECC has to be performed in both states of un-cracked and cracked after deformation. Thus, ECC specimens are preloaded to different strain levels to create the micro-crack damage, prior to any accelerated durability tests. The experimental data determined from these preloaded specimens are considered to be the material durability behavior under combined environmental and mechanical loading. It should be considered that most of these tests

were performed on cracked specimens in the unloaded condition for convenience of experimental testing, which is not simulating the material condition in real structural service as it would be exposed to both loading and environmental exposure at the same time [e.g. Şahmaran and Li, 2007; Şahmaran and Li, 2008].

A number of studies has been conducted in this critical area trying to better understand the durability behavior of the HPCC. Li *et al*. [2003] conducted frost resistance test on ECC and concrete prism specimens for 14 consecutive weeks. After five weeks (110 cycles), the traditional concrete specimens suffered from severe deterioration, which resulted in the termination of the test for those specimens as required by ASTM C666. Contrarily, ECC specimens managed to survive the test exposure for 300 cycles without degradation. As a result, the durability factor of concrete and ECC specimens were 10% and 100% respectively. Regarding uniaxial tension performance, ECC coupons of specimens after freeze-thaw and wet curing exposure at similar age had no significant reduction in the strain capacity at the end of the exposures [Li *et al*., 2003].

Sahmaran *et al*. [2012] studied the effect of using high fly ash volumes and micro poly-vinyl-alcohol fibers on freeze-thaw resistance as well as the microstructure features of the developed ECC mixtures. Two different fly ash (FA) to cement ratios were investigated at a constant *w/cm* of 0.27. In order to study the behavior of the ECC matrix, the durability and microstructure properties for ECC mixtures as well as mortar mixtures of the studied ECC mixtures without fibers were investigated. Regarding freeze-thaw resistance, the specimens were exposed to 300 freeze/thaw cycles according to ASTM C666. It was reported that both ECC mixtures with high FA volumes remained durable, and showed a good tensile strain capacity. While ECC matrix without fibers failed before completing the 300 cycles, where the specimens suffered from severe deterioration,

requiring removal from the testing chamber. Hence, this verifies the role of micro PVA fiber on the improved freeze-thaw resistance of ECC mixtures. It was also found that the higher the FA/cement ratio in the mixture, the higher the residual mechanical and physical characteristics with increasing number of freeze and thaw cycles [Şahmaran *et al*., 2012].

The performance of ECC was also investigated for chloride exposure of un-loaded and preloaded specimens to better understand the behavior of such materials especially if utilized in an application that would include chloride exposure. It was found that the influence of such exposure depends on the crack width from the preloading process, where the influence of chloride ions decreased as the crack width decreased. This is attributed to the reduction in the chemical bond between the fibers and the matrix at the interface [e.g. Sahmaran and Li, 2009]. The alkaline medium is one of the harsh exposures that ECC could suffer from during its life cycle in some applications, so number of studies had been performed to investigate its performance under such exposure. It was found that ECC suffered from an insignificant loss in tensile strength and ductility after the exposure duration, with almost no or very low risk of alkali-silica reactivity [e.g. Sahmaran *et al*., 2007].

2.3.4. Shrinkage

Shrinkage is one of the major aspects that can affect the overall performance of ECC from the mechanical and durability point of view. Whereas, the elimination of coarse aggregate, which restrain the volumetric changes such as shrinkage, leads to higher magnitudes of shrinkage, unlike conventional concrete mixtures. Number of studies have been performed in this area trying to mitigate the effect of these strains or even introduce innovative types of ECC with lower shrinkage strains [e.g. Zhang *et al*., 2009].

Kawashima and Shah [2011] investigated the effect of adding saturated cellulose fibers, in the unsealed and sealed conditions, on the behavior of cementitious materials with respect to early-age shrinkage. The sealed condition represented the autogenous shrinkage, while the unsealed condition represented autogenous shrinkage and drying shrinkage as well. Adding 1% cellulose fibers by mass of used cement showed significant cracking control of drying shrinkage. Moreover, the early-age shrinkage investigation was supplemented by a fiber dispersion analysis, where it was found that enhanced dispersion resulted in the improved properties [Kawashima and Shah, 2011].

New class of ECC with low drying shrinkage properties, excellent tensile strain capacity and controlled crack opening was introduced by Zhang et al. [2009]. The research focused on studying various cement based matrices composed of constant binder content comprising cement and fly ash with different water to cementitious materials ratio (*w/cm*) of 0.45, 0.50, and 0.55 as well as sand to cementitious material ratio (*s/c*) of 0.8, 1.1 and 1.4. Two types of cements, ordinary Portland cement used for traditional ECC matrix and the newly developed composite cement with low drying shrinkage characteristic used for new ECC matrix. The effects of varying *w/cm* and *s/c* on the drying shrinkage, tensile and early-age cracking performance of the developed composites were investigated. Results showed that drying shrinkage was significantly reduced for composites incorporating low shrinkage cementitious material, besides the composite sustained its strain-hardening behavior and multiple cracking properties. In addition, in the multiple cracking and strain-hardening stage, low drying shrinkage ECC had much smaller cracks width when compared to the conventional ECC [Zhang *et al*., 2009].

Moreover, Zhu et al. [2012] investigated the effect of using different slag contents and fly ash, 70% of the total cementitious materials content, on the mechanical behavior as

well as free drying shrinkage properties of ECC mixtures. It was reported that the incorporation of slag slightly increased the drying shrinkage, whereas the 30% slag and 40% fly ash had the lowest dying shrinkage. For instance, the mixture with 40% fly ash and 30% slag had drying shrinkage of 840 micro-strain at 28 days, while it was 1000 micro-strain for the mixture with 70% fly ash and no slag. This could be attributed to the optimized pore distribution induced by the density particle packing of the mixed binder of slag (30%) and fly ash (40%) [Zhu *et al*., 2012].

2.3.5. Impact Performance

The superior tensile load-bearing capacity beyond the first crack formation is the main distinctive property that characterizes SHCC materials. The load-bearing capacity increase is associated with multiple cracks formation, leading to excellent strain capacity. This multiple cracking behavior provides superior energy absorption under both dynamic and quasi-static loading conditions. This qualifies SHCC to be utilized in either reinforcing layer or primary material for structural elements, which are designed to exhibit high deformations from sudden mechanical loading especially impact loading.

However, SHCCs were reported to be sensitive to the strain-rate, in terms of both strain capacity and tensile strength. Thus, the influence of strain rate on the SHCC performance has to be fully understood to ensure safe structural design for structures and strengthening applications [e.g. Curosu *et al*., 2016].

The SHCC tensile behavior containing PVA fibers for strain rates up to 1 s^{-1} was investigated by Yang and Li [2014]. To assess the strain rate effect on the composite's behavior, the behavior of the individual components was analysed and it was reported that each of them was sensitive to the strain-rate. The authors showed that cement-based matrix fracture toughness, PVA fibers tensile strength as well as Young's modulus, besides

chemical bond between the matrix and PVA fibers increased with loading rates increase. It was reported that the irregular changes of the properties of the components under high strain rates resulted in violations of the multiple cracking micromechanical criteria.

The mechanical performance of a normal SHCC subjected to tensile load under high and low strain rates was studied by Mechtcherine et al. [2011]. Regarding strain rates of 10^{-1} s^{-1} and less, SHCC had a moderate tensile strength increase accompanied by decrease in the strain capacity with the strain rate increases. The strain capacity decrease could be attributed to considerable less multiple cracking formations compared with testing under quasi-static loading. Moreover, increasing the loading rate might cause fiber rupture rather than pullout, which became the more common SHCC characteristic at low rates of loading. Similar trends were observed also for tested SHCC at low speed dynamic regime at different temperatures [Mechtcherine *et al*., 2012]. However, when SHCCs were tested at high-speed regimes of strain rates ranging from 10 to 50 s^{-1}, a considerable increase of strain capacity and tensile strength were measured [Mechtcherine *et al*., 2011 (a)], considering that no multiple cracking formations were observed on the specimens.

Curosu *et al*. [2016] studied the performance of normal and high strength SHCCs comprising fine-grained cement and high density polyethylene fibers subjected to impact and quasi-static tensile loading. The tension dynamic testing of notched and un-notched cylinders was carried out using Hopkinson bar with strain rates around 150 s^{-1}. The materials responses under quasi-static and dynamic tensile loading were compared to corresponding results of normal strength SHCC incorporating PVA fibers as found in previous investigations. Cracking patterns as well as conditions of the fracture surface were investigated, to understand the differences in rate influences on the behavior of different SHCC compositions. In addition, parameters which are dependent on strain rates like

individual fibers and fiber matrix interface properties were obtained from single fiber tension as well as fiber pullout tests. Finally, the deduced results provide indications for the critical parameters for material design of SHCC impact resistant types to be used in protective overlays or structural elements [Curosu *et al*., 2016].

Mechtcherine *et al*. [2011 b] studied the performance of the SHCC materials at relatively high tensile strain rates. The results from Hopkinson bar at strain rates between 140–180 s-1 were compared with the quasi-static uniaxial tensile test results at strain rate of $0.001 s^{-1}$. This comparison was performed on the basis of the values of Young's modulus, tensile strength, and fracture energy of the tested specimen, for both notched and un-notched specimens. The differences in the material performance were illustrated through the fiber pullout resistance and crack formation phenomena as presented in **Figures 2.4** and **2.5**.

Dynamic results from Hopkinson bar showed that the good material properties, such as the quasi-ductile behaviour as well as the large capacity of energy absorption, as observed in the case of quasi-static loading, not only preserved but even improved at high strain rates of loading. The explanation of such performance leap at the high strain rates was assumed to be attributed to the formation of a huge number of microcracks orthogonal to and parallel with the direction of loading, besides the fibers extensive plastic deformations during and prior to the fiber pullout. The predominant pullout of fibres during dynamic tensile tests was unusual as the previous investigations reported, where fiber failure probably occurs when strain rates are high [Mechtcherine *et al*., 2011 (b)].

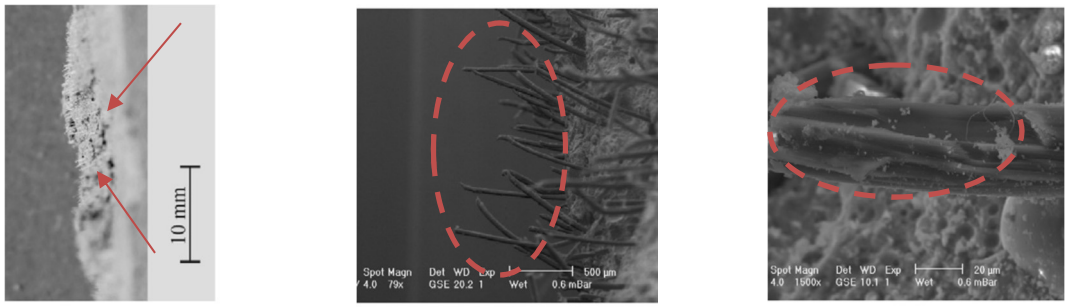

(a) (b) (c)

Figure 2.4: Fibers pullout lengths subjected to quasi-static loading (a and b), typical fiber fracture (c) [adapted from Mechtcherine *et al*., 2011 (b)].

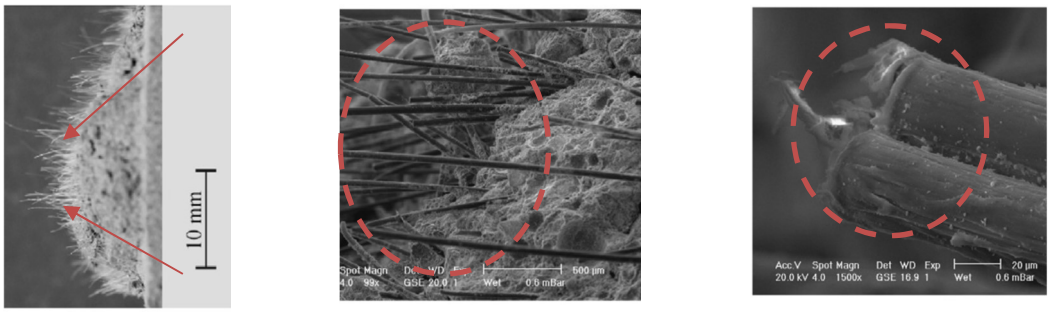

(a) (b) (c)

Figure 2.5: Fibers pullout lengths subjected to high-dynamic loading (a and b), typical fibers pulled-out (c) [adapted from Mechtcherine *et al*., 2011 (b)].

2.4. Cementitious Composites Incorporating Basalt Fibers

Recently, basalt fibers have attracted much attention in the civil engineering field as an excellent construction material owing to their high modulus of elasticity, elastic strength, temperature resistance, corrosion resistance, extended temperature range for operation as well as ease of handling. Basalt fibers are mainly used in shear strengthening, confinement purpose, flexural strengthening as well as internal reinforcement; in addition, they are used in tunnels and bridges as reinforcements. They are used also as a non-combustible material in roofing applications.

Basalt fibers are made out of a single material, which is crushed basalt rocks that has a mineral composition of pyroxene, plagioclase, and olivine. Mainly no other ingredients are added. The basalt rocks are simply washed then sent for being melted down. The basalt fibers manufacturing requires melting of quarried basalt rocks up to 1,400 °C. The molten rocks are then extruded from small nozzles in order to produce continuous basalt fiber filaments. Typically, the fibers have filament diameters between 9 to 13 μm which is far above the required respiratory limit of 5 μm, health hazard, that made basalt fiber suitable for asbestos replacement. Despite the similarity between glass and basalt fibers manufacturing techniques, basalt fiber processing is more complicated, as it has high melting point. Therefore, as a novel type of fiber, basalt fiber has to be thoroughly investigated for its properties and structure applications. Recent studies have been performed in this area to further understand basalt fibers' chemical composition as well as its mechanical, physical, and structural properties in order to provide clear basis for various further applications [e.g. Shi, 2012].

The basalt fibers production process does not produce any environmental by-product waste as well as it is biodegradable and nontoxic. This kind of fiber is non-corrosive and environmentally safe with good thermal endurance and insulating characteristics. Fiber reinforced concrete with basalt is believed to revolutionize the concrete industry owing to its cheap price, green effect, lightweight, as well as eliminating the problem of corrosion that happens to metallic fibers [Iyer *et al*., 2015].

2.4.1. Fresh properties

Various studies dealing with the different properties of cement-based materials reinforced with basalt fibers included investigation on the fresh properties of the developed composites. The most common property that is investigated in these studies is the slump

and slump flow of the composites and the influence of basalt fibers on the workability of the mixtures. As expected, the different studies revealed that the inclusion of basalt fibers negatively influenced the workability of the mixtures to a certain extent according to the mixture design and components.

For instance, Jiang *et al*. [2014] studied the various properties of FRC mixtures incorporating basalt fibers with different dosages. The researchers studied the influence of different basalt fiber dosages on the slump of the developed mixtures. It was found that addition of basalt fibers with volume fraction of 0.05%, 0.1%, 0.3%, and 0.5% caused the slump of the mixtures to fall from 185 mm for the plain mixture to 172 mm, 157 mm, 87 mm, and 65 mm [Jiang *et al*., 2014].

2.4.2. Mechanical and Microstructure Properties

Many studies have been conducted to investigate the behavior of basalt fiber reinforced concrete (BFRC) and composites trying to further improve its mechanical properties [e.g. Iyer *et al*., 2015]. Iyer *et al*. [2015] studied the effect of using basalt fibers in plain concrete of grade 30 MPa and modulus of rupture 4.1 MPa to produce FRC. The authors studied the possible enhancement in the compressive strength after 28-days as well as the modulus of rupture, taking into consideration that the modulus of rupture is a crucial aspect for flatwork applications such as pavements and industrial floors. The BFRC specimens were cast using three different lengths (12, 36 and 50 mm) of basalt fibers with three different quantities (4, 8, 12 kg/m^3 of concrete). Casting and mixing problems occurred at the higher fiber content (12 kg/m^3) due to clumping of fibers. These problems were more severe for the largest fiber length (50 mm) at the highest dosage (12 kg/m^3). The results showed that 36-mm-long basalt filament fibers with fiber content of 8 kg/m^3 had the highest performance

in terms of the modulus of rupture (5 MPa) and compressive strength (38 MPa) [Iyer *et al*., 2015].

Jalasutram *et al*. [2017] investigated the effect of varying basalt fibers volume fraction on the mechanical characteristics of FRC. The fiber amount varied between 0 and 2%. The properties investigated were compressive, splitting tensile and flexural strengths, as well as flexural toughness. Test results indicated that compressive strength of developed concrete decreased slightly with basalt fibers addition in comparison with the plain concrete. However, the FRC mode of failure under compression was converted from brittle to ductile behavior. The splitting tensile strength of concrete was enhanced by 15% when the content of basalt fibers was 2% by volume. A significant rise up to 75% was noticed in the basalt FRC flexural tensile strength, with enhanced post peak residual strength relative to plain concrete. Moreover, flexural toughness of basalt FRC was increased by almost 3 times that of plain concrete depending on round panel tests [Jalasutram *et al*., 2017].

Jiang *et al*. studied the influence of basalt fibers content ranging between 0-0.5% by volume and basalt fiber (BF) lengths of 12 and 22 mm on the mechanical characteristics of FRC. The concrete mixture proportions were shown in **Table 2.3**. Tin addition, the microstructure of basalt FRC was studied using mercury intrusion porosimetry (MIP) and scanning electron microscopy (SEM) analysis. The results showed that the addition of basalt fibers significantly enhanced the tensile and flexural strengths as well as the toughness index, where the compressive strength showed no significant increase.

Table 2.3: Concrete mixture proportions used in this study

Cement (kg)	Fly ash (kg)	Fine Aggregate (kg)	Coarse Aggregate (kg)	Water (kg)
448.84	126.14	624.35	1024.04	318

Moreover, the basalt fiber length had an influence on the mechanical characteristics. Relative to plain concrete, compressive strength, splitting tensile strength and flexural strength for BFRC (basalt fiber length 12 mm) with different dosages increased by 0.18 to 4.68%, 14.08 to 24.34% and 6.30 to 9.58%, respectively. While the corresponding strengths increase for the 22 mm basalt fiber length was 0.55 to 5.72%, 14.96 to 25.51% and 7.35 to 10.37%, respectively. Good bond between basalt and matrix interface was noticed at the early ages. However, the bond showed degradation to specific extent at 28 days. Furthermore, the MIP results showed that the basalt fiber reinforced concrete had higher porosity due to the effect of fibers [Jiang *et al*., 2014].

2.4.3. Early Age Shrinkage Control

Early age shrinkage stands for the volumetric change of cement based matrix, which occurs after placement within the first few hours while being in the plastic state. The volumetric changes are driven by autogenous mechanisms combination besides capillary pressure, which is developed in the pore structure close to the surface when the water evaporation rate from concrete exceeds the rate of water bleeding. If shrinkage is restrained, tensile stresses are induced. If the induced stresses exceed the concrete tensile strength, concrete will crack. Generally, restraints exist to some degree by internal factors in the practical applications such as aggregate, rebar, etc. or even through external factors, like connections to columns and walls. Shrinkage cracks are not only unsightly, but also they permit the penetration of the deleterious substance and can cause the structures rapid deterioration. The most notable deteriorating substances are water and chlorides (e.g. deicing salt), which stimulates the embedded steel reinforcement corrosion. Shrinkage cracks are generally very clear in structures with large surface area relative to volume ratio, such as slab-on-grade, tunnel lining, as well as overlays [Neville, 2011]

Although early age cracking from autogenous and plastic shrinkage often leads to reduction in the concrete structures durability, limited studies have been performed in this area. Branston *et al*. [2016] studied the employment of chopped basalt fibers in cracks' control for concrete mixtures as shown in **Table 2.4**. The study was performed to measure the shrinkage strain magnitude that was developed in the unrestrained state specimens, as well as the severity of cracks that forms in the restrained state. Results showed that basalt fibers succeeded effectively in cracks prevention through reducing the free shrinkage magnitude, and through restricting the formed cracks growth if any as presented in **Figures 2.15** to **2.19** [Branston *et al*., 2016].

Table 2.4: Mass proportions of concrete mixtures

Mixture ID	Cement (kg)	Fine Aggregate (kg)	Coarse Aggregate (kg)	Water (kg)
M1	1	2	0	0.5
M2	1	2	0	035
M3	1	2	2	0.5
M4	1	1	0	0.5
M5	1	1	0	0.35

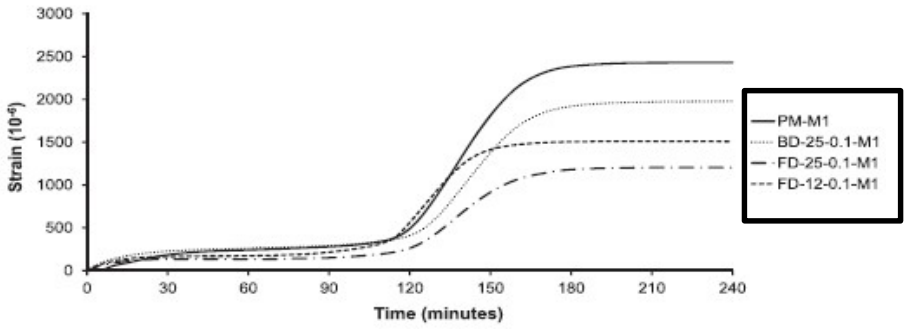

Figure 2.6: Mean curves for developed strain over time for fiber dosage of 0.1% with lengths of 12 and 25 mm [adapted from Branston *et al*., 2016]

PM: No Fibers BD: Bundled Dispersion FD: Filament Dispersion

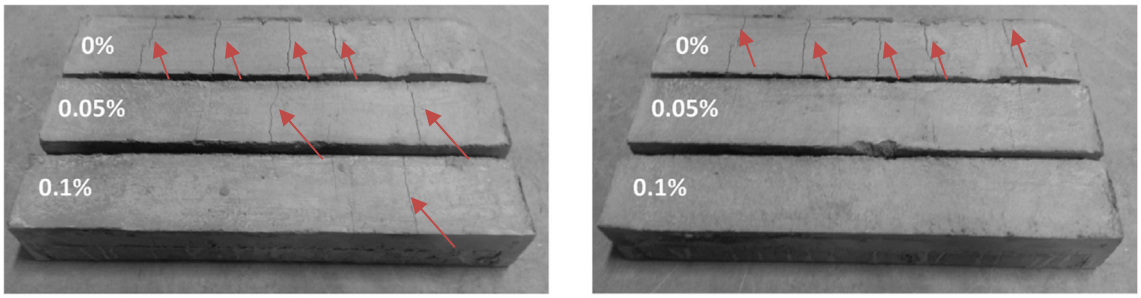

(a) BD (b) FD

Figure 2.7: Exemplar crack area reduction with increasing the fiber dosage in M4 for fibers length of 25 mm [adapted from Branston *et al*., 2016]

Other studies have been done on cement based repair mortars reinforced with basalt fiber, to control its shrinkage potential as well as the formation of the cracks due to restrained condition from old concrete. It was found to be effective to use the basalt fibers in limiting even the shrinkage strain or the formation of the cracks [e.g. Ghazy *et al*., 2016].

2.4.4. Dynamic Properties of BFRC

BFRC is considered to be a multiphase heterogeneous composite material. Besides keeping the high compressive strength advantage, it also has significantly enhanced tensile post-cracking behavior as well as impact performance. In different concrete applications, many structures are designed to resist traditional design loads besides unusual dynamic loads like explosions, impact, earthquake…etc. Hence, the study of BFRC dynamic properties under high rate impact strains is practically significant in the concrete structure dynamic analyses. Recently, basalt fibers applications in concrete to enhance its characteristics have become an attractive research area, yet, still, the studies on dynamic mechanical characteristics under impact loading needs further efforts.

Zhang *et al*. [2017] studied the BFRC impact performance with six volume contents (0 to 0.25%) subjected to different high rates of strain using 74 mm-diameter splits

Hopkinson pressure bar apparatus. The influence of fiber contents and strain rate on the dynamic compression and toughness were investigated according to stress vs strain curves derived from the experiment. Regarding the microscopic aspect, the BFRC micro-properties as well as pore structure were studied. Finally, a BFRC dynamic constitutive law was derived depending on a modified dynamic constitutive model of Zhu-Wang-Tang (ZWT), which considered the damage of the material. It was found that when subjected to impact loading, BFRC damage degree increases with the strain rate increase, where the basalt fiber toughening effect makes the concrete brittleness decrease. Moreover, the dynamic compressive strength growth is almost linear with the strain rate growth. It was reported that the optimum fiber volume fraction is different with the concrete strength grades, while the toughness of the mixtures increases with increasing the basalt fibers' dosage. Regarding the fiber/matrix interfacial bond, it was found that the concrete with higher strength had better bonding at the fiber/matrix interface [Zhang *et al*., 2017].

Zhao *et al*. [2017] studied the influence of using basalt fibers on the impact failure mechanism of concrete mixtures after freeze-thaw cycles (as shown in **Table 2.5**). The falling ball impact test on concrete beam (as per ACI committee 544) was adopted in this research. Different BF contents were studied in this research comprising 0 kg/m^3, 1.0 kg/m^3, 1.5 kg/m^3, 2.0 kg/m^3 and 2.5 kg/m^3 for a fiber length of 18 mm and diameter of 15 μm. Digital image correlation method was used to measure the field strains and perform a real time analysis. Depending on the starting crack points, strain curves and the impact times, the number of impacts for the initial cracking as well as the eventual damage were determined.

Table 2.5: Mixture proportions of the concrete per cubic meter

Cement (kg)	Fine Aggregate (kg)	Coarse Aggregate (kg)	Water (kg)
385.42	695.24	1134.34	185

It was found that as the basalt fiber volume fraction increased, the number of impacts for the specimens' initial cracking as well as the final damage was increased, where the addition of fibers created a 3-D system that could enlarge the range of transmission of the impact stress waves. This enhanced the concrete's elastic deformation behavior, and in turn the initial cracking capability of concrete to impact resistance was improved as shown in **Figure 2.8**. Regarding freeze-thaw resistance, as the number of cycles increased, the impact of the initial crack and final failure dropped, due to the reduction of the concrete specimen's elastic deformation performance because of the freezing and thawing damage [Zhao *et al*., 2017].

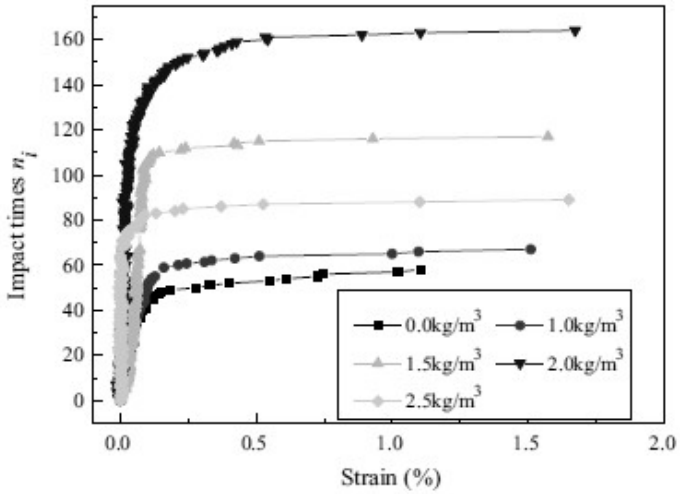

Figure 2.8: The impact times vs the strain for the mixes with various fiber contents [adapted from Zhao *et al*., 2017]

2.4.5. Alkali Resistant Basalt Fibers

Despite the high mechanical properties and cost feasibility of basalt fibers, some studies reported its degradation in alkaline media; which limited to some extent the use of such type of fibers especially in concrete [e.g. Rabinovich *et al*., 2001]. One approach was to limit the use of basalt fibers to only enhance the concrete durability through controlling the early age cracking from early age shrinkage. However, this kind of application ignores the great effect of basalt fibers on the mechanical properties of concrete. Many solutions were introduced to make use of basalt fiber properties and protect it from the alkaline mediums. One of the solutions was to provide the fibers with protective coating like polyamide resin, which was presented by Mahmoud *et al*. [2017], or using zirconia as presented by Lipatov *et al*. [2015]. In addition, one of the new trends to protect the fibers against the alkaline medium of the hosting matrix is to decrease the amount of cement by replacing it with SCM, which decreases the alkalinity of the matrix.

2.5. Applications

Owing to the superior mechanical properties of basalt fibers and cementitious composites, high performance cementitious composites incorporating basalt fibers can be utilized in a suit of repair and rehabilitation applications such as pavements, floorings, runways and bridge decks.

2.5.1. Different repair systems

Concrete flatwork restoration is a series of engineered repair techniques to manage the rate of deterioration due to mechanical and environmental loading regimes. A timely managed and appropriate program would maintain a concrete flatwork surface smoothness, safety, and quiet condition; while extending its service life economically. Corrective and preventive techniques were adopted to restore the concrete element condition close to its

original situation and reduce the need for major or more costly repairs until later in its service life. Different rehabilitation and repair techniques might be adopted such as full-depth and partial depth repairs, joints and cracks resealing, overlays, etc. to restore the performance and serviceability of aging concrete flatwork and infrastructures [Smith and Eng, 2010].

2.5.1.1. Full-depth repair

Full-depth repairs (FDR) fix cracked slabs and joint deterioration by replacing a portion of or the entire existing slab with new concrete. This maintains the structural integrity of the existing slab structure. Such technique also repairs shattered slabs, corner breaks, punch-outs, and some low-severity durability problems. It involves marking the distressed concrete, saw cutting around the perimeter, removing the old concrete, providing load transfer bars, and placing new concrete. Each repair must be large enough to replace all significant distress and resist rocking under the traffic. This technique is fast, easy, and inexpensive, as well as it can be conducted without suspending the traffic.

2.5.1.2. Partial-depth repair

Partial-depth repairs (PDR) correct surface distress and joint/crack deterioration in the upper third (1/3) of the concrete slab. When the deterioration is greater than one-third the slab depth or in contact with the embedded steel, a full-depth repair must be used instead. Placing a partial depth repair involves removing the deteriorated concrete, cleaning the patch area, placing new concrete, and reforming the joint system.

2.5.1.3. Overlays

Concrete overlays are considered to be a rehabilitation and maintenance technique that casts over existing asphalt, concrete or composite (asphalt on concrete) pavements. Concrete overlays serve as cost effective rehabilitation and maintenance solutions for

almost any type of existing pavement, condition, anticipated traffic loading and desired service life. Concrete overlays can be classified with respect to the type of the existing pavement and the condition of bonding between the two layers [Smith et al., 2002]. On this basis, concrete overlays are categorized into two families which are bonded and un-bonded concrete overlays.

Bonded concrete overlays are thin concrete layers (typically from 50 to 150 mm thick), which are bonded to existing substrate pavement. Bonded overlays are used to raise up the existing pavement structural capacity or to enhance its overall skid resistance, ride quality and reflectivity. This type of overlays should be only used when the underlying substrate pavement is free of any structural distresses and in good condition, free of cracks that would reflect through the casted layer. To serve well, the joints of the new layer should be matched with that in the existing layer. Aligned joints help to eliminate reflection of cracks as well as ensure the integrity of the two layers and that they move together and act as one unit.

Un-bonded overlays are new concrete surface layer that has a separation layer from the existing pavement. This separation layer is typically about 2.5 cm made of hot asphalt mix. Separation layer is placed to secure a shear plane which helps preventing cracks reflection from the existing substrate into the newly cast overlay. Moreover, this separation layer works on preventing the mechanical interlocking between the new layer and the already existing pavement, so that both layers are free to move independently. Un-bonded concrete overlays are almost 100 to 300 mm thick. Due to the separation layer, un-bonded overlays can be casted on existing pavements with practically any condition. However, when overlays are cast on pavements in advanced deteriorated stages or with effective materials related problems (like D-cracking or even alkali-silica reactivity), they should be

cautiously considered as expansive materials; where related deteriorations can cause the cracking of the new overlay layer. Some highway agencies assure that joints in the un-bonded concrete overlays must be mismatched with those in the substrate pavement in order to maximize the load transfer property [Taylor *et al*., 2006].

2.5.1.3.1. Overlays Cracking

Fiber reinforced cement based mixtures have been employed widely to enhance the crack resistance of the mixtures relative to plain concrete in recent infrastructure repair or rehabilitation projects. Recently, the use of fiber reinforced cement-based mixtures has grown very fast for thin and ultra-thin overlays on pavements as a pavement maintenance or even strengthening technique. Fibers are considered to be of particular benefit to overlays, as they are expected to control the crack growth and widths, minimize surface spalling, as well as increasing the wear resistance. The main function of fibers is to limit the crack widths besides reducing the rate of crack growth through the matrix by bridging the cracks when they start to open. The extent of the crack reduction has been related to the toughness and fracture energy of the mixtures. Moreover, the joint opening and slab deflection fiber reinforced pavements under traffic loadings are expected also to be reduced because of the fiber bridging effect. Generally, cracks are generated in concrete pavements due to mechanical loading as well as volumetric changes due to different environmental conditions like temperature and humidity. This creates internal stresses that result in cracking at mid-panels, joints, or even at the interface between the original sub-structure and the overlay [Kim *et al*., 2017].

Number of studies have been performed to investigate the cracking phenomena of the pavements and overlays. Carlswärd [2006] found that the crack width of FRC overlays depends on two main factors; the extent of de-bonding and the influence of fiber bridging

of the crack [Carlswärd, 2006]. Kim *et al*. [2017] worked on introducing an equation to predict the width of the early age cracks in thin concrete overlays reinforced with polypropylene fibers with fiber content of 0.5% by volume through finite element modeling and modified prediction equation. The original equation that was developed to predict plain concrete pavements' joint opening width, was modified to consider either the aspect ratio of fibers or the residual strength ratio of FRC [Kim *et al*., 2017].

The effect of cracking on the de-bonding behavior of a plain and fiber reinforced mortar overlays was studied by A.Turatsinze *et al*. [2003]. They reported that the de-bonding of the fiber reinforced repairs was significantly delayed relative to the plain repairs, where this better performance was attributed to the fibers' restraining ability of fibers to control the crack opening width within the repair layer. This helped to minimize the stresses at the substrate-repair interface [Turatsinze *et al*., 2003]. Another study was performed by Granju [1996], where the bonding behavior of fiber reinforced overlays through an experimental and modeling program was investigated. It was found that the de-bonding is mainly a coupled effect of traffic loads besides vertical cracking which is restrained in case of fiber reinforcement resulting in better bond performance [Granju, 1996]. Different types of fibers have been studied to assess their capability to restrain the growth of the cracks, which reflects on the efficiency and overall performance of overlays as well as helps to improve the design procedures of such repair method from the economical and performance point of view [Isla *et al*., 2015].

2.5.1.3.2. Overlays Bonding Behavior

The bonding behavior of cement-based overlays is one of the most important aspects when evaluating the efficiency of a certain overlay of the bonded category. The bond secures the integrity of the new layer with the old substrate as well as it guarantees monolithic behavior

of the system as the bonded overlay main function is to increase the structure capacity of the existing pavement. Owing to the great importance of the bonding performance, number of studies have been performed in this area to enhance the overall pavement performance.

Interfacial bond properties between substrate of normal concrete, and a repair material of UHPFRC were investigated by Tayeh *et al*. [2013]. Different surface preparation mechanisms of the substrate layer were adopted in the study. It was found that the surface preparation significantly affected the bond strength between the two layers, where the sandblasting was found to be more efficient [Tayeh *et al*., 2013]. Another experimental study was performed to investigate the effect of the overlay thickness on early age failure of bonded concrete overlays. A finite element model was also developed to evaluate the stress development as well as the de-bonding behavior from volume changes for different overlay thicknesses. The numerical analysis and experimental measurements demonstrated that the cracking of the overlay surface and the interfacial de-bonding are dependent on the thin overlays. In order to prevent the premature cracking, minimum overlay thickness has to be determined depending on the thermal changes and shrinkage of the concrete overlay, Moreover, the construction practices have to be selected in order to mitigate the thermal gradient and shrinkage through the overlay thickness [Shin and Lange, 2012].

Another study was performed to investigate the scenario of de-bonding of cement based thin bonded overlays. De-bonding of cement-based overlays was found to be governed by the tensile stress perpendicular to the interface between the old and new layer [Granju, 2001]. Even the influence of some construction practices on the bond behavior was studied, where the effect of substrate preparation by moisturizing on the direct shear bond strength between the two layers was assessed. The substrate layer was exposed to

various moisture conditions before overlay application. Quantitative analysis using backscattered electron imaging for the microstructure of the overlay-substrate interface was performed to quantify its characteristics and help in analysing the shear bond testing results. It was found that the common pre-wetting of the substrate layer prior to overlay application provided no benefit towards the bond strength as well as it may badly affect, in some cases, the bond strength. The microstructural studies assured that the pre-saturation of substrates increased the local w/c ratio and porosity at the interface, which was found to be of about 100 μm thickness. This interface in the overlays cast over dry substrates had higher quantity of anhydrous cement and lower porosity [Beushausen *et al*., 2017]. These efforts were done for the importance of bond strength and its influence on the overall performance of the overlay.

2.5.2. Compatibility with old substrates

Compatibility is significantly crucial for the repair and retrofitting systems. Compatibility may be defined as the balance of physical, chemical, and electrochemical properties and dimensions between repair material and existing substrate. This to ensure the resistance of the repair system to all the anticipated stresses induced by volume changes, chemical and electrochemical effects without distress and deterioration over a designed period of time (**Figure 2.9**). However, dimensional compatibility is a major problem in concrete repair systems. Dimensional compatibility impairs the durability and load-carrying capacity of structural repairs, where Dimensional incompatibility may lead to an inability to carry the expected proportion of the loads.

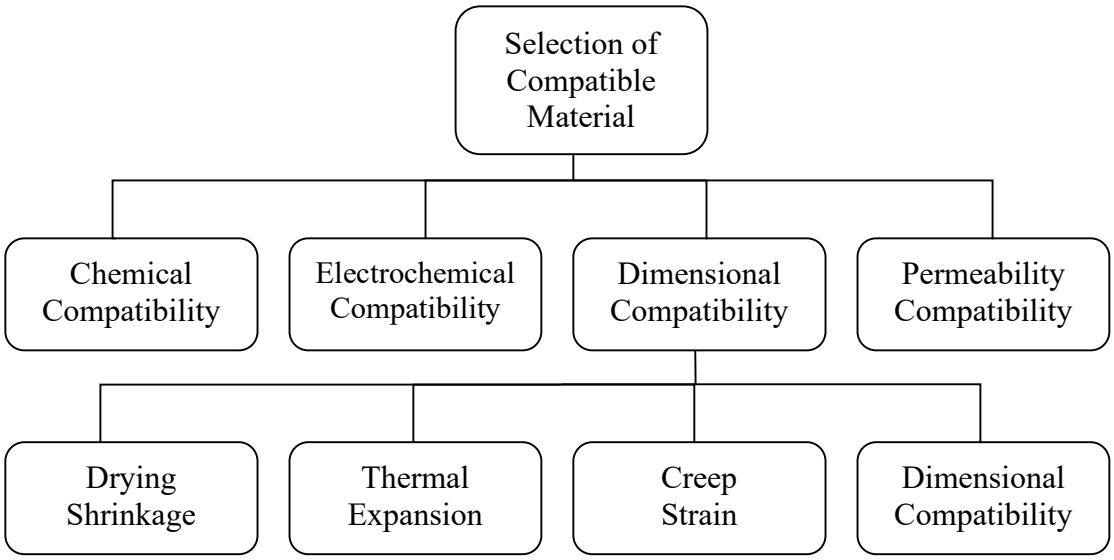

Figure 2. 9: Compatibility factors of repair systems [adapted from Emmons and Vaysburd, 1993]

Different studies have dealt with the compatibility of new repair materials and old concrete substrates for the different aspects of compatibility to study the integrity of the introduced material with the repair system [Emmons and Vaysburd, 1993]. For instance, Ghazy and Bassuoni studied the effect of incorporating nano-silica in cement-based repair material on shrinkage compatibility with concrete substrate. A series of volume stability (shrinkage) tests were conducted to evaluate the performance of nano-modified fly ash concrete as a repair material for concrete pavements. The results indicate that, despite their higher autogenous shrinkage, most nano-modified fly ash concrete mixtures exhibited low total shrinkage (free and restrained) when adequate curing was provided.

2.5.3. Modelling

Different numerical and analytical studies have been conducted to better understand the bonding performance of a repair/overlay system, dealing with the factors that might lead to the de-bonding between the layers.

For instance, Tran *et al*. studied the propagation of de-bonding along with the interface between a substrate and a cement-based thin bonded overlay. The study focussed on obtaining the data necessary for relevant and efficient de-bonding modelling. This work combined experimental and simulation investigation, where two types of overlay materials were investigated (fiber reinforced and plain mortars). Tensile tests were performed to obtain the residual normal stress–crack opening relationship. The substrate overlay interface was investigated by static tensile tests to provide the relationship between de-bonding opening and residual normal tensile stress. Three-point flexural fatigue test was performed on repaired substrate to obtain information on the structural behaviour of the interface. The de-bonding propagation was monitored by a video-microscope with a magnification of 175x. Relying on the identified and quantified parameters, the fatigue test was modelled by finite element method. An appropriate procedure of calculations was conducted to predict the fatigue behaviour of plain mortar and fiber reinforced mortar as repair materials. The numerical prediction showed that the model was an efficient tool to predict cracking and interfacial fracture behaviour [Tran *et al*., 2007].

The same research group performed another analytical study focussed on introducing an analytical approach for the prediction of de-bonding initiation between cement-based overlay and old concrete substrate under monotonous mechanical loading. Based on the linear elastic fracture mechanics, analytical model has been used. The calculations took into account the interlocking between two crack surfaces in the overlay. To validate the model, three point static bending tests on composite specimens were carried out. The de-bonding initiation was assumed to just occur after the crack cutting the overlay layer reaches the overlay-substrate interface, the stress intensity factor of the de-bonding tip could be calculated, allowing prediction of stress fields near the interface de-bonding

tip. With a criterion of de-bonding initiation and propagation depending on the interface tensile strength, the load associated could be determined and might be interesting for the design of thin bonded cement-based overlays. This analytical approach was verified by both experimental data and finite element calculations [Tran *et al*., 2011].

Kim and lee investigated the de-bonding mechanism of bonded concrete overlay due to horizontal traffic loading caused by vehicle braking and accelerating at congested section. This study investigated the de-bonding mechanism of bonded concrete overlay by means of a three-dimensional finite element analysis. A set of numerical analysis was performed to evaluate the horizontal shear stress at the interface of bonded concrete overlay according to horizontal traffic loading. It was found that the bond stresses by horizontal shear stresses did not exceed the 1.4 MPa bond strength criterion suggested by ACPA. However, the bond stresses were close to the bond strength criterion. It means that de-bonding at the interface of bonded concrete overlay might be possibly occurred by cyclic stresses due to the repetition of the horizontal traffic loading. This study indicated that bond-fatigue failure by cyclic loading is needed to be investigated as well as the bond failure caused by monotonic loading.

2.6. Closure

HPFRCC is a novel class of cement-based materials that has superior properties, which qualifies it to be utilized in different structural applications owing to its high performance. Demands for using such new innovative high strength/high ductility cementitious composites incorporating non-metallic fibers for field applications, especially repair and strengthening, have been growing to mitigate the shortcomings associated with the concrete brittleness and the corrosion of metallic fibers. Thus, it was crucial to utilize other types of non-metallic fibers with comparable properties in these composites such as poly-

vinyl-alcohol, polypropylene, and others. In the same context, basalt fibers are recently used excessively in different applications with excellent performance, which makes it a good alternative to be used in cementitious composites. Consequently, BFP represents an innovative non-metallic class of basalt fibers that showed very good potentials when used in cementitious composites comparably to the most commonly used metallic-fiber (e.g. steel fibers). However, there is paucity of research data on the application of BFP in structural application.

Repair and restoration techniques of flatwork systems aim to even just enhance the quality of the concrete slabs or/and increase the structural capacity of the substrate layer. Different cement-based mixtures with and without fiber reinforcement are being employed in these repair systems, however, those mixtures confront some problems related to mechanical and durability issues. This promotes the use of HPFRCC reinforced with BFP in these applications.

In particular, no published work has focused on investigating the effect of incorporating nano-modified cementitious composites reinforced with BFP as a repair material in different flatwork and infrastructure applications, whereas the behavior of such material when utilized in these applications under different mechanical loading and environmental exposures is still questionable. Hence, further investigations in the short/long term performance under ambient and harsh conditions of these composites are required, as it might be affected by a multiplicity of parameters including the composition of the cementitious matrix, the dosage of fiber, as well as the loading and exposure regimes.

CHAPTER 3: PROPERTIES OF HIGH-VOLUME FLY ASH AND SLAG CEMENTITIOUS COMPOSITES INCORPORATING NANO-SILICA AND BASALT FIBER PELLETS

3.1 Introduction

The service life of concrete elements (e.g. pavements, bridge decks, runways, etc.) is linked to multiple factors including the rheological, mechanical and durability characteristics of the materials used, exposure conditions and loading configurations. These interrelated parameters may provoke the initiation and propagation of cracks in concrete, and negatively influence its overall performance and longevity, especially in vulnerable locations such as joints in pavements and bridges [Jones *et al*., 2013]. Exposed concrete elements customarily suffer from different aging factors of loading and environmental schemes, especially in the presence of moisture and salts, which require periodic maintenance with high performance materials. Different rehabilitation and repair techniques and materials such as full-depth and partial depth repairs, joints and cracks resealing, high-performance cementitious composites, etc. have been recommended to restore the performance and serviceability of aging concrete infrastructure [Smith and Eng, 2010; Lepech and Li, 2010].

One of the most viable options to control cracking and improve the ductility in newly constructed or repaired concrete elements is using fibers to reinforce the cementitious matrix. Accordingly, different types of fibers, including steel, synthetic and organic fibers have been applied in cementitious composites (FRCC) to improve their flexural performance [e.g. Benture *et al*., 2006]. Addition of fibers in cementitious composites imparts positive effects on their fresh and hardened states such as reduction of bleeding and plastic settlement, controlling plastic and drying shrinkage cracks and improving impact resistance. The key advantages of high performance FRCC

are their increased deformability, residual strength beyond first cracking and toughness [Benture *et al*., 2006]. Homogenously distributed fibers can bridge and arrest cracks in the cementitious matrix, which are the main mechanisms for improving the energy absorption capacity of FRCC. This behavior depends on the type, dosage, engineering properties and geometry of the fibers, which affect the post-cracking stage through deformation, fiber debonding and pullout processes [Mehta and Monteiro, 2014; ACI 544.1R-10].

Many studies have been conducted in the area of FRCC, including the advent of engineered cementitious composites (ECC) [e.g. Yu *et al.*, 2015]. In addition, high performance FRCC, comprising cement, supplementary cementitious materials (SCMs) and nanoparticles (less than 100 nm) have been recently developed targeting various infrastructure applications including pavements and bridges [e.g. Salemi and Behfarnia, 2013; Kim and Bordelon, 2017; Zhu *et al*., 2012]. The use of SCMs, such as fly ash and slag, as a part of the binder can improve the properties of mortar/concrete, by refining the pore structure as they react with calcium hydroxide/portlandite (CH) to produce calcium-silicate-hydrate (C-S-H) gel [Neville, 2011]. However, the use of high volumes of SCMs in mortar/concrete brings about some technical limitations, including delay of hardening, strength and microstructural development [Mehta and Monteiro, 2014]. Nevertheless, these limitations can be mitigated by adding nano-silica to such binders, as it speeds up the kinetics of cement hydration at early ages by creating nucleation sites for early precipitation of hydration products as well as imparting very rapid pozzolanic activity [Kong *et al*., 2012].

Basalt fibers are a relatively new type of fibers, which are gaining momentum in the construction market owing to its good mechanical properties and low cost, compared to other types of fibers (e.g. glass). Basalt fibers have high tensile strength (3000-4000 MPa), reasonable modulus of elasticity (93-110 GPa) as well as high thermal and corrosion resistance. Hence, they

may be a good candidate for FRCC, as shown by previous studies [e.g. Ghazy *et al.*, 2016a]. Different studies have been performed on using basalt fibers with different dosages, ranging between 0.25% and 3%, incorporated in different formulations of cement-based matrices [Kizilkanat *et al*., 2015; Zhang *et al*., 2017; Iyer *et al*., 2015; Jalasutram *et al*., 2017; Ayub *et al*., 2014]. It was reported that the compressive strength was insignificantly affected by the basalt fiber dosage; however, the toughness of the mixtures was improved as the fibers dosage increased, with strain softening behavior for the mixtures up to failure.

However, basalt fibers were reported to have low alkaline resistance that made them susceptible to degradation when used in alkaline media with pH values of 11-13 [Lee *et al*., 2014; Rabinovich *et al*., 2001]. Good bonding between basalt fibers and cementitious systems was observed at early-age (7 days); however, this bond diminished within 90 days due to degradation of fibers [Jiang *et al*., 2014]. Basalt fibers are susceptible to similar mechanisms of dissolution as glass fibers in concrete, due to reactions between the silicate component in the fibers and alkaline pore solution, resulting in loss of strength and durability of the reinforced composite [Branston *et al*., 2016].

The vulnerability of basalt fibers to alkaline media can be mitigated by encapsulating them with polymeric resins, e.g. epoxy or polyamide, forming basalt fiber pellets (BFP). In a recent study at the University of Manitoba, a novel form of basalt fibers termed as basalt fiber pellets were investigated. These pellets composed of basalt fiber strands encapsulated in polyamide resin. The pellets were designed with a specific surface texture with tailored micro-grooves in the longitudinal direction of the pellets. These grooves provided host for the deposition of the hydration products, which enhance the pellets/matrix interface and improve the bonding properties.

BFP with two different lengths, 25 and 36 mm, were used at a single dosage of 2.5% by volume to develop high performance FRCC comprising 54% cement, 40% slag and 6% nano-silica [Mahmoud *et al*., 2017]. The slag replacement level (40 %) was selected to meet the requirements of the category HVSCM-2 for high supplementary cementitious materials concretes according to CSA 23.1-19 (Annex K). The FRCC with 36 mm BFP had high compressive strength and improved flexural post-cracking performance and toughness. These composites may present an attractive option for a suite of infrastructural applications, including repair and overlays of concrete pavements and bridges. However, various aspects still require further investigation in order to exploit this innovative composite in infrastructure and flatwork applications and identify performance risks/limitations, if any. These aspects comprise the inclusion of higher dosages of BFP and their interaction with other binder formulations (e.g. comprising higher volumes of fly ash or slag) with higher dosages of SCM. Hence, the primary objective of this study was to develop alternative nano-modified cementitious composites containing high-volume (50%) fly ash or slag (to meet the requirements for the category HVSCM-1 according to CSA 23.1-14 "Annex K"), in combination with different dosages of a novel form of basalt fibers (BFP) with a specific designed surface texture; as well as provide fundamental data about these composites. The fresh, hardened and durability properties of these composites were studied and the bulk trends were corroborated by thermal and microscopy studies to evaluate their performance.

3.2 Experimental program

3.2.1 Materials

General use cement (GU), slag and fly ash (meeting CSA-A3001 [CSA-A3001] requirements) were used as the main components of the binders (**Table 3.1**).

Table 3.1: Chemical and physical properties of GU cement fly ash and slag

	GU Cement [a]	Fly ash [a]	Slag [a]
Chemical analysis			
SiO_2 (%)	19.22	55.20	33.40
Al_2O_3 (%)	5.01	23.13	13.40
Fe_2O_3 (%)	2.33	3.62	0.76
CaO (%)	63.22	10.81	42.70
MgO (%)	3.31	1.11	5.30
SO_3 (%)	3.01	0.22	2.40
Na_2Oeq. (%)	0.12	3.21	0.30
Physical properties			
Specific Gravity	3.15	2.12	2.87
Fineness (m^2/kg)	390	290	492

Note: [a] The properties of the materials have been provided by the manufacturers.

In addition, a commercial nano-silica sol was used in the binder; this solution comprises 50% SiO_2 particles dispersed in an aqueous solution. The mean particle size of nano-silica is 35 nm, and its specific surface, viscosity, density, and pH values are 80 m^2/g, 8 cP, 1.1 g/cm^3, and 9.5, respectively (provided by the manufacturer). The fineness of nano-silica was determined by titration with sodium hydroxide [Sears, 1956] Locally available fine aggregate, with a continuous gradation from 0 to 600 μm and fineness modulus of 2.9, according to ASTM C136 [2014], was used in the mixtures. The absorption and specific gravity of the fine aggregate is 1.5% and 2.6, respectively, according to ASTM C128 [2015]. A high-range water-reducing admixture (HRWRA), based on poly-carboxylic acid and complying with ASTM C494 Type F [2017], was added to achieve a target flow of 200±20 mm for all mixtures. BFP with 36 mm length (**Figure 3.1** and **Table 3.2**) were used to reinforce the cementitious composites at different dosages of 2.5%, 4.5% and 6.9% by volume (equivalent to basalt fibers volumes of 1%, 2% and 3%, respectively). The BFP are made of 16 μm basalt roving encapsulated by polyamide resin, and the fiber component represents 60% of the pellet by mass.

Figure 3.1: Reinforcing basalt fiber pellets.

Table 3.2: Physical and mechanical properties of basalt fiber pellets

Property	BFP
Length (mm)	36
Diameter/dimensions (mm)	1.8
Aspect ratio	20
Specific gravity	1.74
Tensile strength (MPa)	2,300
Elastic modulus (GPa)	65

Note: The properties of the BFP have been provided by the manufacturer.

3.2.2 Proportions and Mixing Procedures

Six mixtures were prepared with three dosages of BFP and two different cementitious matrices.

Table 3.3: Mixtures proportions per cubic meter

Mixture ID.	Fly ash (kg)	Slag (kg)	Water [a] (kg)	BFP (kg)	Fine aggregate (kg)	HRWR (l)
F-2.5	350	---	180	43.3	1,045	5.6
F-4.5				78.3	1,000	6.3
F-6.9				119.2	940	7.3
G-2.5	---	350		43.3	1,160	7.6
G-4.5	---			78.3	1,115	8
G-6.9	---			119.2	1,050	8.3

Note: The GU cement content in all mixtures was kept constant at 350 kg/m^3.
[a] Adjusted amount of mixing water considering the water content of nano-silica (aqueous solution with 50% solid content of SiO2).

The base binders were composed of 50% GU cement (350 kg/m^3) and 50% fly ash or slag. Nano-silica was added at a single dosage of 6% (42 kg/m^3 SiO_2) by mass of the base binder (700 kg/m^3), as this dosage was reported to positively influence the hardened properties of concrete [Ghazy *et al*., 2016; Said *et al*., 2012]. For all mixtures, the total cementitious materials (ternary binder: GU cement, slag/fly ash, and nano-silica) content and *w/b* were kept constant at 742 kg/m^3 and 0.3, respectively. The proportions of all the cementitious composites are presented in **Table 3.3**, and the mixtures were reinforced with 1%, 2% and 3% basalt fibers by volume, i.e. 2.5%, 4.5% and 6.9% BFP.

The constituent materials were mixed in a concrete mixer with a speed of 60 rpm. The mixing process comprised mixing the dry constituents followed by the addition of required water, admixtures and nano-silica while constantly mixing until the homogeneity of the mixture was achieved. Subsequently, the BFP were added and the ingredients were mixed for uniform distribution of pellets [Ghazy *et al*., 2016b]. The complete mixing process took about 10 min. For the mixtures ID, the letter "G" refers to slag replacement, whereas the letter "F" refers to fly ash replacement. The second part represents the BFP dosage as a percentage by volume.

3.2.3 Tests

In order to investigate the fresh properties of the developed mixtures four tests were performed to assess the influence of different dosages of BFP and SCM on placement properties. The mortar flow and mortar flow loss tests up to 60 min. were conducted according to ASTM C230/C230M [2014]. In addition, the setting time of the mixtures was determined in accordance with ASTM C403 [2016]; fresh mortar without pellets was placed in a container at room temperature, and the penetration resistance was determined by standard needles at regular time intervals. Also, the air content of the fresh mixtures was measured according to ASTM C231/C231M [2017].

The hardened properties of the composites were assessed by determining the compressive strength and flexural behavior. The compressive strength of the mixtures was determined by testing triplicate cylinders (100×200 mm) at various ages (3, 7, 28, 56, and 90 days) according to ASTM C39 [2018]. The flexural strength and post-cracking behavior of the mixtures at 28 days were determined according to ASTM C1609 [2019], by testing triplicate prisms (100×100×350 mm) in four-point bending. A servo-controlled closed-loop testing machine was used, where the displacement rate relied on the measured net mid-span deflection of the prism. The flexural toughness was calculated, as the area under the load-deflection curve (P-δ) up to a deflection of span/150 (2 mm), and the residual post-cracking strength index (R_i) was calculated according to **Equation 3.1** [Ghazy *et al*., 2019].

$$R_i = \frac{\frac{P_{0.5}+P_{0.75}+P_1+P_{1.25}}{4}}{P_{cr}} \qquad \textbf{(Equation 3.1)}$$

where, $P_{0.5}$, $P_{0.75}$, P_1 and $P_{1.25}$ are the residual loads are deflections at 0.5, 0.75, 1 and 1.25 mm, while P_{cr} is the peak load at first-cracking.

The resistance of the composites to the infiltration of fluids was assessed by the rapid chloride penetration test (RCPT) according to ASTM C1202 [2019]. Also, the chloride penetration depth into concrete was measured in accordance with the procedure described by Bassuoni et al. [2005]. After the RCPT, the specimens were split into two halves and sprayed with 0.1 M silver nitrate solution, which forms a white precipitate of silver chloride in approximately 15 minutes. The average depth of the white precipitate was then measured at five different locations along the diameter of each half specimen. This depth is considered an indication of the ease of ingress of external fluids, and thus the continuity of the microstructure. The resistance of the composites to salt-frost scaling was evaluated by exposing the surface of the specimens to 50 freezing-thawing

cycles and 4% calcium chloride solution according to ASTM C672/C672M [2012]. The surface scaling resistance was assessed by visual examination and mass of the scaled materials from the surface.

Thermal and microscopy studies were conducted to assess the microstructural evolution of the cementitious composites and corroborate the trends obtained from the bulk tests. Portlandite (calcium hydroxide) quantities in the matrix were determined up to 90 days to evaluate the influence of nano-silica, slag and fly ash on the hydration and pozzolanic activities through thermo-gravimetric analysis (TGA). Fracture pieces from specimens were pulverized to fine powder passing sieve #200 (75 μm) and heated at a rate of 10°C/min. The portlandite content was calculated by determining the drop of the ignited mass percentage at a temperature range from 400 to 450°C, and multiplying it by 4.11 (the ratio of the molecular mass of calcium hydroxide to that of water) [Brown, 1998]. Scanning electron microscopy (SEM) with elemental dispersive X-ray (EDX) was carried out on fracture pieces comprising BFP, extracted from the F-4.5 and G-4.5 composites after 28 days. Carbon coating was applied to the fracture pieces to improve their conductivity for the SEM imaging [Goldstein *et al*., 2017].

3.3 Results and Discussion

3.3.1 Fresh Properties

Table 4 presents the fresh properties of the composite mixtures, including flow, flow loss and setting time (initial and final).

Table 3.4 Fresh properties of the cementitious composites

Mixture ID	Flow (mm)					Setting Time (min)	
	Test Time (min)						
	0	**15**	**30**	**45**	**60**	**Initial**	**Final**
F-2.5	180	154	138	129	112	250	360
F-4.5	186	154	134	127	108	270	370
F-6.9	220	202	177	154	133	285	380
G-2.5	205	190	154	142	130	180	285
G-4.5	212	196	173	148	134	195	300
G-6.9	217	187	165	139	118	230	325

All the mixtures achieved the target flow of 200±20 mm (100±20 % of the original base diameter of the mold). The slag-based mixtures required higher dosages of the HRWRA to attain the target flow compared to the fly ash-based mixtures, and the dosages were adjusted according to the content of the BFP (**Table 3.3**). This can be attributed to the angular shape of slag particles (interlocking effect) versus the spherical shape of fly ash particles. The fly ash particles imparted a ball bearing effect, thus enhancing the workability of the mortar mixtures [Neville, 2011]. Moreover, all mixtures retained adequate consistency up to 30 minutes after mixing, since the average flow loss was about 23% of the initial values, irrespective of the type of binder or the dosage of BFP. After 60 minutes, the mixtures retained almost 60% of their initial flow. These trends indicated that the composite mixtures had adequate workability for field applications in terms of placement operations.

Regarding the hardening trends, the fly ash-based mortars had longer initial and final setting times compared with that of the slag-based mortars as presented in **Table 3.4** and **Figure 3.2**. This trend was obtained despite the higher dosages of HRWRA incorporated in the slab-based composites. For instance, mixture F-2.5 had 39% and 26% longer initial and final setting times, respectively relative to mixture G-2.5.

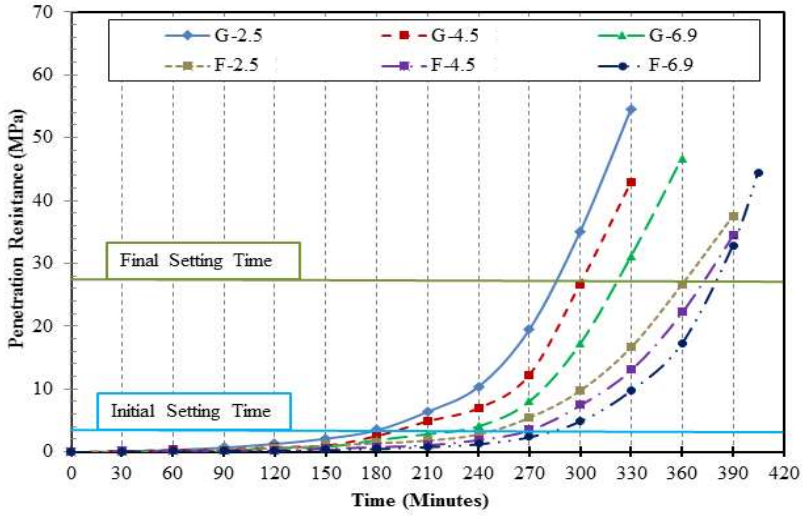

Figure 3. 2: Penetration resistance versus time.

This can be attributed to the retarding effect and slower reactivity of Type F fly ash, which is well-documented in the technical literature [Neville, 2011; Mehta and Monteiro, 2014], relative to the finer (492 kg/m^2) and relatively reactive (Grade 100) slag. Binders containing such high volumes of SCMs typically exhibit final settings times in the range of 9 to 12 h [Neville, 2011]. However, the final setting times of both binders herein remained within the normal range of 4 to 6 h, despite of the high-volume (50%) fly and slag incorporated in these binders. This can be attributed to the ultrafine nature of silica particles (80 m^2/g), resulting in accelerated rate of hardening and early hydration and pozzolanic reactions. These trends agree with findings of previous studies [e.g. Mahmoud *et al*., 2017; Ghazy *et al*., 2016b].

Irrespective of the type of binder, the effect of increasing the dosage of the HRWRA with the BFP dosage, to lubricate the pellets and attain the target mortar flow, did not significantly extend the initial and final setting times. For example, the initial setting time of F-4.5 and F-6.9 was moderately increased by about 8% and 14%, respectively relative to F-2.5, while the final setting time was marginally increased by approximately 2% and 5%, respectively. These trends suggest that the mixture designs of nano-modified cementitious composites herein can be used for most construction applications as they have acceptable rates of hardening.

3.3.2 Compressive Strength

Table 5 presents the average compressive strength for the developed composites at different ages. Cementitious binders comprising high-volume of Type F fly ash (slow reactivity pozzolan) and slag (latent hydraulic binder) blended with GU cement typically exhibit slow rate of strength and microstructural development at early-age, but their reactivity improves with time [Mehta and Monteiro, 2014]. Thus, most codes and standards for concrete [e.g. CSA 23.1/23.2-19] require the properties of concrete, comprising fly ash or slag, to be assessed at 56 or 91 days. However, the results herein indicate that the compressive strengths of all mixtures, comprising 50% fly ash or slag, were greater than 30 MPa at early-age. For example, the compressive strength at three days of the composites with the lowest dosage of BFP (F-2.5 and G-2.5) were 37 and 63 MPa, respectively. In addition, considering the long-term strength (up to 90 days), the mixtures continued to gain strength reaching values in the range of 50 to 84 MPa.

Conforming to the setting time results, the technical limitations (slow rate of reactivity and strength development) of binders incorporating a high-volume of SCMs were mitigated by the nano-silica sol. Addition of 6% nano-silica increased the compressive strength of 50% fly ash- or slag-based specimens even at early ages (3 and 7 days). Nano-silica contributes to improving the hardened properties of cement-based materials by multiple mechanisms, including accelerating the hydration and pozzolanic reactivity [Ghazy *et al*., 2016a; Kong *et al*., 2012], filling effect [Kong *et al*., 2012], and water absorption within the high surface area of nano-silica agglomerates, resulting in reduction of *w/b* in the paste [Kong *et al*., 2012].

The nano-modified slag-based composites showed significantly higher compressive strength at early- and later-ages compared to the fly ash-based counterparts. For example, the compressive strengths of G-4.5 specimens at 3, 7, 28, 56 and 90 days were 70%, 54%, 46%, 35%, and 32%, respectively, higher than that of F-4.5 specimens (**Table 3.5**). This trend was statistically

substantiated by the analysis of variance (ANOVA) at a significance level α of 0.05 (**Table 3.6)** as the F value (e.g. 344.99) of the type of binder (e.g. F-4.5 vs. G-4.5) was much higher than the critical threshold, F_{cr} (7.70). According to Montgomery (2014), if the F-distribution density function exceeds the critical value, the tested variable has a significant effect on the mean value of the results. This strength difference can be attributed to the relatively finer nature of slag (492 kg/m^2) compared to fly ash (290 kg/m^2) which positively influenced the reactivity of slag with the coexistence of nano-silica. In addition, the chemical composition of slag had higher content of lime (CaO) of about 43% which typifies slag with its faster hydraulic property. Comparatively, Type F fly ash had low content of lime (about 11%) and higher content of silica (55%) imparting a pozzolanic reactivity over longer period of time. The relative reactivity of the nano-modidifed fly ash- and slag-based composites is further discussed in the thermal analysis section.

Generally, the effect of increasing the dosage of BFP was statistically significant (**Table 3.6**) at reducing the compressive strength of fly ash- and slag-based composites. For example, at 28 days, **Table 3.5** indicates that the reduction in compressive strength for the fly ash-based composites F-4.5 and F-6.9 was 11% and 14%, respectively relative to that of mixture F-2.5; correspondingly, the reduction for the slag-based composites G-4.5 and G-6.9 was 11% and 27%, respectively relative to mixture G-2.5. Branston *et al.* (2016) reported a similar trend of compressive strength reduction with the increase of BF minibars dosage (0.3, 1 and 2 % by volume) in ordinary concrete (37 MPa). This can be attributed to the creation of additional interfacial transitional zones (ITZs) with higher dosages of BFP, which acted as weak links and stress concentrators in the matrix, thus reducing the compressive capacity of the mixtures.

Table 3.5: Mechanical properties of the cementitious composites

Mixture ID	Compressive Strength (MPa)* Age (Days)					Flexural Test Results at 28 Days				
	3	7	28	56	90	First-peak Strength (MPa)	Residual Strength at *L/600* (MPa)	Residual Strength at *L/150* (MPa)	Residual Post-cracking Strength Index (R_i)	Toughness (J)
F-2.5	36.9	48.8	53.8	58.2	60.8	5.3	4.2	4.0	0.94	27.4
F-4.5	34.7	42.4	47.8	52.8	55.3	4.8	5.9	5.9	1.48	37.4
F-6.9	34.1	41.6	46.3	48.1	50.2	4.6	5.9	6.3	1.65	39.9
G-2.5	63.2	75.3	78.5	82.9	84.2	7.3	4.2	4.5	0.64	30.3
G-4.5	58.9	65.4	69.7	71.3	73.1	5.1	4.8	5.1	1.1	40.3
G-6.9	53.3	55.9	57.6	61.7	63.3	4.8	6.0	5.9	1.32	44.0

Table 3.6: ANOVA for the results of hardened and durability tests

Parameter	Compressive Strength		First-Peak Flexural Strength		Toughness		Physical Chloride Penetration Depth		Frost Scaling Cumulative Mass Loss	
	F	F_{cr}	F	F_{cr}	F	F_{cr}	F	F_{cr}	F	F_{cr}
Binder										
F-2.5 vs. G-2.5	1410*	7.70	40.56*	7.70	20.73*	7.70	2.47	5.32	33.21*	18.51
F-4.5 vs. G-4.5	344.91*	7.70	1.49	7.70	9.32*	7.70	1.26	5.32	216.47*	18.51
F-6.9 vs. G-6.9	57.81*	7.70	0.25	7.70	9.72*	7.70	1.21	5.32	113.29*	18.51
BFP Dosage										
F-2.5 vs. F-4.5	83.67*	7.70	2.41	7.70	271.34*	7.70	0.81	5.32	1.33	18.51
F-4.5 vs. F-6.9	0.15	7.70	0.20	7.70	8.16*	7.70	0.94	5.32	5.82	18.51
F-2.5 vs. F-6.9	29.98*	7.70	6.66	7.70	231.59*	7.70	6.06*	5.32	7.72	18.51
G-2.5 vs. G-4.5	55.06*	7.70	87.37*	7.70	108.76*	7.70	2.47	5.32	---	---
G-4.5 vs. G-6.9	55.06*	7.70	1.73	7.70	7.33	7.70	3.34	5.32	---	---
G-2.5 vs. G-6.9	517.52*	7.70	77.96*	7.70	130.17*	7.70	11.98*	5.32	---	---

*Denotes statistical significance.

However, the range of compressive strength for all mixtures at 28 days was 46 to 79 MPa, which highlights the adequacy of these composites to a suite of infrastructure applications (e.g. roads, bridges, tunnels, repair), which typically require a design compressive strength of 30 to 40 MPa at 28 days [MacGregor *et al*., 1997]. Generally, fibers/pellets are mainly added to mortar/concrete to enhance the flexural post- cracking performance, as discussed in the subsequent section.

3.3.3 Flexural Behavior

Table 3.5 lists the flexural and residual strengths as well as the residual post-cracking strength index (R_i) and toughness for all mixtures at 28 days, based on the load-deflection (P-δ) curves shown in **Figures 3.3** and **3.4**. It was observed that as the BFP dosage increased, the first-peak flexural strength decreased, depending on the type of binder. The reduction of the first-peak flexural strength for the fly ash-based composites F-4.5 and F-6.9 was 11% and 13%, respectively relative to that of F-2.5, while the reduction for the slag-based composites G-4.5 and G-6.9 was 31% and 35%, respectively relative to that of G-2.5. Statistical analysis (ANOVA) showed that this reduction of flexural strength was insignificant (F values of 2.41 and 6.66 vs. F_{cr} of 7.7) in the case of fly-ash based composites, and significant (F values of 87.37 and 77.96 vs. F_{cr} of 7.7) in the case of slag-based counterparts. Conforming to the compressive strength results, this can be attributed to the higher intensity of the ITZs created in the cementitious matrix with the incorporation of higher dosages of BFP. Initiation and propagation of micro-cracks may readily occur in these zones, thus reducing the flexural capacity (based on the first-peak cracking) of the composites, which mainly depend on the cementitious matrix. However, the flexural strength of all composites was in the range of 4.5 to 7.3 MPa, which is appropriate for a

range of infrastructure applications; including roads, bridges, tunnels, and patch repair [MacGregor *et al*., 1997].

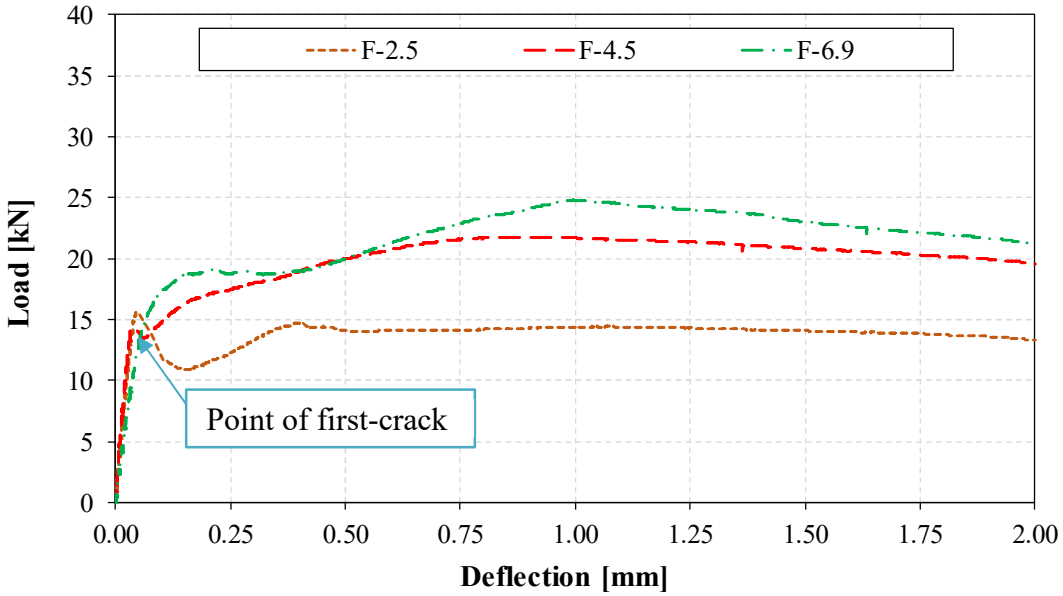

Figure 3.3: Load-deflection (P-δ) curves for the fly ash-based mixtures.

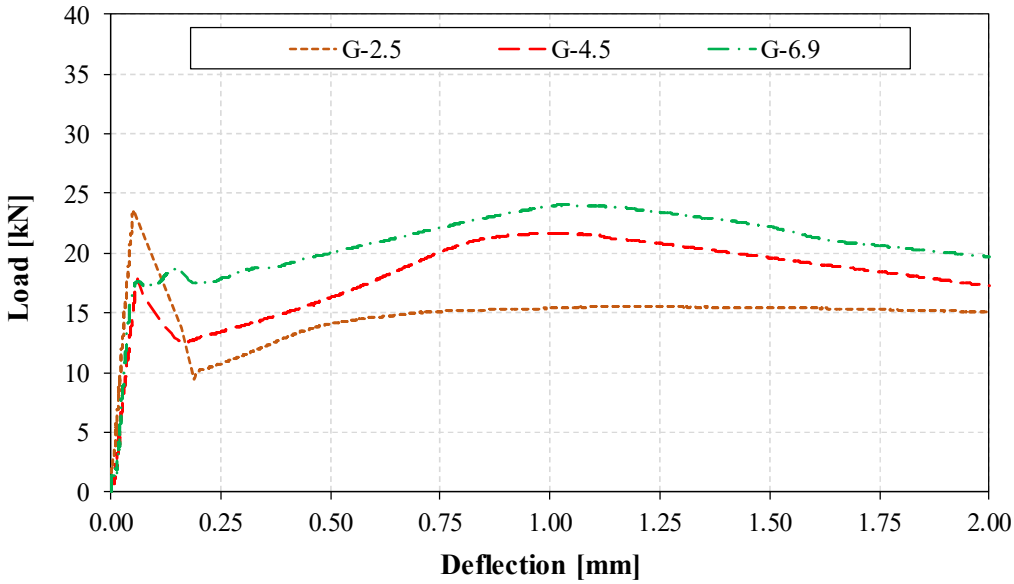

Figure 3.4: Load-deflection (P-δ) curves for the slag-based mixtures.

The P-δ curves for all composites (**Figures 3.3** and **3.4**) exhibited enhanced post-cracking performance, especially at higher BFP dosages (4.5% and 6.9%), owing to the

pullout process of the pellets. In General, the pellets had minor effect on the behavior at the pre-cracking stage relative to the post-cracking one, as a comparable elastic behavior was achieved before the first-cracking of the specimens. After the initiation of the first-crack, a sudden decline of the bearing load was observed. However, the specimens were able to restrain the cracks and restore the load-carrying capacity till reaching a second peak, depending on the binder type and dosage of BFP. Composites with 2.5% BFP showed a deflection softening post-cracking trend. Comparatively, the mixtures with the higher BFP dosages, 4.5% and 6.9%, exhibited a deflection-hardening behavior resembling cementitious composites incorporating ductile fibers such as steel. For example, the average residual strengths of mixtures F-6.9 and G-6.9 at a deflection of 2 mm (*L/150*) were 37% and 23%, respectively higher relative to their first-crack flexural strength.

In the same context, the R_i was determined for all the composites. This index evaluates the post-cracking performance of fiber reinforced concrete (FRC), according to the Canadian Highway Bridge Design Code (CHBDC) [CAN/CSA-S6]. It is stipulated that the appropriate fiber volume in FRC shall be based on the R_i, such that it meets or exceeds specified values ranging between 0 to 0.30 depending on the application and the number of directions of conventional cracking-control reinforcement. The results herein indicated that the R_i of mixtures with BFP of 2.5% were greater than 0.6, whereas it was greater than 1 for the mixtures incorporating BFP of 4.6% and 6.9%. These trends substantiate the efficient post-cracking performance of the developed composites.

At a fixed BFP dosage, the toughness of the slag-based mixtures was relatively higher than that of their fly ash-based counterparts, with statistical significance (**Table 3.6**). The toughness of mixtures G-2.5, G-4.5 and G-6.9 were 10%, 7% and 10% higher than that of the corresponding fly ash mixtures. Testing specimens up to complete failure

revealed that the distribution of BFP in the slag-based mixtures was more even relative to the fly ash composites, which showed uneven settlement/clustering towards the bottom of specimens (e.g. **Figure 3.5**).

Figure 3.5: Distribution of BFP at the failure planes: (a) F-4.5, and (b) G-4.5.

The cohesive nature of the slag-based mixtures, owing to the angular slag particles, might have imparted an interlocking effect allowing homogenous dispersion of the pellets within the cross section during the plastic stage and preventing their settlement. In addition, the relatively faster reactivity of slag compared with fly ash, as discussed in the compressive strength section, led to better bonding between the slag-based matrix and the pellets at 28 days, thus increasing the resistance to pull out and consequently improved toughness. In addition, the toughness of the developed composites significantly increased with the BFP dosage (**Table 3.5** and **3.6**). In the fly ash group, mixtures F-4.5 and F-6.9 had a toughness of 36% and 45% higher than that of mixture F-2.5, which had a toughness of 27.4 J. Correspondingly, the toughness of mixtures G-4.5 and G-6.9 was 33% and 45% higher than that of mixture G-2.5 (30.3 J). The higher BFP dosages provided better chance for the pellets to exist at the failure planes with efficient restraint to propagation of cracks.

Abundant BFP in these locations arrested and bridged micro-cracks, resulting in improved toughness beyond the first-cracking.

3.3.4 Durability Properties

3.3.4.1 Penetrability

The penetrability of all mixtures was assessed by the RCPT at 28 days, and the results of the passing charges as well as the physical chloride penetration depth are presented in **Table 3.7**. **Figure 3.6** shows an example of the penetration depth in F-4.5 and G-4.5 specimens.

Table 3.7: Average rapid chloride penetrability test (RCPT) results

Mixture ID	Passing Charges (Coulombs)	Chloride Ion Penetrability Class (ASTM C1202)	Physical Chloride Penetration Depth (mm)
F-2.5	341	Very Low	5.3
F-4.5	408	Very Low	6.5
F-6.9	711	Very Low	7.8
G-2.5	288	Very Low	3.8
G-4.5	334	Very Low	5.1
G-6.9	417	Very Low	6.8

Figure 3.6: Whitish precipitate indicating the penetration depth of chloride ions into the F-4.5 and G-4.5 composites.

Generally, all the mixtures had low passing charges, implicating fine and disconnected pore structure at this age (28 days). According to the ASTM C1202 classification, all the mixtures had "very low" penetrability class, as the passing charges did not exceed the limit of 1000 coulombs, irrespective of the type of binder or the dosage

of BFP. Correspondingly, these mixtures had markedly low physical chloride penetration of less than 8 mm. Complying with the setting time and strength results, this was ascribed to the mixture design of the composites (high binder content and low *w/b*). In addition, the physical and chemical effects of nano-silica led to improving the hydration level of these binders and densifying the pore structure at 28 days, even with the incorporation of 50% fly ash or slag. The extremely fine particles of nano-silica accelerated and improved the hydration and pozzolanic reactivity of fly ash and slag-based composites, as will be shown in thermal and microstructural section. Besides, the physical filler effect of nano-silica contributed to refining the pore structures [Zhang and Islam, 2012], and thus discounting the penetrability of all composites.

Conforming to the strength results, the slag-based composites had higher resistance to penetration of fluids compared with their fly ash-based counterparts. For instance, the physical chloride penetration depth of G-2.5, G-4.5 and G-6.9 specimens were 29%, 22% and 13%, respectively, less than that of F-2.5, F-4.5 and F-6.9 specimens (**Table 3.7**). As previously discussed, this can be attributed to the finer particle size and chemical composition of slag relative to fly ash, which improved the reactivity and degree of hydration of the matrix, and thus reducing the penetrability of the slag-based composites. On the other hand, increasing the BFP dosages led to increasing the penetrability of the composites (**Table 3.6**). The physical penetration depth of F-4.5 and F-6.9 specimens were 22% and 47%, respectively higher than that of F-2.5 specimens. Correspondingly, it was 34% and 78% higher for G-4.5 and G6.9 specimens, respectively than that of G-2.5 specimens. This might be due to the formation of additional ITZs between the pellets and mortar, which contributed to facilitating the penetrability of fluids into the matrix. This trend complies with the results of Salemi and Behfarnia [2013], which reported faster mass

transport of fluids in concrete with increasing the volume of polypropylene fibers. Nevertheless, all the fly ash- and slag-based composites herein showed very low penetrability, irrespective of the BFP dosage, which may qualify them for exposures involving intrusive fluids carrying deleterious substances such as chloride ions (e.g. pavements, bridges).

3.3.4.2 Frost Scaling

The results of surface scaling test (ASTM C672), which involved the dual action of deicing salt (calcium chloride) and freezing-thawing cycles are shown in **Figures 3.7** and **3.8**. The fly ash mixtures had shown visual ratings from 1 to 3, increasing with the dosage of BFP. The same incremental trend was depicted in the cumulative mass loss results (**Figure 3.8**); however, the maximum cumulative mass loss was 320 g/m^2 for mixture F-6.9. In these mixtures, surface scaling was limited to the superficial crust, exposing surface fibers but without dislodging. Regarding the slag-based composites, all the mixtures had superior salt-frost scaling resistance with a visual rating of 0 and nil mass loss. Only moisture shadowing was observed on the surface of the slag-based specimens at fiber locations, but without any scaling. Ministry of Transportation of Ontario (MTO) [1997] and Bureau du normalization du Quebec (BNQ) [2002] established a quantitative assessment criterion for the salt-frost scaling test, where the failure limit was set at 800 and 500 g/m^2, respectively. Accordingly, taking into account the variation of procedures among the tests (for instance, MTO and BNQ use less aggressive salt solution of 3% sodium chloride), all the developed composites may be considered resistant to salt-frost scaling, despite the high volume of slag and fly ash (50%) incorporated in the binders.

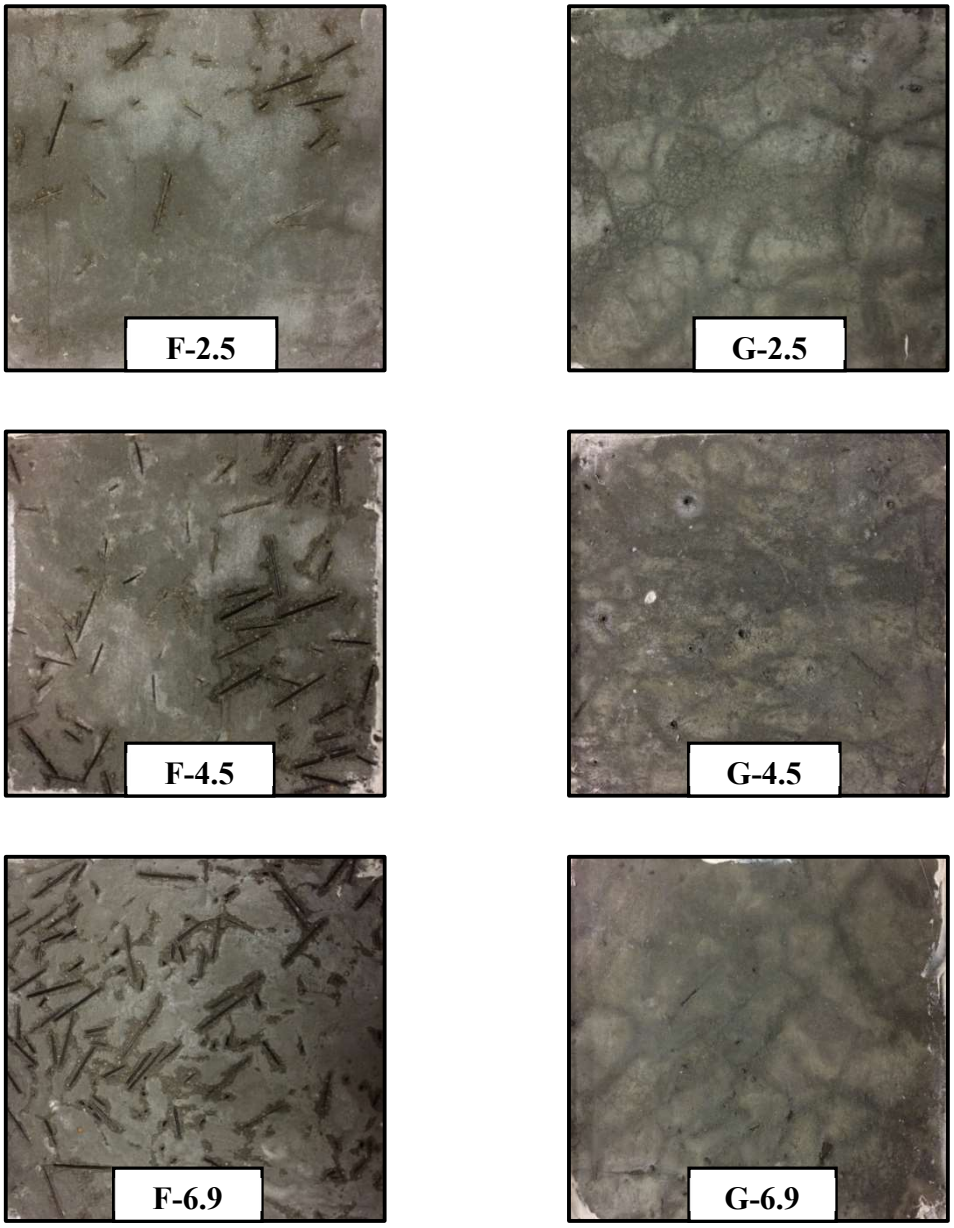

Figure 3.7: Appearance of slabs after 50 freezing-thawing cycles (visual ratings are shown in parentheses).

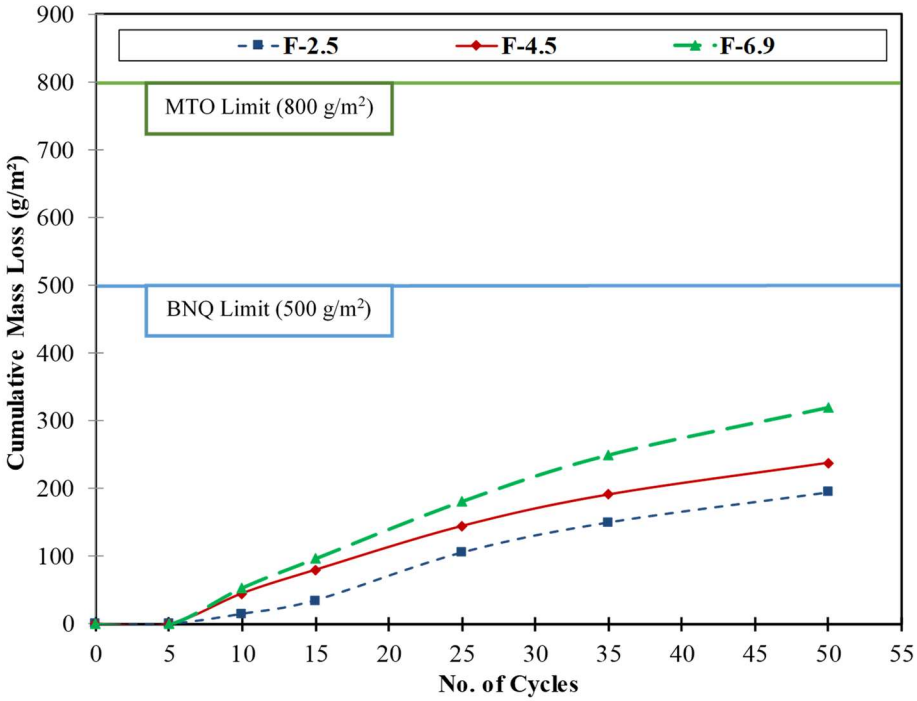

Figure 3.8: Cumulative mass loss of slabs tested according to ASTM C672 (note: all the slag-based mixtures had nil mass loss up to 50 cycles).

This performance might be attributed to the adequate air content (6±1%), which comply with the recommended ranges stipulated in Canadian and American codes and guidelines for concrete to protect it against freezing-thawing exposures [ACI 201.2R]. In addition, the modification of the binders with 6% nano-silica enhanced the hydration and pozzolanic reactivity of cement, fly ash and slag, resulting in densification of the matrix as well as discounting the ingression of the salt solution to limited depths inside the developed composites. Consequently, the composites were not vulnerable to critical saturation and associated frost damage. This conformed to the very low penetrability (less than 8 mm) of the composites in the RCPT. Another possible reason for the frost scaling resistance of the composites was their improved volume stability and post-cracking performance owing to the inclusion of BFP. Upon freezing of solution in capillary pores, hydraulic and osmotic stresses develop in the cementitious matrix, which might exceed its tensile capacity leading

to the formation of micro-cracks and scaling [Mehta and Monteiro, 2014]. Hence, the improved post-cracking performance and fracture resistance of the developed composites might have resulted in enhanced frost scaling resistance. In addition, according to the glue-spall theory [Valenza *et al*., 2007], when the ice layer at the top of the concrete surface cracks, it exerts tensile stresses into the concrete surface leading to the propagation of inward cracks. The inclusion of BFP in the developed composites could have arrested and controlled the propagation of any possible cracks, thus enhancing their resistance to freezing-thawing cycles.

The significantly improved resistance to salt-frost scaling of slag-based composites relative to the fly ash-based counterparts conform to the trends obtained from the previously discussed tests. Again, this alluded to the higher degree of matrix development and stability in the case of nano-modified slag binder, compared with the nano-modified fly ash matrix. In addition, high volumes of fly ash in cement-based materials may result in significant proportions of unbound (unreacted) fly ash particles in the matrix, with higher tendency to surface scaling. These arguments were substantiated by the thermal and microscopy tests. Considering the influence of BFP, the cumulative mass loss was increased with the dosage for the fly ash-based mixtures, while there was no effect observed for the slag-based composites (no mass loss occurred). The cumulative mass losses for F-2.5, F-4.5 and F-6.9 mixtures were 195, 238 and 320 g/m^2, respectively, after 50 freeze/thaw cycles. This could be linked to the creation of additional ITZs within the surface of the composites, which relatively increased the penetrability of the matrix as discussed in the RCPT section. The scaling was, however, limited to the superficial layer of the tested specimens, with no fiber dislodging or influence on the integrity of the composites.

3.3.5 Thermal and Microscopy Analyses

The change of calcium hydroxide (CH) content in the nano-modified cementitious composites as well as reference mixtures (without nano-silica) was determined at 1, 3, 7, 28, 56 and 90 days using TGA to track the progress of hydration and pozzolanic activities, as depicted in **Figure 3.9**. The reference fly ash (F) and slag (G) mixtures followed the well-documented trend of these SCMs when incorporated in concrete; the F and G mixtures showed increase in the contents of CH up to 28 days, followed by a downward (consumption) trend up to 90 days. The former trend was mainly driven by the hydration of cement and resulting production of CH, while the latter originated from the contribution of slow pozzolanic activity of SCM [Neivelle, 2011; Mehta and Monteiro, 2014].

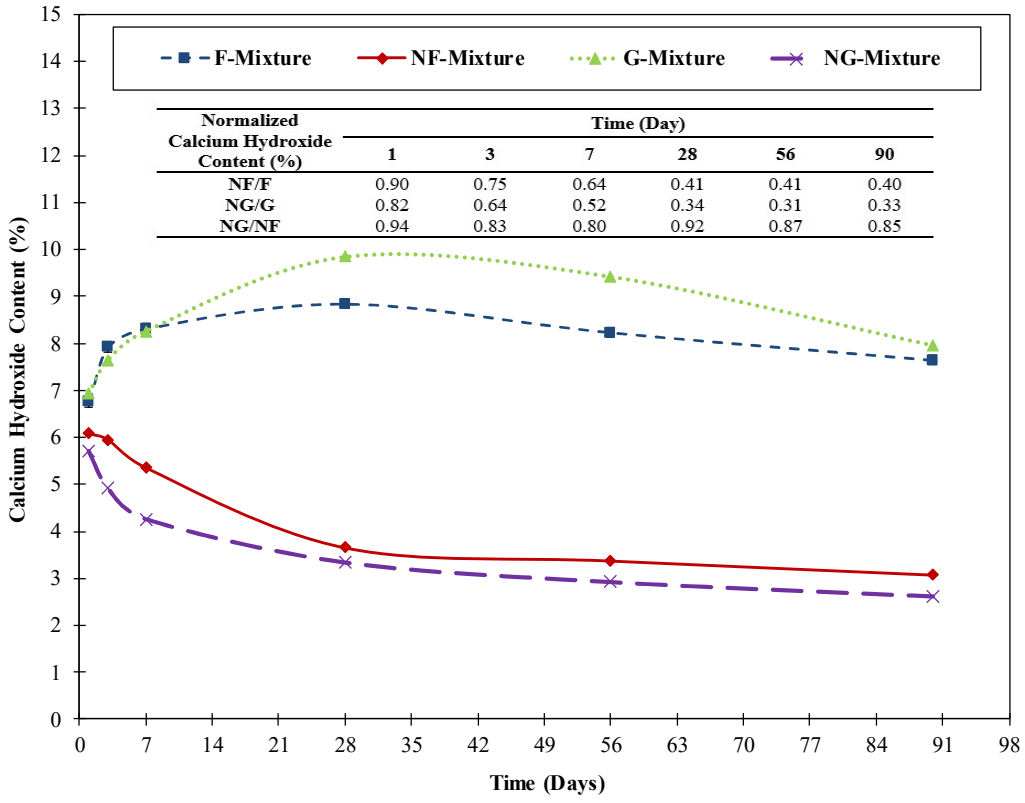

Normalized Calcium Hydroxide Content (%)	Time (Day)					
	1	3	7	28	56	90
NF/F	0.90	0.75	0.64	0.41	0.41	0.40
NG/G	0.82	0.64	0.52	0.34	0.31	0.33
NG/NF	0.94	0.83	0.80	0.92	0.87	0.85

Figure 3.9: TGA results for the CH contents (at a temperature range of 400 to 450°C) in the mixtures.

However, the G mixture had relatively faster/earlier CH production and subsequent consumption **(Figure 3.9)** due to its fineness and chemical composition as discussed earlier. Therefore, most standard codes for concrete [CSA 23.1/23.2-19] require the properties of concrete comprising fly ash and slag to be assessed at 56 or 91 days.

Comparatively, the reduction of CH in the nano-modified fly ash and slag-based mixtures (NF and NG, respectively) started at very-early age, despite of the high dosage of fly ash and slag (50%). For instance, at one day, the normalized contents of CH in the NF and NG mixtures relative to their corresponding reference mixtures were 0.90 and 0.82, respectively. The ultrafine surface of nano-silica acted as nucleation sites for the dissolution of cement and precipitation of hydration products, as indicated by the relatively fast setting (4 to 6 h) of these composites comprising 50% slag or fly ash. Subsequently, the consumption of CH implied vigorous pozzolanic reactivity in the developed mixtures at early-age due to the addition of nano-silica to precipitate additional C-S-H gel in the matrix. Considerable consumption of CH continued up to 28 days, followed by much slower rates of depletion up to 90 days; the average normalized contents of CH in the NF and NG mixtures relative to their corresponding references were 0.41 and 0.33, respectively between 28 to 90 days. This suggested that nano-silica had synergistically catalyzed the reactivity of fly ash and slag in these composites, producing higher degree of hydration. The nucleation, pozzolanic and physical filler effects of nano-silica in the cementitious matrix enhanced the evolution of the composites' microstructure within the first 28 day. In addition, the subsequent reactivity of both binders up to 90 days might be ascribed to the continual pozzolanic effect of fly ash and slag. These trends explain the high early-strength (more than 30 MPa) of these cementitious composites at three days and dense microstructure obtained at 28 days (penetration depth less than 8 mm), which was

adequately resistant to salt-salt frost scaling (surface scaling between 0 and 320 g/m^2), especially with the inclusion of BFP.

The normalized CH contents at different ages of the nano-modified slag-based mixture relative to that of the nano-modified fly ash-based mixture were calculated to determine the relative reactivity between both mixtures. This ratio was consistently less than 1 at early- and later-ages, which substantiated the faster reactivity of the nano-modified slag-based mixture, and consequently deposition of higher volumes of pozzolanic C-S-H. This conformed to the trends of the reference slag mixture without nano-silica, and complied with the enhanced hardened and durability properties (compressive strength, flexural strength, toughness, penetration resistance and frost scaling resistance) of the slag-based composites relative to their fly ash-based counterparts.

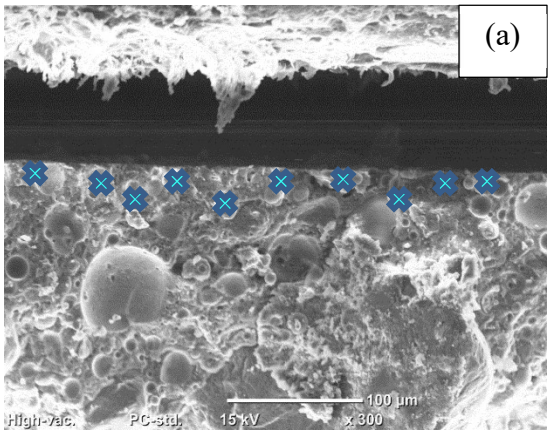

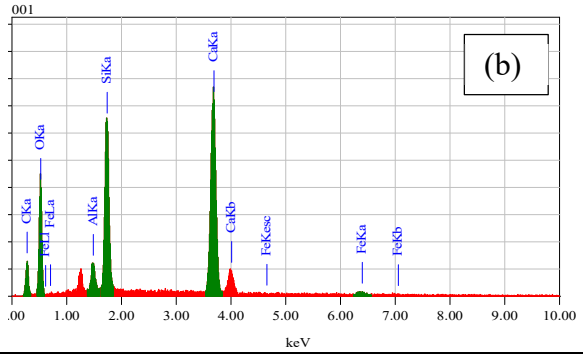

Element	C	O	Al	Si	Ca	Fe	Mean Ca/Si	SE N=10
Atomic Wt %	28.40	57.98	1.12	5.63	6.70	0.17	1.32	0.09

Figure 3.10: SEM for nano-modified fly ash composite showing: (a) ITZ with BFP, and (b) EDX spectrum of paste at the indicated locations (S.E. is standard error)

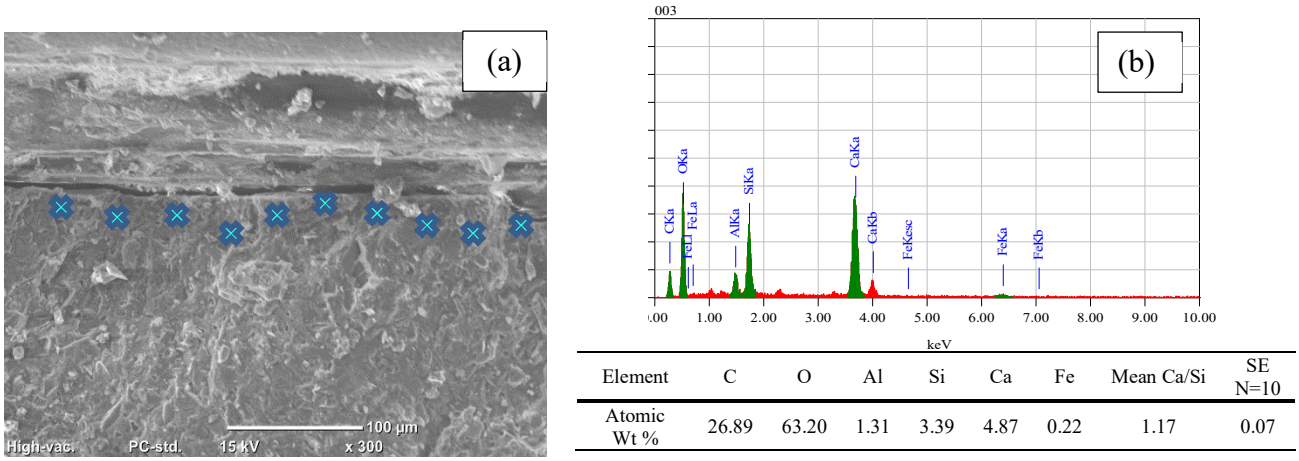

Element	C	O	Al	Si	Ca	Fe	Mean Ca/Si	SE N=10
Atomic Wt %	26.89	63.20	1.31	3.39	4.87	0.22	1.17	0.07

Figure 3.11: SEM for nano-modified slag composite showing: (a) ITZ with BFP, and (b) EDX spectrum of paste at the indicated locations (S.E. is standard error)

Figures 3.10 and **3.11** show exemplar SEM micrographs of fracture specimens with pellets extracted from the F-4.5 and G-4.5 composites after 28 days. Both mixtures showed dense matrix and ITZ between the paste and BFP. This could be ascribed to the synergistic effect of nano-silica with fly ash and slag, as previously discussed. Complying with the TGA trends, it was observed that the slag-based matrix had more homogenous and denser microstructure at 28 days (**Figure 11a**), compared with the fly-ash based matrix comprising abundantly unreacted fly ash particles in the matrix (**Figure 10a**). In addition, the EDX analysis was performed to determine *Ca/Si* for the C-S-H gel in the ITZ for the same specimens (**Figures 10b** and **11b**). It was found that the average *Ca/Si* was 1.17 for the slag-based mixtures, indicating an efficient and accelerated pozzolanic reactivity, resulting in the densification of the ITZ with secondary C-S-H. Comparatively, the average *Ca/Si* was 1.32 for the fly ash-based mixtures, because of its delayed reactivity relative to slag as discussed in the TGA part. It was reported that the *Ca/Si* of the secondary C-S-H resulted from the pozzolanic reactions (1.1) is lower compared to the conventional C-S-H generated from the hydration reaction of cement (1.7) [Detwiler *et al*., 1997].

Regarding the pellets/matrix interaction, **Figure 3.12** shows an example of the surface morphology of BFP embedded in the fly ash (**Figure 3.12a**) and slag-based (**Figure 3.12b**) composites, extracted respectively from F-4.5 and G-4.5 specimens. The BFPs had an overall diameter of approximately 1.8 mm, consisting of a bundle of 16-micron basalt fibers surrounded by polyamide resin (approximately 100 μm). Intentionally created grooves in the longitudinal direction can be noticed on the pellets surface, which enhanced the pellets/matrix bonding interface, with different levels according to the binder type (better reactivity of slag relative to fly ash), due to the interlocking effect as well as the increased available contact area for the hydration products growth and deposition. This explains the superior post-cracking performance of the developed composites, particularly for the 4.5% and 6.9% BFP dosages. Thus, the deflection hardening behavior observed for these composites could be ascribed to the improved gradual pullout of the pellets, which was the major toughening mechanism, during the flexural testing at the failure planes, where no ruptured pellets were observed. In addition, the use of polyamide resin as a protective technique for the basalt fibers against the surrounding alkaline medium seemed to be efficient, where no degradation of the pellets was noticed in the micrographs. This could be attributed to the chemical stability of polyamide in alkaline media [Kutz, 2012], hence mitigating the damaging effect of the alkaline cementitious system (pH value > 11) on the fiber component.

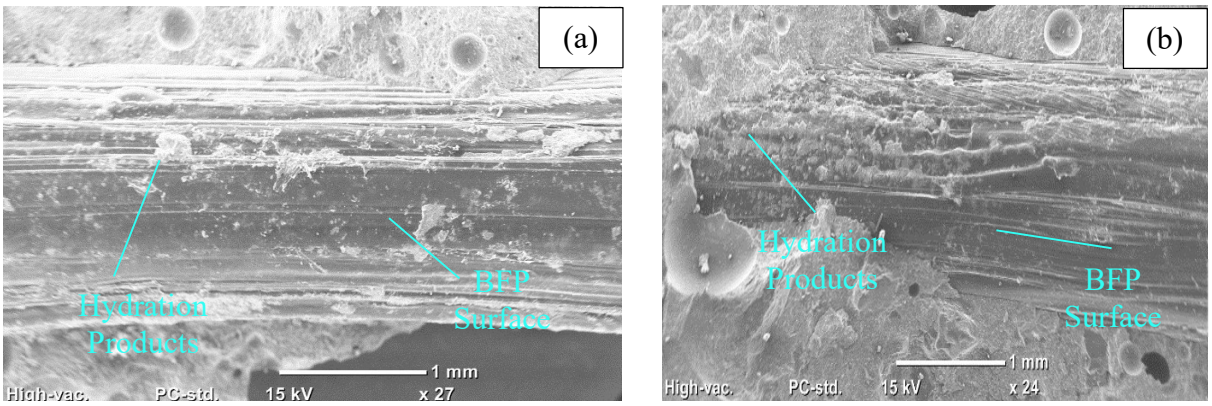

Figure 3.12: SEM images for the surface morphology of the BFP and hydration products in the grooves: (a) nano-modified fly ash mixture, and (b) nano-modified slag mixture.

CHAPTER 4: NANO-MODIFIED CEMENTITIOUS COMPOSITES INCORPORATING BASALT FIBER PELLETS UNDER TENSILE AND IMPACT LOADS

In Chapter 3, the general properties, including fresh, mechanical and durability properties, of nano-modified cementitious composites were investigated to study the potential of employing the developed composites in infrastructure flatwork applications such as concrete pavements and bridge decks. The cementitious composites showed promising performance in terms of fresh and hardened properties that suit different infrastructure applications. Correspondingly, in this chapter, the cementitious composites were investigated under specific loading configuration that might encounter different infrastructure applications as well as correlating bond strength of the pellet/matrice interface with the bulk properties. Thus, the behavior of nano-modified cementitious composites reinforced with innovative basalt fiber pellets (BFP), with specially tailored surface texture was investigated under quasi-static (direct) tensile as well as static and dynamic compression (Split Hopkinson Pressure Bar**)** loading schemes. Moreover, the pellets/matrix interfacial bond properties were assessed using the single pellet pullout test.

4.1 Introduction

Infrastructure elements such as concrete pavements, bridge decks, crash barriers, airfield runways, etc. experience varying and sometimes critical loading configurations during their service lives. This loading involves high-strain rate collisions, impact, and seismic events resulting in material damage or structural failure. Under impact loading, a compressive stress wave is generated at the loading face of concrete; however, this wave

is reflected as a tensile stress wave in concrete away from the boundary face subjected to impact [Malvar and Ross, 1998; Yang and Li, 2012]. The brittle behavior (low tensile strength and fracture toughness) of cement-based materials limit their performance under tensile and impact loads, which may result in technical limitations and safety concerns [Yang and Li, 2012]. This behavior has been among the key motives for the advent of cement-based materials with enhanced ductility; including high-performance fiber reinforced cementitious composites (HPFCC).

Over the last three decades, significant research on HPFCC have been performed to address the brittleness of plain concrete. Multiple types (e.g. steel, polyvinyl alcohol) and geometries of fibers have been used with different binders' formulations (GU cement, fly ash, slag, etc.) and range (0.14 to 0.35) of water-to-binder ratios (*w/b*). Such composites have a wide range of compressive strength (40 to 150 MPa) and different ductile behavior (strain softening or hardening) when subjected to tensile stresses [e.g. Douglas and Billington, 2005; Mechtcherine *et al.*, 2012; Yang and Li, 2014]. The ductility of HPFCC is defined as the sum of the distributed deformations due to the diffused micro-crack damage up to the point where the fibers bridging capacity on one of these micro-cracks is exhausted [Li, 2012].

The selection of the fiber types in HPFCC depends on the fibers' quality, dispersibility and interfacial properties with the cementitious matrix. Basalt fibers are a relatively new type of fibers, presenting a feasible option for the concrete industry, owing to their favorable mechanical properties and cost relative to other types of fibers (e.g. glass). Basalt fibers have high tensile strength of 3,000 to 4,000 MPa and typical modulus of elasticity of 90 to 110 GPa, together with high corrosion and thermal resistance [e.g. Jiang *et al.*, 2014]. Thus, basalt fibers have been used to reinforce cement-based materials

in many studies to test their physical and mechanical properties. However, a few studies reported on the dynamic behavior of cement-based materials reinforced with basalt fibers. For instance, Li and Xu [2008, 2009a] reported that 0.1% basalt fibers by volume improved the performance of normal concrete (35 MPa) in terms of dynamic compressive strength and energy absorption capacity, where the size of the fracture pieces of the basalt fiber reinforced concrete were larger relative to that of reference concrete. Zhang *et al.* [2017] studied the impact behavior of concrete (compressive strength of 25, 35 and 45 MPa) reinforced with low contents of basalt fibers (0 to 0.25% by volume) under various high strain rates (30 to 95 s^{-1}) using Split Hopkinson Pressure Bar (SHPB) apparatus. It was found that as the fiber content increased, the toughness of the basalt fiber reinforced concrete was improved, while the fiber content of 0.1% led to the highest compressive strength [Zhang *et al.*, 2017]. However, these studies did not consider nano-modified binder formulations, novel basalt fiber types, and linkage of bulk trends to fiber/matrix interaction.

On the other hand, basalt fibers were reported to have poor alkaline resistance that made them vulnerable when used in alkaline environments with pH values more than 11 [e.g. Lee *et al.*, 2014]. Adequate bond strength between basalt fibers and cement-based matrices was obtained at early-age (7 days); nevertheless, this bond diminished within 90 days due to degradation of fibers by alkali-silica reactions, between the alkaline pore solution and SiO_2 in fibers, leading to loss of strength and durability of the composite [Jiang *et al.*, 2014]. This can be mitigated by encapsulating the fibers with polymeric resins (e.g., vinyl-ester [Branston *et al.*, 2016], polyamide [Mahmoud *et al.*, 2017].), hence forming basalt fiber pellets (BFP). Yet, research on the use of BFP in concrete and HPFCC is still at an early stage which warrants further investigation in this direction.

4.2 Research Significance

The ongoing demand for high-performance cementitious materials in infrastructure applications (e.g. pavements, bridges, docks, airfield aprons) motivates continual research on resilient composites that can function safely under different loading schemes. BFP were used at the University of Manitoba to produce nano-modified HPFCC with balanced mechanical and durability performance, in terms of high-early and late-strengths and durability [Mahmoud *et al.*, 2017; Azzam *et al.,* 2019]. Yet, other aspects such as the response of these composites to different loading configurations still require research. Therefore, the current study aimed at investigating the performance of nano-modified HPFCC comprising different dosages of BFP under quasi-static tensile and impact loads. Various dosages of BFP in different matrices with high-volume fly ash or slag (50 %) with addition of 6% nano-silica were tested. In addition, single pellet pullout, thermal and scanning electron microscopy tests were conducted to study the efficacy of BFP bonding in these composites. Data from this study should informatively assess the suitability of these composites for applications involving tensile and impact loading scenarios.

4.3 Experimental Program

4.3.1 Materials and Mixtures

The experimental scheme adopted herein is presented in **Figure 4.1**. The base binders comprised 50% general use cement (GU) and 50% supplementary cementitious materials (SCMs), either Type F fly ash or Grade 100 slag, complying with CAN/CSA-A3001 (2018) specifications (**Table 4.1**). For nano-modification, a commercial nano-silica solution (NS) was added at a single dosage of 6% (42 kg/m^3 of solid silica particles) by mass of the base binders (700 kg/m^3). The NS solution comprises 50% SiO_2 particles well-dispersed in an aqueous solution. The NS mean particle size is 35 nm, and its viscosity, specific surface,

specific gravity, and pH are 8 cP, 80 m^2/g, 1.1 g/cm^3, and 9.5, respectively. This NS product is commercially available at a cost of $1/liter, when bought in bulk amounts. According to previous studies [e.g. Mahmoud *et al*. 2017], the 6% NS dosage had favorable effects on the pore structure and hardened properties of mortar/concrete comprising SCMs.

Table 4.1: Chemical and physical properties of GU cement, fly ash and slag

Parameter	GU cement[a]	Fly ash[a]	Slag[a]
Chemical analysis			
SiO_2 (%)	19.22	55.20	33.40
Al_2O_3 (%)	5.01	23.13	13.40
Fe_2O_3 (%)	2.33	3.62	0.76
CaO (%)	63.22	10.81	42.70
MgO (%)	3.31	1.11	5.30
SO_3 (%)	3.01	0.22	2.40
Na_2Oeq. (%)	0.12	3.21	0.30
Physical properties			
Specific Gravity	3.15	2.12	2.87
Fineness (m^2/kg)	390	290	492

Note: [a]The properties of the materials were provided by the manufacturer.

Locally available finely graded sand (0 to 600 μm) with fineness modulus of 2.9 was used in the mixtures. The specific gravity and absorption of the fine aggregate is 2.6 and 1.5%, respectively. A high-range water-reducing admixture (HRWRA), poly-carboxylic acid-based complying with ASTM C494 Type F, was used to maintain a flow of 180±20 mm for all the mixtures. The HRWR dosages varied according to the incorporation of nano-silica, the type of binder, and the dosage of BFP as reported in [Azzam *et al*., 2019]. The cementitious composites were reinforced with BFP of 36 mm length (**Figure 4.2 (a)** and **Table 4.2**) at different dosages of 2.5%, 4.5% or 6.9% by volume (equivalent to 1%, 2% or 3%, respectively basalt fibers by volume). BFP are made of 16-μm basalt roving encapsulated by polyamide resin, and the fiber component represents 60% of the pellet by mass. In addition, continuously-deformed steel wire fibers (**Figure 4.2 (b)** and **Table 4.2**) of 1.14 mm diameter and 38 mm long was also used in

reference mixtures. The steel fibers were used at a single dosage of 1% by volume as a benchmark for mixtures reinforced with 2.5% BFP.

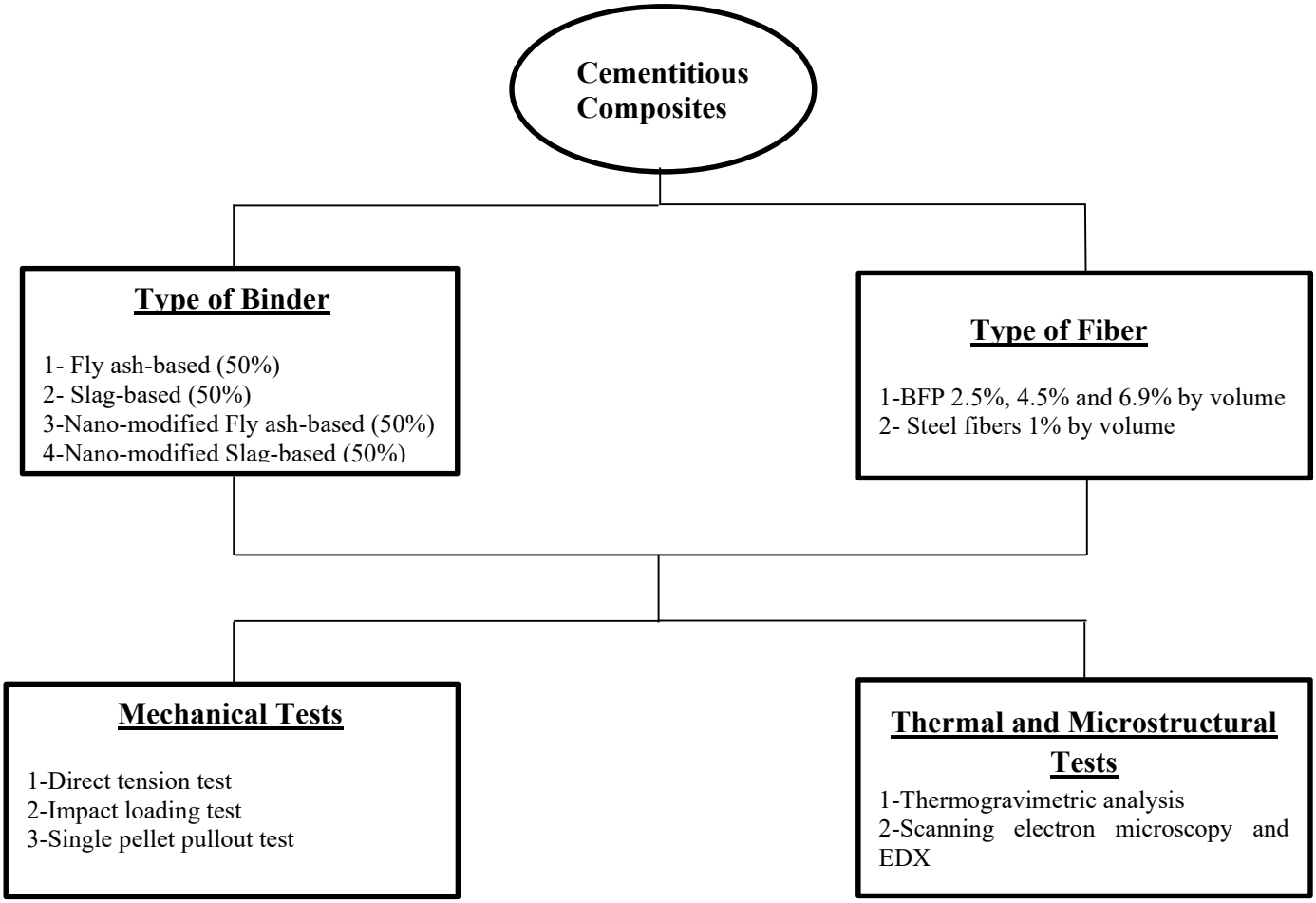

Figure 4. 1: Schematic diagram of the experimental scheme

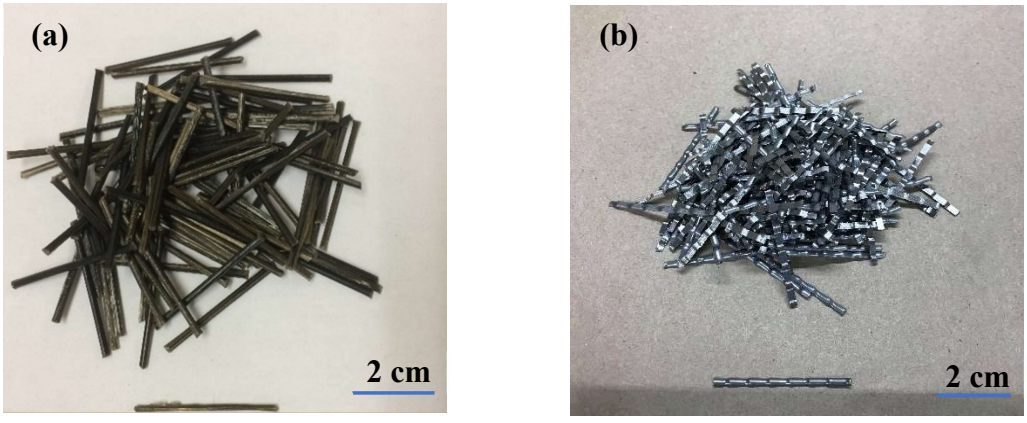

Figure 4. 2: Reinforcing fibers: (a) basalt fiber pellets (BFP), and (b) continuously-deformed steel fibers

Table 4.2: Physical and mechanical properties of BFP and steel fibers

Property	BFP[a]	Steel fibers[a]
Length (mm)	36	38
Diameter/dimensions (mm)	1.8	1.14
Aspect ratio	20	34
Specific gravity	1.74	7.7
Tensile strength (MPa)	2,300	966-1242
Elastic modulus (GPa)	65	200

Note: [a]The properties of the fibers were provided by the manufacturers.

The total contents of the base (GU cement and slag/fly ash) and nano-modified binders were 700 kg/m^3 and 742 kg/m^3, respectively with a constant *w/b* of 0.3, respectively. The proportions of the developed cementitious composites are listed in **Table 4.3**. Regarding the mixtures' ID, the letters F, G and N denote fly ash, slag and nano-silica, respectively, while the letters B and S indicates BFP and steel fibers, respectively. The number represents the volume of pellets of fibers in the composite. A pan concrete mixer with 60 rpm speed was used. Initially, the dry constituents were mixed without the fibers, followed by introducing the required water, HRWR and nano-silica sol while continuously mixing until the mixture homogeneity was attained. Finally, the fibers were added and the ingredients were mixed until uniform distribution of fibers, where the total mixing process took approximately 8-10 minutes. After casting, all specimens were covered with polyethylene sheets, demolded after 24 hours and placed in a standard curing room at 22±2°C and least 95% relative humidity until the age of testing (56 days).

Table 4.3: Mixtures proportions per cubic meter

Mixture ID.	Cement (kg)	Fly ash (kg)	Slag (kg)	Water[a] (kg)	Nano-silica (kg)	BFP (kg)	Steel fibers (kg)	Fine aggregate (kg)	HRWR (l)
F-B-2.5	350	350	--	210	--	43.3	--	1,130	2.5
G-B-2.5	350	--	350	210	--	43.3	--	1,245	6.0
N-F-S-1	350	350	--	180	84	--	77	1,090	5.6
N-G-S-1	350	--	350	180	84	--	77	1,200	7.7
N-F-B-2.5	350	350	--	180	84	43.3	--	1,045	5.6
N-F-B-4.5	350	350	--	180	84	78.3	--	1,000	5.0
N-F-B-6.9	350	350	--	180	84	119.2	--	940	4.4
N-G-B-2.5	350	--	350	180	84	43.3	--	1,160	7.6
N-G-B-4.5	350	--	350	180	84	78.3	--	1,100	7.3
N-G-B-6.9	350	--	350	180	84	119.2	--	1,050	7.0

Note:
[a] Adjusted amount of mixing water considering the water content of nano-silica (aqueous solution with 50% solid content of SiO_2).

4.3.2 Testing

4.3.2.1 Direct Tension

The uniaxial quasi-static tensile test was performed on triplicate cylindrical (75×250 mm) specimens. These were reported to reliably reflect the tensile behavior of fiber-reinforced cementitious composites due to the constant cross section, which increases the probability of first-cracking occurrence away from the gripped ends of the specimen [e.g. Mechtcherine *et al*., 2011; Curosu *et al.*, 2016]. The cylinders were glued at both ends using rapid-setting high modulus adhesive epoxy to threaded steel sleeves such that the bonded length of the specimen to each sleeve was 75 mm and the remaining/free length was 100 mm. The sleeves were then screwed into testing platens to prevent rotation at the cross heads. A servo-controlled closed-loop testing machine was used, where the deformations were measured on each side of the specimen using two LVDTs (linear variable displacement transducers). The tests were performed in a displacement-control mode at a rate of 0.2 mm/min conforming to the common ranges used in the literature [e.g.

Yu *et al.*, 2018; Zhou and Qiao, 2020] and complying with the rates described in the ASTM standard for flexural testing of fiber reinforced concrete (ASTM 1609).

The parameters determined from the recorded data were the first-cracking strength, the elastic modulus, the strain hardening modulus as well as the energy absorption capacity. The first-cracking strength was specified as the inflection point between the elastic and strain hardening parts on the stress-strain curve. However, fluctuations in some of the tested specimens occurred in the elastic section and then increased up to the strain-hardening portion; hence, in these cases, the first-cracking strength was determined using the starting point of the strain-hardening part. While the elastic modulus was determined as the slope of the curve in the elastic stage. On the other hand, the strain hardening modulus was determined as the slope of the tangent at the post-cracking stage up to the failure limit. The energy absorption capacity was calculated by the integration of the area under the stress-strain curves up to a limit of 4% strain, at which the stress-strain relationship either reached a plateau or dropped to zero.

4.3.2.2 Impact Test

The SHPB test was used to assess the response of composites to impact loading. The splitting configuration was employed to assess the dynamic properties of the composites: dynamic compressive strength, stress-strain relationship, and dynamic increase factor (DIF). Triplicate discs for each mixture, where the total diameter and thickness of the discs were 75 mm and 38 mm, respectively, but the effective diameter on which the projectile hit the specimen was 38 mm diameter. The specimens were fixed at the end of the transmitter bar as shown in **Figure 4.3**.

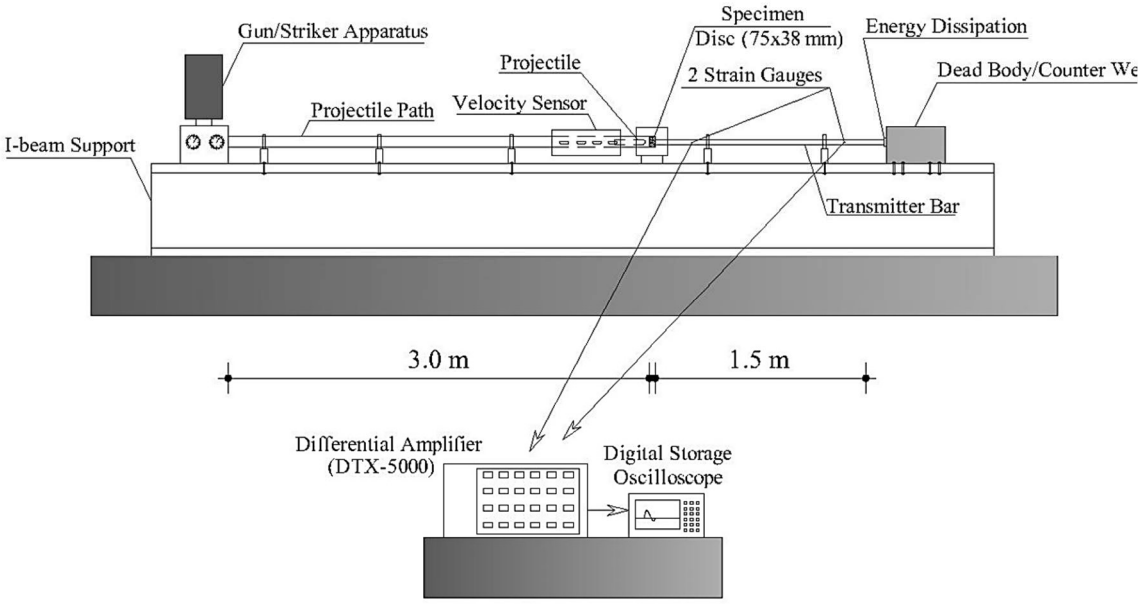

Figure 4. 3: Schematic of the SHPB test set-up.

The impact load was applied to the specimens by the striker (projectile) via a fired gas gun, and was then transferred to the transmission bar and counterweight. The specimens were tested under an impact pressure of 0.3 MPa, which is within the range of SHPB impact loading reported by previous studies on cement-based materials [e.g. Zhang *et al.*, 2017; Al-Salloum *et al.,* 2015]. In this configuration, the strain rate is dependent on the pressure under which the projectile is launched amidst other parameters, where the representative strain rate of the loading wave adopted in the present study was taken as the strain rate corresponding to the ultimate stress, which had an average value of 50 s^{-1}.

The fundamentals of SHPB test is the propagation theory of elastic stress-wave [Wang 2005], which is based on two main assumptions. The first is every cross-section of elastic bar remains plane during the wave propagation process (plane assumption), while the second assumption is that stresses in the bar are the same everywhere (stress assumption) [Ravichandran & Subhash, 1994]. The elastic wave signal was recorded and stored through the oscilloscope, which was used to generate the dynamic stress-strain plot,

according to the equations described by [Asala *et al.,* 2018], where the true strain *(ε_t)* was calculated by:

$$\varepsilon_t = ln\frac{l(t)}{l_o} \quad \textbf{(Equation 4.1)}$$

where, l_o(m) is the initial sample length and $l(t)$ (m) is the instantaneous change in length, which can be obtained directly from the known function of force, $f(t')$:

$$l(t) = l_o - v_o t + \frac{2}{ZA}\int_0^t f(t')dt' \quad \textbf{(Equation 4.2)}$$

where, v_o(m/s) is the impact velocity, z (N·s/m) is the mechanical impedance of the bar which is the complex ratio of force to velocity at a given point in a mechanical device and A (m2) is the cross-section area of the bar. The equivalent true stress, σ (MPa) is obtained by:

$$\sigma = \sigma_t - \sigma_r \quad \textbf{(Equation 4.3)}$$

where, σ_t (MPa) is the experimental stress obtained by:

$$\sigma_t = \frac{F(t)}{A(t)} \quad \textbf{(Equation 4.4)}$$

where, $F(t)$ (N) is the load pulse corresponding to time t (s) and A (mm2) is the initial cross-section area, and the radial stress σ_r (MPa) due to inertia during impact deformation is estimated:

$$\sigma_r = \frac{3\rho}{8}\left(\frac{a_0}{l_0}\right)^2 \frac{v_0}{(1-\epsilon(t))^3} \quad \textbf{(Equation 4.4)}$$

where, a_0 (m) is the initial radius of the specimen, ρ (kg/m3) is the density of the bar and $\epsilon(t)$ is the engineering strain.

4.3.2.3 Bonding, Thermal and Microstructural Tests

The single pellet pullout test was used to evaluate the interfacial bonding between the cementitious matrices and BFP, when subjected to tensile stresses at different rates. Five replicates of matrix blocks with dimensions of 100×100×50 mm including a single pellet embedded to a length of 18 mm in the middle of the prism as shown in **Figure 4.4** were tested. Two displacement rates, 0.2 mm/min and 50 mm/min, were implemented to assess the load-slip interaction between the pellet and matrix. These rates reflect the quasi-static tensile and impact responses, respectively.

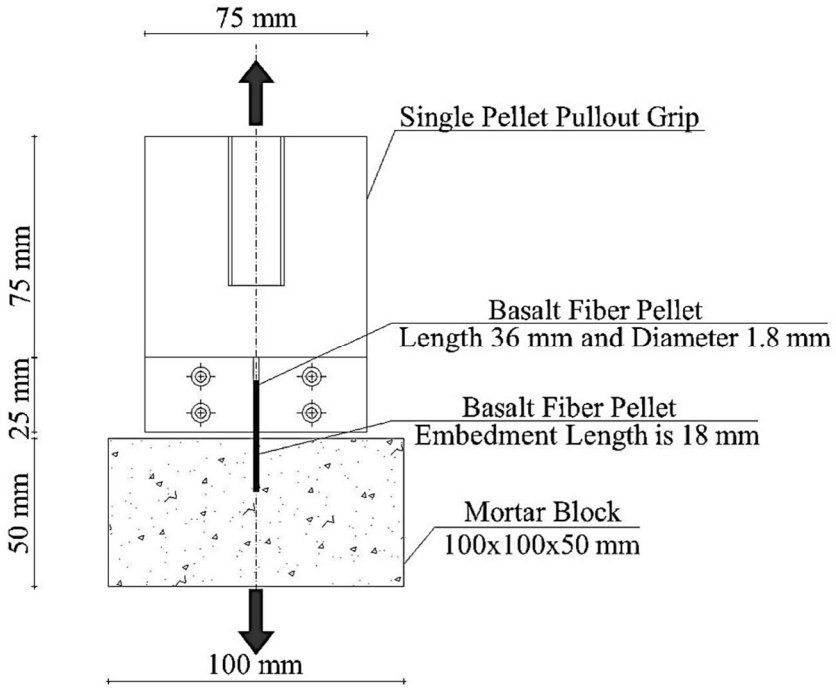

Figure 4.4: Single pellet pullout test set-up

To corroborate the trends obtained from the macro-scale tests, thermal and microscopy investigations were conducted to assess the evolution of the cementitious composites' microstructure. Portlandite (CH) quantities in the matrix were determined up to 90 days to assess the effect of nano-silica, fly ash, and slag on the hydration and pozzolanic reactions by thermogravimetric analysis (TGA). Fracture pieces from

specimens were pulverized to fine powder passing sieve #200 (75 μm) and heated at a rate of 10°C/min. The portlandite content was calculated by determining the drop of the ignited mass percentage at a temperature range from 400 to 450°C, and multiplying it by 4.11 (the ratio of the molecular mass of CH to that of water). The characteristics of the interface between the pellets and matrix were investigated by scanning electron microscopy analysis (SEM) assisted by JED-2300 energy-dispersive X-ray spectroscopy (EDX). The tests were performed on fracture pieces taken from the specimens and individual pellets, which were carbon coated to enhance conductivity for the SEM imaging.

4.4 Results

4.4.1 Direct Tension Load

Table 4.4 lists the tensile properties obtained for the composites based on the stress-strain curves of the quasi-static direct tension test, as for example shown in **Figure 4.5**. Most specimens failed by transverse cracks within the middle section (e.g. **Figure 4.6**), due to the uniform geometry of the specimens used, which minimized stress concentration and failure near the griping ends. The first-cracking strength of the nano-modified composites was higher compared with that of corresponding reference mixtures without nano-silica, depending on the type of binder. For instance, the increase in the first-cracking strength for mixture N-F-B-2.5 was 25% relative to the reference mixture F-B-2.5, while it was 52% for N-G-B-2.5 relative to its counterpart without nano-silica (G-B-2.5).

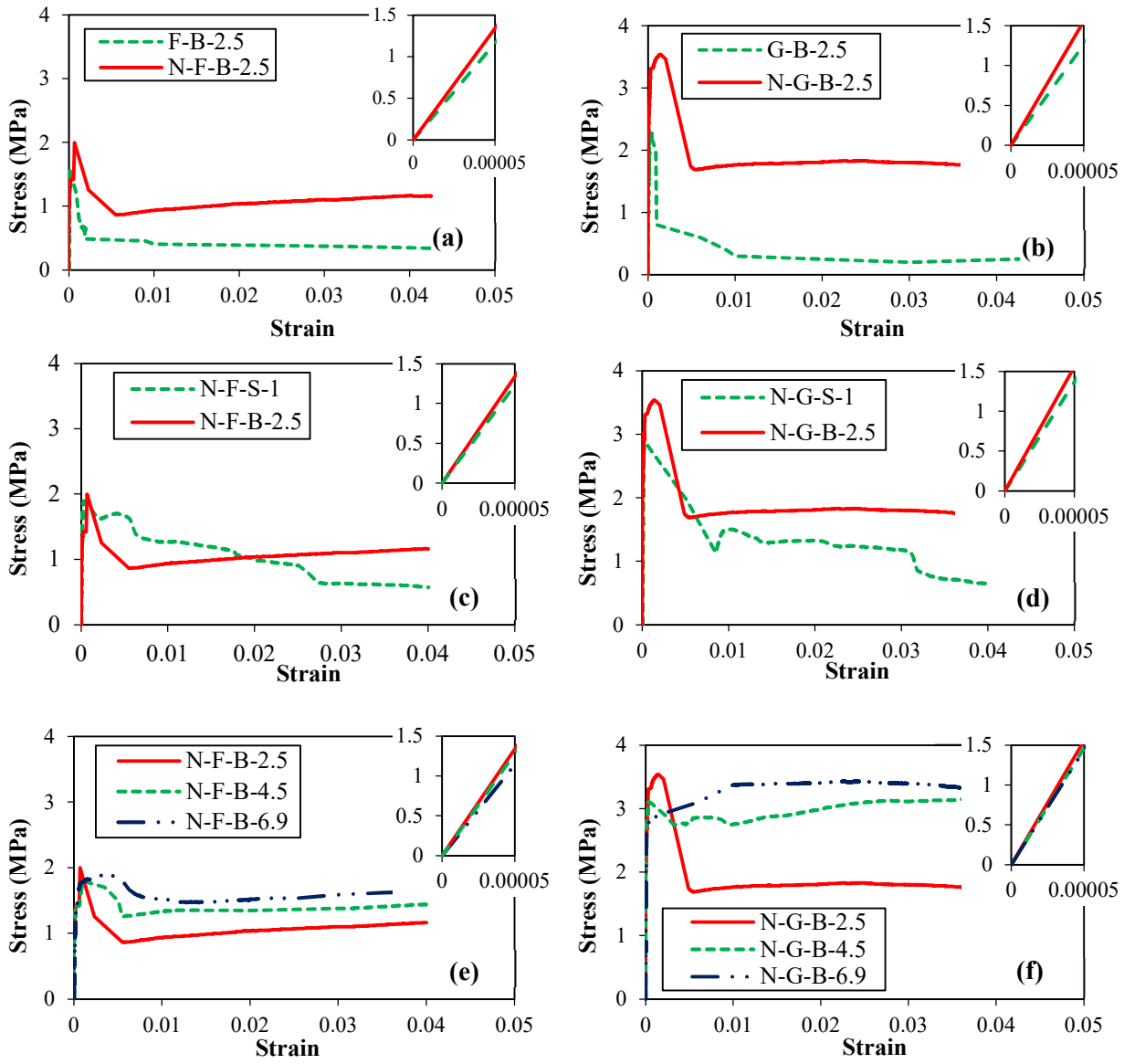

Figure 4.5: Exemplar stress-strain relationships of the fly ash-based [left: (a), (c), (e)], and slag-based [right: (b), (d), (f)] composites from the tension test. (Note: the initial part in the elastic stage is enlarged in top right corner)

Correspondingly, nano-modification of the mixtures affected the modulus of elasticity of the developed composites, since N-F-B-2.5 (26.2 GPa) and N-G-B-2.5 (31.1 GPa) were 12% and 23% higher than that of their corresponding reference mixtures (**Table 4.4**). In addition, the post cracking performance of the nano-modified composites was enhanced relative to that of the reference mixtures. For example, the energy absorption capacity of N-F-B-2.5 and N-G-B-2.5 mixtures were 32% and 178% higher than that of

their reference counterparts without nano-silica [**Table 4.4** and **Figures 4.5(a)-(b**)]. These results highlight the significant role of nano-silica at improving the performance of fiber reinforced cementitious binders incorporating high-volume fly ash or slag.

Table 4.4: Tensile properties of the composites

Mixture ID.	First-cracking strength (MPa)	Elastic modulus (GPa)	Strain hardening modulus (MPa)	Energy absorption capacity (kJ/m^3)
F-B-2.5	1.6 (0.3)	23.2 (3.2)	--*	18.1 (1.6)
G-B-2.5	2.3 (0.4)	25.1 (3.1)	--*	20.9 (2.1)
N-F-S-1	1.9 (0.2)	24.6 (2.4)	--*	19.9 (1.9)
N-G-S-1	2.7 (0.4)	27.4 (2.8)	--*	53.5 (3.8)
N-F-B-2.5	2.0 (0.3)	26.2 (2.2)	3.8 (0.3)	24.0 (2.9)
N-F-B-4.5	1.8 (0.2)	25.5 (2.1)	3.2 (0.2)	55.7 (4.7)
N-F-B-6.9	1.8 (0.2)	22.9 (2.4)	4.6 (0.6)	64.3 (4.9)
N-G-B-2.5	3.5 (0.3)	31.1 (2.7)	3.5 (0.4)	58.2 (4.2)
N-G-B-4.5	3.1 (0.4)	29.6 (2.9)	17.3 (1.4)	82.2 (8.5)
N-G-B-6.9	2.8 (0.3)	28.9 (2.6)	26.7 (2.9)	140.2 (10.2)

Note: Numbers in parentheses indicate standard deviations.
*These mixtures experienced strain softening in the post-cracking stage.

Nano-modified cementitious composites with a specific dosage of steel fibers (1%) were used as references to conjugate composites reinforced with 2.5% BFP, i.e. 1% basalt fibers. The results [**Table 4.4** and **Figures 4.5(c)-(d)**] showed that the BFP reinforced mixtures had comparable or better performance (in terms of initial cracking and energy absorption) relative to that of the steel reinforced mixtures, despite the higher modulus of elasticity of the steel fibers compared with BFP. For instance, the first-cracking strength and energy absorption capacity of N-F-B-2.5 was 5% and 20%, respectively higher than that of N-F-S-1, whereas these properties for N-G-B-2.5 was 29% and 8%, respectively, higher than that of N-G-S-1. Beyond first-cracking, the composites reinforced with BFP (N-F-B 2.5 and N-G-B-2.5) had limited strain softening stage followed by a plateau, while the composites with steel fibers (N-F-S-1 and N-G-S-1) had a strain softening behavior **[Figures 4.5(c)-(d)**]. These trends allude to improved bonding between BFP and the

cementitious matrix compared with steel fibers, as will be elucidated in the Discussion section.

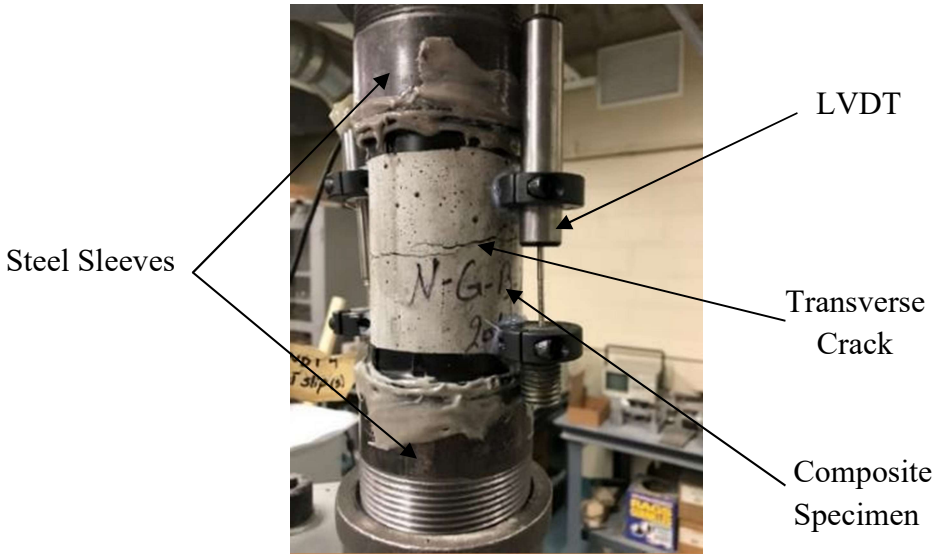

Figure 4.6: Exemplar mode of failure of N-G-B-4.5 specimens in the direct tension test

The first-cracking tensile strength of all the nano-modified composites reinforced with BFP was in the range of 1.8 to 3.5 MPa, which represents approximately 50% of the tensile strength obtained from flexural tests for similar composites, using ASTM C1609 [Azzam *et al.*, 2019]. Flexural tests typically give tensile strength in the range of 40 to 100% higher than that obtained from direct tension tests for the same concrete, as in the former only part of the specimen's cross section (bottom part in the middle-third span) is subjected to maximum tension. Thus, the likelihood of existence of weak links in the specimen is higher in the direct tension configuration, with more uniform stress distribution on the entire cross section [Mehta and Monteiro, 2014]. A relatively analogous elastic behavior was obtained before first-cracking of the nano-modified composites reinforced with BFP, as narrow ranges of elastic moduli were obtained for the fly-ash (23 to 26 GPa) and slag (29 to 31 GPa) mixtures (**Table 4.4**). This implied a dominant effect of the

cementitious matrix during this stage. The average strength at first-cracking of these composites slightly decreased as the BFP dosage increased. For instance, the reduction of the first-cracking strength for the fly ash-based composites N-F-B-4.5 and N-F-B-6.9 was 11 and 13 %, respectively relative to that of N-F-B-2.5. However, this reduction of strength was insignificant, considering the overlapping range of results (**Table 4.4**).

The stress-strain relationships of the developed composites with BFP [**Figures 4.5(e)**-(**f)**] showed enhanced post-cracking performance with the higher dosages of BFP (4.5% and 6.9 %). After first-cracking, a sudden drop of the load occurred; however, the specimens were able to restrain growth of cracks and partially/totally restored their load carrying capacity, depending on the BFP dosage and type of binder. Nano-modified fly-ash based composites reinforced with BFP had a limited strain softening behavior followed by a plateau or with small staring hardening moduli (average of 3.6 MPa). The energy absorption capacity of the mixtures N-F-B-4.5 and N-F-B-6.9 were 132 and 167%, respectively, higher than that of mixture N-F-B-2.5 (24 kJ/m^3). Nano-modified slag-based composites reinforced with BFP with higher (4.5 and 6.9%) BFP dosages showed strain-hardening trend in the direct tension test (strain hardening moduli of 17.3 and 26.7 MPa, respectively). Correspondingly, mixtures N-G-B-4.5 and N-G-B-6.9 had energy absorption capacity of 41 and 140%, respectively higher than that of mixture N-G-B-2.5 (58.2 kJ/m^3) [**Table 4.4**]. This suggested improved interaction and bonding of BFP with the nano-modified slag-based binder.

4.4.2 Impact Load

The mode of failure of the specimens under impact loading is for example shown in **Figure 4.7**. The pattern was comminution of the mortar with various sizes of scattered fragments. The failure of the fibers (BFP or steel) was found to be through pull-out rather than

breakage. It was observed that the fractured fragments of the composites reinforced with BFP were larger compared with that of steel reinforced composites with no notable difference among the composites with different BFP dosages (e.g. **Figure 4.7**).

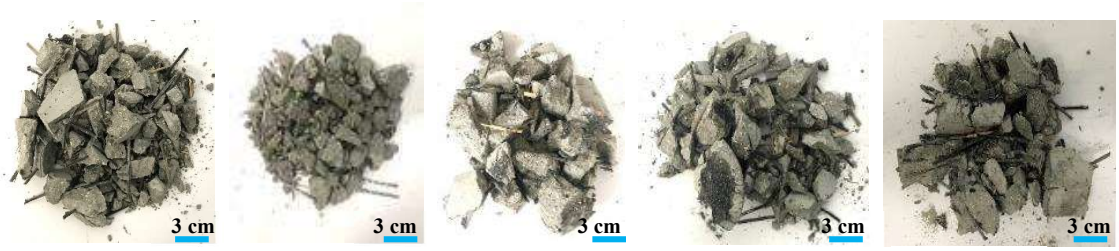

F-B-2.5 N-F-S-1 N-F-B-2.5 N-F-B-4.5 N-F-B-6.9

Figure 4.7: Exemplar failure patterns for the fly ash-based mixtures after impact loading

Table 4.5 lists the mechanical performance of the developed composites subjected to quasi-static compression and compressive impact waves generated from a projectile. The stress-strain curves for the composites under the impact loading are for example shown in **Figure 4.8**.

Table 4.5: Static and dynamic performance parameters of the composites

Mixture ID.	Static compressive strength (MPa)	Dynamic compressive strength (MPa)	DIF	Strain at failure (%)	Energy absorption capacity (kJ/m^3)
F-B-2.5	60.0 (1.1)	82.9 (2.7)	1.4	0.532	356 (16)
G-B-2.5	80.7 (1.0)	95.9 (2.6)	1.2	0.884	706 (26)
N-F-S-1	71.4 (1.2)	83.3 (2.6)	1.2	0.405	284 (18)
N-G-S-1	86.6 (1.1)	98.6 (2.8)	1.1	0.693	585 (23)
N-F-B-2.5	65.2 (0.6)	89.0 (2.4)	1.4	0.622	406 (19)
N-F-B-4.5	54.8 (0.8)	80.9 (2.3)	1.5	0.671	440 (21)
N-F-B-6.9	48.0 (0.8)	73.3 (2.4)	1.5	0.713	458 (17)
N-G-B-2.5	82.9 (0.9)	111.9 (2.5)	1.3	1.406	1122 (36)
N-G-B-4.5	71.3 (1.0)	91.8 (2.2)	1.3	1.642	1130 (41)
N-G-B-6.9	61.7 (0.8)	89.9 (2.3)	1.4	1.734	1170 (32)

Note: Numbers in parentheses indicate standard deviations.

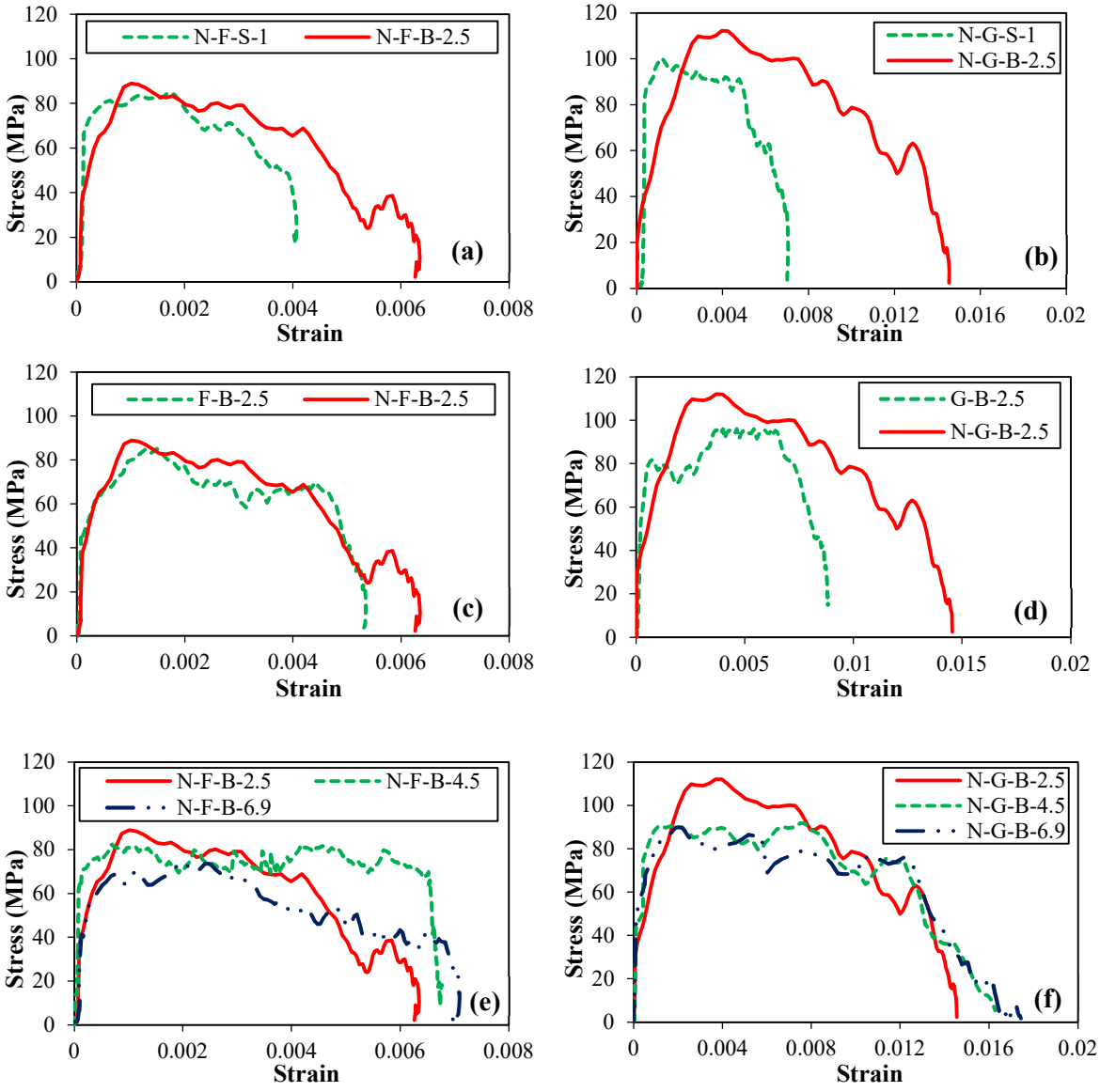

Figure 4.8: Exemplar stress-strain relationships of the fly ash-based [left: (a), (c), (e)] and slag-based [right: (b), (d), (f)] composites from the impact test

The compressive strength of the composites increased with increasing the strain rate, as indicated by the dynamic increase factor (DIF: ratio between the dynamic and quasi-static compressive strengths), which ranged between 1.1 and 1.5 (**Table 4.5)**. This is related to growth of micro-cracks into macro-cracks in the cementitious matrix during the testing duration, which is a function of the applied rate of loading/deformation. In quasi-static tests (strain rate of $1.5e^{-6}$ s^{-1}), there was ample time for slower initiation of micro-

cracks and their growth to macro-cracks in the cementitious matrix contributing to reducing its capacity. Comparatively, the very short time of the impact loading (strain rate of 40 to 70 s^{-1}), did not allow the growth of multiple micro-cracks in the specimens, which led to higher ultimate strength (dynamic compressive strength) of the cementitious matrix.

The dynamic performance of the composites under impact compression waves showed similar trends to those obtained from the quasi-static tensile loading test. This could be ascribed to the fact that the failure due to impact loading is a result of a reflected tensile stress wave after hitting a free boundary on the distal side of the element [Malvar and Ross, 1998]. It was observed that the dynamic compressive strength as well as the ductility of the nano-modified composites were relatively higher than that of reference mixtures without nano-silica. The increase in the dynamic compressive strength of N-F-B-2.5 and N-G-B-2.5 specimens was 9% and 17%, respectively, relative to that of F-B-2.5 and G-B-2.5. Correspondingly, the energy absorption capacity of N-F-B-2.5 and N-G-B-2.5 were 14% and 59% higher than that of their corresponding mixtures without nano-silica [**Table 4.5** and **Figures 4.8(a)**-(**b**)].

Specimens reinforced with BFP (2.5% BFP, i.e. 1% basalt fibers) had comparable or improved dynamic performance compared with their counterparts reinforced with 1% steel fibers. The dynamic compressive strength of N-F-B-2.5 and N-G-B-2.5 was 7% and 13%, respectively, higher than that of N-F-S-1 and N-G-S-1. Furthermore, the composites reinforced with BFP showed enhanced ductility relative to that of the steel fiber reinforced composites, as the energy absorption capacity of N-F-B-2.5 and N-G-B-2.5 were 43% and 92%, respectively higher than that of their steel fiber reinforced counterparts [**Table 4.5** and **Figures 4.8(c)**-(**d**)]. Similar to the tensile test trends, the ductility behavior in the

dynamic mode of loading, alluded to improved bonding between the BFP and the cementitious matrix, especially the one comprising nano-silica and slag.

The impact stress-strain curves of the nano-modified composites reinforced with different pellet contents showed that the tested specimens exhibited comparable elastic stage before the peak stress was reached, depending on the type of binder. However, the average dynamic compressive strength of the nano-modified composites reinforced with BFP significantly decreased as the BFP dosage increased. For instance, the dynamic compressive strength for the slag-based composites N-G-B-4.5 and N-G-B-6.9 was 18 and 20 %, respectively, lower than that of N-F-B-2.5 (111.9 MPa). However, the ductility of nano-modified composites reinforced with BFP was generally improved with the higher dosages of BFP (4.5% and 6.9 %). Once the peak stress was reached, a strain softening trend was mostly observed [**Figures 4.8(e)**-(**f)**]. The bridging effect of the pellets was observed according to the binder type; as the pellets' dosage increased, the downward trend gradually diminished with increase in the failure strain. For example, the strain at failure for the fly ash-based composites N-F-B-4.5 and N-F-B-6.9 was increased by 8% and 15%, respectively, relative to N-F-B-2.5 (0.622%). On the other hand, the slag-based composites showed enhanced performance relative to the fly ash-based ones at the same BFP dosage. The dynamic compressive strength of the mixtures N-G-B-2.5, N-G-B-4.5, and N-G-B-6.9 were 26%, 13%, and 23% higher than that of the fly ash counterparts. In addition, the energy absorption capacity of mixtures N-G-B-2.5, N-G-B-4.5, and N-G-B-6.9 were 176%, 157%, and 155% higher than that of the corresponding fly ash composites (**Table 4.5**). Again, this alluded to the better bonding between BFP and the nano-modified slag-based binder.

4.5 Discussion

4.5.1 Effect of Binder

The mechanical performance of composites containing nano-silica showed marked improvement under the tensile and impact loads. According to previous studies (e.g. Madani *et al.*, 2012; Oertel *et al.*, 2013), the mechanisms imparted by nano-silica to modify cement-based materials are attributed to nucleation, pozzolanic and filler effects. Ultrafine nano-silica (80,000 m^2/kg) can accelerate the hydration of cement by creating additional surfaces for early precipitation of hydration products (nucleation effect). In addition, nano-silica sols (originally dispersed to their primary sizes) were found to form small-enough agglomerates to impart a filler effect in the cementitious matrix [Oertel *et al.*, 2013]. In addition, Kong *et al*. [2012] reported that when small nano-silica agglomerates form, water is absorbed into their high nano-porosity which can reduce the *w/b* in the paste; hence improving the matrix microstructure. It was postulated that silica particles (nano- or micro-scale) result in multiplication of links between the calcium silicate hydrate (C-S-H) phase, producing stronger and more stable matrix [Szeląg, 2018; Du *et al.*, 2014].

In the current study, the impact of nano-silica on the reactivity of binders was assessed by determining the change of calcium hydroxide (CH) contents in the nano-modified cementitious composites relative to the reference mixtures (without nano-silica) up to 90 days (**Table 4.6**). The reduction of CH in the nano-modified fly ash and slag-based binders (N-F and N-G, respectively) began at early-age in spite of the high dosage of fly ash and slag (50 %), which are classified as slow reactivity SCMs. For example, at one day, the normalized contents of CH in N-F and N-G mixtures were 0.90 and 0.82, respectively, relative to their corresponding reference mixtures (F and G, respectively).

Table 4.6: Thermal analysis of the binders

Calcium hydroxide content (%)	Time (Days)					
	1	**3**	**7**	**28**	**56**	**90**
F	6.75	7.92	8.31	8.84	8.23	7.64
G	6.94	7.64	8.26	9.84	9.42	7.96
N-F	6.07	5.95	5.35	3.65	3.37	3.07
N-G	5.81	4.92	4.32	3.34	3.11	2.47
Relative comparison	**Normalized calcium hydroxide Content**					
N-F/F	0.90	0.75	0.64	0.41	0.41	0.40
N-G/G	0.83	0.64	0.52	0.34	0.33	0.31
N-G/N-F	0.94	0.83	0.80	0.92	0.87	0.85

Note: Precision of measurement is ± 0.20%.

The ultrafine surface of nano-silica acted as nucleation sites for the dissolution of cement and precipitation of hydration products. Subsequently, quick consumption of CH verified the vigorous pozzolanic activity in the nano-modified binders at early-age due to the addition of nano-silica to generate secondary C-S-H gel in the matrix. Significant consumption of CH (average normalized contents of 0.41 and 0.34 in the N-F and N-G binders, respectively) occurred within 28 days, followed by nil or very slow rate of depletion up to 90 days (**Table 4.6**). This suggested that nano-silica had synergistically catalyzed reactivity of fly ash and slag-based binders, resulting in a higher degree of maturity and microstructural densification at 28 days, which mitigated the slower reactivity of the base binders used without nano-silica (F and G).

Single pellet pullout tests were carried out at two different displacement rates (0.2 mm/min and 50 mm/min) to quantify the influence of nano-silica on the interfacial bonding between the developed binders and BFP. It was found that the influence of nano-silica on the developed mixtures (fly ash and slag-based matrices) was reflected on the single pellet pullout parameters [**Figures 4.9(a)-(b)**] at both rates. For instance, the pullout force of BFP from the nano-modified fly ash and slag mixtures under the slow rate (0.2 mm/min) were 12% and 25%, respectively, higher than that of their corresponding reference mixtures without nano-silica. The pozzolanic and filler effects of nano-silica densified the interfacial

transition zone (ITZ) with BFP and resulted in the deposition of hydration products in the pellets micro-grooves, leading to the improvement of the interfacial bond strength between the matrix and BFP.

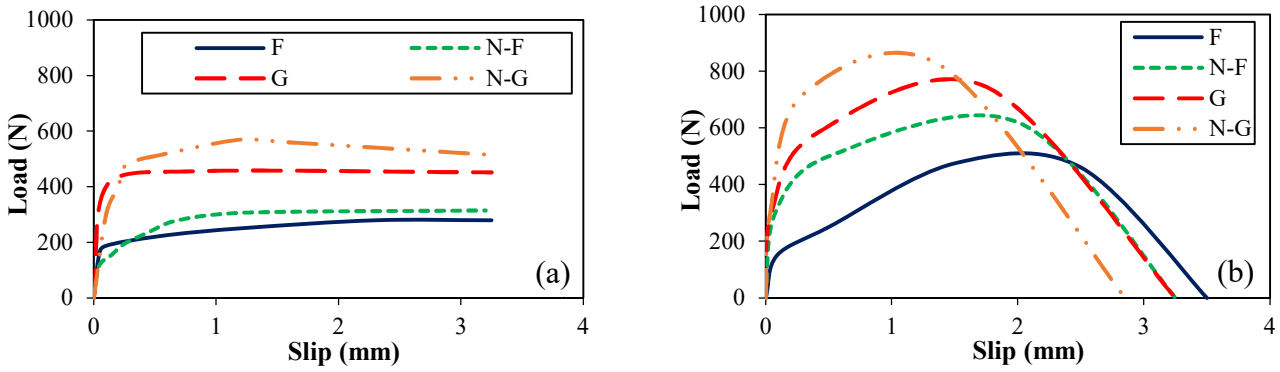

Figure 4.9: Load-slip curves of single BFP pullout test for slag and fly ash-based matrices without and with nano-silica at a displacement rate of: (a) 0.2 mm/min, (b) 50 mm/min

Figures 4.10 and **4.11** show exemplar SEM micrographs of fracture specimen with BFP extracted from G-2.5 and N-G-2.5 composites after 28 days. Dense microstructure matrix and ITZ was noticed between the mortar and BFP for N-G-2.5, while coarser matrix with unreacted slag was observed for G-2.5. EDX analysis was performed to determine calcium-to-silicate ratio (*Ca/Si*) for the cement gel in the ITZ. It was found that the average *Ca/Si* was 1.21 for the nano-modified slag-based matrix, indicating precipitation of pozzolanic C-S-H in this zone (**Figure 4.11**), whereas the *Ca/Si* was 1.75 for the reference matrix without nano-silica due to the slower reactivity of the base binder (**Figure 4.10**). The *Ca/Si* of C-S-H from the pozzolanic reaction tends to 1.1, whereas primary C-S-H generated from the hydration reactions of cement tends to 1.7 [Detwiler *et al.*, 1996].

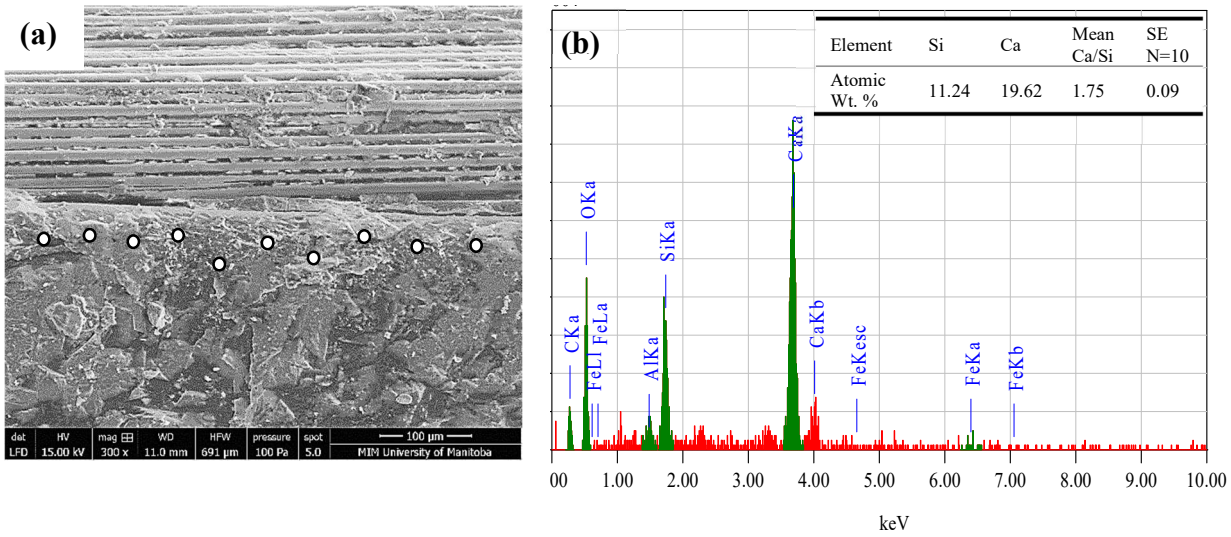

Figure 4.10: Exemplar SEM micrograph for the slag composite without nano-silica at 28 days showing: (a) ITZ with BFP, and (b) EDX spectrum of paste at the indicated locations (SE: standard error)

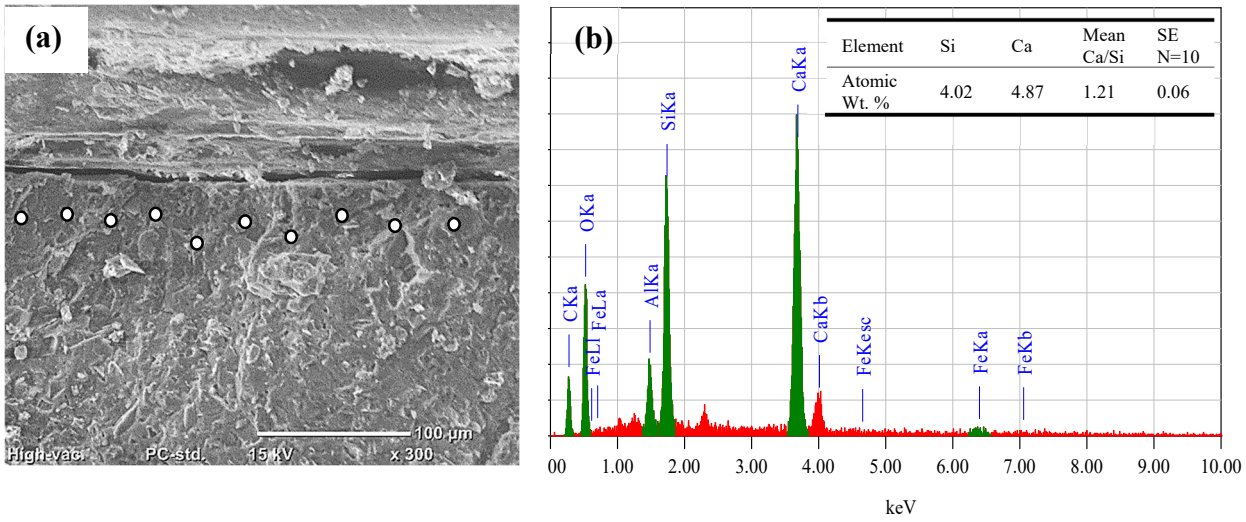

Figure 4.11: Exemplar SEM micrograph for the nano-modified slag composite at 28 days showing: (a) ITZ with BFP, and (b) EDX spectrum of paste at the indicated locations (SE: standard error)

Under the tensile and impact loads, the slag-based composites showed enhanced mechanical performance relative to the fly ash-based ones at the same BFP dosage. The tensile strength test specimens were tested up to complete failure and they showed better distribution of BFP in the slag-based matrix (e.g. **Figure 4.12**). This can be ascribed to the cohesive nature of slag binders in the fresh state, due to the angular shape of the slag

particles, which might have induced an interlocking effect. Comparatively, more flowable fly-ash based binders (due to the ball bearing effect of rounded fly ash particles) might have allowed plastic settlement of BFP, which influenced the distribution pellets. In addition, the improvement in the hardened state, originated from the higher reactivity of slag relative to fly ash (which was accelerated with the coexistence of nano-silica). This could be attributed to the finer nature of slag (492 kg/m^2) and higher content of lime (about 44 %-latent binder) compared with that of fly ash (290 kg/m^2, 10%-slowly reactive pozzolan, respectively). **Table 4.6** showed the normalized CH contents in the nano-modified slag-based mixture compared with that in the nano-modified fly ash-based mixture at various ages to determine the relative reactivity between both mixtures. This ratio was consistently less than 1 at both early- and later-ages, which indicated the accelerated reactivity of the nano-modified slag-based binder, thus consuming the portlandite in the system and depositing higher amounts of pozzolanic C-S-H gel.

(a) (b)

Figure 4.12: Distribution of BFP in the failure planes of: (a) N-G-B-2.5, and (b) N-F-B-2.5 after the direct tension test.

The improved reactivity of the slag-based composites produced higher quality ITZs between the pellets and the matrix [**Figure 4.11 vs. Figure 4.13]**, and consequently better interfacial bond strength which was substantiated by the single pellet pullout test [**Figures 4.9 (a)-(b)**]. Accordingly, the slag-based matrices without and with nano-silica modification had 62% and 81%, respectively higher bond strength (pullout force) with the BFP relative to their fly ash counterparts. Correspondingly, the average *Ca/Si* of the paste in the ITZ of the nano-modified slag-based binder was 1.21, compared with 1.32 in the fly ash-based binder, substantiating the more efficient and accelerated reactivity of the former. This was reflected on the stress transfer ability between the slag-based matrix and BFP that alleviated the stress concentration at the cracking regions, resulting in enhanced ductility.

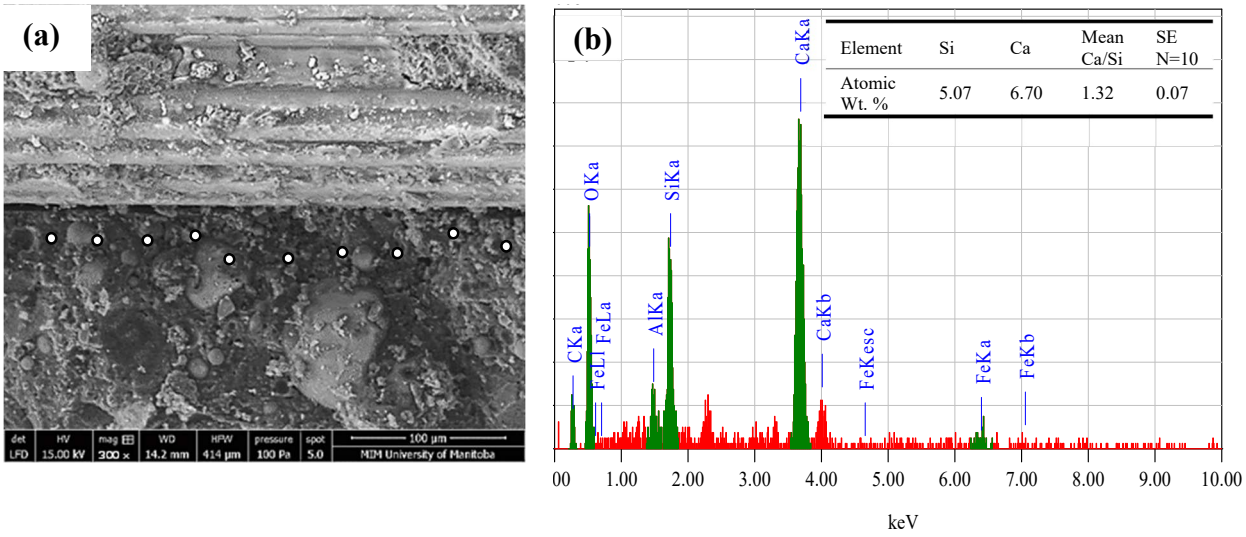

Figure 4.13: Exemplar SEM micrograph for the nano-modified fly ash composite at 28 days showing: (a) ITZ with BFP, and (b) EDX spectrum of paste at the indicated locations (SE: standard error)

4.5.2 Effect of BFP

BFP and steel fibers had limited contribution to the behavior of composites during the pre-cracking stage relative to the post-cracking one, as comparable elastic behavior was obtained before first-cracking of the specimens depending on the type of binder. The influence of BFP and steel fibers on the composites' performance was more evident after the development of macro-cracks due to the interaction between the matrix and the pellets/fibers, resulting in significant changes in the ductility of composites. The composite behavior in the pre-cracking stage was mainly affected by the matrix quality. However, the inclusion of BFP at higher dosages decreased the ultimate tensile strength of the composites, and it reduced the ultimate compressive strength for both the static and dynamic loading schemes. This is attributed to the creation of additional ITZs within the matrix as the pellets' dosage increased, where micro-cracks commence at such weak links and areas of stress concentration. In addition, in a previous study by the authors [Azzam et al. 2019], it was observed that the inclusion of higher dosages of BFP increased the volume of air in the hardened paste, which reduced the ultimate strength of the composites.

For both types of binders, the cementitious composites incorporating BFP had comparable performance in the pre-cracking stage with their steel fibers counterparts, due to the dominant effect of the matrix at this stage as discussed earlier. However, using BFP in the nano-modified composites was more efficient relative to steel fibers in the post-cracking stage in terms of improving ductility, which was conspicuous in the dynamic compression test results. This could be ascribed to the tailored micro-grooves in the longitudinal direction on the pellets' surface, which imparted an interlocking action between the pellets and the matrix, through the increased contact surface and provision of host locations for deposition of hydration products, as for example shown in **Figure**

4.14(a). Comparatively, the smooth surface of crimped steel fibers did not have such morphological features [**Figure 4.14(b)**]. Thereby, the improved pellets/matrix interfacial bonding enabled BFP to bridge the developed cracks and restrain their growth in the matrix resulting in high resistance to pullout, which was the key toughening mechanism responsible for improving the energy absorption capacity of the developed composites. This also explains the higher dynamic compressive strength for the BFP reinforced composites relative to that of their steel fibers counterparts. When fiber reinforced cementitious composites are subjected to compressive impact loading, the cement mortar starts to crack first and the fibers/pellets resist the rapid growth of cracks. If the load is sufficiently high, interfacial damage between the mortar and fibers/pellets initiates leading to their pullout [Zhang *et al.*, 2018]. During this process, considerable energy is required to overcome the cracking resistance of fibers/pellets, resulting in improving the dynamic compressive strength and ductility, especially in the case BFP.

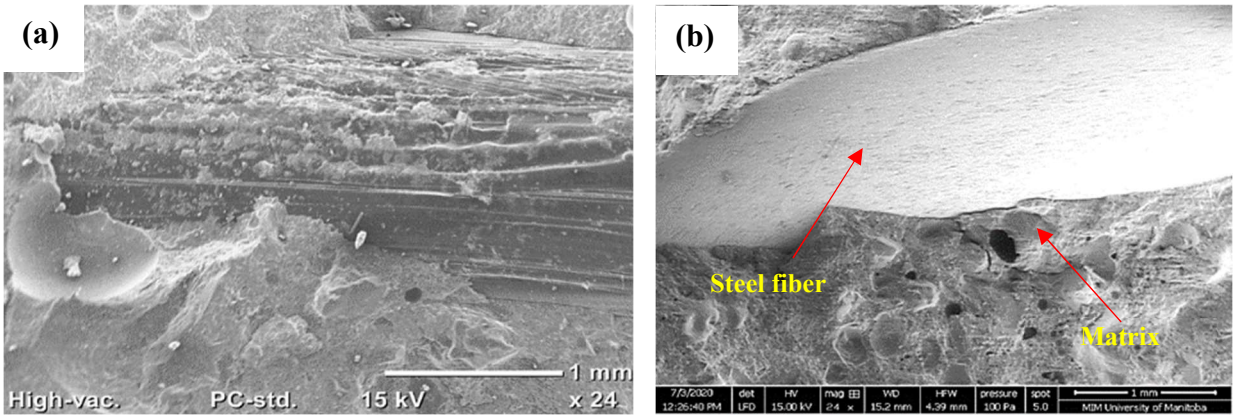

Figure 4.14: Exemplar SEM micrographs for the surface morphology of: (a) BFP in N-G-B-2.5, and (b) steel fiber in N-G-S-1 specimens before loading

The increase of BFP dosage enhanced the post-cracking response of the composites. Higher pellets dosages offered better chance for the BFP to exist in failure planes, which efficiently restrained propagation of cracks; abundant pellets in these locations bridged and arrested cracks, which enhanced the toughness of composites. According to the fiber

spacing theory [Romualdi and Mandel, 1964], as propagating cracks in the cement-based matrix reach the interface between fibers and matrix, a stress field is created restraining further propagation through the fiber bridging action that minimizes the stress concentration at the tip of the crack. As deformation of the composite increases, more cracks are generated producing more internal energy to counteract the external energy exerted on the composite. Thus, the increase of pellets dosage provoked the generation of more cracks leading to increasing the level of energy absorption, which was clearly reflected by the results of the direct tension test. However, in the impact test, the influence of BFP dosage on the composites' ductility was marginal. This could be ascribed to the small size of the specimens in SHPB test and very short test duration compared with that in the quasi-static tensile test.

The sensitivity of BFP interfacial bonding with matrix to loading configurations was assessed by performing single pellet pullout tests at displacement rates of 0.2 and 50 mm/min (**Table 4.7**) to match the static and dynamic loading schemes, respectively. Whereas the high displacement rate attained by the single pellet pullout test-setup was lower than that of the average rate in the SHPB test, the obtained trends herein conformed to the observations from the impact test results. Thus, it could qualitatively reflect the tendency of performance change at high strain rates. In **Table 4.7,** the bond strength values were calculated as the ratio of the ultimate force on the force-slip curve over the embedded shear surface of BFP, and the debonding energy was the area under this curve up to a slip of 3 mm.

Table 4.7: Single pellet pullout parameters at different displacement rates

Mixture ID.	Bond strength (MPa)		DIF	De-bonding energy up to 3 mm slip (J)	
	0.2 mm/min	50 mm/min		0.2 mm/min	50 mm/min
F	2.76 (0.22)	4.66 (0.41)	1.7	0.70 (0.08)	1.04 (0.11)
N-F	3.09 (0.32)	6.09 (0.51)	1.9	0.85 (0.09)	1.45 (0.16)
G	4.48 (0.31)	7.32 (0.68)	1.6	1.34 (0.14)	1.75 (0.19)
N-G	5.60 (0.38)	8.02 (0.71)	1.4	1.63 (0.18)	1.82 (0.21)

Note: Numbers in parentheses indicate standard deviations.

The increase in the pullout displacement rate caused a pronounced increase in BFP interfacial bonding with the matrix (all DIF greater than 1.0). For instance, the bond strength of BFP with the nano-modified slag-based matrix (N-G) at the high displacement rate (50 mm/min) was 43% higher than the one at the lower rate (0.2 mm/min). It was also observed that the slower rate of pellet dislodging from the matrix at the low displacement rate resulted in a smoother surface with minimal hydration products and no evidence of pellet damage [**Figure 4.15(a)**], which matched the features observed in failure plane of specimens after the quasi-static tension test. In the case of the high displacement rate, more hydration products were attached to the pulled pellet [**Figure 4.15(b)**] with signs of surface damage. Correspondingly, matrix fragments attached to de-bonded pellet were observed in the impact test. The low strain rate applied to the specimens provided ample time for the load to significantly influence the ITZ and cause marked weakening of the interfacial bonding between BFP and the matrix, which was reflected by the smoother surface of the tested pellets and lower bonding strength and debonding energy [**Table 4.7]**. Conversely, the high strain rate had very limited time to progressively weaken interfacial bonding between the pellets and the matrix, which resulted higher pullout resistance of BFP under such a scenario. Hence, the pullout behavior of BFP from the cementitious matrix was sensitive to the stain rate applied.

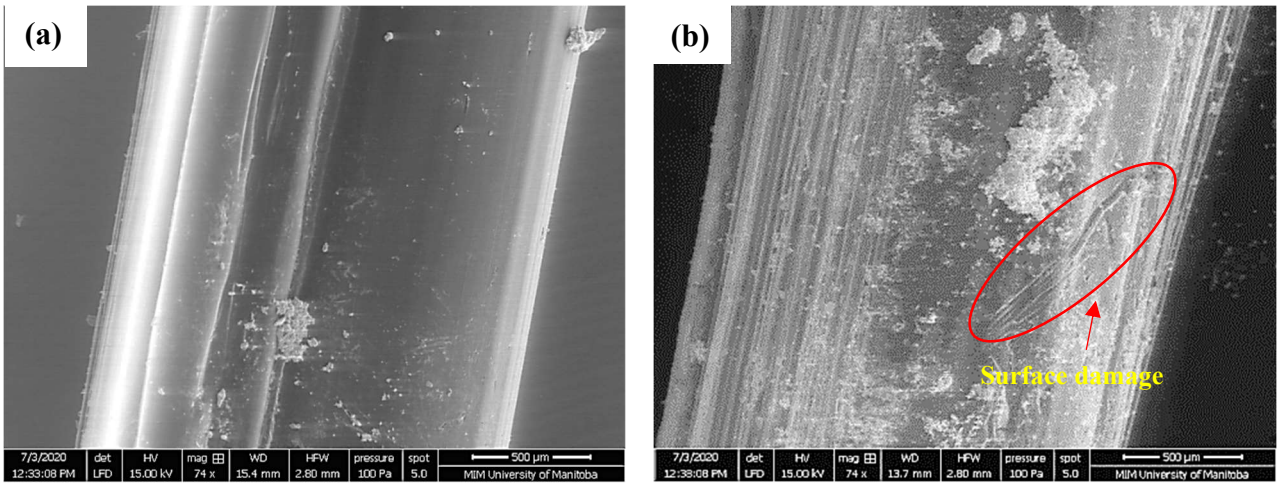

Figure 4.15: BFP from single pellet pullout tests in the nano-modified slag-based matrix (N-G) with displacement rates of: (a) 0.2 mm/min, and (b) 50 mm/min.

CHAPTER 5: PERFORMANCE OF NANO-MODIFIED CEMENTITIOUS COMPOSITES REINFORCED WITH BASALT FIBER PELLETS UNDER ALKALINE AND SALT-FROST EXPOSURES

In Chapters 3 and 4, the general properties as well as especiality mechanical properties of the cementitious composites were investigated to study the potentials of the cementitious composites to be employed in various infrastructure applications. In the current chapter, the durability properties a well as the self-healing potentials of the cementitious composites were studied under different aggravated exposures for prolonged periods (6 months) and compared with reference exposure of standard curing for the same duration for virgin and pre-cracked specimens. This was to examine the performance of the cementitious composites under anticipated different chemical and environmental exposures for infrastructures during their service life and the effect of these exposures on pre-existing distresses (pre-induced cracks).

5.1 Introduction

Durability of cement-based materials is of utmost concern for infrastructure elements exposed to aggressive environments. Reduced cracking and high ductility of cement-based materials are essential for their longevity and structural safety. Since the 1990s, research efforts to alter the brittle nature of ordinary mortar/concrete has resulted in the advent of high-performance fiber reinforced cementitious composites (HPFCC). Depending on the mixture design parameters, these composites are characterized by compressive strength in the range of 35-140 MPa, flexural strength in the range of 3.5-15 MPa, and high tensile strain in the range of 2-5%, with a strain hardening behavior after first-cracking for some

types [e.g. Corinaldesi and Nardinocchi, 2016; Savastano *et al*., 2009; Li *et al*., 1991]. With controlled cracking, high toughness and presumably improved durability, HPFCC represent an attractive option for infrastructure applications such as overlays or partial-depth repair for concrete flatwork, filler for joints between precast connections, industrial flooring systems, etc.

Various types of fibers (e.g. steel, glass, polyvinyl alcohol) have been used in HPFCC with different binders (plain cement, or cement blended with supplementary cementitious materials (SCM): fly ash, slag, silica fume, etc.) at a content of (350-1250 kg/m^3) and water-to-binder ratios (*w/b*) (0.14 to 0.35) [e.g. Jiang *et al*., 2018; Curosu *et al*., 2016]. Nano-modified binders have been used to produce cement-based materials with high-volume SCM, to mitigate the technical limitations associated with slowly reactive SCM (e.g. fly ash, slag) on early-age properties. For example, the incorporation of nano-silica with fly ash or slag significantly reduced the initial and final setting times and improved the early-age strength of concrete, due the accelerated hydration and pozzolanic reactivity of the nano-modified binder [e.g. Ghazy *et al*., 2016; Zhang and Islam, 2012].

Basalt fibers are a relatively new type of fibers, with high potential in the concrete industry owing to its mechanical properties (tensile strength of 3,000 to 4,000 MPa and modulus of elasticity of 93 to 110 GPa), non-corrosive nature, and low cost relative to other types of fibers (e.g. steel, glass) [e.g. 8]. Basalt fibers have been successfully used to reinforce cement-based materials in many studies, based on assessment of physical and mechanical properties [e.g. Jiang *et al*., 2014; Xu *et al*., 2021; Jalasutram *et al*., 2017]. However, it was reported that basalt fibers are vulnerable to alkali-silica reactions, which made them susceptible to degradation when incorporated in cementitious binders (high pH of 11-13) within 90 days [Lee *et al*., 2014]. For example, Sim *et al*. [2005] investigated the

influence of constantly submerging basalt fibers in 1N NaOH solution at 40°C for a duration ranging between 7 and 28 days. Due to significant degradation of the basalt fibers, 50% and 80% reductions in tensile capacity of fibers were observed at 7 and 28 days, respectively.

Highly alkaline media represent an aggressive exposure that could affect the microstructure and mechanical properties of cement-based materials incorporating vulnerable types of fibers (e.g. basalt fibers). Along with the high alkalinity of the matrix pore solution, concrete elements can be exposed to the ingress of external alkaline chemicals (e.g. sodium chloride, hydroxide, and carbonate) from soil, groundwater, or de-icing salts. Few studies investigated the effect of alkaline loading on HPFCC. For instance, Sahmaran and Li [Şahmaran and Li, 2009] studied the effect of 1 N sodium hydroxide solution at 38°C for 30 and 90 days on HPFCC (55% and 70% fly ash replacement by mass of the binder [1250 kg/m^3], *w/b* of 0.26 and 2% polyvinyl alcohol fibers by volume). Slight to intermediate loss of tensile ductility (13% to 21%) were reported according to the state of specimens (un-cracked or pre-cracked). Basalt fibers maybe coated by a polymeric resin (e.g. epoxy, polyamide), termed as basalt fiber pellets (BFP) to protect them from the surrounding environment [Mahmoud *et al*., 2017]. As of yet, whether BFP in HPCC can fully resist alkaline environments has not been investigated.

Accelerated deterioration of exposed concrete elements such as highway pavements and bridge decks is a key issue in cold regions, due to recurring freeze-thaw cycles and prevalent use of de-icing salts. This deterioration is linked to physical mechanisms (frost damage, salt crystallization) [Scherer, 1999; Valenza and Scherer, 2006] and/or chemical interaction of high concentration de-icing salts with the hydration products of cement paste resulting in voluminous reaction products and disintegration of the matrix

[Peterson *et al*., 2013]. Limited information has been reported on the performance of HPFCC under freezing-thawing cycles with deicing salts of HPFCC [e.g. Şahmaran and Li, 2007; Zhu *et al*., 2012]. For instance, Sahmaran and Li [Şahmaran and Li, 2007] investigated the mechanical and salt-frost scaling resistance of non-air entrained HPFCC after a typical exposure (25 and 50 cycles subjected to 4% calcium chloride solution), according to ASTM C672. The composites incorporated a total binder content of 1250 kg/m^3 (two binder formulations of fly ash/cement ratio 1.2 and 2.2), *w/b* of 0.26 and 2% fiber content (polyvinyl alcohol fibers). High resistance to surface scaling and high residual tensile capacity of the composites were reported after this exposure. Yet, there is scarce data [e.g. Azzam *et al*., 2019] on the freeze-thaw resistance (without/with different concentrations of deicing salts) of HPFCC incorporating basalt fibers or BFP.

5.2 Research Significance

There is a growing demand for HPFCC in various infrastructure applications such as highway and airfield pavements as well as bridges drives the need for research on resilient composites that can function efficiently and safely under severe chemical and environmental conditions. BFP were used at the University of Manitoba to develop nano-modified HPFCC with balanced mechanical (high strength and ductility) and durability (resistance to ingress of fluids, and salt-frost scaling [ASTM 672]) performance [Mahmoud *et al*., 2017; Azzam *et al*., 2019]. The pellets are composed of basalt fiber strands encapsulated by a polyamide resin, with micro-grooves in the longitudinal direction. The nano-modified cementitious composites contain high-volume (50%) SCM (complying with the requirements for the category HVSCM-1 according to CSA 23.1-19 "Annex K" [CSA-A23.1/A23.2-19] with nano-silica addition, and different dosages of BFP. Nevertheless, various aspects still require further investigation to identify performance

risks and limitations, if any, of these composites under aggravated exposures. Hence, the primary objective of the current study was to investigate the performance of these composites (un-cracked and pre-cracked) under an alkaline medium at an elevated temperature, and cyclic freezing-thawing coupled with high concentration de-icing salt, with respect to a reference moist curing exposure. The physico-mechanical properties of the composites were determined, and the trends were corroborated by thermal, mineralogical and microstructural analyses. Findings from this study can provide informative data on the suitability of these composites for various infrastructure systems vulnerable to similar chemical/environmental loadings, and providing rational expectations for their durability-based design.

5.3 Experimental Program

5.3.1 Materials and Mixtures

The selected base binder content of all mixtures was 700 kg/m^3 at a constant *w/b* of 0.3. For the reference mixtures, the single binder was composed of 100% general use (GU) cement, while the binary binders comprised 50% GU cement and 50% SCM, either Type F fly ash or Grade 100 slag, complying with CAN/CSA-A3001 [2018] specifications (**Table 5.1**).

Table 5.1: Chemical and physical properties of GU cement, fly ash and slag

Parameter	GU cement[a]	Fly ash[a]	Slag[a]
Chemical analysis			
SiO_2 (%)	19.22	55.20	33.40
Al_2O_3 (%)	5.01	23.13	13.40
Fe_2O_3 (%)	2.33	3.62	0.76
CaO (%)	63.22	10.81	42.70
MgO (%)	3.31	1.11	5.30
SO_3 (%)	3.01	0.22	2.40
Na_2Oeq. (%)	0.12	3.21	0.30
Physical properties			
Specific Gravity	3.15	2.12	2.87
Fineness (m^2/kg)	390	290	492

Note: [a]The properties of the materials were provided by the manufacturer.

The nano-modified binders consisted of the reference binders amalgamating nano-silica sol as an additive at a single dosage of 6% (42 kg/m^3 solid nano-silica particles) by mass of the base binder. According to the previous studies [Mahmoud *et al*., 2017; Azzam *et al*., 2019], the 6% NS dosage had favorable effects on the pore structure and hardened properties of mortar/concrete comprising SCM. A commercial nano-silica sol was used, composed of 50% SiO_2 particles well-dispersed in an aqueous solution. The nano-silica mean particle size is 35 nm, and its viscosity, specific surface, specific gravity, and pH are 8 cP, 80 m^2/g, 1.1 g/cm^3, and 9.5, respectively.

Locally available continuously-graded sand (0 to 600 μm) was used in the mixtures with fineness modulus 2.9. The specific gravity and absorption of the sand are 2.6 and 1.5%, respectively. A high-range water-reducing admixture (HRWRA), based on poly-carboxylic acid and complying with ASTM C494, Type F [2017], was used to maintain a flow of 180±20 mm for all mixtures. The cementitious composites were reinforced with basalt fiber pellets (BFP) at two different dosages of 2.5% and 4.5% by volume (equivalent to 1% and 2%, respectively, basalt fibers by volume). The pellets are 36 mm in length and 1.8 mm in diameter with an aspect ratio of 20 (**Figure 5.1**). They are made of 16-μm basalt roving encapsulated with polyamide resin (Nylon 6), and the fiber component represents 60% of the pellet by mass. BFP has a specific gravity of 1.74 with tensile strength and modulus of elasticity of 2300 MPa and 65 GPa, respectively.

Figure 5.1: Reinforcing basalt fiber pellets.

Eight composites were prepared and their proportions are listed in **Table 5.2**. For the mixtures' ID, the letter N indicates nano-silica, while the letters GU, F and G denote general use cement, fly ash and slag, respectively. The last number represents the volume of BFP dosage in the composite.

A pan concrete mixer with 60 rpm speed was used. Initially, the dry constituents were mixed without the pellets, followed by introducing the required water, HRWR and nano-silica sol while continuously mixing until the mixture homogeneity was attained. Finally, the pellets were added, and the ingredients were mixed until uniform distribution of BFP, where the total mixing process took approximately 8-10 min. After casting, all specimens were covered with polyethylene sheets, demolded after 24 h and stored in a standard curing room at 22±2°C and at least 95% relative humidity until the age of testing.

Table 5.2: Mixtures proportions per cubic meter

Mixture ID.	Cement (kg)	Fly ash (kg)	Slag (kg)	Water[a] (kg)	Nano-silica (kg)	BFP (kg)	Fine aggregate (kg)	HRWR (l)
GU-2.5	700	--	--	210	--	43.3	1,220	4.0
F-2.5	350	350	--	210	--	43.3	1,130	2.5
G-2.5	350	--	350	210	--	43.3	1,245	6.0
N-GU-2.5	700	--	--	180	84	43.3	1,180	6.7
N-F-2.5	350	350	--	180	84	43.3	1,045	5.6
N-F-4.5	350	350	--	180	84	78.3	1,000	5.0
N-G-2.5	350	--	350	180	84	43.3	1,160	7.6
N-G-4.5	350	--	350	180	84	78.3	1,100	7.3

Note: [a]Adjusted amount of mixing water considering the water content of nano-silica (aqueous solution with 50% solid content of SiO_2).

5.3.2 Initial Characterization of Composites

The initial physico-mechanical properties of all composites were assessed after 56 days of curing. Replicate 100×100×350 mm prisms and 100×200 mm cylinders were prepared for the various tests and exposures. Using triplicate specimens, the initial weight, comparative length [ASTM C157/C157M], dynamic modulus of elasticity [ASTM C215] and compressive strength [ASTM C39/C39M] were determined for the composites. The flexural strength and toughness were determined on triplicate prisms according to ASTM C1609 [ASTM C1609/C1609M], up to a net deflection of 2 mm (span/*150*). The flexural toughness of the un-cracked specimens was calculated, as the area under the load-deflection curve (P-δ) up to a deflection of 2 mm. In addition, the flexural toughness after first-cracking was calculated for the un-cracked specimens as the area under the load-deflection curve from deflection point at first-cracking (the drop at the load-deflection curve) up to a deflection of 2 mm; for pre-cracked specimens, this was calculated as the toughness of the re-loading stage, i.e. following pre-cracking.

The initial penetrability (physical resistance) of the composites at 56 days were determined by conducting the rapid chloride penetrability test (RCPT) according to ASTM

C1202 [2019] on triplicate discs (100 mm diameter and 50 mm thickness). To mitigate the influence of electrolysis bias and temperature fluctuations on the standard passing charges, the physical penetration depth of chloride ions into concrete was determined as it better correlates to the physical characteristic of the pore structure. Subsequent to the RCPT, the discs were split into two halves and sprayed with 0.1 M silver nitrate solution. This solution forms a white precipitate of silver chloride, to determine the average physical penetration depth of chloride ions across 10 locations on the split discs [Bassuoni *et al*., 2006]. In addition, the pore structure features of the composites were studied at 56 days by mercury intrusion porosimetry (MIP). Test samples were six to eight small pea-sized chunks (4-7 mm) taken from two cylinders from each mixture. Pre-conditioning of samples was done by oven drying at 50°C until constant mass was reached, within five to eight days, to minimize the formation of drying shrinkage cracks and decomposition of hydration phases with associated higher temperatures [Ghazy and Bassuoni, 2017]. Assuming cylindrical geometry of the pores, the mercury contact angle and the surface tension were 130° and 485 dynes/cm, respectively; where the high pressure limit (228 MPa) of the MIP apparatus yields a pore radius of about 3 nm, implying intrusion of all capillary pores.

5.3.3 Pre-cracked Specimens

In addition to un-cracked specimens, a companion group of pre-cracked specimens was used in each exposure to assess the performance of the composites in this state. At 56 days, triplicate prisms were initially cracked before being subjected to any exposure**.** This was done according to the cracking protocol in ASTM C1399 [2015], where a steel plate (12 mm thickness) was used under the flexural (bottom) side to support the concrete prism during the initial loading cycle and control the net deflection (maximum of 0.2 mm) when the prism cracks. This led to crack widths in the range of 120 to 380 μm in the flexural face

after unloading the specimens; the crack width measurements were determined as the average width of five points on the bottom surface of the specimen along the crack by an optical microscope with a precision of 20 μm. Subsequently, the initial properties (mass, length, dynamic modulus of elasticity, and toughness after first-cracking using ASTM C1609) of pre-cracked specimens were determined.

5.3.4 Exposures

Triplicate prisms of un-cracked and pre-cracked specimens from all composites were subjected to one of three types of exposure for a duration of six months after initial curing, as follow:

Reference Exposure: this exposure presents a prolonged curing regime for the specimens to achieve ideal conditions for reactivity of the binders and microstructural development of the paste. Thus, specimens were kept in a curing room under temperature of 22±2°C and relative humidity of at least 95%. The test results of the specimens under this exposure represented a benchmark for comparison with the results of corresponding specimens under the other exposures.

Alkaline Exposure: this exposure was designed to assess the ability of BFP and its interface with the matrix to resist a highly alkaline medium. It simulates contact with high-alkaline media from soil, groundwater, de-icing salts, or an industrial process. Specimens were continuously immersed in 1 N NaOH (pH of 14) solution at 38°C, similar to the protocol adopted by Sim *et al.* [2005] and Şahmaran and Li [2009]. The alkaline solution was replaced with a fresh one every month.

Salt-Frost Exposure: This exposure was adopted to investigate the influence of high concentration salt solution coupled with freeze-thaw cycles on the performance of the composites. This regime simulates field scenarios in cold regions, where flatworks (e.g.

pavements, bridges) are exposed to chemical and environmental loadings. Specimens were subjected to high concentration calcium chloride solution (13.6% calcium chloride) combined with freeze-thaw cycles according to the temperature profiling of ASTM C666 [2015] Test, Procedure A. The duration of each freeze-thaw cycle was 8.5 hours (freezing at −18±1°C for 4.5 hours and thawing at 4±1°C for 3.5 hours, and 15 minutes for ramping to the minimum freezing temperature or the maximum thawing temperature). The frequency of the thermal cycles was 2.8 cycles/day for a total of 508 cycles in six months. According to the phase diagram of calcium chloride and cycling profile adopted, this exposure simulated a severe scenario of ice plus solution, thus provoking both physical and chemical damage of concrete [Ghazy *et al*., 2018].

5.3.5 Testing after the Exposures

5.3.5.1 Visual and Physico-Mechanical Tests

Specimens were removed from the three exposures every 30 days, where the comparator length reading of the prisms was immediately measured. Subsequently debris, if any, were removed by a nylon brush, and the specimens were allowed to dry under 20°C and 50% RH for 30 minutes before visual inspection and measurement of mass and fundamental transverse frequency. Relative to the initial values, the change in mass, length and dynamic modulus of elasticity (RE_d) versus time of exposure were determined. The change in surface crack width of pre-cracked specimens was monitored using plain light optical microscopy. In addition, the residual flexural parameters of all specimens were determined in accordance with ASTM C1609 [2019] after all exposures.

5.3.5.2 Microstructural, Thermal and Mineralogical Tests

To interpret the trends from bulk tests and capture the effects of exposures on the composites, additional tests were conducted on pre-cracked specimens in the vicinity of

the cracking zone. The pore structure features of the composites were studied by MIP, to capture the alteration of microstructure relative to its initial state before exposure. The mineral phases within the cementitious matrix were analyzed by X-ray diffraction (XRD, Cu-Kα) at a scanning rate of 0.5°/min. The portlandite (CH) contents in the matrix were determined by thermo-gravimetric analysis (TGA) at a heating rate of 10°C/min. Fracture pieces were extracted from the pre-cracked specimens and then kept in an oven containing calcium sulfate for three days at 45±2°C. Subsequently, they were pulverized using a mechanical grinder to fine powder passing sieve #200 (75 μm) for the XRD and TGA tests. The portlandite content was calculated by determining the drop of the ignited mass percentage at a temperature range from 400°C to 450°C and multiplying it by 4.11 (the ratio of the molecular mass of CH to that of water). Environmental scanning electron microscope (ESEM) was used without any prior specimen preparation (e.g. drying, coating). In this test, fracture pieces were extracted from the pre-cracked prisms after flexural testing and used as test samples. Elemental quantification of phases observed under the ESEM was performed by EDX using ZAF method standardless analysis at voltage of 15 kV, probe current of 1 nA and acquisition time of 90 sec.

5.4 Results

5.4.1 Reference Exposure

Table 5.3 summarizes the initial hardened properties of the composites after curing for 56 days, and **Table 5.4** indicates the evolution of physico-mechanical properties of these composites after additional six months in standard curing conditions (22°C and RH ≥ 95%; reference exposure). After initial curing, mixtures GU-2.5 and N-GU-2.5 showed the highest mechanical capacity amongst the developed composites; also, composites comprising high-volume fly ash (slow reactivity pozzolan) and slag (latent hydraulic

binder) had high mechanical properties (e.g. compressive strength in the range of 55 to 82 MPa) due to the extended curing (56 days) that allowed continual reactivity of these binders. After the reference exposure (additional 6 months of curing), the mechanical properties of composites were improved depending on the mixture design parameters (**Table 5.4**).

Table 5.3: Initial physico-mechanical properties of the composites at 56 days

Mixture ID.	Unit weight (kg/m^3)	Dynamic modulus of elasticity (GPa)		Compressive strength (MPa)	First-cracking flexural strength (MPa)	Toughness (J)
		Un-cracked	Pre-cracked*			
GU-2.5	2391 [26]	43.6 [3.2]	27.3 [5.8]	83.6 [1.4]	8.2 [0.8]	35.8 [3.8]
F- 2.5	2202 [44]	32.4 [2.3]	21.4 [4.7]	60.0 [1.3]	6.0 [0.5]	24.3 [2.9]
G-2.5	2342 [38]	34.9 [2.5]	22.1 [6.4]	79.7 [1.4]	6.2 [0.5]	26.5 [3.2]
N-GU-2.5	2305 [32]	44.8 [3.1]	25.2 [3.7]	85.4 [1.1]	8.6 [0.8]	38.1 [4.1]
N-F-2.5	2211 [46]	36.1 [4.8]	24.2 [5.4]	65.2 [0.8]	6.5 [0.7]	28.3 [3.5]
N-F-4.5	2184 [32]	34.6 [2.1]	24.6 [3.5]	54.8 [0.5]	5.5 [0.6]	44.2 [5.6]
N-G-2.5	2314 [36]	42.4 [4.4]	26.4 [6.5]	81.9 [1.2]	7.0 [0.7]	35.7 [4.1]
N-G-4.5	2285 [41]	39.2 [3.2]	24.9 [4.3]	71.3 [0.9]	6.4 [0.6]	53.4 [6.6]

Note: Numbers in brackets indicate standard deviations.
*Specimens were cracked after 56 days and then tested for dynamic modulus of elasticity.

Subsequent to the reference exposure, the un-cracked specimens had low shrinkage values that did not exceed 0.007%, whereas counterpart pre-cracked specimens yielded low expansion in the range of 0.002 to 0.005%. The relative dynamic modulus of elasticity (RE_d) of composites showed consistent increase with time according to the state of specimens. The length change and increase in RE_d of specimens were accompanied by a marginal (less than 1%) increase in the mass of the specimens (average unit weight of 2250 kg/m^3). Un-cracked specimens had a maximum increase of 11% (average dynamic modulus of elasticity 38 GPa), whereas the pre-cracked specimens had a maximum increase of 29% with an average dynamic modulus of elasticity of 24 GPa.

Table 5.4: Physico-mechanical properties of the composites after the reference exposure

Mixture ID.	Specimens	Length change** (%)	Mass change (%)	RE_d (%)	First-cracking flexural strength (MPa)	Toughness (J)	Toughness after first-crack (J)
GU-2.5	Un-cracked	-0.006 [0.001]	0.2 [0.1]	103 [7]	8.9 [0.8]	41.2 [4.7]	36.4 [5.9]
F- 2.5		-0.007 [0.001]	0.3 [0.1]	106 [2]	6.3 [0.6]	29.2 [3.1]	27.4 [3.0]
G-2.5		-0.005 [0.001]	0.2 [0.1]	108 [2]	6.8 [0.4]	31.7 [3.6]	28.4 [3.9]
N-GU-2.5		-0.002 [0.001]	0.2 [0.0]	109 [3]	9.4 [0.9]	43.9 [4.9]	37.8 [4.5]
N-F-2.5		-0.005 [0.002]	0.3 [0.1]	104 [4]	7.1 [0.8]	32.6 [3.2]	28.3 [3.1]
N-F-4.5		-0.004 [0.001]	0.4 [0.1]	105 [2]	5.9 [0.6]	51.9 [4.2]	49.2 [3.7]
N-G-2.5		-0.005 [0.001]	0.3 [0.1]	111 [4]	7.5 [0.6]	40.1 [4.3]	38.7 [3.8]
N-G-4.5		-0.004 [0.001]	0.2 [0.1]	108 [1]	6.9 [0.5]	62.1 [5.4]	57.4 [4.6]
GU-2.5	Pre-cracked*	0.005 [0.001]	0.5 [0.1]	119 [16]	--	--	26.3 [4.3]
F- 2.5		0.005 [0.001]	0.5 [0.1]	122 [13]	--	--	20.5 [4.8]
G-2.5		0.004 [0.001]	0.3 [0.1]	129 [12]	--	--	22.8 [3.8]
N-GU-2.5		0.003 [0.001]	0.4 [0.1]	111 [9]	--	--	29.5 [4.6]
N-F-2.5		0.005 [0.001]	0.3 [0.0]	116 [11]	--	--	28.1 [2.2]
N-F-4.5		0.004 [0.001]	0.5 [0.1]	122 [15]	--	--	42.4 [4.1]
N-G-2.5		0.003 [0.001]	0.2 [0.0]	113 [6]	--	--	31.8 [4.8]
N-G-4.5		0.002 [0.001]	0.4 [0.1]	115 [9]	--	--	54.9 [4.2]

Note: Numbers in brackets indicate standard deviations.
*These specimens were cracked before the reference exposure and their initial properties are listed in **Table 5.3**.
**(-) refers to shrinkage and (+) refers to expansion.

The composites exhibited high flexural performance after prolonged curing (eight months) that depended on the key mixture design variables. Exemplar flexural load-deflection curves of the composites for un-cracked and pre-cracked specimens after the reference exposure are shown in **Figures 5.2 (a)-(b),** respectively. Comparing the un-cracked specimens to the pre-cracked ones, there was a notable difference in the initial stiffness of specimens under flexural loading, due to re-opening of cracks within the pre-cracked zone after elastic recovery and during the reloading stage. This led to lower resistance to the applied load, as the crack opened to its previous width prior to re-engagement of BFP. Once fiber bridging was functional in the cracked matrix, the load carrying capacity of composites resumed. The influence of the cracking process on the performance of the composites could be assessed by comparing the residual toughness of

pre-cracked specimens to that of un-cracked specimens after first-cracking stage after the reference exposure (**Table 5.4**). The pre-cracked specimens containing high-volume SCMs experienced smaller reduction of toughness after cracking when compared to their un-cracked counterparts. For example, the toughness after cracking for the pre-cracked specimens of composites N-F-4.5 and N-G-4.5 was 14% and 4% low, respectively, relative to their un-cracked counterparts. This highlighted the efficient post-cracking performance of such composites reinforced with BFP.

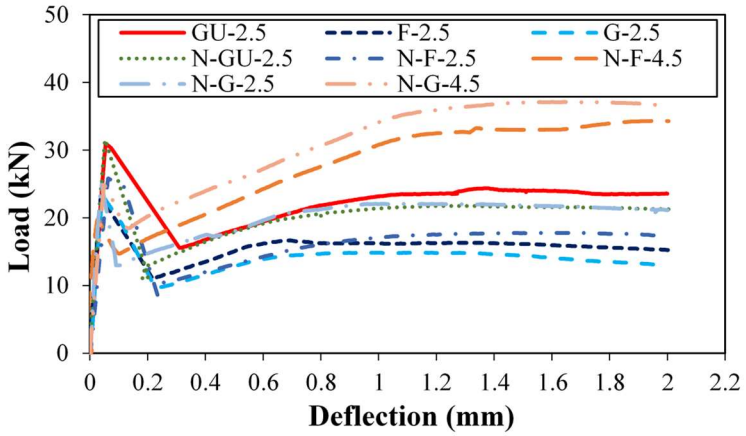

(a)

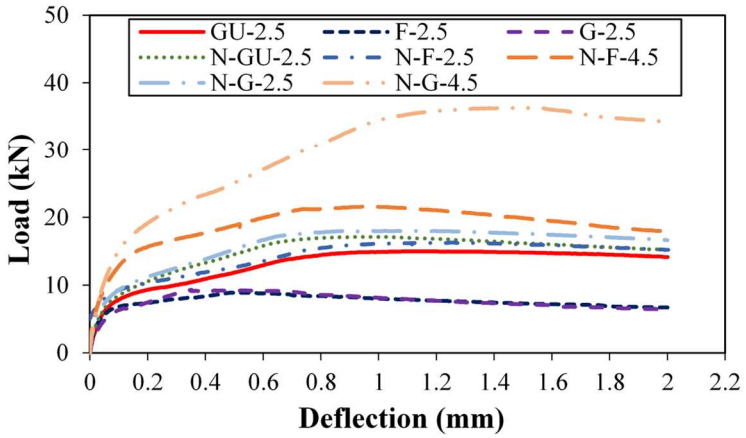

(b)

Figure 5. 2: Exemplar load-deflection (P-δ) curves for the composites after the reference exposure: (a) un-cracked, and (b) pre-cracked specimens.

The first-cracking flexural strength of the nano-modified mixtures was higher relative to that of their corresponding counterparts without nano-silica. However, the significance of this trend depended on the type of binder. Moreover, the influence of nano-silica on mechanical capacity of mortar/concrete has been reported to be conspicuous in the short-term (1 to 28 days), but it diminishes with continual reactivity of cementitious binders over longer-term [Zhang and Islam, 2012]. For instance, the increase in the first-cracking flexural strength for mixture N-F-2.5 was 13% higher relative to its counterpart without nano-silica (F-2.5), and it was 10% higher for N-G-2.5 relative to that of its counterpart mixture G-2.5 (**Table 5.4**). Correspondingly, the toughness of N-F-2.5 and N-G-2.5 un-cracked specimens was 11% and 26% higher than that of their corresponding mixtures without nano-silica [**Table 5.4** and **Figure 5.2(a**)]. The ductility results of the pre-cracked specimens conformed to the trends drawn from un-cracked specimens, which highlighted the role of nano-silica at enhancing the performance of composites.

The strength of the composites decreased with increasing the BFP dosage. For instance, the first-cracking flexural strength of N-F-4.5 was 17% lower than that of N-F-2.5, whereas the reduction was 8% for N-G-4.5 relative to N-G-2.5 (**Table 5.4**). Considering similar types of binder, the flexural load-deflection curves of the composites showed a comparable elastic stage before the first-cracking load was reached, irrespective of the pellets' dosage [**Figure 5.2(a)**]. After first-cracking, a sudden drop of the load occurred; yet, the specimens were able to restrain the growth of the cracks and partially/totally restored their load carrying capacity, according to the pellets' dosage and type of binder. The composites with the lower BFP dosage (2.5%) exhibited a strain softening behavior followed by a plateau, and the total toughness of the mixtures N-F-2.5 and N-G-2.5 were 32.6 J and 40.1 J, respectively. The composites with the higher BFP

dosage (4.5%) showed strain-hardening trend, and mixtures N-F-4.5 and N-G-4.5 had toughness of 54% and 59%, respectively higher than that of mixtures N-G-2.5 and N-G-2.5 (**Table 5.4**). Similarly, pre-cracked specimens of composites comprising high dosage of BFP showed enhanced ductility relative to corresponding composites with low BFP dosage; the toughness after first-cracking stage of pre-cracked composites N-F-4.5 and N-G-4.5 were 51% and 72%, respectively higher than that of N-F-2.5 (28.1 J) and N-G-2.5 (31.8 J).

The type of binder had a significant effect on the mechanical performance of the composites. The binary nano-modified binder had improved performance relative to the ternary nano-modified binder, with better results for the slag-based composites relative to their fly ash-based counterparts. For instance, the first-cracking flexural strength of N-GU-2.5 and N-G-2.5 was 32% and 5% higher than that of their corresponding fly ash mixture [N-F-2.5] (**Table 5.4**). Correspondingly, at a fixed BFP dosage, the toughness of mixture N-GU-2.5 and N-G-2.5 was 35% and 23% higher than that of their fly ash-based counterparts, while the toughness of the pre-cracked specimens for mixtures N-GU-2.5 and N-G-2.5 was 35% and 23% higher relative to that of mixture N-F-2.5. This suggests improved interaction and bonding of BFP with nano-modified cement (N-GU) or slag-based (N-G) binders.

5.4.2 Alkaline Exposure

After six months under the alkaline exposure, un-cracked and pre-cracked specimens from all composites remained intact without notable damage manifestations in the cementitious matrix or BFP (**Figure 5.3**). **Table 5.5** lists the results of physico-mechanical properties of all composites after the alkaline exposure, which were generally comparable to that

obtained from the reference (extended curing) exposure except for the toughness that showed notable reductions.

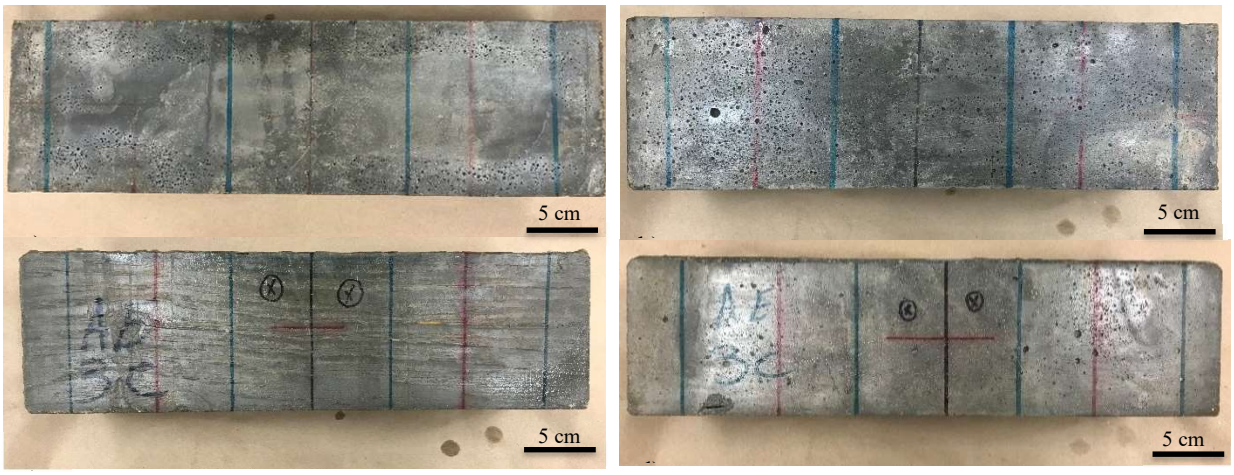

Figure 5.3: Exemplar visual features for the composites after the alkaline exposure: (a) F-2.5, (b) N-F-2.5, (c) G-2.5, (d) N-G-2.5.

Table 5.5: Physico -mechanical properties of the composites after the alkaline exposure

Mixture ID.	Specimens	Length change** (%)	Mass change (%)	RE_d (%)	First-cracking strength (MPa)	Toughness (J)	Toughness after first-crack (J)
GU-2.5	Un-cracked	-0.009 [0.001]	0.3 [0.1]	105 [2]	7.9 [0.5]	33.8 [2.8]	25.7 [1.2]
F- 2.5		-0.011 [0.002]	0.4 [0.1]	108 [5]	5.3 [0.5]	22.3 [2.1]	16.5 [2.2]
G-2.5		-0.009 [0.001]	0.1 [0.1]	107 [2]	7.4 [0.4]	23.7 [1.9]	18.4 [1.9]
N-GU-2.5		-0.006 [0.001]	0.2 [0.1]	109 [4]	8.6 [0.6]	36.5 [2.9]	27.5 [2.3]
N-F-2.5		-0.009 [0.001]	0.1 [0.1]	105 [4]	6.4 [0.4]	26.1 [3.7]	17.2 [1.5]
N-F-4.5		-0.005 [0.001]	0.2 [0.1]	110 [1]	5.2 [0.3]	40.2 [4.8]	34.5 [2.8]
N-G-2.5		-0.007 [0.002]	0.2 [0.1]	108 [3]	7.5 [0.4]	32.9 [3.4]	19.8 [2.1]
N-G-4.5		-0.004 [0.001]	0.4 [0.2]	109 [6]	6.7 [0.6]	47.2 [4.5]	37.8 [2.7]
GU-2.5	Pre-cracked*	0.011 [0.002]	0.40 [0.2]	123 [8]	--	--	14.4 [1.2]
F- 2.5		0.009 [0.004]	0.55 [0.2]	124 [10]	--	--	14.6 [1.6]
G-2.5		0.007 [0.001]	0.50 [0.3]	127 [12]	--	--	13.9 [0.9]
N-GU-2.5		0.003 [0.005]	0.30 [0.1]	119 [4]	--	--	20.2 [2.4]
N-F-2.5		0.008 [0.001]	0.35 [0.2]	120 [5]	--	--	15.1 [1.1]
N-F-4.5		0.005 [0.001]	0.20 [0.1]	118 [8]	--	--	25.8 [2.8]
N-G-2.5		0.006 [0.001]	0.30 [0.1]	114 [4]	--	--	17.4 [1.5]
N-G-4.5		0.004 [0.001]	0.60 [0.3]	115 [7]	--	--	32.1 [3.3]

Note: Numbers in brackets indicate standard deviations.
*These specimens were cracked before the reference exposure and their initial properties are listed in **Table 5.3**.
**(-) refers to shrinkage and (+) refers to expansion.

Similar to the reference exposure, specimens from all composites exhibited slight length change after the alkaline exposure (maximum of ±0.011%). Un-cracked specimens

showed small shrinkage that ranged between 0.004% and 0.011%, depending on the type of binder and the BFP dosage. The reference mixtures had marginally higher shrinkage compared to their nano-modified counterparts (**Table 5.5**), while increasing the pellets' dosage restrained the volumetric change of specimens. Comparatively, the pre-cracked specimens showed small expansion at the end of the alkaline exposure, where this expansion ranged between 0.003% and 0.011%. Similar to the reference exposure, RE_d showed consistent increase with time for the composites with a maximum increase of 9% for the un-cracked specimens and 27% for the pre-cracked specimens. The marginal volumetric change, increase in RE_d and slight gain (maximum 0.6%) in mass of specimens suggested no damage of composites.

The flexural performance parameters of the composites for the un-cracked and pre-cracked specimens after the alkaline exposure are summarized in **Table 5.5**, and representative flexural load-deflection curves are shown **Figure 5.4**. Relative to corresponding specimens under the reference exposure, the specimens subjected to the alkaline exposure showed comparable or minor reduction in first-cracking strength, while the toughness of the composites was adversely affected to different extents, depending on the type of binder. For instance, specimens from mixtures GU-2.5 and F-2.5 experienced reduction of the first-cracking flexural strength by 11% and 16%, respectively compared with that of counterparts under the reference exposure (8.9 and 6.3 MPa, respectively). The nano-modified version of these mixtures (N-GU-2.5 and N-F-2.5) had lower reduction of flexural strength under the alkaline exposure of 9% and 10%, respectively. Comparatively, the slag-based composites showed marginal improvement or comparable first-cracking flexural strength relative to their corresponding specimens under the reference exposure. For instance, the reference and nano-modified slag-based composites G-2.5 and N-G-2.5

had 9% increase and similar flexural strength, respectively to their corresponding specimens under the reference exposure (6.8 MPa and 7.5 MPa, respectively). These trends conformed to the visual assessment, length, mass change and RE_d results, which indicated no apparent degradation of the specimens after the alkaline exposure.

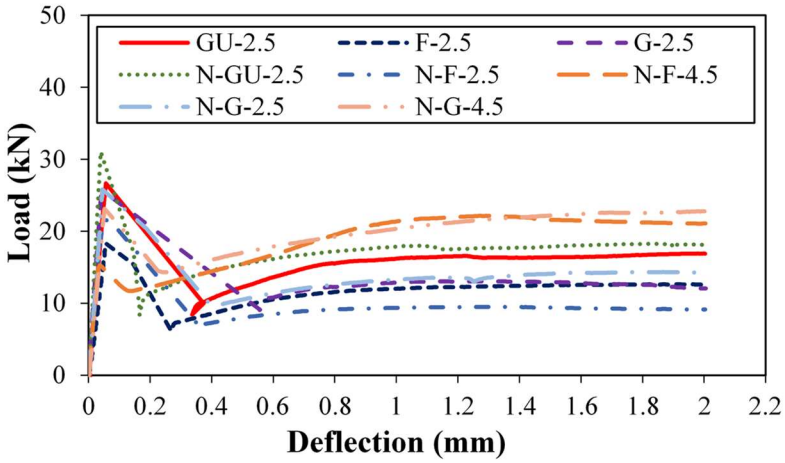

(a)

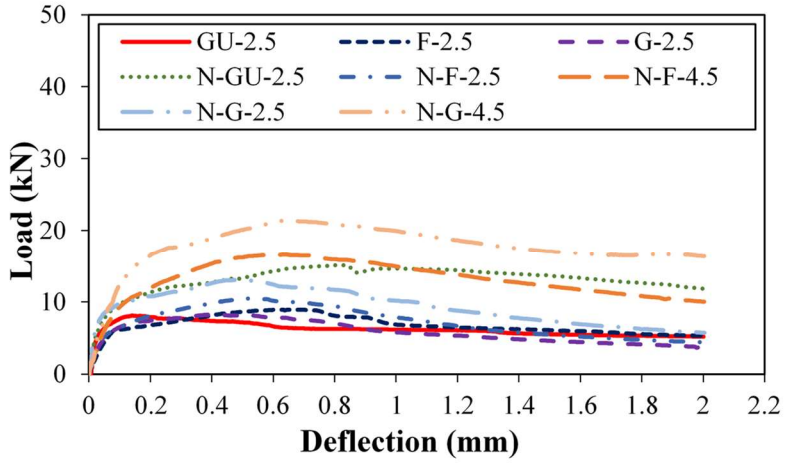

(b)

Figure 5.4: Exemplar load-deflection (P-δ) curves for the composites after the alkaline exposure: (a) un-cracked, and (b) pre-cracked specimens.

As depicted in **Figure 5.4**, the post-cracking flexural behavior of the composites, which was mainly dependent on BFP, did not change after the alkaline exposure, i.e. strain softening and hardening for the composites with BFP dosages of 2.5% and 4.5%, respectively. Moreover, the adverse influence of increasing the BFP dosage on the first-cracking flexural strength remained the same as in the reference exposure. However, the toughness of the composites (un-cracked and pre-cracked specimens) was negatively affected by this exposure. Considering the reference mixtures without nano-silica, the toughness of the un-cracked specimens from mixtures GU-2.5, F-2.5 and G-2.5 were reduced by 18%, 24% and 25%, respectively compared with that of their counterparts under the reference exposure (41.2 J, 29.2 J and 31.7 J, respectively). The toughness of the nano-modified mixtures N-GU-2.5, N-F-2.5 and N-G-2.5 was reduced by 17%, 20% and 18%, respectively relative to the corresponding mixtures (43.9 J, 32.6 J and 40.1 J, respectively) in the reference exposure (**Table 5.5**). Reduction of toughness, relative to the reference exposure, was conspicuous for the higher pellets' dosage (4.5%), as the toughness of N-F-4.5 and N-G-4.5 was significantly reduced by 23% and 24%, respectively. The negative effect of the alkaline exposure on the toughness of the composites was more pronounced in the pre-cracked specimens (**Table 5.5** and **Figure 5.4**). For example, the toughness after first-cracking of the pre-cracked specimens from mixtures GU-2.5 and N-GU-2.5 was decreased by 45% and 32%, respectively compared with their corresponding specimens (26.3 J and 29.5 J, respectively) in the reference exposure. The same trend was replicated for the fly ash and slag-based composites, alluding to deterioration of the pellet/matrix interface due to the alkaline exposure.

5.4.3 Salt-Frost Exposure

The salt-frost exposure (508 thermal cycles in six months) revealed performance risks for some composites, as shown in **Figure 5.5**. The degree of deterioration depended on the type of binder and original state. Un-cracked specimens from all mixtures tested showed no evidence of deterioration with mass change in the range of 0.1% to -0.4%. The reference fly ash (F-2.5) and slag (G-2.5) composites experienced minor scaling at the edges of the specimens with a mass loss of less than 0.5% (**Table 5.6**).

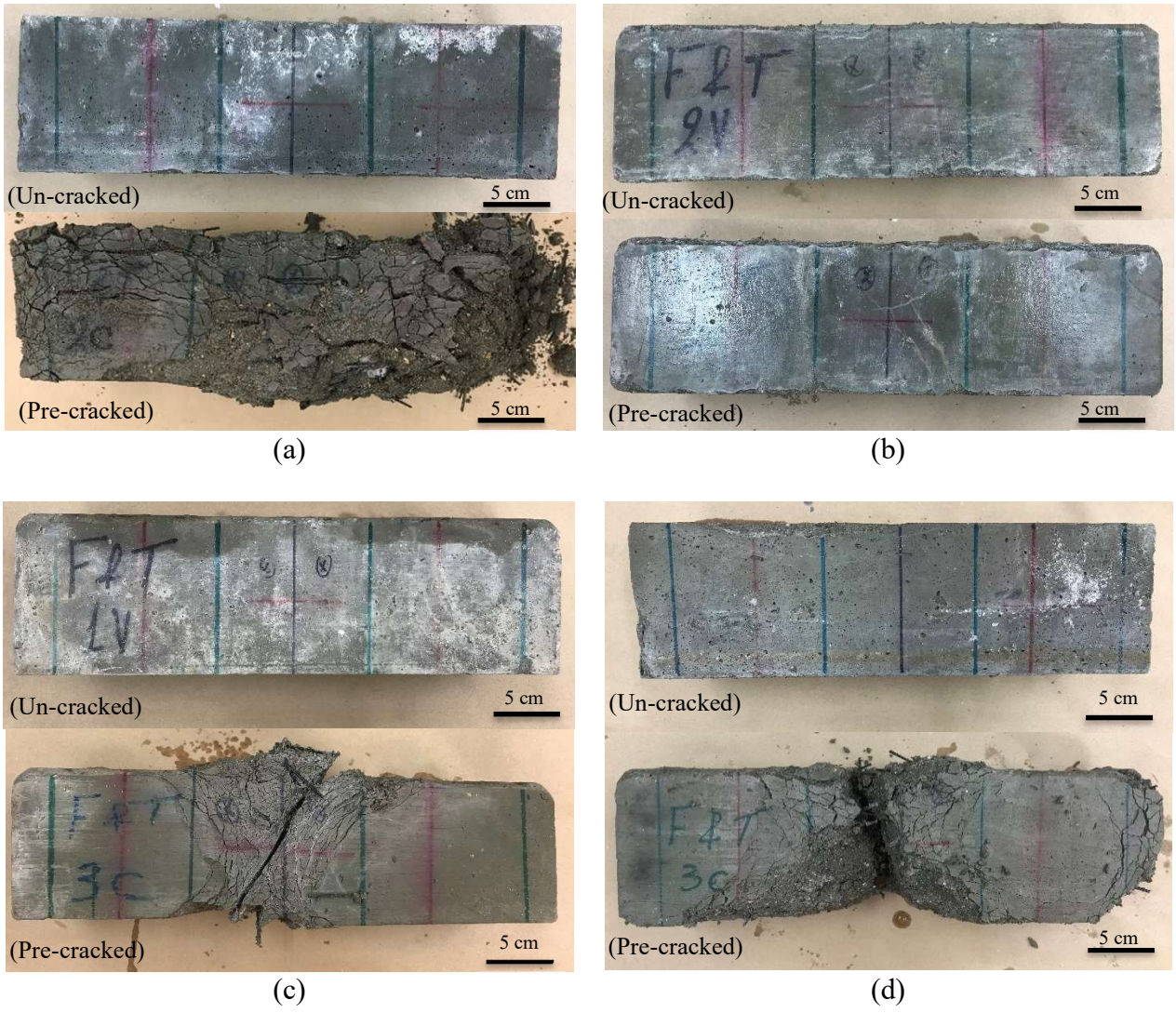

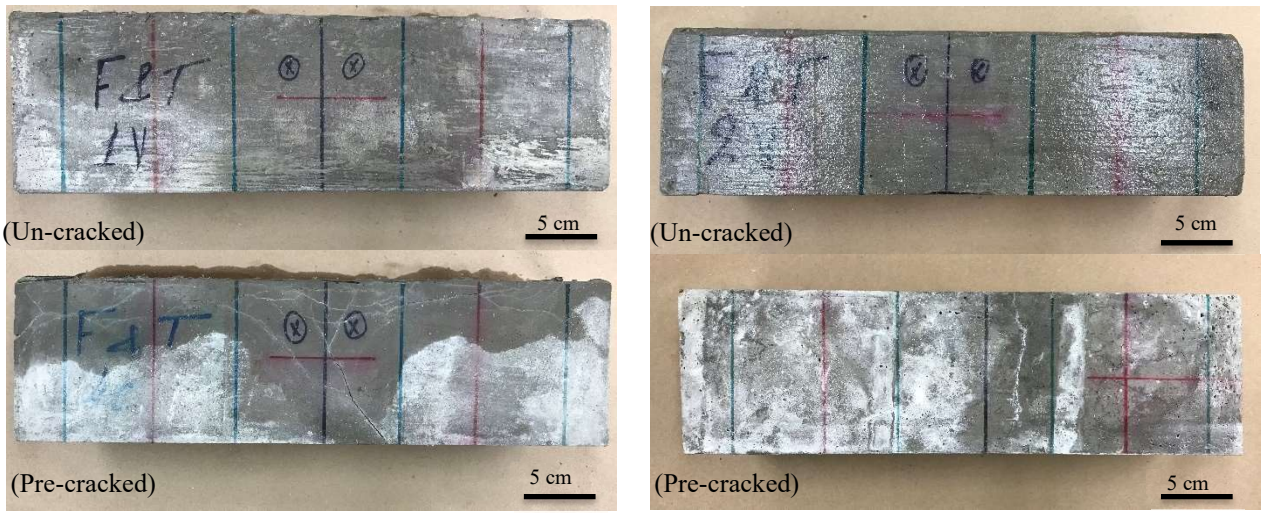

(e) (f)

Figure 5.5: Exemplar visual features for the composites after the salt-frost exposure: (a) GU-2.5, (b) N-GU-2.5, (c) F-2.5, (d) N-F-2.5, (e) G-2.5, and (f) N-G-2.5.

Table 5.6: Physico-mechanical properties of the composites after the salt-frost exposure

Mixture ID.	Specimens	Length change (%)	Mass change (%)***	Time of failure at RE_d = 60% (Days)	RE_d (%)	First-cracking strength (MPa)	Toughness (J)	Toughness after first-cracking (J)
GU-2.5	Un-cracked	0.009 [0.002]	0.1 [0.0]	None	102 [6]	6.1 [0.8]	25.6 [3.2]	20.9 [2.4]
F- 2.5		0.012 [0.004]	-0.4 [0.2]	None	91 [4]	4.0 [0.5]	18.4 [2.5]	15.8 [1.9]
G-2.5		0.011 [0.003]	-0.1 [0.0]	None	94 [5]	4.7 [0.7]	22.4 [2.1]	16.8 [2.2]
N-GU-2.5		0.007 [0.002]	0.1 [0.0]	None	96 [3]	6.4 [0.8]	28.5 [3.3]	24.8 [2.8]
N-F-2.5		0.013 [0.004]	-0.1 [0.0]	None	94 [5]	4.9 [0.5]	24.5 [1.9]	16.7 [1.9]
N-F-4.5		0.012 [0.002]	-0.1 [0.0]	None	96 [3]	4.1 [0.6]	32.6 [2.8]	29.1 [3.4]
N-G-2.5		0.011 [0.002]	0.1 [0.0]	None	98 [5]	5.6 [0.6]	30.6 [3.7]	17.9 [2.7]
N-G-4.5		0.009 [0.002]	0.1 [0.0]	None	103 [6]	5.1 [0.7]	36.3 [3.8]	33.4 [4.2]
GU-2.5	Pre-cracked*	0.046 [0.009]**	-0.6 [0.3]**	82	--	--	--	--
F- 2.5		0.041 [0.008]**	-0.3 [0.1]**	94	--	--	--	--
G-2.5		0.022 [0.005]	-0.2 [0.1]	None	63 [5]	--	--	10.6 [1.7]
N-GU-2.5		0.029 [0.004]	0.1 [0.0]	None	78 [6]	--	--	17.1 [2.3]
N-F-2.5		0.038 [0.008]**	-0.4 [0.1]**	128	--	--	--	--
N-F-4.5		0.034 [0.007]**	-0.2 [0.0]**	156	--	--	--	--
N-G-2.5		0.019 [0.005]	0.3 [0.2]	None	90 [5]	--	--	16.5 [2.1]
N-G-4.5		0.011 [0.003]	0.2 [0.1]	None	87 [3]	--	--	28.9 [3.6]

Notes: Numbers in brackets indicate standard deviations.
*These specimens were cracked before exposure and their initial properties are listed in **Table 5.3**.
**The readings of these specimens were taken at the time of failure.
***(-) refers mass loss and (+) refers to mass gain.

For pre-cracked specimens, the reference plain cement (GU-2.5) and fly ash-based (F-2.5, N-F-2.5, and N-F-4.5) composites experienced significant swelling (**Table 5.6**) and macro-cracking in the pre-cracked middle-third span and/or towards the edge of specimens. This resulted in disintegration of specimens [**Figure 5.5(a)**] or splitting the specimens into two-halves by the end of the exposure [**Figures 5.5(c-d)]**. Pre-cracked G-2.5 specimens showed branched cracking towards the top of specimens [**Figure 5.5(e)]**. On contrary, pre-cracked specimens from the nano-modified cement (N-GU-2.5) and slag composites (N-G-2.5, and N-G-4.5) remained intact during the entire exposure [**Figures 5.5(b, f)]**.

The physico-mechanical properties for the un-cracked and pre-cracked specimens after the salt-frost exposure are listed in **Table 5.6**. The un-cracked specimens experienced expansion after this exposure in the range of 0.007% to 0.013%, unlike the reference and alkaline exposures in which the specimens experienced low shrinkage (average value of 0.006%). The pre-cracked specimens yielded higher expansion (0.011% to 0.046%) than that of their counterparts under the reference and alkaline exposures, which was accompanied by reduction in RE_d and surface macro-cracks, resulting in failure of the reference plain cement (GU-2.5) and fly ash-based (F-2.5, N-F-2.5, and N-F-4.5) mixtures (**Table 5.6**). Compared with the un-cracked specimens, the pre-cracked specimens exhibited significant increase in expansion under the salt-frost exposure, especially the mixtures that failed before the end of the exposure. For instance, the expansion of pre-cracked specimens from the fly ash-based composites (F-2.5, N-F-2.5, and N-F-4.5) were 241%, 192%, and 183%, respectively higher than that of the corresponding un-cracked specimens.

Complying with the expansion trends, the un-cracked specimens showed small reductions in RE_d, which did not exceed 10% after this aggravated exposure. In contrast,

corresponding pre-cracked specimens had marked reductions in RE_d, especially for the specimens that showed swelling and macro-cracking. The reference mixture (GU-2.5) and the fly ash-based mixtures (F-2.5, N-F-2.5, and N-F-4.5) did not survive the targeted six months exposure of aggravated freezing-thawing cycles coupled with de-icing salt. The RE_d of these composites fell below the failure limit stipulated by ASTM C 666 (60%) before the end of exposure, considering that this limit is set for 300 freezing-thawing cycles in water (procedure A). The reference mixtures GU-2.5 and F-2.5 reached the failure limit at a relatively early-age of 82 and 94 days, respectively, while the nano-modified fly ash-based mixtures survived relatively longer up to 128 days for N-F-2.5 and 156 days for the higher BFP dosage composite (N-F-4.5). These specimens were kept under the same exposure conditions until the completion of the exposure period, where excessive damage was evident as shown in **Figure 5.5 (a, c** and **d)**. Conversely, pre-cracked specimens from the nano-modified cement composite (N-GU-2.5) and slag-based composites (G-2.5, N-G-2.5, N-G-4.5) remained intact with RE_d ranging between 63% and 90% at the end of the exposure regime (**Table 5.6**), where the slag-based composite without nano-silica showed the least RE_d (63%). It is worth noting that the pre-cracked specimens of G-2.5 were on the verge of failure (RE_d reaches 60%) according to the calculated RE_d at the end of the exposure.

The flexural properties of the composites for un-cracked and pre-cracked specimens after the salt-frost exposure are listed in **Table 5.6** and representative load-deflection curves are shown in **Figure 5.6**. Unlike the reference and alkaline exposures, the composites were negatively affected by the salt-frost exposure as reflected by the residual first-cracking flexural strength. For example, the reference mixtures GU-2.5, F-2.5 and G-2.5 showed significant reduction of the first-cracking flexural strength of 31%, 37% and

31%, respectively, relative to their corresponding specimens under the reference exposure. This trend was replicated for the nano-modified mixtures; however, these mixtures had higher first-cracking flexural strength (4.9 to 6.4 MPa) than that of the reference composites after this exposure. Similar to the reference and alkaline exposures, the increase in BFP dosage marginally decreased the first-cracking flexural strength according to the type of binder. The first-cracking flexural strength of N-F-4.5 and N-G-4.5 was 16% and 9%, respectively less than that of their corresponding mixtures with 2.5% BFP after the salt-frost exposure.

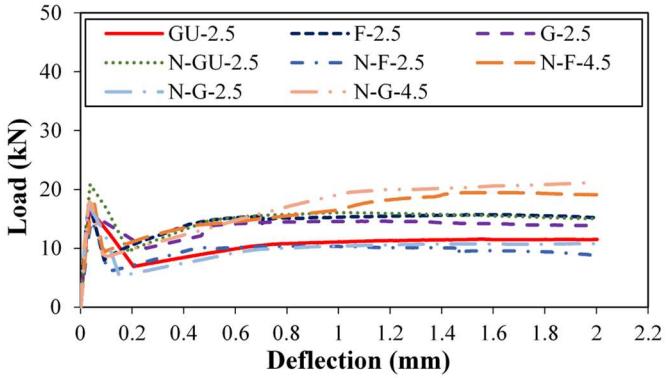

(a)

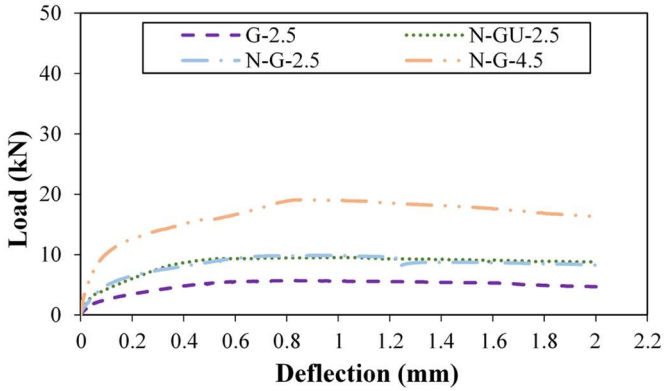

(b)

Figure 5.6: Exemplar load-deflection (P-δ) curves for the composites after the salt-frost exposure: (a) un-cracked, and (b) survived pre-cracked specimens.

Generally, the post-cracking behavior of the developed composites did not change after the salt-frost exposure, where the composites with the lower BFP dosage (2.5%)

exhibited strain softening and the composites with the higher BFP dosage (4.5%) experienced strain hardening. However, the ability of the composites to restore their load carrying behavior after first-cracking was compromised due degradation of the composites. Regarding the toughness of the reference mixtures, the un-cracked specimens from GU-2.5, F-2.5 and G-2.5 were reduced by 38%, 37% and 29%, respectively relative to their counterparts (41.2 J, 29.2 J and 31.7 J respectively) under the reference exposure. On the other hand, the toughness of the nano-modified mixtures N-GU-2.5, N-F-2.5 and N-G-2.5 was 35%, 25% and 24% less compared with the same mixtures (43.9 J, 32.6 J and 40.1 J respectively) under the reference exposure (**Table 5.6**). The toughness reduction was more conspicuous for the higher BFP dosage (4.5%), where the toughness of N-F-4.5 and N-G-4.5 was decreased by 37% and 41%, respectively, relative to their corresponding mixtures under the reference exposure.

Similar to the alkaline exposure, the deleterious effect of the salt-frost exposure on the flexural performance of the pre-cracked specimens was more pronounced relative to the un-cracked specimens, due to the direct access of the salt solution within the cracking plane. However, the alkaline exposure did not result in the failure of any pre-cracked composite. The toughness of the pre-cracked specimens for N-GU-2.5 after salt-frost exposure was 42% less compared with its counterpart mixture (29.5 J) under the reference exposure, while the reduction was 32% after the alkaline exposure. The toughness of pre-cracked specimens for the slag-based composites G-2.5 and N-G-2.5 was reduced by 54% and 48%, respectively, relative to their corresponding mixtures (22.8 J and 31.8 J respectively) under the reference exposure, whereas the reduction was 39% and 45% after the alkaline exposure. The influence of this exposure herein was more pronounced on the nano-modified slag-based mixture with higher BFP dosage (N-G-4.5); where the toughness

was reduced by 47% relative to its corresponding mixture under reference exposure (54.9 J), while the reduction was 42% after alkaline exposure.

5.5 Discussion

5.5.1 Initial performance of Composites before Exposures

The initial mechanical performance of the composites containing nano-silica showed improved behavior under compression and flexural loadings. Reduction of CH in the nano-modified binders (N-GU, N-F and N-G) started at early-age with an accelerated manner, but it continued afterwards at slower rates especially after 28 days, as indicated by the normalized CH contents (**Table 5.7)**.

Table 5.7: Thermogravimetric analysis of the binders used

Calcium hydroxide content (%)	Time (Days)				
	1	**3**	**7**	**28**	**56**
GU	8.6	9.9	10.1	10.9	11.1
F	6.8	7.9	8.3	7.7	6.7
G	6.9	7.6	8.2	7.1	6.1
N-GU	7.5	7.6	7.8	8.1	8.3
N-F	6.1	5.9	5.3	3.6	3.3
N-G	5.8	4.9	4.3	3.3	3.1
Normalized calcium hydroxide contents					
N-GU/GU	0.87	0.77	0.77	0.74	0.74
N-F/F	0.90	0.75	0.64	0.47	0.49
N-G/G	0.84	0.64	0.52	0.46	0.51
N-F/N-GU	0.81	0.78	0.68	0.44	0.40
N-G/N-GU	0.77	0.64	0.55	0.41	0.37
N-G/N-F	0.95	0.83	0.81	0.92	0.94

The ultrahigh specific surface area of nano-silica (80 m^2/g) provided nucleation sites for the dissolution of cement and the precipitation of the hydration products. Early consumption of CH in the matrix suggested vigorous pozzolanic activity of nano-silica at early-ages generating secondary C-S-H gel in the microstructure of the matrix. The accelerated CH consumption in binders with high volume SCMs indicated synergistic

effects of nano-silica with fly ash or slag, which catalyzed the reactivity of these binders. In addition to accelerated nucleation, pozzloanic effects, and filler action [Oertel *et al*., 2013], nano-silica agglomerates can absorb water into their high nano-porosity surfaces, thus reducing the *w/b* in the paste and consequently densifying the matrix [Kong *et al*., 2012]. For instance, MIP results (**Table 5.8**) showed that addition of 6% nano-silica in mixture N-GU-2.5, N-F-2.5 and N-G-2.5 decreased the 56 days porosity by 20%, 8% and 9%, respectively, and increased the proportion of micro-pores by 17%, 23% and 18%, respectively relative to that of the reference counterparts without nano-silica.

Table 5.8: Summary of MIP and penetrability results before exposures (56 days)

Mixture ID	MIP parameters			RCPT penetration depth (mm)
	Apparent total porosity (%)	Threshold pore diameter (μm)	Proportion of micro-pores (<0.1 μm)	
GU-2.5	12.8	0.10	41	13.2
F- 2.5	13.8	0.14	35	17.6
G-2.5	12.9	0.09	39	9.1
N-GU-2.5	10.2	0.06	48	4.3
N-F-2.5	12.7	0.08	43	9.8
N-F-4.5	13.5	0.12	39	10.9
N-G-2.5	11.8	0.07	46	4.6
N-G-4.5	12.6	0.09	42	5.8

The relatively higher mechanical properties of the cement-based (GU) mixtures at 56 days than that of mixtures comprising high-volume SCMs could be attributed to the dilution of cement (hydraulic binder) with high content (50%) of fly ash (slow reactivity pozzolan) or slag (latent hydraulic binder). Accordingly, the CH contents in the former were consistently higher than that in the latter at all ages (**Table 5.7**). Thus, the GU-based paste had relatively higher degree of maturity at 56 days, as suggested by the relatively denser microstructure. For example, the porosity of N-GU-2.5 was 20% and 14% less than that of N-F-2.5 and N-G-2.5, respectively, and the threshold pore diameter was 25% and 14%, respectively less than that of its fly ash and slag counterparts (**Table 5.8**). The slag-

based composites were found to have enhanced mechanical performance compared with the fly ash-based mixtures. This improvement, especially with the coexistence of nano-silica, could be attributed to the faster reactivity of slag due to its finer nature (492 kg/m^2) and higher content of lime (about 44 %-latent hydraulic binder) relative to that of fly ash (290 kg/m^2, 10%, respectively, slowly reactive pozzolan). **Table 5.7** showed that the normalized CH contents of the nano-modified slag-based mixtures relative to the nano-modified fly ash-based mixtures were consistently less than 1, indicating faster binder reactivity. Accordingly, the slag-based mixtures showed refined microstructure (lower porosity/penetrability, and higher proportion of micro-pores, **Table 5.8**) compared with the fly ash-based counterparts.

BFP had marginal contribution to the behavior of the developed composites during the pre-cracking stage compared to the post-cracking one, since comparable elastic behavior was observed before first-cracking of the specimens depending on the type of binder. The composites' performance in the pre-cracking stage was principally influenced by the matrix quality; however, the incorporation of BFP at a high dosage (4.5%) decreased the first-cracking flexural strength of the composites, and reduced its compressive strength. This is attributed to the creation of additional ITZs (pellets/matrix interfacial transitional zones) within the matrix, as micro-cracks commence at such weak areas and zones of stress concentration. Thus, the addition of 4.5% BFP in mixtures N-F-4.5 and N-G-4.5 increased the 56 days threshold pore diameter by 50% and 28%, respectively, relative to their counterparts with 2.5% BFP (N-F-2.5 and N-G-2.5), and increased the penetrability by 11% and 26%, respectively.

The effect of the pellets on the composites' performance was conspicuous after the development of macro-cracks depending to the matrix/pellets interaction, which resulted

in significant improvement of ductility with dosage. The efficacy of BFP in the enhancement of the post-cracking stage could be attributed to the tailored micro-grooves in the longitudinal direction on the pellets' surface. This imparted an interlocking action between the pellets and the matrix, through the increased contact surface and provision of host locations for deposition of hydration products (**Figure 5.7**).

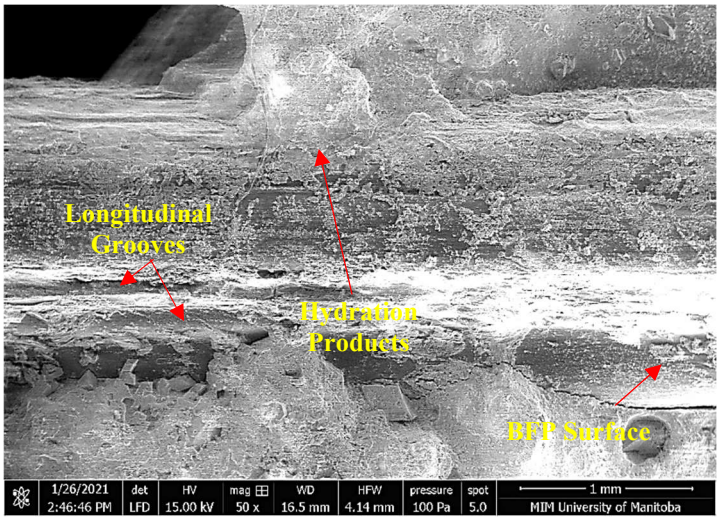

Figure 5.7: Exemplar SEM micrograph for the surface morphology of BFP in N-G-2.5.

Hence, the improved pellets/matrix bonding enabled by the BFP texture led to efficient control of cracking and high resistance of pullout, which was the key toughening mechanism responsible for improving the ductility composites. A higher BFP dosage provided better chance for the pellets to exist across failure planes, which enhanced the efficiency of restraining the propagation of cracks. According to the fiber spacing theory [Romualdi and Mandel, 1964], as the cracks propagate in the cement-based matrix and reach the fibers/matrix interface, a stress field is created restraining further propagation of the crack through the fiber bridging action that controls the stress concentration at the tip of the crack. As the deformation of the composite increases, more cracks are initiated generating more internal energy to counteract the external energy on the composite. Hence,

the increase of pellets dosage facilitated the generation of more cracks leading to the increase of energy absorption level, which was evident by the results of the flexural test in terms of strain hardening of the composites comprising 4.5% BFP dosage.

5.5.2 Performance of Composites after the Reference and Alkaline Exposures

All composites exposed to the reference and alkaline exposures showed marginal changes in length and mass, with increased stiffness. Correspondingly, the first-cracking flexural strength of the composites, which depends on the matrix quality, were maintained or slightly increased after these exposures relative to the initial values at 56 days. This indicated that the long-term hydration and/or pozzolanic reactivity of the binders continued under the favorable conditions of the reference and alkaline exposures. Furthermore, the pre-cracked composites experienced autogenous healing during these exposures, as all composites (without/with nano-silica) experienced blockage of the induced cracks. For example, **Figure 5.8** shows a pictorial of the nano-modified pre-cracked slag-based specimens' surfaces (before exposures) almost filled with self-healing products (after exposures), which conformed to the relative expansion of these specimens and increase in RE_d due to facilitated water/solution ingress through the cracking planes and in turn reactivity of the binders, forming cement gel. Elemental composition of these products indicated C-S-H gel and calcite. Precipitation of calcite could be due to reaction of CH and carbon dioxide in gaseous (reference exposure) and dissolved (alkaline exposure) forms over long-term [Huang *et al*., 2014].

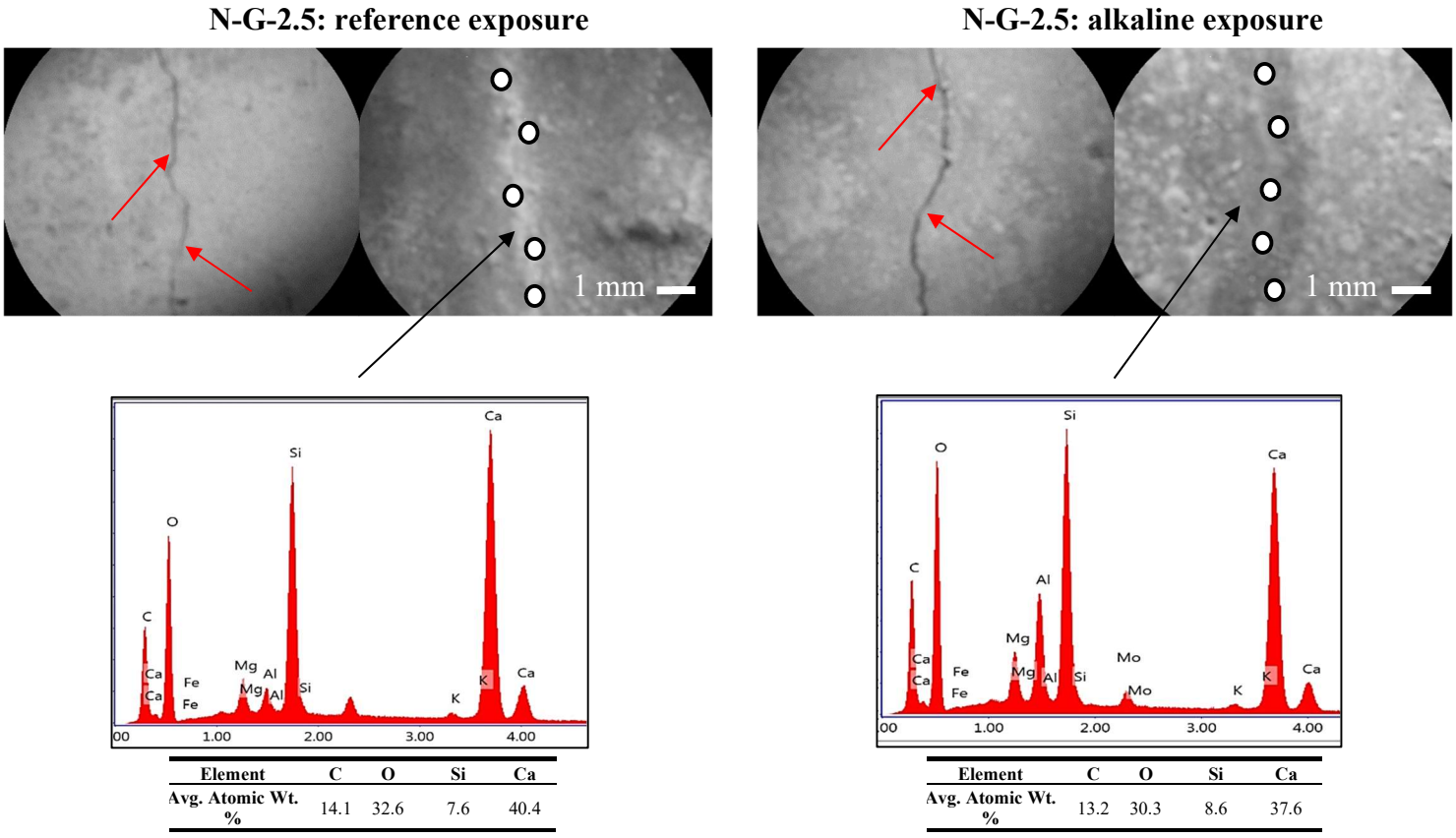

Element	C	O	Si	Ca
Avg. Atomic Wt. %	14.1	32.6	7.6	40.4

Element	C	O	Si	Ca
Avg. Atomic Wt. %	13.2	30.3	8.6	37.6

Figure 5.8: Exemplar pictorial of cracked surfaces before (left) and after (right) the reference and alkaline exposures under plain light microscopy at 40 X, and associated EDX spectra under the ESEM at the marked locations.

Under the prolonged reference and alkaline exposures, the reactivity of the binders continued as indicated by the portlandite contents in the matrix after six months as listed in **Table 5.9** compared to the initial values after 56 days (**Table 5.7**). The CH contents in the reference cement-based mixture without nano-silica increased by 9% and 14%, respectively due to progression of hydraulic reactions, whereas the CH contents in reference fly ash- and slag-based mixture significantly depleted (more than 50% reduction) in these exposures due to the long-term pozzolanic reactivity of SCM. Similar long-term trends were obtained for the nano-modified binders, considering that the accelerated reactivity of nano-silica was evident within the first 28 days, resulting in further reduction of the initial CH contents (**Table 5.7**). Correspondingly, under the reference and alkaline

exposures, the average calcium-to-silicate ratio (*Ca/Si*) was 1.82 and 1.74, respectively in the ITZ with BFP of the N-GU matrix; due to the precipitation of primary C-S-H from the hydration process of cement (**Figure 5.9)**. The *Ca/Si* ranged between 1.1 and 1.2 for the nano-modified fly ash or slag-based composites, indicating precipitation of secondary (pozzolanic) C-S-H (**Figure 5.10**). The *Ca/Si* of primary C-S-H from the hydration reactions tends to 1.7, while the secondary C-S-H generated from the pozzolanic reaction of cement tends to 1.1 [Detwiler *et al*., 1996].

Table 5.9: Thermal analysis of the binders after six months under different exposures

Calcium hydroxide content (%)	Exposure		
	Reference	**Alkaline**	**Salt-Frost**
GU	12.1	12.6	9.8
F	2.6	2.8	3.2
G	2.0	2.2	2.8
N-GU	9.4	9.6	6.4
N-F	1.2	1.8	2.5
N-G	1.3	1.4	2.1

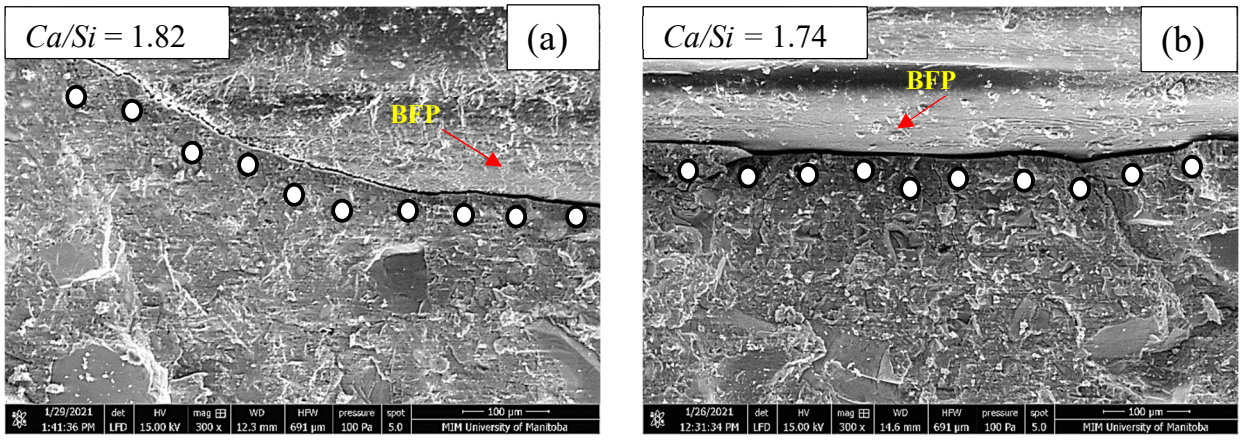

Figure 5.9: Exemplar SEM micrographs for the N-GU-2.5 matrix showing ITZ with BFP after the: (a) reference, and (b) alkaline exposures. (Note: *Ca/Si* values are the average for the marked locations)

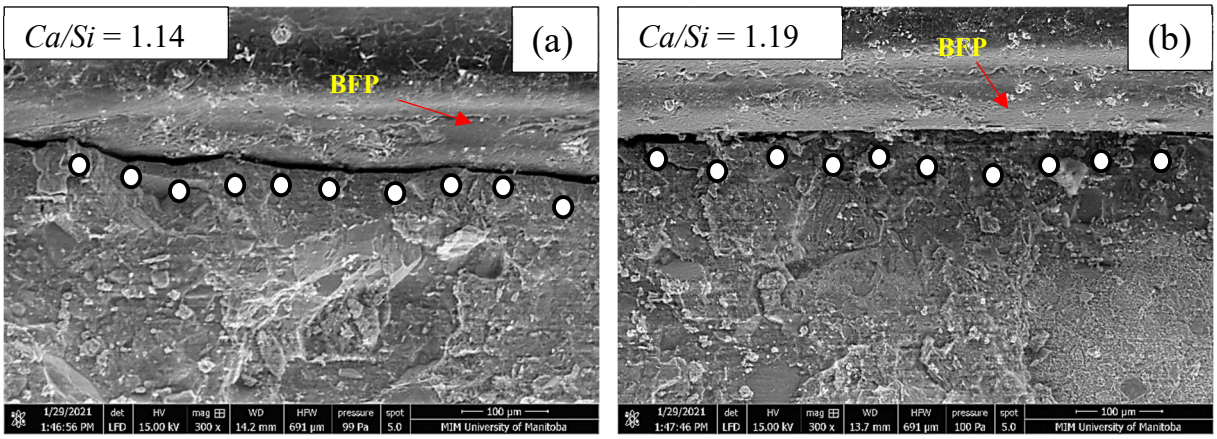

Figure 5.10: Exemplar SEM micrographs for the N-G-2.5 matrix showing ITZ with BFP after the: (a) reference and (b) alkaline exposures. (Note: *Ca/Si* values are the average for the marked locations)

The continual reactivity of the binders under both the reference and alkaline exposures led to refining the pore structure of the composites as listed in **Table 5.10**.

Table 5.10: Summary of MIP results after six months under different exposures

Mixture ID	Reference exposure			Alkaline exposure			Salt-frost exposure		
	Apparent total porosity (%)	Threshold pore diameter (µm)	Proportion of micro-pores [<0.1 µm] (%)	Apparent total porosity (%)	Threshold pore diameter (µm)	Proportion of micro-pores [<0.1 µm] (%)	Apparent total porosity (%)	Threshold pore diameter (µm)	Proportion of micro-pores [<0.1 µm] (%)
GU-2.5	10.2	0.05	66	7.6	0.04	65	16.0	0.13	35
F- 2.5	13.9	0.05	63	11.4	0.05	62	15.7	0.16	29
G-2.5	8.8	0.04	65	6.9	0.04	67	14.1	0.10	31
N-GU-2.5	9.2	0.02	72	6.9	0.03	70	11.9	0.08	43
N-F-2.5	11.4	0.04	68	10.7	0.04	68	13.9	0.10	37
N-F-4.5	12.4	0.05	62	11.6	0.05	64	14.7	0.15	34
N-G-2.5	8.2	0.03	68	6.7	0.02	70	12.4	0.09	41
N-G-4.5	8.8	0.04	64	7.3	0.03	66	12.9	0.10	39

For instance, the threshold pore diameter of all composites after both exposures ranged between 0.02-0.05 µm, i.e. one order of magnitude less than the initial values before exposures (**Table 5.8)**, and the proportion of micro-pores significantly increased (higher than 60%). The refinement of the pore structure of the matrices was also conspicuous in the quality of the ITZ between the pellets and matrix (**Figures 5.9** and **5.10)**. This links to

the positive effects of both exposures on the matrix quality, which complied with the intactness of specimens, maintenance of flexural capacity and stiffness and closure of surface cracks. The comparable performance of composites under the reference and alkaline exposures, despite the higher alkalinity (pH of 13-14) and temperature (38±2°C) in the latter, which might speed up the kinetics of binders' reactivity, could be ascribed to the high quality of the binders tested (content of 700 or 742 kg/m^3 and low *w/b* of 0.3). With progressive reactivity under both exposures, the penetrability of all composites reduced, particularly for the nano-modified binders, which likely restricted the direct ingress of fluids (water/alkaline solution) to the crust of the specimens and in vicinity of cracks in the case of pre-cracked specimens. Accordingly, the bulk core/volume of specimens was maintained under comparable conditions of high moisture levels. Moreover, the long-term (six months) duration of both exposures contributed to comparable levels of paste maturity.

The key difference between the reference and alkaline exposures was observed for the ductility of the composites, which depended on BFP and its interface with the matrix. It was reported that polyamides (representing 40% by mass of BFP) are moisture sensitive, which can have a negative effect on their dimensional stability and thus durability, in cases of high moisture intake [e.g. Silva *et al*., 2013]. However, such an effect was intangible under the prolonged reference exposure, where specimens were kept in the standard curing room at 20°C and 95% RH. This was substantiated by the improved toughness of all specimens after the reference exposure relative to their initial values after 56 days due to the progressive development of the matrix and ITZ with pellets as discussed earlier. This led to improved interfacial bonding between the pellets and matrix with time, without any

evidence of pellets' deterioration after flexural loading (**Figure 5.11**); hence, the pullout toughening mechanism was fully engaged to increase the ductility of composites.

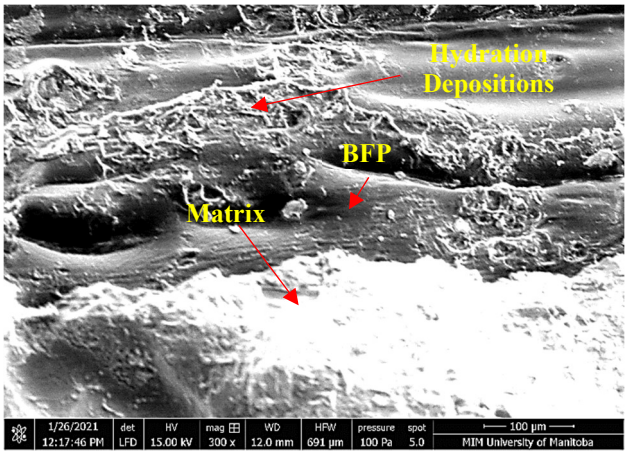

Figure 5.11: Exemplar SEM micrograph for the surface of BFP after flexural testing of pre-cracked N-G-2.5 after the reference exposure showing no evidence of surface wear.

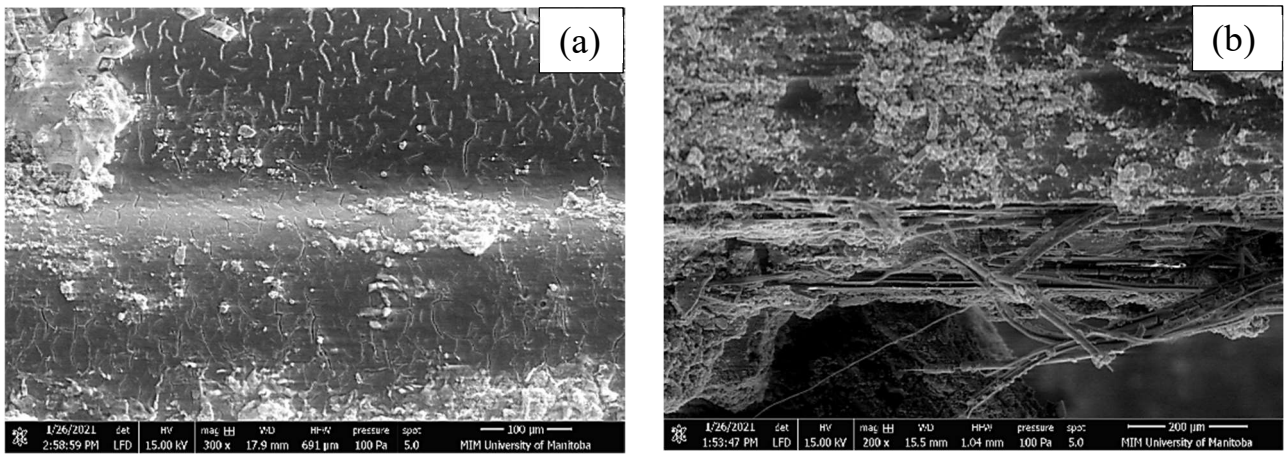

Figure 5.12: Exemplar SEM micrographs for the surface of BFP after flexural testing of pre-cracked N-G-2.5 after the alkaline exposure showing: (a) resin tearing/micro-cracking, and (b) rupture of basalt strands.

Conversely, significant drop in composites' ductility was observed after the alkaline exposure. The comparable improvement of the matrix quality and refinement of pore structure and ITZ after both the reference and alkaline exposure suggested that this reduction was linked to the performance of BFP. Microstructural analysis by ESEM showed that BFP underwent significant deterioration under the alkaline exposure. For

example, **Figure 5.12(a)** shows extensive micro-cracking and tearing of the polyamide resin, while **Figure 5.12(b)** shows decomposition of resin and rupture of basalt strands after flexural loading; hence, the BFP bridging capacity was compromised and the efficacy of the pullout process had been limited by fibers' rupture.

Several studies reported a dramatic decrease in the mechanical properties (strength and elastic modulus) of polyamides after continuous submersion in water, where the elastic modulus and the tensile strength were reduced [e.g. Ksouri and Haddar, 2018; Taktak *et al*., 2015]. The prolonged alkaline exposure, where composites were constantly immersed in a highly alkaline medium at an elevated temperature, promoted solution imbibition into the near surface and exposed (pre-cracked specimens) BFP, which are subjected to the maximum tensile stresses under flexural loading. It was reported that the diffusivity of fluids within polymers is remarkably enhanced with increase in temperature [Silva *et al*., 2013]. This likely led to significant moisture intake of pellets, swelling, softening or breakage of the secondary bonds between polar groups, and weakening of the chain interaction among monomers, thus reducing mechanical properties and lowering glass transition temperature [e.g. Chaichanawong *et al*., 2016]. Therefore, progressive deterioration of the protective resin facilitated access of the alkaline solution to basalt strands, thus reducing their tensile capacity as indicated by the rupture of strands, and in turn decreasing the flexural toughness of composites.

5.5.3 Performance of Composites after the Salt-Frost Exposure

All un-cracked specimens survived this exposure due to the mixture design parameters (high binder content and low *w/b*) used, especially the nano-modified ones, and initial curing period (56 days) applied, which discounted the penetrability of the solution and thus potential for physical and chemical damage. However, cyclic freezing-thawing in a salt

solution revealed performance risks for some pre-cracked composites including high expansion, reduction of flexural strength/stiffness/toughness, and or complete failure. All composites did not intentionally incorporate an air-entraining agent, to clearly capture the effects of binders and BFP on the performance of composites under this aggravated exposure.

After this exposure, the CH contents in all reference and nano-modified binders, including GU mixtures, were consumed or significantly decreased relative to their initial values at 56 days (**Table 5.7**). However, unlike the reference and alkaline exposures, the pore structure features of the composites became coarser **(Table 5.10**). For instance, the porosity of GU-2.5, F-2.5 and G-2.5 increased by 25%, 14% and 9%, respectively, relative to their initial state, while the proportion of micro-pores decreased by 15%, 17% and 21%, respectively. These results indicated the development of microstructure of all binders was impeded during this exposure, although to varying levels, due to the concomitant actions of low/freezing temperatures and salt solution. This was also reflected by deterioration of the physico-mechanical performance of all specimens, especially the pre-cracked specimens that had direct ingress of solution through the crack walls.

The initial physical resistance is a key factor that influenced the extent of deterioration of each binder during the salt-frost exposure (**Table 5.8**). For instance, mixtures GU-2.5, F-2.5 and G-2.5 had chloride penetration depths of 13.2, 17.6 and 9.1 mm, respectively, while the penetration depth was 4.3, 9.8 and 4.6 mm for their nano-modified counterparts. The relatively coarser pore structure of the reference mixtures and the nano-modified fly ash-based mixtures (although survived longer than the reference fly ash mixture) led to more connected channels for easier ingress, and thus critical saturation, of salt solution into the pre-cracked matrix from the beginning of exposure. This resulted

in early damage of the microstructure of these mixtures by frost action, which has been explained by multiple theories (osmotic/hydraulic pressures, ice accretion, and crystallization pressure [e.g. Powers and Helmuth, 1953; Powers, 1975; Liu and Hansen, 2015]). This conformed to progressive expansion and reduction of stiffness for the pre-cracked specimens (**Table 5.6**) under this exposure. Internal micro-cracking of the matrix led to the coarser microstructure observed after this exposure (**Table 5.10**), loss of integrity with the pellets at the ITZ (**Figure 5.13)**, and thus reduction of flexural strength and toughness (**Figure 5.6**).

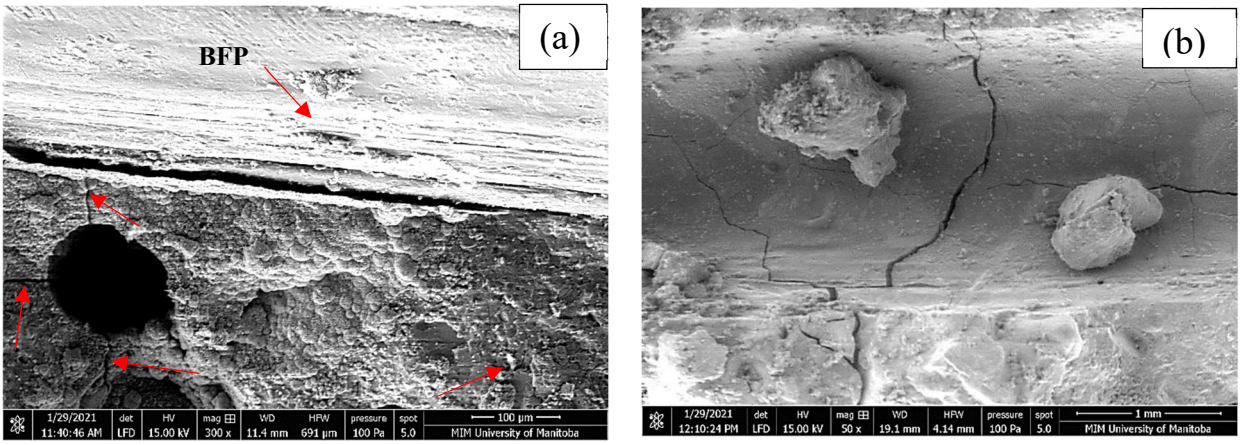

Figure 5.13: Exemplar SEM micrographs after the salt-frost exposure showing ITZ with BFP in N-F-2.5: (a) micro-cracking of matrix, and (b) micro-cracking of matrix/pellet interface after dislodgement of BFP.

Another key aspect that affected the performance of the composites is the chemical resistance of the binders. The XRD patterns showed comparable phases of calcite, quartz, dolomite and ettringite after the reference (**Figure 5.14)** and salt-frost (**Figure 5.15)** exposures. The portlandite (CH) phase was observed only after the reference exposure in the GU, F and G and N-GU binders, and it diminished after the salt-frost exposure, complying with the TGA trends (**Table 5.9**). In addition, Friedel's salt, ettringite and calcium oxychloride phases occurred in specimens from the reference (GU, F, G) and nano-

modified fly ash-based (N-F) mixtures, which were markedly damaged under this exposure. The lower physical resistance of these binders allowed further ingress of solution, provoking chemical attack as indicated by consumption of portlandite in the binders and concurrent formation of calcium oxychloride (xCa(OH)$_2$·yCaCl$_2$·zH$_2$O [COX]; where x, y and z depend on Ca(OH)$_2$/CaCl$_2$ molar ratio). High concentration of Ca^{2+}, Cl^-, and OH^- ions within the surface crust of specimens as well as low temperatures and high relative humidity create favorable conditions for crystallization of COX [Ghazy and Bassuoni, 2017] (partially dehydrated COX [Ca(OH)$_2$·CaCl$_2$ (1:1:0) or Ca(OH)$_2$·CaCl$_2$·2H$_2$O (1:1:2)] were traced due to the drying involved in the preparation process). Consequently, swelling as well as deterioration of the cementitious matrix were observed. In addition to frost action, this led to further deterioration of the pore structure (**Table 5.10**). The formation of Friedel's salt was likely a result of the replacement of sulfate ions in monosulfate by chloride ions, or reaction of the solution with other aluminate phases. The releasable sulfate ions might react with the remaining monosulfate and part of the Friedel's salt already formed in the presence of moisture, precipitating ettringite. This finding was supported by higher peaks of ettringite compared with the corresponding mixtures after reference exposure (**Figures 5.14** and **5.15**). The deposition of these crystals in the confined pore space, might have contributed additional damage to these composites. The higher physical resistance of N-GU and N-G composites, i.e. less Cl^- ions, and the less initial CH contents in the latter, decelerated this chemical attack process, and thus the reaction compounds appeared only as traces in these pre-cracked composites, which survived longer under this exposure.

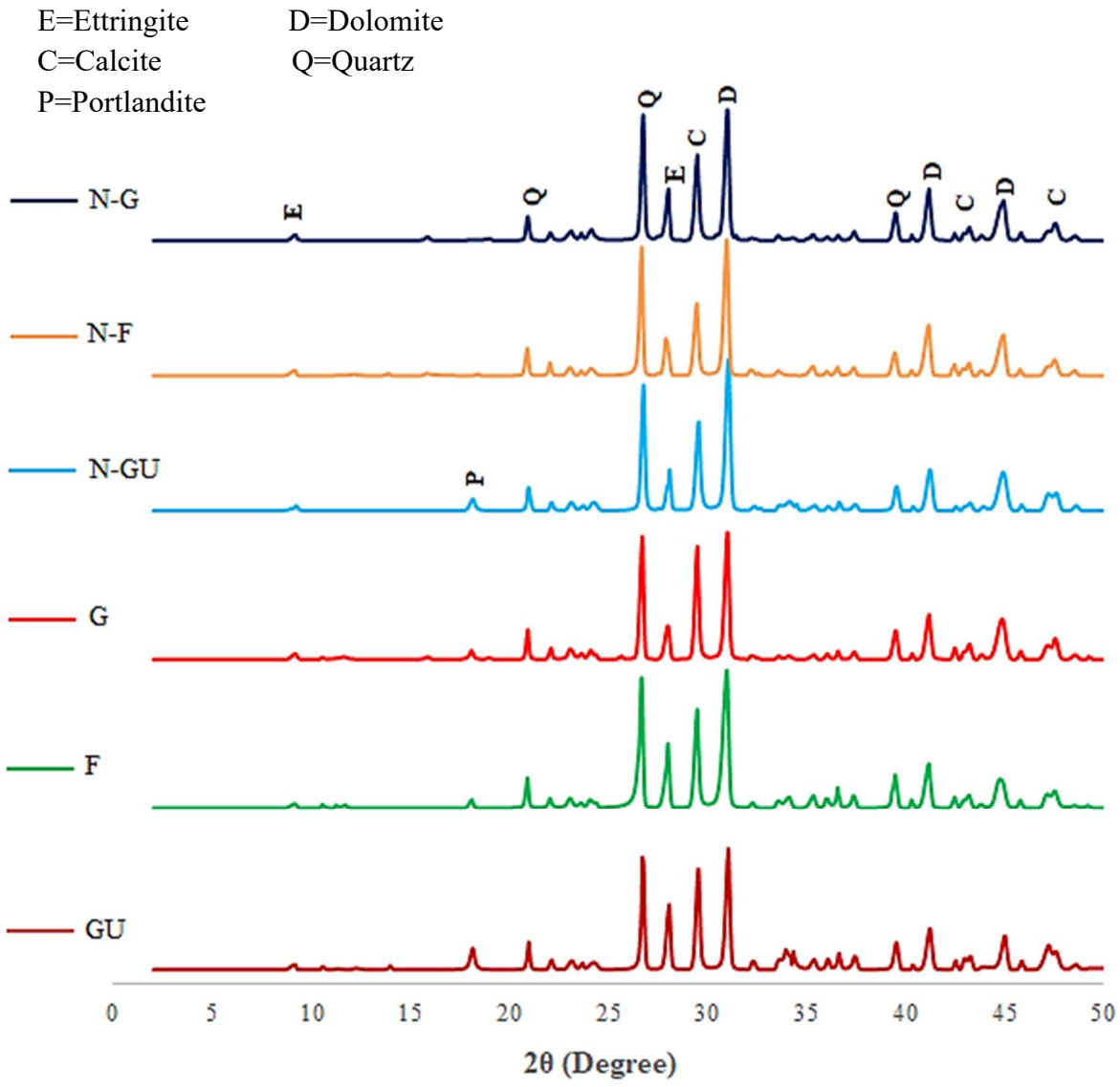

Figure 5.14: XRD patterns of the binders after the reference exposure.

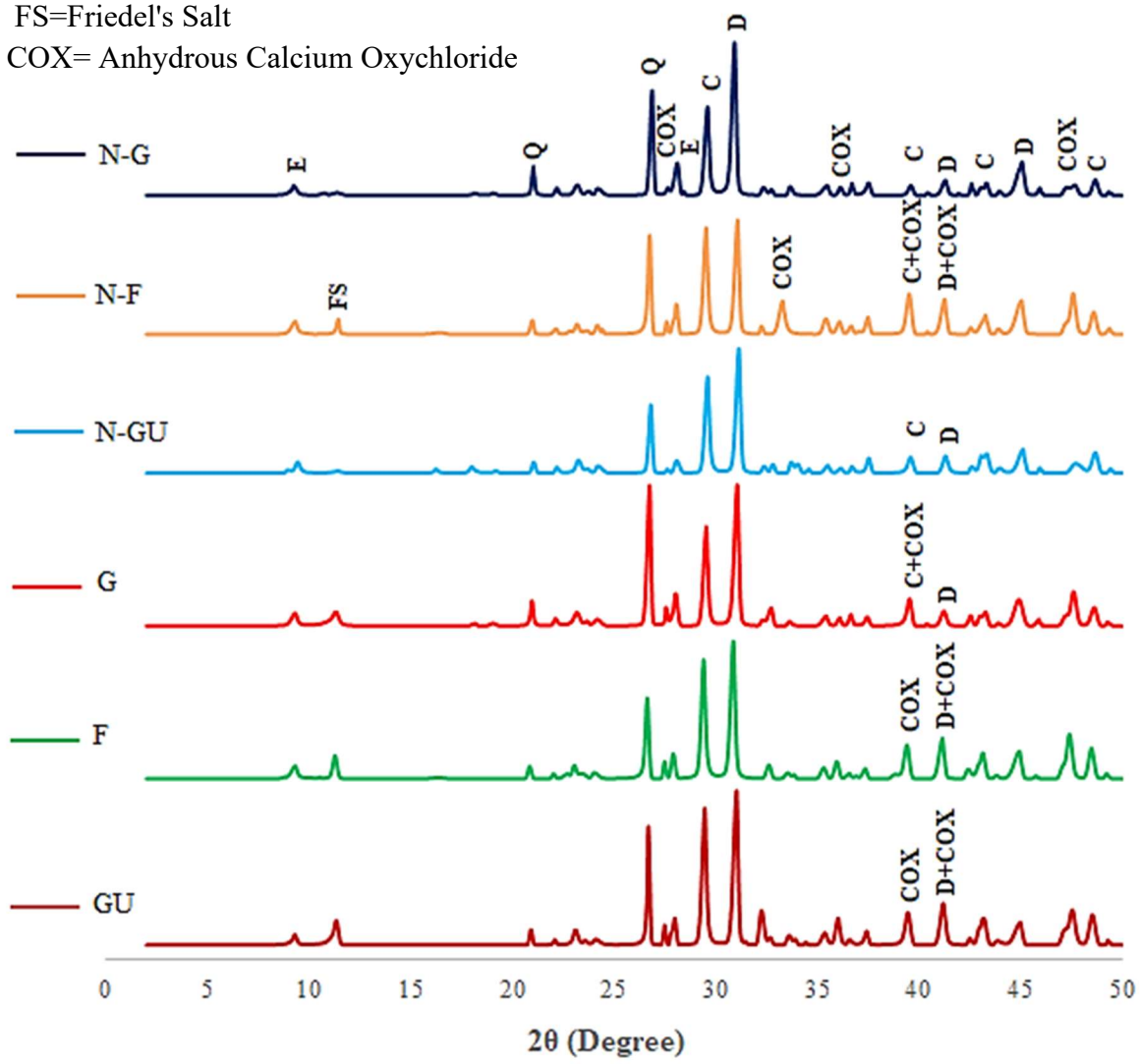

Figure 5.15: XRD patterns of the binders after the salt-frost exposure.

Accordingly, the ductility of the composites after the salt frost exposure was significantly reduced relative to that after the reference exposure as well as the initial ductility at 56 days. The physical and chemical processes explained earlier had deleterious effects on the microstructure of the composites, depending to the type of binder, thus reducing the matrix/pellet bonding and consequently facilitating fiber pullout during flexural testing. Unlike the alkaline exposure, the pellet component had no contribution to

the loss of ductility of composites under the salt-frost exposure, since no evidence of BFP deterioration was observed on the surface of pellets after flexural loading (**Figure 5.16**). Thus, increasing the BFP dosage to 4.5% was beneficial to restrain cracking/swelling, and thus longevity of composites.

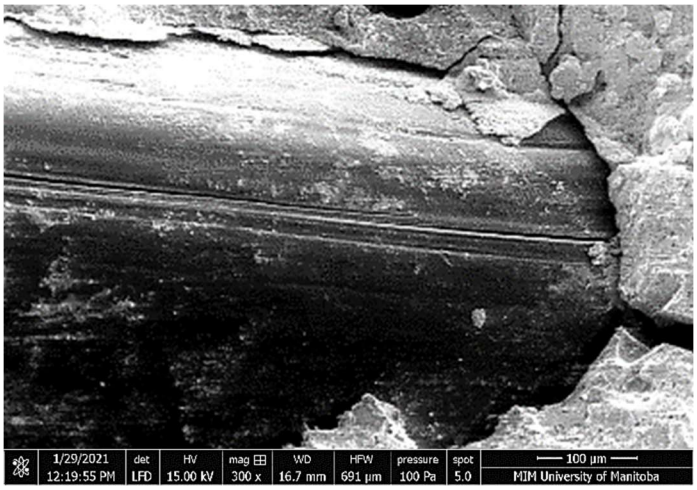

Figure 5.16: Exemplar SEM micrograph for the surface of BFP in N-G-2.5 subjected to the salt-frost exposure after flexural loading showing no evidence of pellet deterioration.

CHAPTER 6: NANO-MODIFIED CEMENTITIOUS COMPOSITES WITH BFP: REPAIR/OVERLAY OPTION

The preceding chapters presented an extensive investigation and evaluation of the performance for nano-modified cementitious composites incorporating BFP, where different fresh, mechanical and durability properties were investigated to assess the suitability of such cementitious composites for various infrastructure applications. In this chapter, the different properties and aspects required for repair and overlay materials employed in flatwork infrastructure applications were examined, particularly compatibility (thermal, elastic and mechanical) of the cementitious composites with conventional paving concrete mixture used by the City of Winnipeg, to elucidate the potential of cementitious composites as a viable alternative as a rehabilitation material for infrastructures.

6.1 Introduction

Different rehabilitation and preventive techniques such as full and partial-depth repairs, joint sealing, overlays, etc. as well as materials such as fiber-reinforced concrete, polymer-modified concrete, etc. have been used to restore and/or improve the performance of concrete infrastructure [e.g. Frentress and Harrington, 2012; Fick and Harrington, 2016]. Partial-depth repair replaces unsound/damaged concrete in the top one-third to one-half of the concrete section (e.g. pavements, bridge decks), restores its serviceability, and deter further deterioration [Smith *et al*., 2014]. Overlays are employed to restore or add structural capacity of concrete, eliminate surface distresses of existing concrete that are in good to fair structural conditions, and mitigate damage due to service conditions (e.g. de-icing salts, impact loads). The repair/overlay materials should work monolithically with substrate concrete to ensure integrity and continuity of deformation of the assembly. Thus, the

performance of a repair/overlay system relies on the properties of the topping material used and its bond characteristics with the base concrete [ACI PRC-546-14; ACI PRC-325.13-06].

Repair/overlay specifications [e.g. Frentress and Harrington, 2012; Fick and Harrington, 2016] of concrete pavements and bridges typically require a rapid-strength gaining material for quick opening to traffic. While numerous high early-strength cementitious repair materials are commercially available, many of these materials are vulnerable to cracking, poor bonding, and premature deterioration. This has been ascribed to a number of interrelated factors including the brittle nature of the materials used, occasional impact loads, frost action, high shrinkage deformations, and incompatibility of the applied material with the existing concrete [e.g. Soliman and Shalaby, 2014]. The use of high-performance fiber-reinforced cementitious composites (HPFRCC) in repair/overlay applications might mitigate these technical issues, due to improving the toughness of the cementitious matrix by controlling the initiation, coalescence and propagation of cracks [e.g., Sahmaran *et al*., 2015].

Basalt fibers are a relatively new type of fibers, with high potential for the concrete industry due to its mechanical properties (tensile strength of 3,000 - 4,000 MPa and modulus of elasticity of 93 - 110 GPa), non-corrosive nature, and low cost compared with other types of fibers (e.g. steel, glass) [Jiang *et al*., 2014]. However, it was reported that basalt fibers are susceptible to degradation in alkaline media, which made them vulnerable to decomposition in cementitious matrices (high pH of 11-13) within 90 days due to possible alkali-silica reactivity [Lee *et al*., 2014]. To mitigate this technical limitation, basalt fibers can be encapsulated with polymeric resins (e.g., vinyl-ester [Branston *et al.*, 2016], polyamide [Mahmoud *et al.*, 2017, Azzam *et al*., 2019]), hence creating a new form

termed basalt fiber pellets (BFP). However, research on the use of BFP in concrete and cementitious composites is still at an early stage, which warrants further investigation to explore their suitability for multiple applications.

Extensive studies on supplementary cementitious materials (SCM) such as fly ash and slag showed that their incorporation in cementitious binders generally enhances the mechanical and durability properties of concrete [e.g. Malhotra *et al*., 2000]. However, the delay in setting time, strength gain, and microstructural development at early ages are considered the major shortcomings for cement-based materials incorporating high-volume SCM to be widely accepted as repair/overlay materials [Mindess *et al*., 2003]. Moreover, concerns related to salt-frost scaling of concrete incorporating high-volumes of SCM were reported [ACI 201.2R, 2016]. Thus, nano-materials (e.g. nano-silica) have been used to produce cement-based materials with high-volume SCM, to alleviate the technical limitations associated with SCM (e.g. fly ash) on early-age properties and durability [e.g. Zhang *et al*., 2012]. The ultrafine nature of nano-silica (80,000 m^2/kg) accelerates the hydration process of the binder through securing additional surfaces for the early precipitation of the hydration products, besides its early vigorous pozzolanic activity. Nano-modified HPFRCC comprising novel BFP have been developed at the University of Manitoba [Mahmoud *et al.*, 2017]. The binder comprises high content (50% by mass of binder) SCM (complying with the requirements for the category HVSCM-1 according to CSA 23.1-19 "Annex K" [CSA 23.1]) with nano-silica addition (6%). The composites showed superior mechanical properties (static and dynamic compressive strengths, tensile ductility, impact resistance) and adequate resistance to salt-frost scaling (according to ASTM 672) [Azzam *et al*., 2019; Azzam *et al*., 2021]. Yet, other aspects related their

suitability for specific field applications such as repair/overlay systems have not been explored, hence the motive for the current study.

6.2 Research Significance

The constant demand for high-performance repair/overlay materials for vital infrastructure applications (e.g. pavements, bridges, airfield aprons) prompts continual research on resilient and sustainable composites that function efficiently and safely under severe conditions. Hence, in the current study, an effort was made to investigate the suitability of nano-modified cementitious composites comprising BFP for repair/overlay systems over concrete. The composites were integrally tested for fresh characteristics, mechanical properties, resistance to infiltration of fluids, and thermal/elastic compatibility with substrate concrete before and after aggravated conditions. Such HPFRCC with balanced performance may present an attractive rehabilitation/protection option in heavy traffic zones.

6.3 Experimental Procedure

6.3.1 Materials and Mixtures

The base binders comprised 50% general use cement (GU) and 50% SCM, Type F fly ash or Grade 100 slag, in compliance with CAN/CSA-A3001 [2018]. A commercial nano-silica sol (NS) was added at a single dosage of 6% (42 kg/m^3 of solid NS particles) by mass of the total base binder (700 kg/m^3). The colloid contains 50% well-dispersed NS particles in a water-based solution; the mean particle size of NS is 35 nm, and its pH, viscosity, specific gravity, and specific surface are 9.5, 8 cP, 1.1 g/cm^3, and 80 m^2/g, respectively. Previous studies [e.g. Mahmoud *et al*. 2017, Azzam et al., 2019] showed that a dosage of 6% of this

NS solution has a positive effect on the microstructural evolution and hardened properties of mortar/concrete with SCM.

Locally available quartz sand, with a continuous grading from 0 to 600 μm with fineness modulus of 2.8 was used in the composites. The absorption and specific gravity of the sand is 1.5% and 2.6, respectively. High-range water-reducing admixture (HRWRA), poly-carboxylic acid-based, was used to achieve a target flow of 180±20 mm for all composites. The composites were reinforced with BFP at two different dosages of 2.5% and 4.5% by volume (equivalent to 1% and 2%, respectively, of basalt fibers by volume). The pellets are 36 mm in length and 1.8 mm in diameter with an aspect ratio of 20 (**Figure 6.1**). They are made of 16-μm basalt roving encapsulated with polyamide resin, and the fiber component represents 60% of the pellet by mass. BFP has a specific gravity of 1.74 with tensile strength and modulus of elasticity of 2300 MPa and 65 GPa, respectively.

Figure 6.1: Reinforcing basalt fiber pellets (BFP).

The formulations of the composites stem from high-performance concrete perspective that would be typically required for concrete repair/overlay systems [e.g. Frentress and Harrington, 2012; Fick and Harrington, 2016]. The total content of the base/reference binders (GU cement and fly ash/slag) and nano-modified binders were 700

kg/m^3 and 742 kg/m^3, respectively at a low *w/b* of 0.30. The proportions for the composites are presented in **Table 6.1**.

Table 6.1: Mixture proportions for the composites per cubic meter

Mixture ID.	Cement (kg)	Fly ash (kg)	Slag (kg)	Water* (kg)	Nano-silica (kg)	BFP (kg)	Fine aggregate (kg)	HRWR (l)
F-2.5	350	350	--	210	--	43.3	1,130	2.5
N-F-2.5	350	350	--	180	84	43.3	1,045	5.6
N-F-4.5	350	350	--	180	84	78.3	1,000	5.0
G-2.5	350	--	350	210	--	43.3	1,245	6.0
N-G-2.5	350	--	350	180	84	43.3	1,160	7.6
N-G-4.5	350	--	350	180	84	78.3	1,100	7.3

*Adjusted amount of mixing water considering the water content of nano-silica (aqueous solution with 50% solid content of SiO_2).

Regarding the mixtures' ID, the letter N denotes nano-silica, while the letters F and G indicates fly ash and slag, respectively. The number represents the dosage of the pellets in the composite by volume. The mixing protocol introduced by Azzam *et al*. (2019) was followed herein, where dry ingredients was mixed first, followed by the liquid phases and finally BFP. After casting, the specimens were covered with a polyethylene sheet, and demolded after 24 hours. Subsequently, the specimens were stored at 22±2°C and at least 95% relative humidity (RH) in a curing room until the age of testing or exposure (56 days).

6.3.2 Testing

For the fresh properties, the mortar flow and retention was done according to ASTM C230/C230M [2021]. The initial and final setting times of the composites were determined according to ASTM C403 [2016], where 150 mm cubes of fresh mortar without pellets were prepared and kept at room temperature. In addition, the fresh air content of the mixtures was measured in accordance with ASTM C231/C231M [2017]. The mechanical properties of the composites were evaluated by the development of compressive strength at various ages (1, 3, 7, 28, 56, and 90 days) using triplicate cylinders of 100 diameter and 200 mm length cylinders in accordance with ASTM C39 [2021]. Moreover, the flexural

strength and toughness of the composites at 56 days was determined according to ASTM C1609 [2019] using triplicate 100×100×350 mm prisms. The composites' resistance to infiltration of fluids was evaluated by the rapid chloride penetrability test (RCPT), according to ASTM C1202 [2019], on triplicate discs (100 mm diameter and 50 mm length). In addition, the depth of chloride penetration into the composites was measured according to the procedure described by Bassuoni et al. [2005]. Subsequent to the RCPT, the disc specimens were split into two halves, and 0.1 M silver nitrate solution was sprayed on the split faces giving a white precipitate of silver, where the average penetration depth of this precipitate was measured.

To evaluate the compatibility between the composites (repair/overlay) and substrate/parent concrete, coefficient of thermal expansion (CTE), restrained shrinkage and pull-off tests were performed. CTE was determined according to AASHTO T336 [2015] using triplicate cylinders with dimensions 100 diameter and 178 mm length for each mixture at 56 days. Repair/overly systems in concrete pavements and bridge decks are primarily restrained by substrate (parent) concrete at the interface (e.g. Type I and II partial depth repair and concrete overlays Frentress and Harrington, 2012; Fick and Harrington, 2016]. Thus, the layered restrained shrinkage configuration, which promotes formation of multiple cracks at the surface of concrete [Ghazy and Bassuoni, 2017] can project the dimensional stability of the repair/overlay material relative to parent concrete and its effect on the bonding between the two layers. Accordingly, triplicate layered prisms (65×100×350 mm) for restrained shrinkage and duplicate slabs (250×250×130 mm) were prepared for the pull-off tests. The parent concrete for these prims and slabs was a typical concrete pavement mixture used in Manitoba [CW 3310-R17] (400 kg/m^3 GU cement with 15% fly ash replacement at *w/b* of 0.4). The parent concrete was kept in the curing room

(22±2°C and at least 95% RH) for 7 days followed by storage in laboratory conditions (22±2°C and at least 55±5% RH) for 180 days to eliminate residual shrinkage strain. Subsequently, the surfaces of the prisms and slabs were wire brushed, cleaned and misted to acting as a substrate layer. The composites (repair/overlay layer: 35 mm for the prisms and 70 mm for the slabs, representing approximately 1/3 of the total assembly thickness) was poured on top of the parent concrete. In addition, two extra slabs were prepared for each of the N-F-4.5 and N-G-4.5 mixtures to investigate the influence of bonding agents (commercial acrylic grout "BG" and NS sol) on the bond strength of the repair/overlay assembly.

To determine the restrained shrinkage of the composites, eight demec points were fixed to the surface of the repair/overlay layer after 1 hour of casting [in the longitudinal (200 mm apart) and transverse (60 mm a part) directions]. The shrinkage of the repair/overlay layer was measured under the curing conditions for 56 days using a dial gauge extensometer. The specimens were then moved to a hot/dry exposure of 40±1°C and 35±5% RH, where the cumulative shrinkage of the repair/overlay layer was monitored up to 180 days from casting. The adopted layered prismatic specimens for the restrained shrinkage test simulated a critical repair/overlay scenario at the joint location (repair Type II) in concrete pavement [Frentress and Harrington, 2012], with high surface-to-volume ratio. Regarding the pull-off test, slabs were partially cored at 56 days from casting the repair/overlay to assess the bond between the composites and parent concrete CSA A23.2-6B. Furthermore, the pull-off strength of the repair/overlay assembly was determined after 50 freezing-thawing and 50 wetting-drying cycles to simulate successive winter and summer seasons [Yasien *et al*., 2021]. ASTM C672 regime was followed for the freezing-

thawing cycle using water, while the wetting-drying cycles consisted of 22±2℃ and 95% RH for 16h followed by 8h at 40±1℃ and 35±5% RH.

The bulk tests were corroborated by thermal and microstructural studies. The calcium hydroxide (CH) content in the binders was determined from 1 to 90 days using thermo-gravimetric analysis (TGA). Fracture pieces were extracted from the specimens and pulverized to fine powder (passing sieve #200), then heated at a rate of 10°C/min up to 600°C. The CH content was calculated by determining the decrease in the ignited mass percentage at a range 400 to 450°C, multiplied by 4.11 (the molecular mass of calcium hydroxide to water ratio). To evaluate the pore structure features of the composites, mercury intrusion porosimetry (MIP) was conducted at 56 days. Small pea chunks (4-7 mm) were extracted from the specimens and kept at 45±2℃ in an oven until reaching constant mass, to avoid the decomposition of hydration products or severe shrinkage cracking that might occur at higher temperatures. The mercury contact angle as well as the surface tension were 130° and 485 dynes/cm, respectively. In addition, the microstructure of composites was investigated using an environmental scanning electron microscope (ESEM) with elemental disperse X-ray (EDX) on fracture pieces from specimens.

6.4 Experimental Results and Discussion

6.4.1 Fresh Properties

The fresh properties of the composites are summarized in **Table 6.2.** All composites achieved the initial target flow of 180±20 mm (180±20% of the 100 mm base diameter of the mold), which provided high consistency for casting, compaction and finishing of specimens, suggesting suitability for field placement practices. All mixtures retained adequate consistency up to 60 minutes from mixing, as all flow values remained above 100% of the base diameter of the mold. For instance, the average flow loss at 45 min for

the mixtures without and with nano-silica was 29% and 33%, respectively, of the initial values, which implicate ample placement time (typically 30 to 40 min) required for quick batch repair operations in concrete pavement [e.g. Patel *et al*., 1993].

Table 6.2: Fresh properties of the cementitious composites

Mixture ID.	Flow (mm)					Air content (%)	Setting time (min.)	
	Test Time (min)							
	0	15	30	45	60		Initial	Final
F-2.5	172	157	144	132	113	5.3	378	451
N-F-2.5	166	134	124	112	105	6.6	270	370
N-F-4.5	182	162	147	128	111	7.1	245	355
G-2.5	185	163	144	122	109	6.4	297	386
N-G-2.5	172	156	136	118	106	7.6	190	305
N-G-4.5	197	177	155	126	112	8.2	180	285

Higher dosages of HRWR (5 to 7.5 l/m^3) were required for the nano-modified mixtures relative to the reference mixtures, according to the type of binder and BFP dosage (**Table 6.1**). This was ascribed to the ultra-high surface area of nano-silica (80 m^2/g) and hence increased cohesiveness of the mixtures, which required higher dosages of HRWR to achieve the target flow. The fly ash-based mixtures required lower dosages of HRWRA compared with the slag-based mixtures due to the geometry of particles. The spherical shape of fly ash particles imparted a ball bearing effect, hence enhancing the workability of the mixtures, while the angular shape of slag particles led to interlocking of constituents and in turn harsher consistency [Neville, 2011].

Increasing the fibers' content typically reduces the workability of cement-based mixtures, due to friction, interlocking and clustering/balling effects [Mehta and Monteiro, 2014]. However, the increase of BFP dosage from 2.5% to 4.5% led to improving the workability of mixtures, and in turn, relatively less HRWR was required to achieve the target flow (**Table 6.1**). This could be attributed to the foaming action due to the inclusion of macro-BFP in the mixtures, resulting in the generation of air bubbles acting as a lubricant

reducing the friction among the mixtures' constituents, and hence improving the consistency of mixtures [Mehta and Monteiro, 2014]. This was substantiated by the increase in the fresh air content of the composites with increasing the BFP dosage (**Table 6.2**), where the average air content ranged between 5% to 8%. The measured air content conforms to the recommended values stipulated in the Canadian and American codes and guidelines for cement-based materials to resist freezing-thawing exposure scenarios [CSA-A23.1/A23.2, ACI 201.2R]. In addition, the stiff nature of BFP and dosages selected resulted in ease of mixing process without experiencing notable clustering or balling of the pellets. Furthermore, BFP was included as a replacement of fine aggregate (0 to 600 μm), which have higher specific surface compared to the pellets, resulting in more free water available for lubrication and flowability of mixtures with increasing the dosage of BFP.

Despite the increase in the HRWRA dosage, the nano-modified composites had shorter initial and final setting times relative to their reference composites (**Table 6.2)**. Binders containing high volumes of SCMs typically exhibit extended hardening rates, according to the type of SCM and total binder content [Neville, 2011]. However, the final setting times of the nano-modified composites herein were within the normal range of 4 to 6 h, despite the high content (50%) of fly ash/slag, which complies with the various setting time requirements of repair/overlay applications for concrete pavements and bridges in different jurisdictions [e.g. Wilson *et al*., 2001; Burnham *et al*., 2016; ElBatanouny *et al*., 2020]. This could be attributed to the boosting effects of nano-silica on the hydration and pozzolanic processes of these blended binders, as will be discussed in the thermogravimetric analysis, thus accelerating the hardening rates of the composites conforming to findings of previous studies [e.g. Zhang *et al*., 2012]. The fly ash-based composites had longer setting times than that of slag-based counterparts as (**Table 6.2)**.

For example, mixture N-F-2.5 had 42% and 21% longer initial and final setting times, respectively, compared to that of mixture N-G-2.5. This was ascribed to the well-documented [Mehta and Monteiro, 2014] slow reactivity of Type F fly ash (fineness of 290 m^2/kg and CaO content of 10.81%), relative to the finer (492 m^2/kg) and relatively more reactive slag (CaO content of 42.70%). The hardening rates obtained herein suggest the suitability of the composites for placement operations of repair/overlay in the field, which can be further adjusted through the inclusion of accelerating or retarding admixtures to achieve special project requirements.

6.4.2 Mechanical Properties and Hydration Development

The average compressive strength at different ages as well as the flexural strength and toughness at 56 days of the composites are presented in **Figures 6.2** and **6.3**.

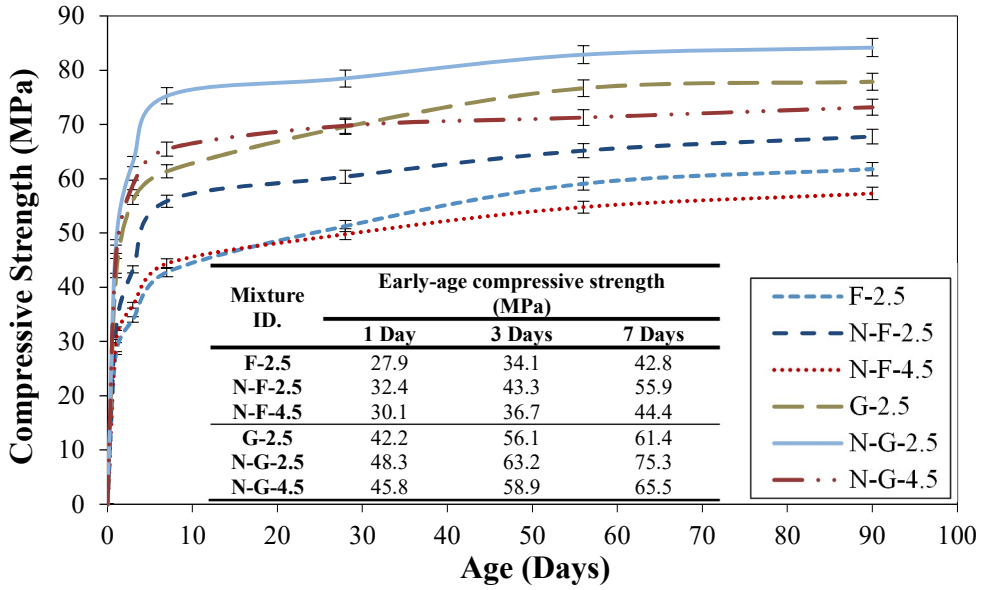

Mixture ID.	Early-age compressive strength (MPa)		
	1 Day	3 Days	7 Days
F-2.5	27.9	34.1	42.8
N-F-2.5	32.4	43.3	55.9
N-F-4.5	30.1	36.7	44.4
G-2.5	42.2	56.1	61.4
N-G-2.5	48.3	63.2	75.3
N-G-4.5	45.8	58.9	65.5

Figure 6.2: Compressive strength versus time. (Note: error bars represent standard deviations).

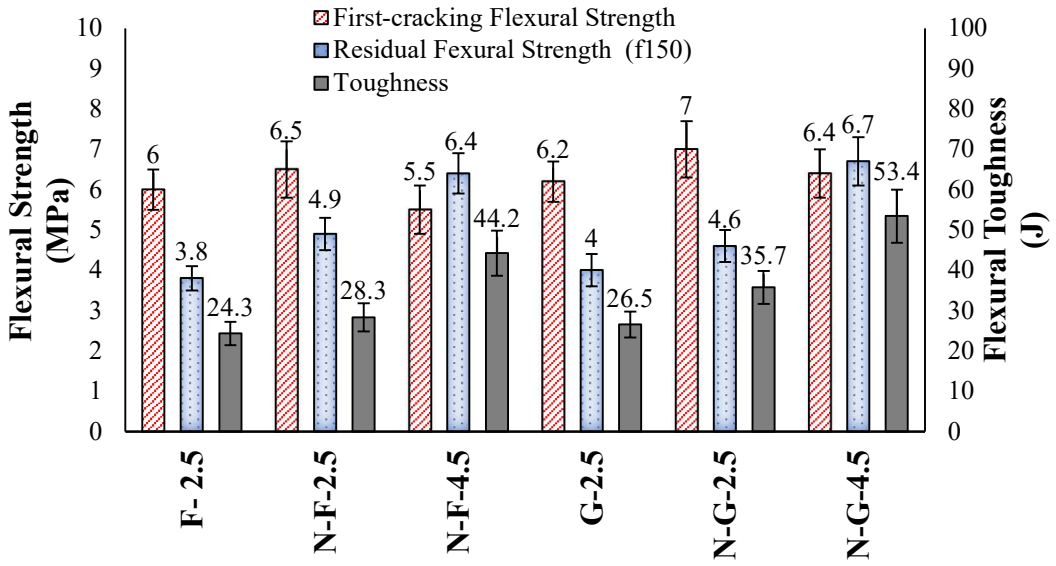

Figure 6.3: Flexural parameters of the composites at 56 days. (Note: error bars represent standard deviations).

Blended binders incorporating high-volume Type F fly ash (slowly reactive pozzolan) or slag (latent hydraulic binder) typically exhibit slow rate of strength and microstructural development at early-age, but their reactivity improve with time [Mehta and Monteiro, 2014]. Thus, most standards and codes for concrete [e.g. CSA-A23.1/A23.2 (2019)] require the assessment of concrete comprising fly ash or slag at 56 or 91 days. The results obtained from this study showed that the compressive strength of all composites at early-age was high, due to the high binder content and low *w/b*. The nano-modified composites achieved compressive strength in the range of 30 to 48 MPa and 37 to 63 MPa at one and three days, respectively. These ranges, for example, meet the strength requirements of quick repair and fast-track overlays applications in concrete pavements and bridges, which stipulate a minimum strength of 15 to 25 MPa for early opening to traffic [e.g. CW3310-R17; Smith *et al*., 2014, ACI 325.13R-06].

Conforming to the accelerated hardening rates, addition of 6% NS significantly improved the compressive strength of the composites with high-volume SCM at early-ages

(1, 3 and 7 days). The average increase in compressive strength at early ages for mixtures N-F-2.5 and N-G-2.5 was 25% and 17%, respectively relative to that of the reference mixtures F-2.5 and G-2.5. The ultrafine nature of NS (80,000 m^2/kg) accelerated the hydration process of cement through providing additional surfaces for the early precipitation of the hydration products (nucleation effect) [Kong *et al*., 2012]. Moreover, colloidal NS solutions (primarily dispersed to nano-sizes) were found to create silica-agglomerates imparting a filler effect in the cementitious matrix [Oertel *et al.*, 2013]. Kong *et al*. [2012] observed that water could be absorbed in the high nano-porosity of NS agglomerates, thus decreasing the *w/b* in the paste and in turn densifying the pore structure. The functionality of nano-silica was captured by the thermogravimetry results (**Table 6.3)**. The decrease of CH contents in the nano-modified fly ash (N-F) and slag (N-G) binders, started at early-age, despite the high content (50%) of SCM. The normalized content of CH at one to seven days for the N-F and N-G binders relative to their reference counterparts ranged between 0.90 and 0.64 and 0.83 to 0.52, respectively. Notable consumption of CH during this period indicated vigorous pozzolanic activity of NS in these binders at early-age resulting in additional precipitation of C-S-H gel in the matrix, thus improving microstructure and strength.

Table 6.3: Thermal analysis of the binders

Calcium hydroxide content (%)	Time (Days)					
	1	**3**	**7**	**28**	**56**	**90**
F	6.75	7.92	8.31	7.96	7.23	6.64
G	6.94	7.64	8.26	7.82	7.02	6.32
N-F	6.07	5.95	5.35	4.85	4.37	3.78
N-G	5.81	4.92	4.32	3.84	3.31	2.96
Relative comparison	**Normalized calcium hydroxide Content**					
N-F/F	0.90	0.75	0.64	0.61	0.60	0.57
N-G/G	0.83	0.64	0.52	0.49	0.47	0.47
N-G/N-F	0.94	0.83	0.80	0.79	0.75	0.78

Note: Precision of measurement is ± 0.20%.

The nano-modified composites continued gaining later-age compressive strengths, though at lower rates, in the range of 50 to 79 MPa at 28 days and 57 to 84 MPa at 90 days (**Figure 6.2**). Correspondingly, addition of NS improved the flexural performance of the composites at 56 days (**Figure 6.3**). The first-cracking flexural strength of N-F-2.5 and N-G-2.5 was increased by 8% and 13% relative to that of the reference mixtures without NS, and toughness was increased by 16% and 35%, respectively. This conformed to the slower rates of CH depletion that were observed for the nano-modified mortars between 28 to 90 days (marginal/nil reduction in the normalized CH contents, **Table 6.3**). Hence, the slower later-age strength evolution for the nano-modified composites was ascribed to the long-term pozzolanic reactivity of fly ash and slag and filling effect of NS particles. The obtained ranges for compressive strength at later ages highlights the adequacy of the composites for high-strength repair/overlay applications. The compressive strength ranges comply or exceed the strength requirements (30 to 65 MPa after 28 or 56 days) for repair and overlay applications in concrete pavements and bridges [e.g. ACI PRC-325.13-06; COW Tender 245-2020; Wilson *et al*., 1999].

The slag-based composites, without and with NS, had higher mechanical properties relative to that of their fly ash-based counterparts (**Figures 6.2 and 6.3**). For example, the compressive strength of N-G-2.5 at 1, 3, 7, 28, 56 and 90 days were 49%, 46%, 35%, 30%, 27%, and 24%, respectively, higher than that of N-F-2.5. This can be ascribed to the higher reactivity of slag (higher fineness 492 kg/m^2] and lime (CaO) [43%]; latent hydraulic binder) relative to fly ash (low fineness [290 kg/m^2] and CaO content [approximately 11%], slowly reactive pozzolan) which enhanced level of maturity of slag-based binders and in turn mechanical properties. This was substantiated by thermogravimetry results as the normalized CH contents of N-G/N-F was consistently less than 1.0 at all ages, indicating

the catalyzed reactivity of the nano-modified slag-based mixture and subsequently more formation of secondary/pozzolanic C-S-H gel. The improved reactivity of the slag-based composites resulted in higher quality of the ITZ between the BFP and the matrix (**Figure 6.4)**, and consequently better interfacial bond strength. Correspondingly, the average calcium to silicate ratio (*Ca/Si*) of the paste in the ITZ of the nano-modified slag-based composite (N-G-2.5) was 1.16, compared with 1.37 for the fly ash-based counterpart, substantiating the more efficient and accelerated reactivity of the former. The *Ca/Si* of C-S-H from the pozzolanic reaction tends to 1.1, whereas primary C-S-H generated from the hydration reactions of cement tends to 1.7 [Detwiler *et al.*, 1996].

Regarding the effect of BFP on the mechanical capacity of composites, increasing the dosage from 2.5% to 4.5% led to decreasing the compressive and first-cracking flexural strengths values (**Figures 6.2** and **6.3**). For instance, the compressive strength of the nano-modified composites N-F-4.5 and N-G-4.5 at 28 days was reduced by 18% and 11%, respectively relative to that of their counterparts with the lower BFP dosage (2.5%), and the first-cracking flexural strength was reduced by 15% and 9%, respectively. This can be linked to the increase of air content (**Table 6.2**) and creation of additional interfacial transitional zones (ITZs) with the higher dosage of BFP, which represented weak links and stress concentrators in the matrix, thereby decrease the capacity of the matrix. However, these aspects did not reduce the high early- (30.1 MPa for N-F-4.5 and 45.8 MPa for N-G-4.5 at 1 day) and later-age (49.8 MPa for N-F-4.5 and 69.8 MPa for N-G-4.5 at 28 days) strength of the composites below the typical requirements for repair and overlay applications in concrete pavements and bridges, as outlined earlier. Moreover, the minimum flexural strength for the studied composites was 5.5 MPa, which is higher than

the minimum concrete flexural strength (4.5 MPa) requirement for concrete overlays stipulated by most transportation agencies [ACI PRC-325.13-06]

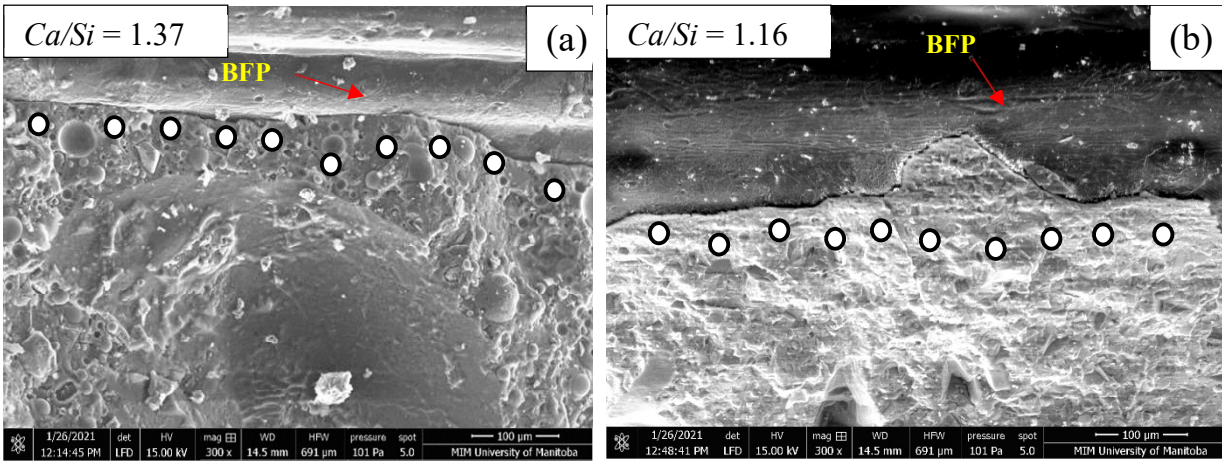

Figure 6.4: Exemplar SEM micrographs for the nano-modified composites at 56 days showing ITZ with BFP in: (a) N-F-2.5, and (b) N-G-2.5. (Note: Ca/Si value is the average for the EDX analysis at marked locations)

The composites had high toughness and residual strengths, even at the lower BFP dosages (**Figure 6.3**), complying the guidelines' requirements for overlay systems comprising fiber reinforced cementitious materials, which stipulate an average residual strength (f_{150}) of 0.65 to 4.5 MPa (according to binder content/formulation and fiber content/type/size) [ACI PRC-325.13-06]. This is attributed to the designed microgrooves on the surface of the pellets in the longitudinal direction imparted an interlocking effect between the matrix and the pellets, through increasing the contact surface as well as providing host locations for the deposition of hydration products (**Figure 6.5**).

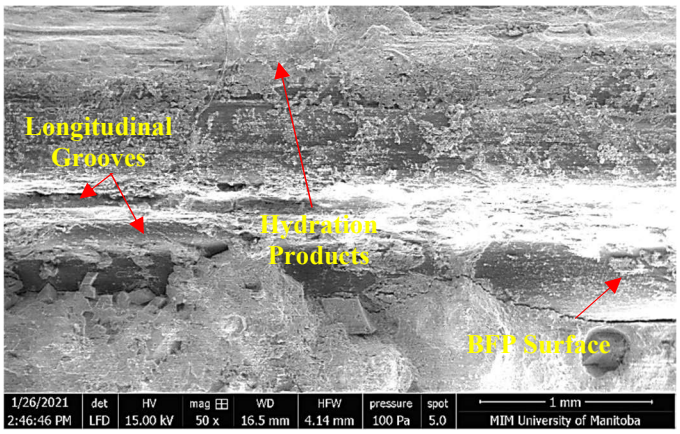

Figure 6.5: Exemplar SEM micrograph for the surface morphology of BFP in N-G-2.5.

Accordingly, this resulted in the high resistance to pullout of the BFP, which is the key toughening mechanism responsible for improving the ductility of the composites. Unlike the matrix strength, increasing the BFP dosage in the composites significantly enhanced the post-cracking flexural performance of the composites in terms of toughness and residual strength (f_{150}) at deflection of *l/150* (**Figure 6.3**). For instance, the toughness of composites N-F-4.5 and N-G-4.5 was increased by 56% and 50%, respectively relative to that of their corresponding mixtures with 2.5% BFP. This is ascribed to abundance of pellets at cracking planes, which restrained and bridged cracks resulting in strain hardening that improved toughness beyond the first-cracking stage. The high ductility of the composites may allow for thinner overlays and/or longer joint spacing, controlling differential movement due to heavy loads, curling/warping, and shrinkage. This highlights the adequacy of the composites to be implemented in high-performance overlay applications, such as heavy duty or critical locations s(e.g. bridge decks, roads' intersections).

6.4.3 Penetrability and Microstructural Features

The penetrability and microstructural feature of the composites are summarized in **Table 6.4.** All the composites had passing charges less than 1000 coulombs at 56 days, and thus

'very low' penetrability, in accordance with ASTM C1202 classification. This can be ascribed to the mixture design of the composites (high binder content and low *w/b*), which produced dense cementitious matrix.

Table 6.4: Summary of penetrability and MIP results at 56 days

Mixture ID	RCPT parameters			MIP parameters		
	Passing charges (coulombs)	Chloride ion penetrability class (ASTM C1202)	Physical chloride penetration depth (mm)	Apparent total porosity (%)	Threshold pore diameter (µm)	Proportion of micro-pores, <0.1 µm (%)
F- 2.5	980	Very Low	14.6 (2.8)	13.8	0.12	35
G-2.5	688	Very Low	9.1 (2.3)	12.9	0.09	39
N-F-2.5	630	Very Low	9.8 (2.6)	12.7	0.08	43
N-F-4.5	684	Very Low	10.9 (2.1)	13.8	0.11	39
N-G-2.5	348	Very Low	4.6 (0.5)	11.8	0.07	48
N-G-4.5	379	Very Low	5.8 (0.8)	12.6	0.09	45

Notes: Numbers in brackets indicate standard deviations.

Various guidelines and specifications for repair and overlay systems in concrete pavements and bridges require low penetrability to reduce moisture infiltration/saturation into the cementitious matrix, thus improving its durability against chemical and/or physical mechanisms (e.g. de-icing salt and/or frost action). For example, the recommended target passing charges according to ASTM C1202 for such applications at 56/90 days is less than 1500/1000 coulombs [Smith *et al*., 2014; COW Tender 245-2020].

The physical chloride penetration depth, which ranged between 4.6 and 14.6 mm, indicated differences in microstructural features among composites based on the type of binder and BFP dosage, complying with the trends of mechanical properties. For instance, addition of 6% NS in mixtures N-F-2.5 and N-G-2.5 decreased the physical penetration depth by 33% and 49%, respectively relative to that of the reference composites without NS. Correspondingly, the porosity of N-F-2.5 and N-G-2.5 was reduced by 8% and 9%, respectively compared with that of their reference counterparts; while the proportion of

micro-pores was increased by 23% and 17%, respectively, and the threshold pore diameter was increased by 33% and 22%, respectively. These trends highlight the functionality of NS with high-volume SCM binders at improving the maturity level of and densifying the cementitious matrix by multiple mechanisms, as discussed earlier. Hence, the nano-modified binders had higher mechanical capacity and reduced penetrability.

Complying with the strength and hydration development trends, the slag-based composites (without/with NS) had higher resistance to penetration of fluids and improved microstructure relative to their fly ash-based counterparts (**Table 6.4**). For example, the physical penetration depth in G-2.5, N-G-2.5 and N-G-4.5 specimens was 38%, 53% and 47%, respectively less than that of F-2.5, N-F-2.5 and N-F-4.5 specimens. Correspondingly, the threshold pore diameters of these slag-based composites were 25%, 13% and 18%, respectively less than that of their fly ash-based counterparts, while the proportion of micro-pores was increased by 11%, 12% and 15%, respectively (**Table 6.4**). As previously discussed, this can be attributed to the improved reactivity of slag relative to fly ash (**Table 6.3**), thus refining the microstructure of slag-based composites and reducing their penetrability at 56 days.

Increasing the BFP dosage led to higher penetrability in the composites due to altering their microstructural features (**Table 6.4**). For instance, the physical penetration depths in N-F-4.5 and N-G-4.5 specimens were 11% and 26%, respectively higher than that of their corresponding specimens with the lower BFP dosage (2.5%) [**Table 6.4**]. Correspondingly, the apparent porosity of N-F-4.5 and N-G-4.5 increased by 9% and 7%, respectively relative to that of N-F-2.5 and N-G-2.5, and the proportion of micro-pores was reduced by 9% and 6%, respectively. The foaming action observed during mixing of BFP with other ingredients led to increasing the air content of composites with dosage (**Table**

6.2), especially with the absence of coarse aggregate and higher viscosity of the composites in the fresh state relative to conventional concrete [Powers, 1964]. This led to preventing some air bubbles from rising to the surface during vibration. Moreover, increasing the BFP dosage led to the formation of additional ITZs between the pellets and the mortar, which contributed to the relatively coarser microstructure of the matrix and increased penetrability. Nevertheless, all the fly ash- and slag-based composites herein had 'very low' penetrability, regardless of the BFP dosage, which indicate high resistance to exposures involving intrusion of fluids. The penetrability and microstructure features of the studied composites conform to the acceptable and high salt-frost scaling resistance of the fly-ash and slag-based composites, respectively reported in the previous study by the authors [Azzam *et al*., 2019].

6.4.4 Compatibility with Substrate Concrete

6.4.4.1 Coefficient of Thermal Expansion

The coefficients of thermal expansion (CTE) of the composites are listed in **Table 6.5.** The CTE value of parent concrete was also measured (10.9×10^{-6}/°C). The composites had comparable CTE to that of the parent concrete, indicating thermal compatibility between both components. For instance, the fly ash-based mixtures had an average CTE of 10.6×10^{-6}/°C, while it was 10.1×10^{-6}/°C for the slag-based mixtures. These close results of CTE with parent concrete comply with recommendations of various guidelines for repair/overlay systems [e.g. ACI PRC-546R-14; ACI PRC-325.13-06; Fowler *et al*., 2008; Frentress and Harrington, 2012; Fick and Harrington, 2016] to mitigate the detrimental effects (cracking, poor bonding, delamination) of thermal mismatch between the repair material and parent concrete.

Table 6. 5: Summary of coefficient of thermal expansion and restrained shrinkage results

Mixture ID	Coefficient of thermal expansion (micro-strain/°C)	Restrained shrinkage (micro-strain)			
		1 Day	7 days	56 days	180 days
F- 2.5	11.1 (0.9)	43 (3)	91 (5)	224 (10)	438 (16)
G-2.5	10.6 (0.7)	51 (4)	109 (9)	236 (14)	442 (29)
N-F-2.5	10.9 (0.8)	58 (2)	133 (8)	231 (11)	446 (18)
N-F-4.5	9.8 (0.6)	52 (3)	119 (5)	216 (18)	416 (26)
N-G-2.5	10.1 (0.6)	74 (4)	171 (6)	244 (13)	454 (22)
N-G-4.5	9.6 (0.7)	66 (2)	157 (7)	229 (17)	419 (14)

Note: Numbers in brackets indicate standard deviations.

The inclusion of NS and type of binder (fly ash/slag) had insignificant effects on the CTE of the composites, where F-2.5 and N-F-2.5 had CTE of 11.1×10^{-6}/°C and 10.9×10^{-6}/°C, respectively, while G-2.5 and N-G-2.5 had CTE of 10.6×10^{-6}/°C and 10.1×10^{-6}/°C. This conforms to Mindess *et al*. [2002] who reported CTE values of mortar with siliceous sand ranging between 10-12 $\times10^{-6}$/°C according to the volume ratio of the sand, where a marginal influence of the *w/b* and binder type on the CTE of cement-based materials was reported as well. The presence of stiff macro-BFP (elastic modulus of 65 GPa), randomly oriented in the matrix, restrained the thermal deformations of high volume of paste in the composites; thus compensating for the absence of coarse aggregate and keeping close CTE ranges to that of normal substrate concrete. Increasing the BFP dosage in the matrix further restrained its volumetric change due to thermal gradients, albeit to a marginal extent. Thus, the CTE of mixtures N-F-4.5 and N-G-4.5 was reduced by 10% and 5%, respectively, compared to that of their counterpart mixtures with the lower BFP dosage (2.5%). In addition, this insignificant reduction of CTE could be attributed to the inclusion of more BFP with low CTE (1.4×10^{-6}/°C) in the matrix.

6.4.4.2 Restrained Shrinkage

Large differential deformations of the repair/overlay layer relative to the substrate concrete can lead to surface cracking and de-bonding at the interface [ACI PRC-546R-14; ACI

PRC-325.13-06]. Hence, a restrained shrinkage test was conducted herein, and the results are summarized in **Table 6.5** including cumulative restrained shrinkage of the composites up to 180 days (56 days in standard curing followed by 124 days in hot/dry) conditions. It is conceivable that different field conditions including frequent rise of RH, precipitation and/or frequent drop of temperature might partially reverse/reduce the total shrinkage of composites compared with the aggressive drying conditions implemented herein. However, this extreme scenario was selected to project performance risks/limitations that might arise with the composites in the field.

After 1 and 7 days of curing, the nano-modified composites, yielded higher rates of restrained shrinkage relative to that of their corresponding reference composites. For instance, the average restrained shrinkage at 7 days for N-F-2.5 and N-G-2.5 was 46% and 57%, respectively higher than that of their reference counterparts without NS (91 and 109 micro-strain). This could be ascribed to the boosting effect of NS on the hydration of both fly ash- and slag-based binders at the early-age; yet, this trend diminished with time, complying with the thermogravimetry results. Hence, composites with/without NS showed comparable values of shrinkage at 56 days, since the total shrinkage of the reference and nano-modified composites had restrained shrinkage in the narrow range of 224 to 244 micro-strain. The higher shrinkage values for the nano-modified composites up to 56 days can be attributed to the moist conditions that secured favorable environment for the hydration development, particularly with the high binder content used (700 kg/m^3). Conforming to thermogravimetry results, the slag-based composites experienced higher restrained shrinkage values compared with that of the fly ash-based counterparts. For instance, the average restrained shrinkage at 1 and 7 days for N-G-2.5 was 28% and 29%, respectively, higher than that of N-F-2.5 (58 and 133 micro-strain). This could be ascribed

to the higher reactivity of the slag-based binder, particularly with the coexistence of NS, as explained earlier. The difference in the shrinkage values between fly ash- and slag-based binders became insignificant with time, due to the prolonged moist conditions that allowed for the later-age microstructural development and hence mechanical capacity of both types of binders.

Irrespective of the type of binder, the shrinkage behavior of the composites was affected by the inclusion of BFP. Increasing the BFP dosage controlled the restrained shrinkage of the composites yielding lower values (**Table 6.5**), particularly at the early-age, without any signs of surface cracking. The restrained shrinkage of N-F-4.5 and N-G-4.5 at 7 days was 12% and 9%, respectively lower than that of their corresponding mixtures with the lower BFP dosage (2.5%). This highlighted the contribution of BFP in restraining shrinkage of the composites relative to the base concrete, thus eliminating the potential for early-age surface cracking that might compromise the integrity of the repair/overlay system.

After subjecting the composites to drying conditions at 40±2°C and 35±5% RH for 124 days, the restrained shrinkage values were amplified. However, at the end of this drying regime, no cracks were observed at the surface of the specimens, due to the restraining action of BFP (**Figure 6.6)**.

Figure 6.6: Exemplar surface conditions of the repair/overlay assembly after 180 days (56 days standard curing plus 124 days in hot/arid conditions); (a) N-F-2.5, and (b) N-G-2.5

In a previous study Ghazy and Bassuoni [2017] observed surface cracking of similar restrained shrinkage assembly under drying conditions for some nano-modified fly ash concrete mixtures, but without fibers. The cumulative shrinkage strains for the composites at the end of the drying exposure ranged between 416-454 micro-strain. These values are significantly lower than the ACI PRC-546R-14 performance criterion (maximum drying shrinkage of 1000 micro-strain) for dimensional stability of cement-based repair materials. This could be attributed to the low *w/b* of the composites and restraining role of BFP, especially with the efficacy of the nano-modified binders at providing better pellet/matrix bonding (**Figure 6.5**) and the continuous microstructural development and thus stiffness, as shown by the mechanical properties. Accordingly, the higher BFP dosage (4.5%) led to the lowest shrinkage values at the end of drying period,

owing to abundance of randomly distributed BFP in the matrix, thus reducing paste deformations and suppressing propagation of micro- and macro-cracks in the matrix.

6.4.4.3 Bond Strength

A key parameter for the integrity of repair/overlay systems is the bond strength between the applied material and substrate (parent) concrete. Due to thermal and/or elastic mismatch, the two layers may deform differentially resulting in incompatibility of the system, and thus failure at the interface [ACI PRC-546R-14; ACI PRC-325.13-06]. The bond strength between the proposed composites and parent concrete was evaluated before and after a combined exposure of cyclic freezing-thawing and wetting-drying that may occur in the field (**Figure 6.7**).

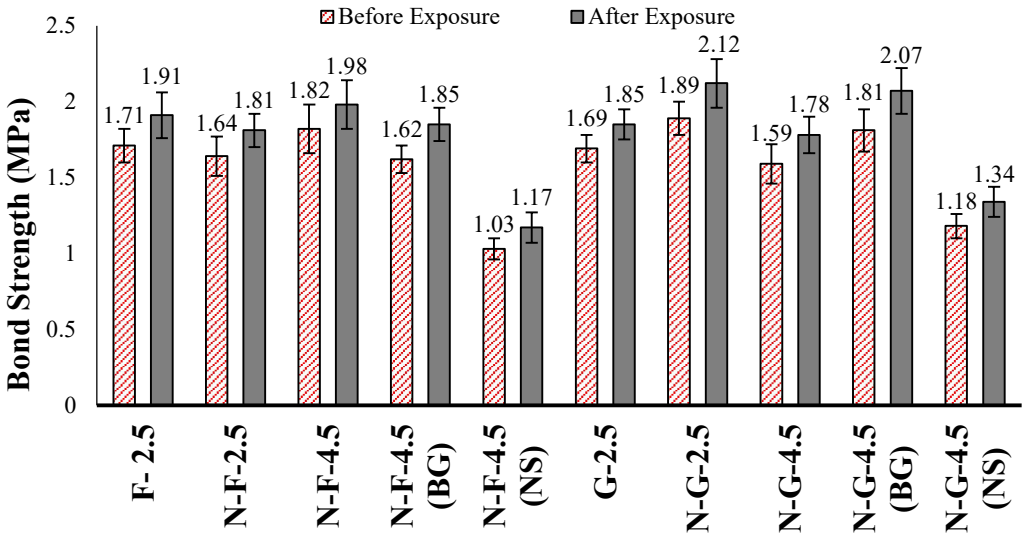

Figure 6.7: Bond strength of the repair/overlay assembly before and after exposure (Note: error bars represent standard deviations; BG and NS denote bonding grout and nano-silica colloid applied at the interface).

Before exposure, all composites, without bonding agents, had bond strength in the narrow range 1.59 to 1.89 MPa, regardless of the binder type and pellets' dosage, and the failure of the assembly took place in the substrate layer (10 to 70 mm below the interface). Complying with the CTE and restrained shrinkage trends, this indicated efficient

compatibility between the two layers and integrity of the proposed repair/overlay systems. Accordingly, the bond strength had a close range as it represented the tensile strength of the substrate layer (same concrete mixture) in the test assembly (weakest link). The trend can be ascribed to the adequate curing period provided to the applied composite layer (56 days), resulting in significant hydration and microstructural development of the matrix as shown by the thermogravimetry results, which was reflected on the interfacial bond strength between the repair/overlay and substrate layers. Moreover, it indicated that there was no preferential plastic sedimentation of BFP towards the interface, which would have otherwise caused de-bonding between the two layers, thus failure at the interface.

The bond strength of the assembly comprising the bonding grout at the interface of N-F-4.5(BG) and N-G-4.5(BG) showed comparable values to that of the corresponding assemblies without bonding agent (**Figure 6.7**), and the failure occurred in the substrate layer (i.e. high compatibility). On contrary, the use of NS colloid as a coating at the interface compromised the integrity of the repair/overlay system. Before exposure, the bond strength of N-F-4.5(NS) and N-G-4.5(NS) was reduced by 43% and 26%, respectively relative to that of corresponding assembly without NS interfacial coating, where the failure occurred at the interface between the two layers (i.e. low compatibility). Microscopy analysis showed that when NS colloid was applied at the interface, the remaining/unreacted NS formed a condensed layer at the interface acting as a separator (e.g. **Figure 6.8**), which impaired the adhesion between the two layers of the assembly. The combined exposure led to increasing the bond strength by 9 to 14% with the parent concrete, and the dominant mode of failure was in the substrate concrete [**Figure 6.9(a)**]. Similar to before exposure trends, mixtures N-F-4.5(NS) and N-G-4.5(NS) with the NS colloid applied at the interface showed the lowest bond strength of 1.17 and 1.34 MPa,

respectively, where the assembly failed at the interface [**Figure 6.9(b)**], due to forming a separating layer as discussed earlier.

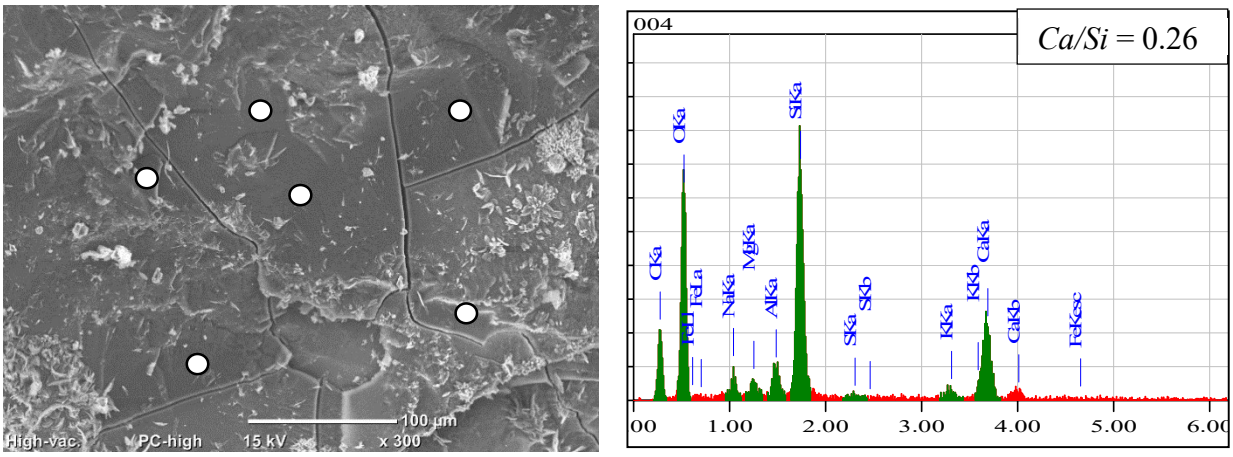

Figure 6.8: SEM and EDX for specimen extracted from the NS coated interface between N-G-4.5 and the parent concrete after pull off test (Note: the EDX analysis is an exemplar for 6 points at marked locations).

After the freezing-thawing portion of the exposure, it was observed that the fly ash-based composites showed streak lines/shadowing surrounding near surface fibers [**Figure 6.10(a)**], whereas the slag-based composites did not show such features [**Figure 6.10(b)**]. This can be ascribed to the higher fluid penetrability and relatively coarser microstructure of fly ash-based mixtures relative to that of slag-based composites, as explained in the Penetrability section. However, the increase of bonding strength of fly ash-based composites at the end of the combined exposure was not adversely affected by this superficial phenomenon. This conformed to observations from a previous study by the authors [Azzam *et al*. 2019], as similar fly-ash based composites had more tendency to salt-frost scaling compared with the slag-based composites (no scaling was experienced).

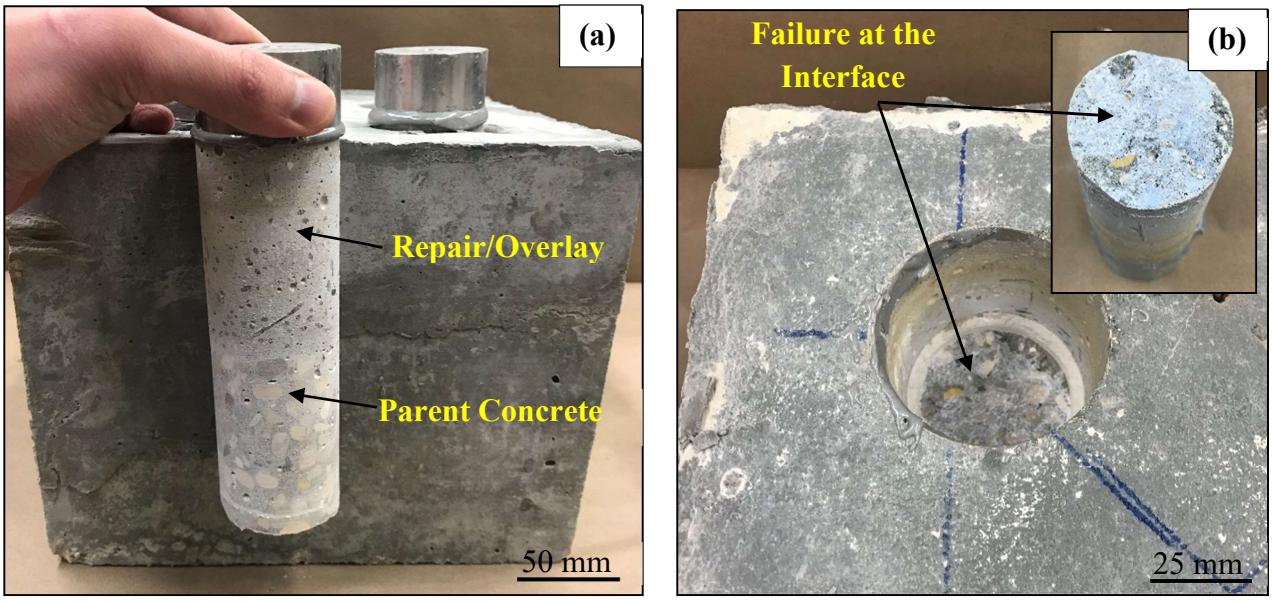

Figure 6.9: Exemplar mode of failure of layered slabs obtained from the pull-off test after the combined exposure: (a) N-G-4.5, and (b) N-G-4.5(NS).

The increased interfacial bonding after the combined exposure can be attributed to the long-term hydration and pozzolanic reactivity of the binders in the composite and substrate layers, which both comprised GU cement with SCM, especially during the thawing and wetting regimes of the combined exposure, due to the increased saturation and temperature conditions. In particular, the prolonged reactivity of high-volume fly ash/slag led to more consumption of portlandite available within the composite layer and interface with substrate concrete, resulting in production of secondary C-S-H and thus improved adhesion between the two layers. In addition, the coexistence of BFP controlled potential swelling/shrinkage deformations and micro-cracking from the cyclic conditions projecting long-term compatibility of this repair/overlay system. This complies with the recommendations of [ACI PRC-546R-14; ACI PRC-325.13-06] for concrete repair/overlay systems, where integrity of the layered system is a crucial requirement.

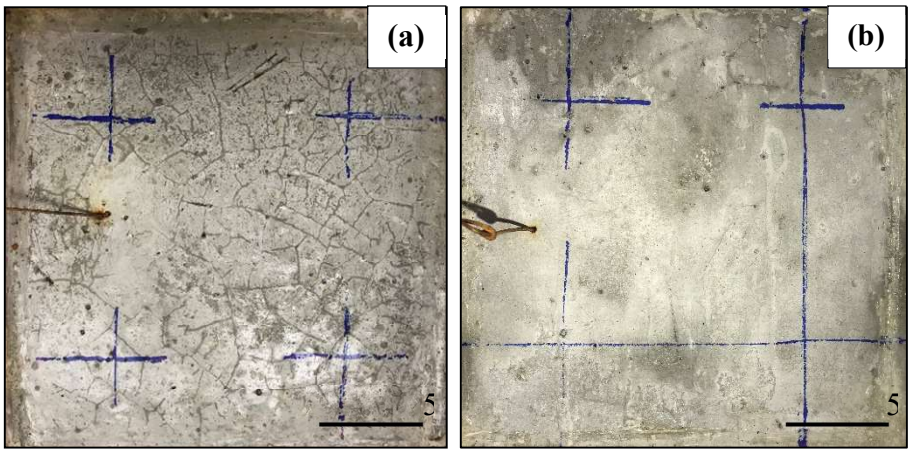

Figure 6.10: Exemplar surface condition of specimens after 50 freezing-thawing cycles: (a) N-F-4.5, and (b) N-G-4.5.

CHAPTER 7: FLEXURAL PERFORMANCE OF NANO-MODIFIED CEMENTITIOUS COMPOSITES WITH BFP AS A BONDED OVERLAY

The current chapter expands on the previous chapter and aims at investigating the efficacy of employing the cementitious composites in bonded concrete overlay application and the effect of pre-existing distress/joint in the substrate parent concrete on the performance of the overlay systems. Experimental work was adopted to examine the potentials of the cementitious composite in concrete bonded overlay systems, where numerical modeling was further utilized to support the experimental results and study the influence of selected variables on the performance of the systems such as effect of changing the overlay thickness and the influence of substrate concrete compressive strength on the performance of the system.

7.1 Introduction

The American Society of Civil Engineers (ASCE) most recent infrastructure report card [2021] indicates that 43% of public roadways in U.S. are in poor or moderate conditions, and the projected rehabilitation costs for existing roads and bridges are estimated at $550 billion. Repair, rehabilitation and preventive maintenance techniques such as full and partial-depth repairs, joint and crack sealing, bonded and unbounded overlays have been used to restore and/or improve the performance of concrete infrastructure. High-performance materials such as fiber-reinforced concrete and polymer-modified concrete have been proposed as a viable alternative for different rehabilitation techniques as they offer optimal durability and good bond to old concrete substrate [Lin *et al*., 2013]. For

concrete pavements and bridge decks under moderate to heavy traffic, a common rehabilitation technique is to cast a bonded overlay over the existing surface to restore/improve its structural capacity, eliminate existing distresses, and improve ride quality [Smith *et al.*, 2014].

For optimal performance, bonded overlay systems must perform monolithically with substrate concrete; hence, their effectiveness depends on the properties of the overlay material and its bond capacity in addition to its compatibility with existing old concrete [ACI PRC-546, 2014; ACI PRC-325.13, 2006]. Premature failure of overlays in concrete pavements and bridge decks is occasionally observed and results in significant technical and socioeconomic losses [Al-Ostaz *et al.*, 2010]. For instance, reflective cracking impairs the performance of concrete overlays; this phenomenon occurs when cracks in the underlying/parent concrete reflect randomly into the newly constructed topping layer [ACI PRC-325.13, 2006]. Extensive cracking in a bonded overlay would negatively reduce its load carrying capacity, provides direct paths for ingress of moisture and aggressive agents such as deicers, and increases surface roughness [Fick and Harrington, 2016; Yucel *et al.*, 2013]. Differential deformational between the overlay material and parent concrete may result in delamination along the bonded interface between the two layers starting from existing cracks [Zhang and Li, 2002]. Moreover, overlay specifications for concrete pavements and bridges may require rapid-hardening materials to allow fast opening to traffic [Fick and Harrington, 2016]. However, many of such materials are susceptible to cracking and inferior bonding due to a number of interrelated factors including the brittle nature of these materials, frequent exposure to impact loads and incompatibility with the existing concrete [Soliman and Shalaby, 2014]. Therefore, control of cracking and

prevention of overlay delamination in bonded overlay systems are crucial for the success of the assembly.

Employing fiber reinforced cement-based materials in bonded overlay applications can alleviate these technical issues, due to their enhanced toughness through preventing and/or controlling the commencement, coalescence and growth of cracks [Sharma *et al.*, 2013]. Concerted research efforts are being expended in this direction, including high-performance fiber-reinforced cementitious composites (HPFRCC), with wide range of binder types and formulations, binder contents (600-1300 kg/m3), water-to-binder ratios [w/b] (0.2-0.4) as well as fibers' types, sizes and contents [Sahmaran *et al.*, 2015; Qian *et al.*, 2013]. Numerous studies on binders comprising supplementary cementitious materials (SCM) (fly ash, slag) showed that they enhance the mechanical and durability properties of cementitious composites/concrete [Malhotra *et al.*, 2000]. Nevertheless, some limitations may hinder their wider use in high volumes, as they typically delay setting time, strength gain and microstructural development of cement-based materials [Mehta and Monteiro, 2014]. Furthermore, concerns regarding salt-frost scaling of concrete incorporating high-volume SCM were reported [ACI PRC-232.2, 2018]. Nano-materials (e.g. nano-silica) have been used successfully in the production of cementitious composites and concretes with high-volume SCM to mitigate these technical limitations, as they catalyze the reactivity of cement and SCM and consequently accelerate hardening rates and improve the maturity level of the hardened matrix [Zhang and Islam, 2012].

Basalt fibers are a relatively new fiber type with promising potential in the concrete industry due to their excellent mechanical properties (tensile strength of 3000-4000 MPa and elastic modulus of 93-110 GPa), low-cost relative to other fiber types (e.g. steel, glass,

carbon) as well as non-corrosive nature [Jiang *et al.*, 2014]. However, basalt fibers were reported to be vulnerable in alkaline environments (e.g. cementitious matrices) as they are susceptible to alkali-silica reactions, and thus decomposition [Lee *et al.*, 2014]. To mitigate this shortcoming, encapsulation of basalt fibers with polymeric resins (e.g., vinyl-ester [Branston *et al.*, 2016] or polyamide [Mahmoud *et al.*, 2017, Azzam *et al.*, 2019]) was proposed as a viable solution, which resulted in creating a new class of fibers termed basalt fiber pellets (BFP). Research on BFP and its use in concrete and cementitious composites is still at an early stage, which warrants further studies to explore their suitability in multiple applications such as HPFRCC for bonded overlay systems.

7.2 Research Significance

The persistent demand for high-performance overlay materials in vital infrastructure (e.g. pavements and bridges) prompts continual research on sustainable and resilient cementitious composites. Nano-modified HPFRCC incorporating BFP was developed at the University of Manitoba [Mahmoud *et al.*, 2017]. The binder comprises high content of SCM (50% fly ash/slag by mass of binder) that complies with HVSCM-1 requirements according to CSA 23.1 [2019] "Annex K" with nano-silica addition (6%). The composites showed superior mechanical properties (static and dynamic compressive strengths, tensile ductility as well as impact resistance) with adequate salt-frost scaling resistance [Azzam *et al.*, 2019; Azzam *et al.*, 2021]. Yet, other aspects relevant to their suitability for specific construction applications such as concrete overlays still need to be explored, hence the motive of this research. Success of such HPFRCC with balanced early- and long-term performance might present an attractive rehabilitation option for moderate to heavy traffic zones. In the current study, the cementitious composites were evaluated in terms of their

flexural performance in bonded overlay configurations with substrate concrete. The effect of reflective cracking originating from the substrate concrete layer on the performance of the system was also investigated. In addition, 3D finite element modelling (FEM) was employed to simulate the two bonded configurations (intact and pre-cracked) and parametrically examine the effect of overlay thickness and substrate compressive strength on the performance of the systems.

7.3 Experimental Program

7.3.1 Materials and Mixtures

The base binders comprised 50% General Use cement (GU) in addition to 50% SCM, Type F fly ash or Grade 100 slag, complying with CAN/CSA-A3001 [2018]. A commercial nano-silica sol (NS) was added at a single dosage of 6%, with 42 kg/m3 NS solid content, by mass of the base binder (700 kg/m3). The colloid comprises 50% well-dispersed nano particles of silica in a water-based solution; the mean particle size of NS particles is 35 nm, and its viscosity, pH, specific gravity, and specific surface are 8 cP, 9.5, 1.1 g/cm3, and 80 m2/g, respectively. Previous studies (Mahmoud *et al.* 2017, Azzam *et al.*, 2019) revealed that a dosage of 6% of NS sol improved the microstructural evolution and hardened properties of mortar/concrete with high content SCM.

Continuously graded (0 to 600 μm) quartz sand with a fineness modulus of 2.8 was used in the composites. The absorption and specific gravity of the sand are 1.5% and 2.6, respectively. A superplasticizer, poly-carboxylic acid-based, was added to improve the consistency of the fresh cementitious composites. The mixtures were reinforced by basalt fiber pellets (BFP) at a single dosage of 4.5% by volume (equivalent 2% of basalt fibers by volume). The pellets are 36 mm long and 1.8 mm in diameter with an aspect ratio of 20

(**Figure 7.1**). The pellets are made of 16-μm basalt roving coated with polyamide resin (Nylon 6), where the fiber component is 60% of the BFP by mass. BFP has a specific gravity of 1.74 with tensile strength and modulus of elasticity of 2300 MPa and 65 GPa, respectively. Preceding studies by the authors showed that 4.5% BFP had an optimum effect on the composites in terms of strain hardening and ductility [Azzam *et al.*, 2019, and 2021].

Figure 7.1: Reinforcing basalt fiber pellets.

The total content of the binders (GU cement and fly ash/slag) in addition to NS was held at 742 kg/m3, with a constant w/b of 0.30. The proportions of the composites are listed in **Table 7.1**. Each mixtures ID indicates the letter 'N' for nano-silica, and the letters 'F' or 'G' for fly ash or slag, respectively. The number represents the dosage of the pellets in the composite by volume. A mixing procedure introduced by Azzam *et al.* [2019] was followed herein, where dry constituents were mixed first, followed by the liquid phases and finally the BFP. The target flowability for all composites was 180±20 mm, while the setting times and fresh air content ranged between 4 to 6 hours (common range for normal concrete) and 5 to 8% (conforming to the recommended values stipulated in CSA A23.1/A23.2 [2019] to resist freeze-thaw exposures), respectively [Azzam *et al.*, 2019].

After casting, the specimens were covered with polyethylene sheets, and demolded after 24 hours. The specimens were then placed in a standard curing room at 22±2°C and a minimum 95% relative humidity (RH) until the age of testing.

Table 7.1: Mixture proportions for the composites per cubic meter

Mixture ID.	Cement (kg)	Fly ash (kg)	Slag (kg)	Water* (kg)	Nano-silica (kg)	BFP (kg)	Fine aggregate (kg)	HRWR (l)
N-F-4.5	350	350	--	180	84	78.3	1,000	5.0
N-G-4.5	350	--	350	180	84	78.3	1,100	7.3

*Adjusted amount of mixing water considering the water content of nano-silica (aqueous solution with 50% solid content of SiO_2).

7.3.2 Testing

The mechanical properties of the composites were evaluated through the development of compressive strength at various ages (3, 7, 28 and 56 days) using triplicate cylinders of 100 mm diameter and 200 mm length cylinders in accordance with ASTM C39 [2021]. Moreover, the flexural strength as well as the post-cracking behavior of the composites were determined at 56 days in accordance with ASTM C1609/C1609M [2020], by testing triplicate prisms of 100×100×350 mm in four-point bending configuration with flexural span of l = 300 mm. A servo-controlled closed-loop testing machine was used, where the displacement rate was controlled through the measured net mid-span deflection of the prisms. Two linear variable differential transducers (LVDT) were fixed on the test setup to measure the net flexural deflection of the specimens at the mid-span. The flexural toughness of the composites was calculated, as the total area under the load-deflection curve (P-δ) up to a deflection of *l/150* (2 mm), and the residual post-cracking strength was calculated at deflections *l/600* (0.5 mm) and *l/150*.

In addition, an overlay assembly was used to evaluate the mechanical compatibility between the proposed cementitious composites (overlay) and parent concrete. The assembly consisted of a 50 mm overlay of cementitious composites bonded to a 50 mm concrete substrate as depicted in **Figure 7.2**. First, triplicate prisms (50×100×350 mm) were prepared for the flexural test of the overlay system. The concrete substrate layer for these prims was a typical concrete mixture [CW 3310-R17, 2017] (400 kg/m3 GU cement with 15% fly ash replacement at w/b of 0.4). The parent concrete was kept in the curing room (22±2°C and at least 95% RH) for 7 days followed by storage in laboratory conditions (22±2°C and at least 55±5% RH) for 180 days to eliminate residual shrinkage strains. Afterwards, the surfaces of the prisms were roughened and wire brushed, then cleaned and misted with water to act as a substrate layer. Subsequently, the 50 mm cementitious composite overlay layer (N-F-4.5 and N-G-4.5) was poured on top of parent concrete.

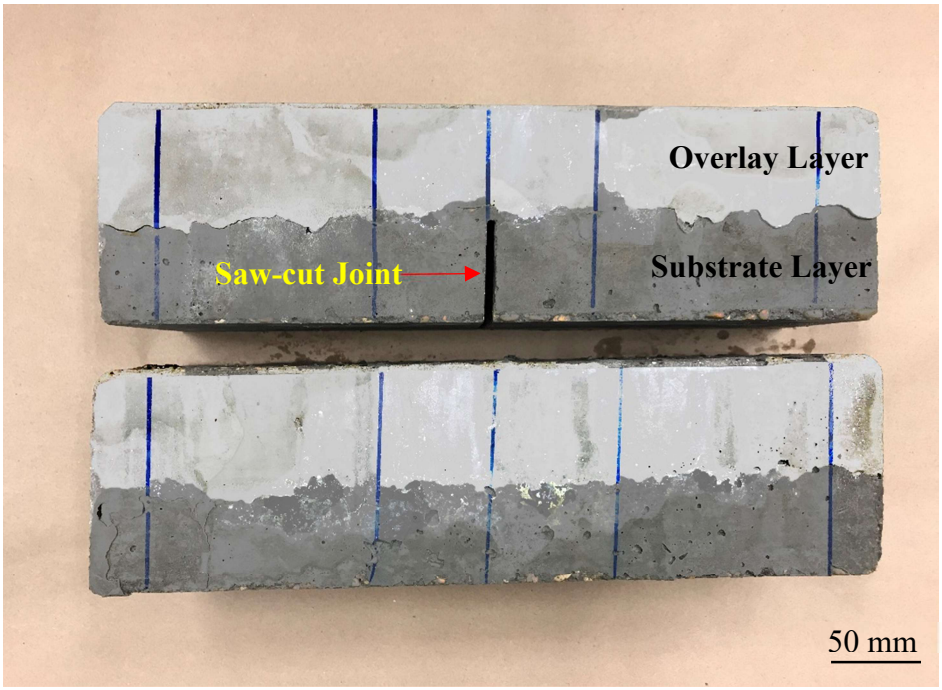

Figure 7.2: Exemplar overlay assembly for N-G-4.5 specimens.

All specimens were demolded after 24 hours and placed in the curing room (22±2°C and at least 95% RH) until the day of testing (56 days). The flexural performance of the overlay-substrate assembly was then evaluated by ASTM C1609/C1609M. Reflective cracking in overlay systems, particularly above joints/cracks in the original substrate, is a commonly observed phenomenon leading to failure of the assembly [Harrington and Fick, 2014; Yucel *et al.*, 2013]. To investigate the effect of reflective cracking on the proposed assembly, another group of pre-cracked prisms (**Figure 7.2**) were prepared in a similar configuration to Kamada and Li [2000] and Zhang and Li [2002] and tested for flexural performance. After casting and curing of the overlay layer, the substrate concrete layer was fully cut out with a diamond saw with a width of 3 to 4 mm at the middle of the prism up to the interface with the cementitious composite layer, to form a pre-induced joint (pre-cracked substrate) in the substrate concrete layer center.

The bulk tests were corroborated with thermal and microstructural studies. The calcium hydroxide (CH) content in the binders was determined from 1 to 56 days using thermogravimetric analysis (TGA). Fracture pieces were extracted from the specimens and pulverized to fine powder (passing sieve #200), then heated at a rate of 10°C/min up to 600°C. The CH content was calculated by determining the decrease in the ignited mass percentage at a range 400 to 450°C, and multiplying it by 4.11 (the molecular mass of calcium hydroxide to water ratio). In addition, the microstructure development of the composites was investigated using environmental scanning electron microscope (ESEM) with elemental disperse X-ray (EDX) on fracture pieces from the tested specimens.

7.4 Finite Element Modeling

7.4.1 Theoretical Formulation

According to the concept of composite actions, horizontal interfacial shear is generated due to the change of the internal forces along the section axis. Bending moment (M) and shear force (V) are generated in a simply supported composite beam with depth (d) and width (b) subjected to flexural loading configuration. The acting moment generates the compression force (Fc) and the tension force (Fs), acting at a lever arm (z). Numerous studies have been made on behavior of concrete-to-concrete interfaces, under shear flow stresses, which can be predicted using 'shear-friction theory' and its modifications [e.g. Birkeland and Birkeland, 1966; Mattock and Hawkins, 1972].

Considering an infinitesimal element with length (dx), the moment change can be presented as the change of the compressive force (dFc) and tensile force (dFS) [Lenz, 2010]. For a composite section, horizontal shear stresses (τ) acting at the interface between the concrete layers are generated. The compression force from the acting moment can be expressed as Fc = M/z, while the moment changes along the element dx with the shear force V by dM = V·dx. For interfaces in the tension zone, the full compression force must be transferred across the interface [Lenz, 2010]. Hence, extracting the composite section at the interface, the force equilibrium at the lower concrete layer gives the relation in **Equation 7.1**.

$$\tau \cdot dx \cdot b = dF_c \qquad \textbf{(Equation 7.1)}$$

The shear stress at the interface can be determined by **Equation 7.2**:

$$\tau = dF_c/(dx \times b) = dM/(dx \times b \times z) = V \times dx/(dx \times b \times z) = V/(b \times z) \qquad \textbf{(Equation 7.2)}$$

The tested overlay assembly is considered as a bi-material system, as it is composed of two layers with different mechanical properties. The initiation of cracks in the assembly (lower/substrate layer) and their propagation can be described by fracture mechanics principles. Under flexural loading, a crack propagates from the lower layer (substrate concrete) to the top layer (cementitious composite) if the two layers are fully bonded. A direct approach to illustrate the propagation of a crack in cementitious materials is through linear elastic fracture mechanics, where the crack can be classified as an opening mode [Shah *et al.*, 1995]. The elastic stress field in the proximity of a crack tip can be expressed by:

$$\sigma_x = \frac{K_I}{(2\pi r)^{0.5}} \cos\frac{\theta}{2}\left(1 - \sin\frac{\theta}{2} \times \sin\frac{3\theta}{2}\right) \quad \textbf{(Equation 7.3)}$$

$$\sigma_y = \frac{K_I}{(2\pi r)^{0.5}} \cos\frac{\theta}{2}\left(1 + \sin\frac{\theta}{2} \times \sin\frac{3\theta}{2}\right) \quad \textbf{(Equation 7.4)}$$

$$\tau_{xy} = \frac{K_I}{(2\pi r)^{0.5}} \sin\frac{\theta}{2} \times \cos\frac{\theta}{2} \times \cos\frac{3\theta}{2}\right) \quad \textbf{(Equation 7.5)}$$

where, (r) is the distance to the crack tip, θ is the angle of inclination, while the stress intensity factor for crack opening mode(K_I) is:

$$K_I = \sigma \times \sqrt{\pi a}\, f(a/b) \quad \textbf{(Equation 7.6)}$$

where, (σ) is the applied stress on the structure, while (a) is the crack length, and (a/b) is the geometry factor that can be obtained from a linear elastic fracture mechanics handbook [Tada *et al*., 1985].

According to the elastic stress field given by **Equations 7.3-7.5**, the stresses tend to infinity at the crack tip where (r) approaches zero. This phenomenon is known as stress

singularity at an elastic crack tip [Shah and Ouyang, 1994]. Since infinite stresses cannot develop in realistic behavior of materials, a certain zone of inelasticity must exist at the tip of the crack. The value of KI indicates the intensity of the stress field in the vicinity of the crack tip, which depends on load, specimen size and geometry, crack length and boundary conditions. A crack grows when K_I is equivalent to a threshold value of critical stress intensity factor (K_{IC}), where K_{IC} is considered a material fracture parameter. This can also be expressed in terms of fracture energy:

$$G = G_{IC} \qquad \textbf{(Equation 7.7)}$$

where, $G = (K_I)^2/E'$ is the rate of strain energy release, and $G_{IC} = (K_{IC})^2/E'$ is the critical rate of strain energy release, where E' = E (Young's Modulus) for the plane stress condition, $E' = E/(1 - U^2)$ for the plane strain condition, and U is Poisson's ratio.

The cementitious material used for the overlay layer in the current study is HPFRCC with strain hardening behavior as will be illustrated later in the Results and Discussion section. Thus, when considering the fiber-crack interactions using fracture mechanics concepts, distinctive processes need to be considered. Romualdi and Batson [1963] were the first to use linear elastic fracture mechanics concepts to analyze the crack suppression mechanics in a cementitious matrix induced by the fibers' presence. Upon initiation of cracks, the matrix tends to deform more than the fibers, owing to the stress concentration just ahead of the tip of the crack (process zone), where the fibers counteract such tendency. Through interfacial shear bond stresses, fibers apply pinching forces, which reduce K_I. Accordingly, higher stresses are required to generate a stress field ahead of the tip of the crack, where the maximum stress exceeds K_{IC} of the cementitious matrix. The concept of fictitious crack model has been adopted and modified by Hillerborg [1980] to

describe fiber reinforced cement-based materials. The main parameter in this model is the crack bridging function that describes the stress change (σω) over the range of (ω), which is the crack opening up to 2 mm. These concepts were applied in a number of studies [Li *et al.*, 1993] that aimed to identify the conditions needed to exhibit strain hardening or quasi-plastic behavior, which are also described as steady-state cracking behavior. The characteristic σ–ω curve for discrete fibers with random distribution was modelled through averaging the contribution of individual fibers that cross the cracking plan in the matrix [Li, 1992], as for example expressed by **Equation 7.8**:

$$\sigma(\delta) \begin{cases} = \sigma_{cu}\left[\left(2\delta/\delta_p\right)^{\frac{1}{2}} - \left(\frac{\delta}{\delta_p}\right)\right]; \; for \; \delta \le \delta_p \\ = \sigma_{cu}(1 - 2\delta/L_f)^2 \; ; \quad for \; \delta_p \le \delta \le L_f/2 \\ = 0 \quad ; \quad for \; L_f/2 \le \delta \end{cases} \qquad \textbf{(Equation 7.8)}$$

where, (σ_{cu}) is the maximum bridging stresses that can be supported by the fibers, (δ_p) is the crack opening after which a decline in the stress may take place, (δ) is the crack opening, and L_f is the fiber length.

7.4.2 Numerical Simulation of the Bonded Overlay Assembly

3-D finite element models (FEM) were developed to describe the flexural behavior of the overlay assemblies and enable a parametric study for the effect of overlay thickness and parent concrete strength. The analysis package ANSYS 19.2 Workbench platform [2020] was used for this purpose. The models were governed by the properties of the materials tested, full bonding assumption between the two layers, and free span configuration with no supports in the middle and rigid supports at the ends.

SOLID185 eight-node 3D solid element was used to model the overlay/cementitious composite layer (**Figure 7.3**). The element has three degrees of freedom at each node. Each node has translation freedom degree in the nodal x, y, and z directions. The element supports plasticity, hyperelasticity, creep, stress stiffening, large deflection, and large strain capabilities. SOLID65 eight-node 3D solid element was used to model the substrate concrete layer (**Figure 7.3**). The element has three degrees of freedom at each node in the nodal x, y, and z directions. The element is capable of simulating cracking in tension and crushing in compression as in concrete.

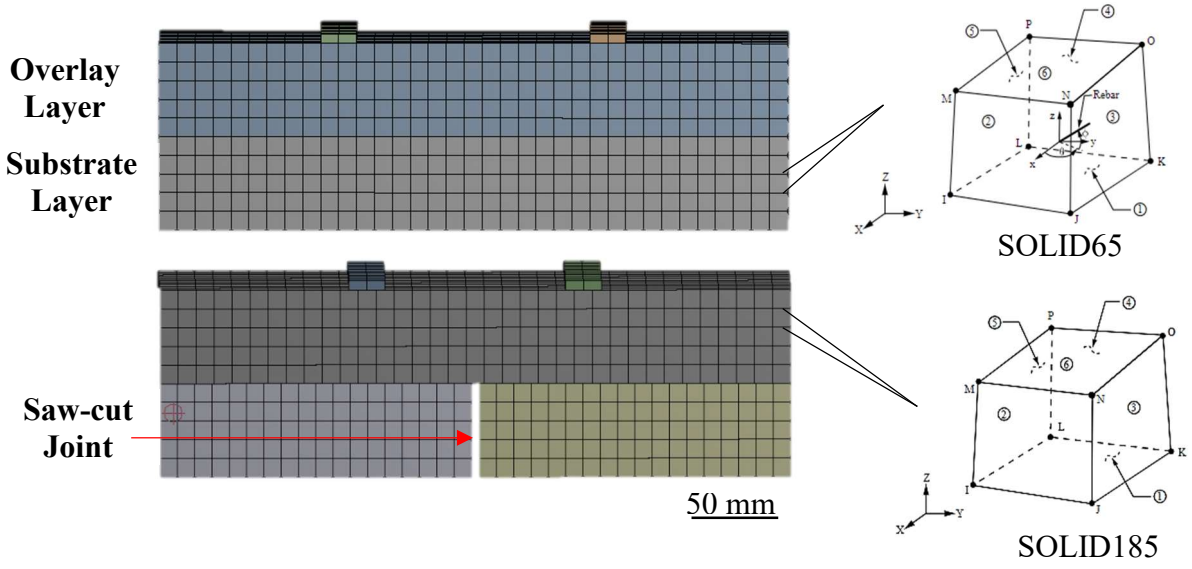

Figure 7.3: Finite element representation of the overlay assemblies.

The mechanics of contact between the two layers involve normal as well as tangential contact stiffness. The normal contact stiffness governs the penetration between the two surfaces. The model estimates the normal contact stiffness between two surfaces according to the materials' properties input, and it can be refined based on experimental values. The tangential stiffness controls the slip between contact surfaces relative to each other and it is proportional to the contact stiffness and the coefficient of friction. The

friction scheme is dependent upon Coulomb's friction, where sliding occurs when shear stress exceeds the resistance to sliding (τ) expressed as follows:

$$\tau = \mu p + c \qquad \textbf{(Equation 7.9)}$$

where, (μ) is the friction coefficient, (p) is the normal contact pressure, and (c) is the two layers' cohesion sliding resistance. The bonded model was selected in the current study for investigating the behavior of the overlay systems, as the experimental trends of this study revealed fully bonded condition of the overlay systems. This feature is convenient for modeling different cases of surface interaction without having to manually change interface spring stiffness values as in previous studies [e.g. Wu *et al*. 1998].

The input parameters for the composites and concrete properties including compressive strength, tensile strength and modulus of elasticity needed to create the FEM were obtained by testing the individual materials. Poisson's ratio was assumed as 0.18 for the substrate concrete and 0.2 for the cementitious composites according to the strength and young's modulus of each material [Mehta and Monteiro, 2014]. A linear curve was used to express the flexural behavior of normal concrete for the substrate layer, while a multilinear curve was adopted in the numerical model in order to approximate the experimental results of the cementitious composites used as the overlay layer.

7.5 Results and Discussion

7.5.1 Experimental

7.5.1.1 Mechanical Properties of Composites

The average compressive strength at different ages and flexural performance parameters of the cementitious composites are listed in **Table 7.2**. Blended binders comprising high-

volume SCM (Type F fly ash "slowly reactive pozzolan" or slag "latent hydraulic binder") have slow rates of strength gain and microstructural development at early-age, but their reactivity enhance with time [Mehta and Monteiro, 2014]. Hence, most codes and standards for concrete [e.g. CSA-A23.1/A23.2, 2019] require testing of concrete incorporating fly ash/slag at 56 or 91 days. The results obtained herein showed that the compressive strength of both composites at early-age was high (more than 30 and 40 MPa at three and seven days, respectively), due to nano-modification, high binder content and low *w/b*.

Table 7.2: Mechanical properties of the composites

	N-F-4.5	**N-G-4.5**
Compressive strength (MPa)		
3 days	36.7 (0.8)	58.9 (1.5)
7 days	44.4 (1.1)	65.5 (1.8)
28 days	49.6 (1.4)	69.8 (2.3)
56 days	54.8 (2.1)	71.3 (3.2)
Flexural performance		
First-cracking strength (MPa)	5.1 (0.5)	6.1 (0.6)
Residual strength at *l/600* (MPa)	6.3 (0.8)	7.8 (1.0)
Residual strength at *l/150* (MPa)	7.3 (0.9)	8.5 (1.1)
Toughness (J)	45.8 (3.8)	54.7 (4.3)

Note: Numbers in parentheses indicate standard deviations.

The ultrafine nature of NS (80,000 m2/kg) boosted the hydration of cement through providing extra surfaces for early precipitation of hydration products (nucleation effect) [Kong *et al.*, 2012]. The NS sol (initially dispersed to the nano-size) were found to form silica-agglomerates with multi-scale filling effect at the nano- and micro-ranges in the cementitious matrix [Oertel *et al.*, 2013]. Kong *et al.* [2012] reported that free water could be entrapped in the nano-porosity of the NS agglomerates, hence decreasing the paste w/b and in turn densifying the cementitious matrix. The chemical activity of nano-silica was detected by TGA (**Table 7.3**). The decrease of calcium hydroxide (CH) contents in the

nano-modified fly ash (N-F) and slag (N-G) binders, commenced at early-age, despite the high content (50%) of SCM. The normalized CH contents at three days for the nano-modified binders (N-F and N-G) were 0.75 and 0.64, respectively relative to their reference binders without NS, while it was 0.64 and 0.52, respectively at seven days. Significant consumption of CH during the early-age period indicated a vigorous pozzolanic activity of NS in the binders resulting in additional precipitation of calcium silicate hydrate (C-S-H) gel in the matrix, hence enhancing microstructural development and strength gain.

Table 7.3: Thermal analysis (TGA) of the binders

Calcium hydroxide content (%)	**Time (Days)**			
	3	**7**	**28**	**56**
F	7.92	8.31	7.96	7.23
G	7.64	8.26	7.82	7.02
N-F	5.95	5.35	4.85	4.37
N-G	4.92	4.32	3.84	3.31
Relative comparison	**Normalized calcium hydroxide content**			
N-F/F	0.75	0.64	0.61	0.60
N-G/G	0.64	0.52	0.49	0.47
N-G/N-F	0.83	0.80	0.79	0.75

Note: Precision of measurement is ± 0.20%.

The composites continued gaining later-age compressive strengths, though at lower rates, and N-F-4.5 and N-G-4.5 had compressive strengths of 55 and 71 MPa, respectively, at 56 days (**Table 7.2**). This complies with the slower CH depletion rates that were noted for the nano-modified binders between 28 to 56 days (marginal reduction in the normalized CH contents, **Table 7.3**). Thus, the slower later-age strength gain for the composites could be ascribed to the long-term reactivity of fly ash and slag as well as filling effect of NS particles. Moreover, the first-cracking flexural strength of N-F-4.5 and N-G-4.5 were 5.1 MPa and 6.1 MPa, respectively, at 56 days. These strengths exceeded the minimum required flexural strength (4.5 MPa) for cement-based overlays stipulated by most

transportation agencies [ACI 325.13R, 2006]. The obtained ranges for compressive and first-cracking flexural strengths at later ages highlight the adequacy of these composites for high-strength overlay applications [e.g. ACI 325.13R, 2006; Wilson *et al.*, 1999].

The slag-based composite, N-G-4.5, had higher mechanical properties relative to that of its fly ash-based counterpart (**Table 7.2** and **Figure 7.4**). For instance, the compressive strength of N-G-4.5 at 3, 7, 28, and 56 days were 60%, 48%, 41%, and 30%, respectively higher than that of N-F-4.5. This can be ascribed to the higher reactivity of slag (higher fineness [492 kg/m^2] and lime (CaO) [43%]; latent hydraulic binder) relative to fly ash (lower fineness [290 kg/m^2] and CaO content [approximately 11%], slow reactive pozzolan), which improved the level of maturity for the slag-based binder and correspondingly its mechanical properties.

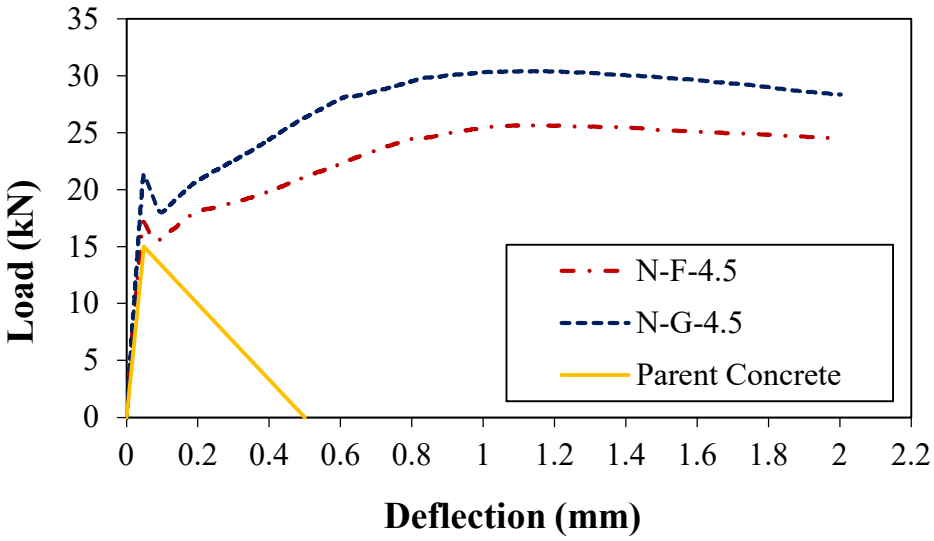

Figure 7.4: Load-deflection (P-δ) curves for the cementitious composites and normal (substrate) concrete.

This was corroborated by the TGA results as the normalized CH contents of N-G/N-F at different ages were consistently less than 1.0, reflecting the catalyzed reactivity of NS with the slag-based binder relative to the fly ash-based binder, and in turn the

formation of more secondary/pozzolanic C-S-H gel. The enhanced reactivity of the slag-based composite led to higher quality of ITZ (interfacial transition zone) between the matrix and the pellets (**Figure 7.5**), and consequently better interfacial bonding strength. Accordingly, the average calcium to silicate ratio (Ca/Si) of the matrix at the ITZ with BFP in the slag-based composite (N-G-4.5) was 1.16 compared to 1.37 in the fly ash-based corresponding mixture, which substantiated the higher efficiency and accelerated reactivity of the slag-based binder. Ca/Si of C-S-H gel from pozzolanic reactions tends to 1.1, while primary C-S-H generated from the normal hydration reactions of the cement tends to 1.7 [Detwiler *et al*., 1996].

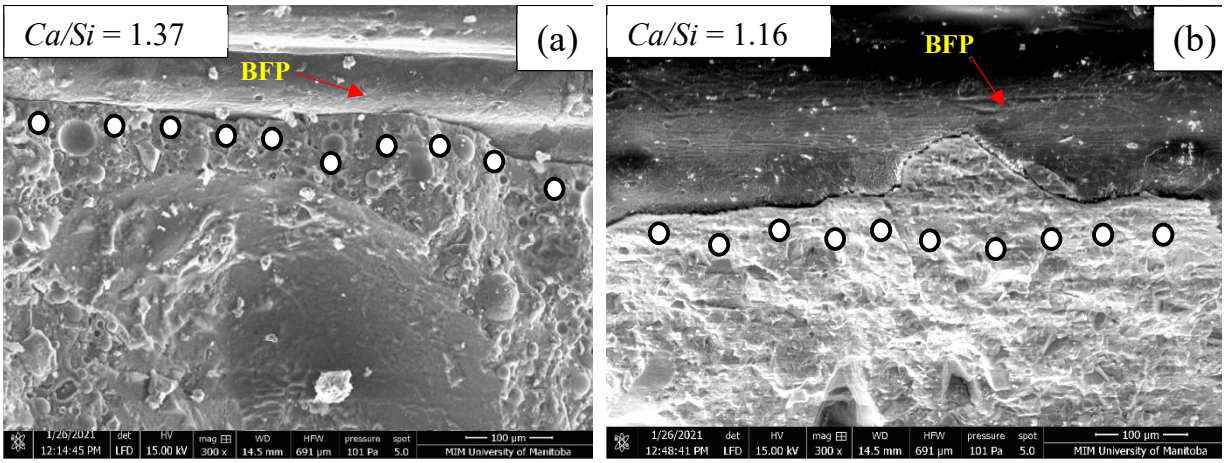

Figure 7.5: Exemplar SEM micrographs for the nano-modified composites at 56 days showing ITZ with BFP in: (a) N-F-2.5, and (b) N-G-2.5. (Note: *Ca/Si* value is the average for the EDX analysis at marked locations).

The cementitious composites showed high ductility, owing to the surface tailored microgrooves in the longitudinal direction of the pellets, which imparted an interlocking effect between the pellets and the matrix. Furthermore, the pellets surface microgrooves increased the contact surface with the matrix and provided host locations for deposition of extra hydration products (**Figure 7.6**). Accordingly, a higher pullout resistance of the BFP

from the matrix was achieved, which is the primary toughening mechanism responsible for enhancing the ductility of the composites. The composites showed strain hardening behavior after first-cracking, and they showed enhanced post-cracking flexural performance in terms of toughness and residual strength at deflections *l/600* (0.5 mm) and *l/150* (2 mm) as presented in **Figure 7.4** and **Table 7.2**. The toughness of the composites N-F-4.5 and N-G-4.5 was 45.8 J and 54.7 J, respectively, while the residual strength at *l/150* was 7.3 MPa and 8.5 MPa, respectively.

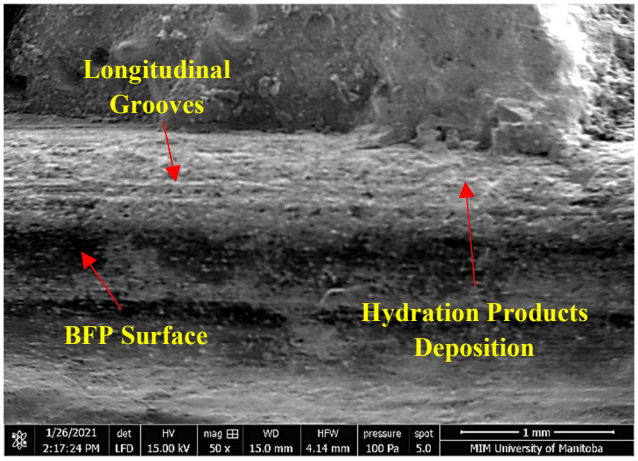

Figure 7.6: Exemplar SEM micrograph for the surface morphology of BFP in N-G-4.5.

These results fulfil target requirements for overlay systems comprising fiber-reinforced cementitious materials, which stipulate a residual strength of at least 0.7 MPa at deflection *l/150* (according to the binder content/formulation and the fiber content/type/size) [e.g. Barman and Hansen, 2018]. The improved pellet/matrix interfacial bonding with abundance of BFP in the matrix resulted in efficiently bridging initiated cracks and restraining their propagation. This may allude to the adequacy of the composites to be implemented in high-performance overlay applications with thinner cross sections

and/or longer joint spacing to control differential movements from shrinkage, heavy loads, and curling/warping.

7.5.1.2 Performance of Overlay Assemblies

7.5.1.2.1 Intact substrate

The load-deflection curves and flexural performance parameters of N-F-4.5 and N-G-4.5 overlay assemblies with intact substrate as well as parent concrete (reference) specimens are presented in **Figure 7.7** and **Table 7.4**. The overlay systems had comparable first-cracking flexural strength (4.5 to 5.1 MPa) to that of reference concrete (4.5 MPa). However, the overlay specimens had superior post-cracking performance owing to the incorporation of BFP in the composites. For instance, the toughness at the test deflection limit of 2 mm for the overlay assemblies N-F-4.5 and N-G-4.5 were 324% and 471%, respectively, higher than that of the reference concrete specimens.

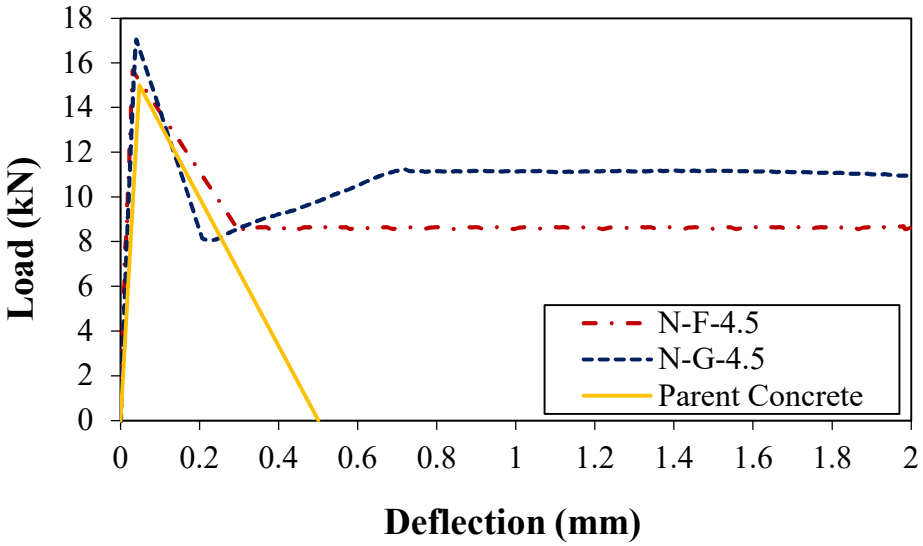

Figure 7.7: Load-deflection (P-δ) curves for the overlay assemblies with intact concrete substrate.

The comparable first-cracking flexural strength of all specimens was ascribed to the fact that the parent/reference concrete in all specimens was located at the tension side of the specimens (bottom layer) exposed to the maximum tensile stresses, and thus firs-cracking. Cracks in the parent concrete layer propagated and reflected into the overlay, regardless of the type of the binder (fly ash or slag), but the growth of cracks was controlled by BFP. This mode of failure indicated intact bonding between the parent concrete and overlay layers with no visible signs of delamination between the two layers, as the initiated crack in the bottom layer (parent concrete) did not diverge transversely at the interface between the two layers exhibiting a monolithic behavior of the system (**Figure 7.8**).

Table 7.4: Experimental and modeling flexural performance results for the overlay assemblies

Flexural parameters	Experimental values		FEM values		Error (%)	
	N-F-4.5	**N-G-4.5**	**N-F-4.5**	**N-G-4.5**	**N-F-4.5**	**N-G-4.5**
Intact substrate						
First-cracking strength (MPa)	4.7 (0.6)	5.1 (0.4)	4.9	5.3	4.0	3.9
Residual strength at *l/150* (MPa)	2.6 (0.2)	3.3 (0.3)	2.7	3.6	3.8	9.0
Toughness (J)	18.1 (1.8)	21.7 (2.2)	19.9	23.8	9.9	9.6
Pre-cracked substrate						
First-cracking strength (MPa)	5.2 (0.4)	6.3 (0.9)	5.3	6.4	1.9	1.6
Residual strength at *l/150* (MPa)	7.4 (0.7)	9.3 (1.2	8.1	9.7	9.4	4.3
Toughness (J)	11.6 (1.4)	15.9 (1.7)	12.7	17.1	9.5	7.5

Notes: [1] The strength values of the cracked substrate specimens are calculated based on the depth of the overlay layer (50) mm above the joint location.
[2] Numbers in parentheses indicate standard deviations.

The high ductility of the composite layer, owing the incorporation of 4.5% BFP, alluded to the efficacy of pellets in restraining the propagation of the reflected cracks from

the substrate layer. Once cracks were reflected into the overlay (N-F-4.5 or N-G-4.5 composites), a sudden drop occurred in the load carrying capacity of the specimens. Subsequently, the pellets were engaged in resisting the induced stresses from flexural loading at the failure plane through efficient bonding of the pellets with the matrix, as shown by the microstructural features (**Figure 7.6**) discussed in the preceding section. This resulted in the obtained ductile behavior of both overlay systems, originating from the pellets' pull out process, as indicated by the steady-state load-deflection plateau for both cementitious composites in the overlay systems during the post-cracking phase (**Figure 7.7**). This highlighted the capability of the cementitious composite/overlay layer to restrain and control the reflected cracks from the substrate layer, without causing an abrupt brittle failure of the entire system.

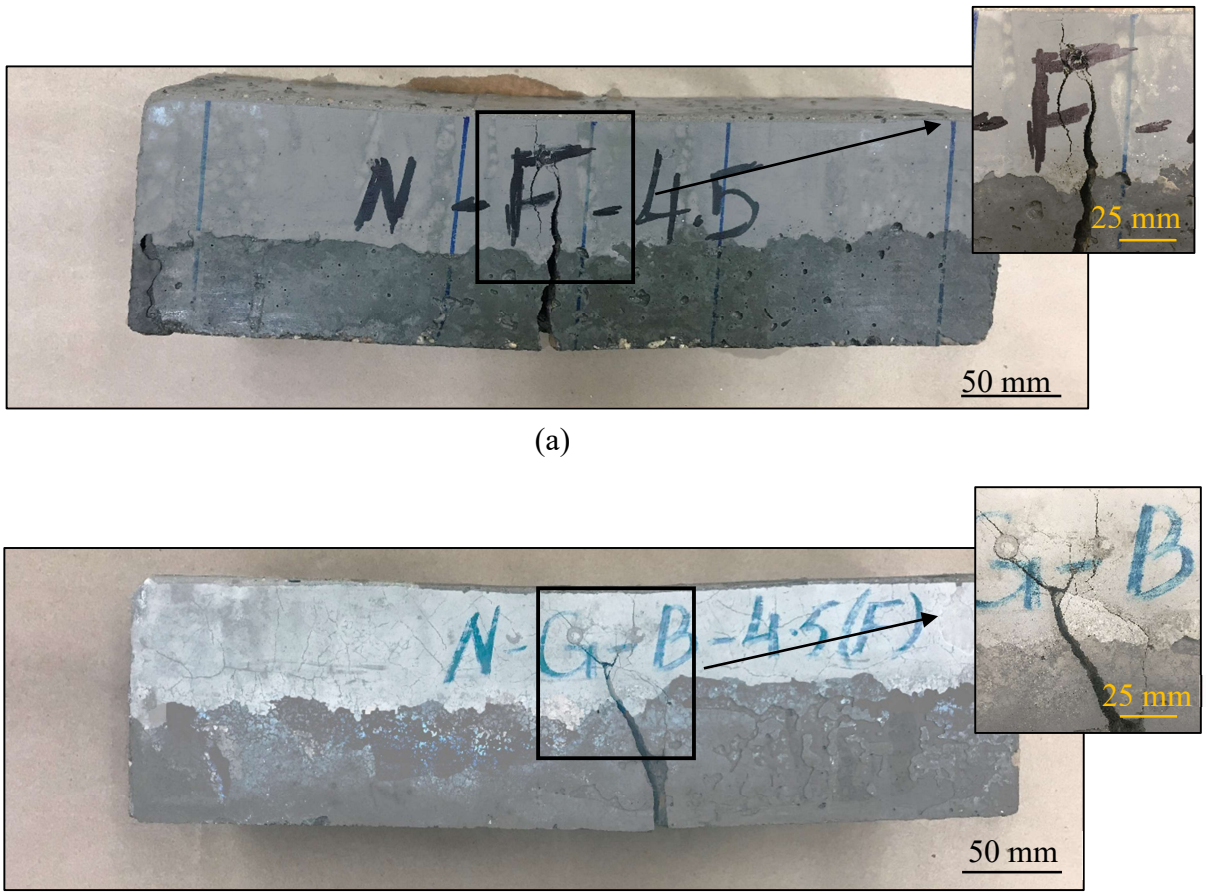

Figure 7.8: Crack propagations in the overlay assembly with intact concrete substrate after the flexural test: (a) N-F-4.5, and (b) N-G-4.5.

Although the 50 mm cementitious composite overlay could not restore the full load capacity of the system compared to the 100 mm prisms, the 4.5% BFP dosage ensured that an adequate volume of pellets existed across failure planes, which was effective to restrain the growth of reflective cracks without brittle failure of the assembly. The difference in the load carrying capacity, and thus flexural parameters, between the overlay assemblies and full cementitious composite prisms could be ascribed to the smaller amount/number of pellets available at the cracking plane in the former. According to the fiber spacing theory [Romualdi and Mandel, 1964], as the cracks grow in the cementitious matrix and reach the fibers/matrix interface zone, a stress field is generated restraining further propagation of

the crack via fibers' bridging action that alleviate the stress concentration at the crack's tip proximity. More cracks are commenced as the deformation increases, producing more internal energy to resist the external energy exerted on the system. Thereby, the selected pellets dosage facilitated the initiation of more internal cracking to increase of the energy absorption level (toughness), which was evident by the post-cracking load deflection behavior.

The slag-based overlay system had improved post-cracking flexural performance relative to the fly ash-based overlay assembly. For example, the toughness of (N-G-4.5) assembly was 20% higher than that of the fly ash-based overlay system (N-F-4.5), which was 18.1 J. Moreover, the residual strength of the slag-based overlay system at l/600 and l/150 was 15% and 27%, respectively higher than that of the fly ash-based corresponding specimens. This was attributed to the faster reactivity of slag relative to fly ash, and hence the higher degree of maturity of the cementitious matrix and bonding with pellets (**Figure 7.5**), which was substantiated by TGA (**Table 7.3**). This led to more efficient control of cracking in the slag-based matrix and higher resistance to pullout of the pellets, which are the key toughening mechanisms responsible for improving the ductility of the cementitious composites and in turn the entire overlay system. However, the results revealed the adequacy of both composites as a viable option for bonded overlay systems, owing to their monolithic behavior/compatibility with the normal concrete substrate used and achieved ductility (residual strength and toughness).

7.5.1.2.2 Pre-cracked substrate

The failure happened for the assemblies with pre-cracked substrate in the top (cementitious composite) layer over the joint part in the parent concrete with no signs of cracking in the

substrate layer, even in the vicinity of the joint (**Figure 7.9)**. Similar to the overlay assembly with intact substrate layer, no transverse delamination occurred between the two layers, since the stress build up at the interface, even at the critical joint zone, did not exceed the bonding strength between the two layers. This highlighted efficient bonding between the two layers verifying the monolithic behavior of the system. The mode of failure of the pre-cracked assembly indicated that the performance of the system was governed by the properties of the overlay/composite layer with minimal contribution of the substrate layer. Thus, all the strengths (first-cracking strength and residual strengths) were calculated based on the top layer (50 mm) [**Table 7.4]**.

The first-cracking and residual strengths of these assemblies were comparable to the first-cracking strength of the full cementitious composite prisms (**Table 7.2**), with small variations due to the size effect between thickness of the composite (50 mm) in the overlay assembly and full prism (100 mm), where there was less likelihood of flaws (weak links) in the smaller volume. For instance, the residual strengths of the fly ash-based overlay assembly with pre-cracked substrate at deflections *l/600* and *l/150* were 8% and 1%, respectively higher than that of the corresponding N-F-4.5 full prism specimens. Similarly, the residual strengths of the slag-based overlay assembly with pre-cracked substrate at deflections *l/600* and *l/150* were 5% and 9%, respectively, higher than that of the N-G-4.5 full prism specimens. This indicated that the 50 mm thickness was sufficient for the fly ash- and slag-based overlay composites for achieving improved post-cracking residual strengths (deflection-hardening process), matching the trends of full depth prisms of the composites.

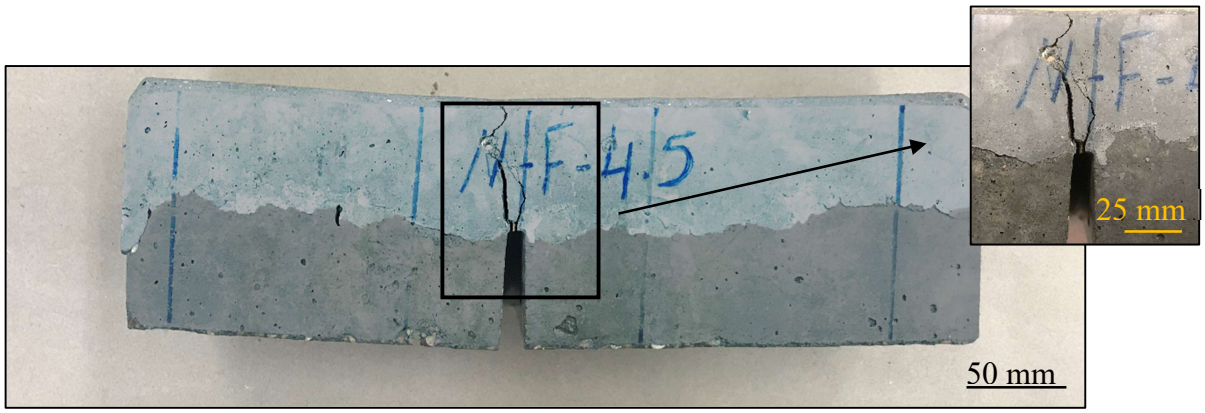

(a)

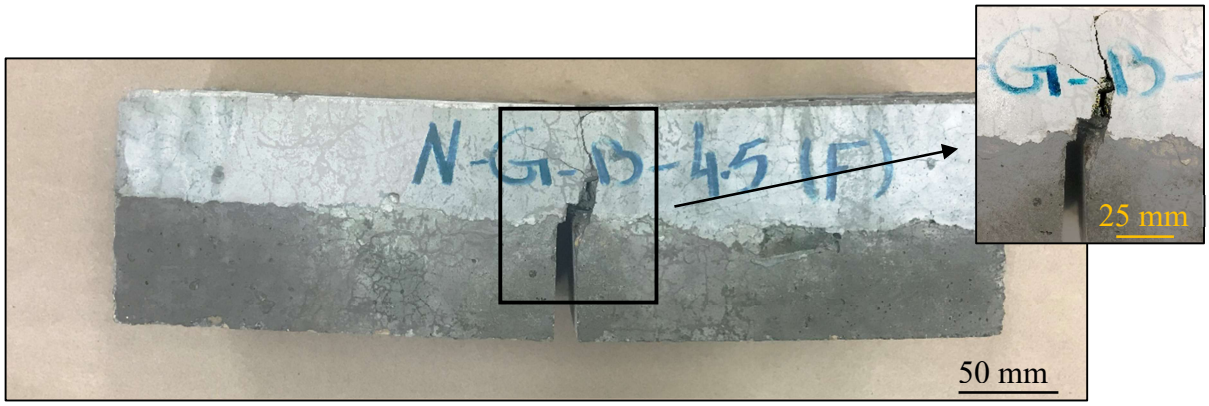

(b)

Figure 7.9: Crack propagations in the pre-cracked overlay assembly after the flexural test: (a) N-F-4.5, and (b) N-G-4.5.

Comparatively, the overlay assemblies showed prominently reduced toughness compared with the full prism composites specimens (**Figure 7.10** vs. **Figure 7.4**). For example, N-F-4.5 and N-G-4.5 overlay assemblies had toughness of 74% and 71% lower than that of their full prism cementitious composites counterparts. This drastic reduction of the toughness could be ascribed to the fact that the overlay layer (50 mm) is the effective fraction in the cracked assemblies that is responsible for the flexural performance and in turn the toughness of the system (**Figure 7.9**). In the full prism composites, the thickness of the specimens responsible for the flexural performance including the toughness is the

entire 100 mm, which provided more materials (matrix and pellets) to dissipate higher energy through the failure process. Similarly, the pre-cracked overlay assemblies showed significant reduction of toughness relative to the corresponding intact assemblies (**Figure 7.10** vs. **Figure 7.7**). For example, N-F-4.5 and N-G-4.5 pre-cracked overlay assemblies had 36% and 27% less toughness compared to their intact overlay assemblies counterparts. This reduction of the toughness could be alluded to the larger effective cross-section of the intact overlay assembly that resulted in higher load carrying capacity of the assembly compared with the pre-cracked corresponding assemblies, which in turn reflected on the toughness of the system.

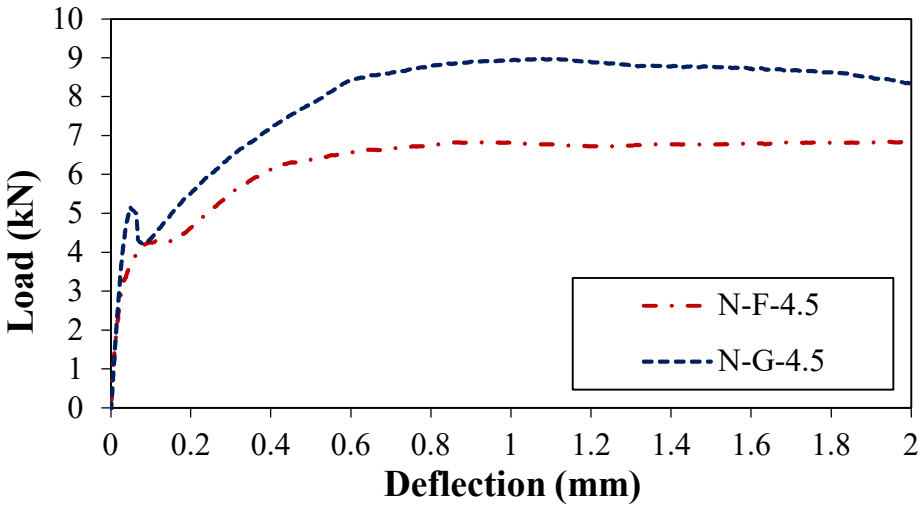

Figure 7.10: Load-deflection (P-δ) curves for the overlay assemblies with pre-cracked concrete substrate.

As aforementioned, the slag-based overlay system had improved performance relative to the fly-ash based counterpart, owing to the finer particle size as well as enhanced reactivity of the slag relative to fly ash, particularly with the coexistence of NS as previously discussed. Nevertheless, the introduced composites (N-F-4.5 and N-G-4.5) showed high potential to be implemented in overlay systems exhibiting controlled cracking and monolithic performance with the parent concrete, even in the presence of some

deficiencies in the substrate layer or at locations of joints mismatch between the substrate and the topping layer.

7.5.2 Finite Element Modeling

7.5.2.1 Models' Accuracy

The accuracy of models developed for both overlay systems (N-F-4.5 and N-G-4.5) in the conditions tested (intact and pre-cracked substrate layer) was verified versus the experimental results. The main flexural performance parameters calculated from the models versus the corresponding experimental results are listed in **Table 7.4,** and the cracking pattern in both overlay systems under the conditions tested is shown in **Figure 7.11**.

Similar to the experimental trends, the FEM results showed that the first-cracking flexural strength of the intact substrate assembly, were governed by the capacity of parent concrete (average of 5.1 MPa). Subsequently, there was a drop in the load carrying capacity due to stress transfer between the two layers and upward crack propagation in the composite layer (**Figure 7.11**). Correspondingly, the residual strength of N-F-4.5 and N-G-4.5 assemblies reached 2.7 and 3.6 MPa, respectively, and the toughness was 19.9 and 23.8 J, respectively, owing to ductility of the composites. In the pre-cracked assembly, the overlay/composite layer was primarily responsible for resisting the load over the joint configuration with nil contribution from the substrate-cracked layer.

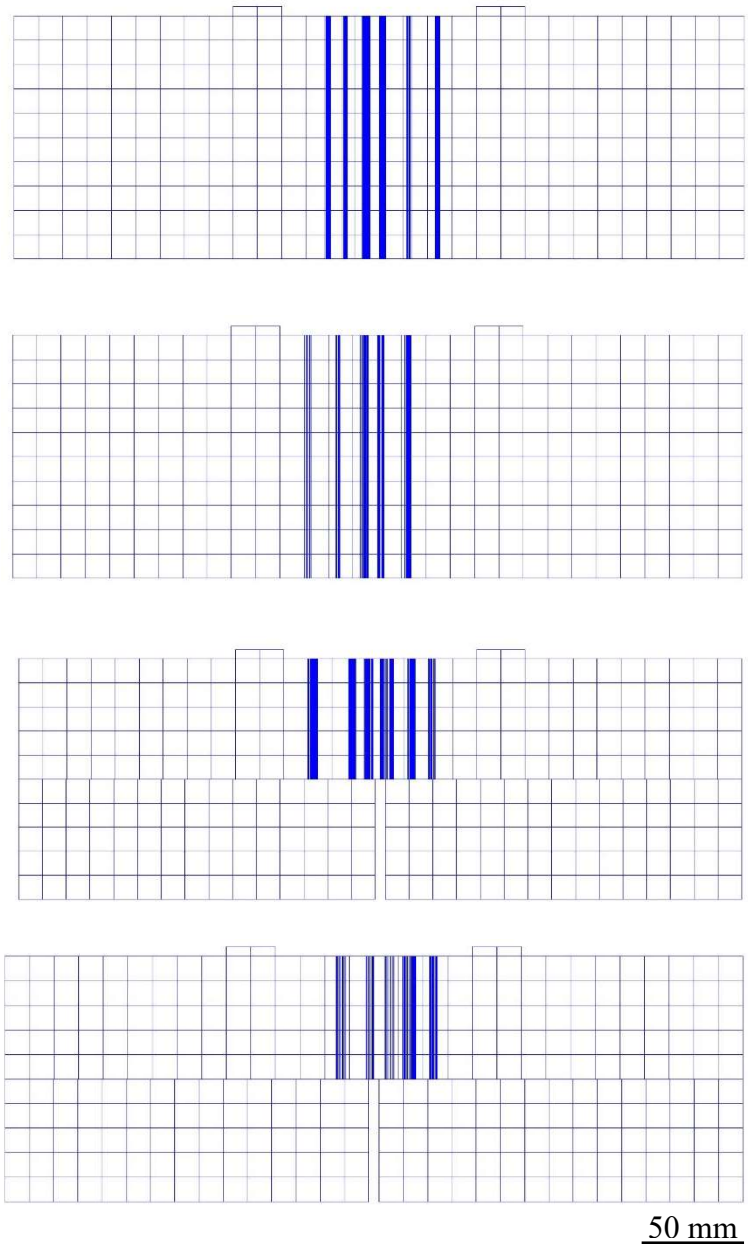

Figure 7.11: Schematic diagrams from the FE models showing the crack patterns and location for the different overlay systems tested.

The failure happened in the top layer over the pre-induced crack with no delamination at the interface (**Figure 7.11)** showing similar strain hardening behaviour (residual strength of 8.1 and 9.7 MPa) to the full cementitious composite prism, but with lower toughness (12.7 and 15.9 J) values due to reduction of the composite thickness (50

mm). All the flexural performance parameters from the models for the slag-based composite were higher than that of the corresponding values for the fly-ash based counterparts, due to the finer particles and higher reactivity of slag relative to fly ash especially with the coexistence of NS. The numerical results revealed that the models were reliable and reasonably accurate in simulating the experimental behaviour, and the error among all numerical and experimental parameters did not exceed 10% (**Table 7.4**). Hence, the models were used to perform parametric analysis.

7.5.2.2 Parametric Analysis

7.5.2.2.1 Effect of overlay thickness

The effect of changing the thickness of the overlay layer (40 to 100 mm) was examined, at a fixed substrate thickness (50 mm), using the developed FEM for both overlay systems with intact and pre-cracked substrate layer (**Figures 7.12** and **7.13**). In addition, the corresponding flexural parameters of both systems (first-cracking flexural strength, residual strength at *l/150*, and toughness) were calculated and listed in **Table 7.5**. As anticipated, the load carrying capacity of the assembly increased with the thickness of the overlay layer, regardless of the type of binder (fly ash or slag) or substrate condition (intact or pre-cracked) [**Figures 7.12** and **7.13**], where the cracking for all overlay thicknesses proceeded from bottom to top as obtained in the experimental results and model verification.

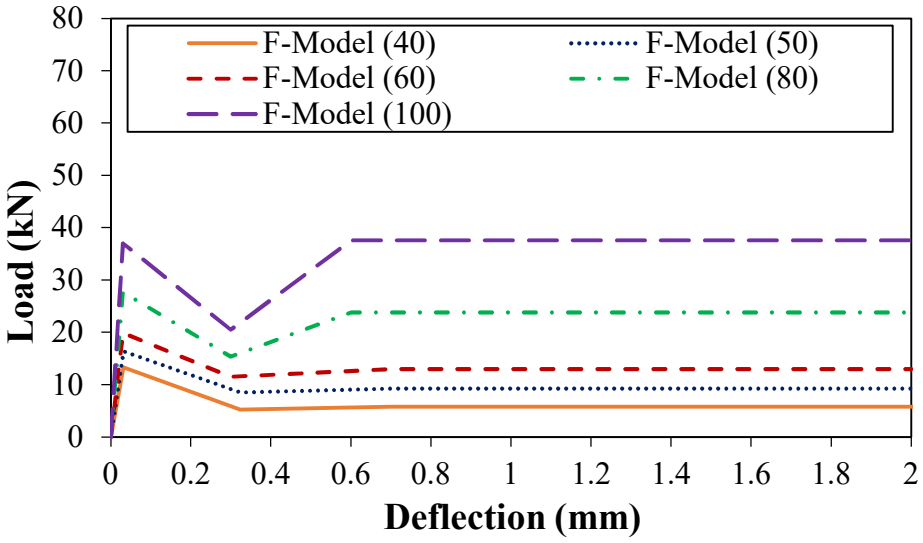

(a)

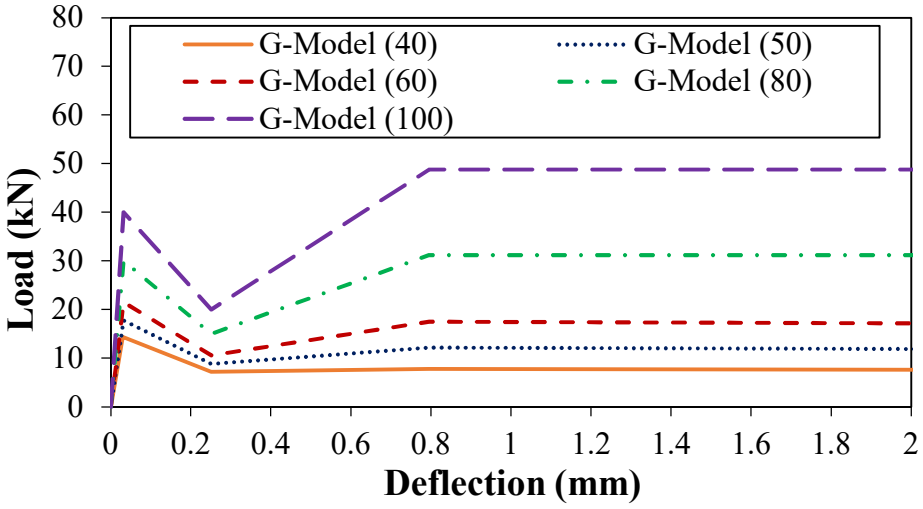

(b)

Figure 7.12: Load-deflection (P-δ) curves for the assemblies with different overlay thicknesses and intact concrete substrate: (a) N-F-4.5, and (b) N-G-4.5. (Notes: F = N-F-4.5; G = N-G-4.5; the number between parentheses is the overlay thickness in mm).

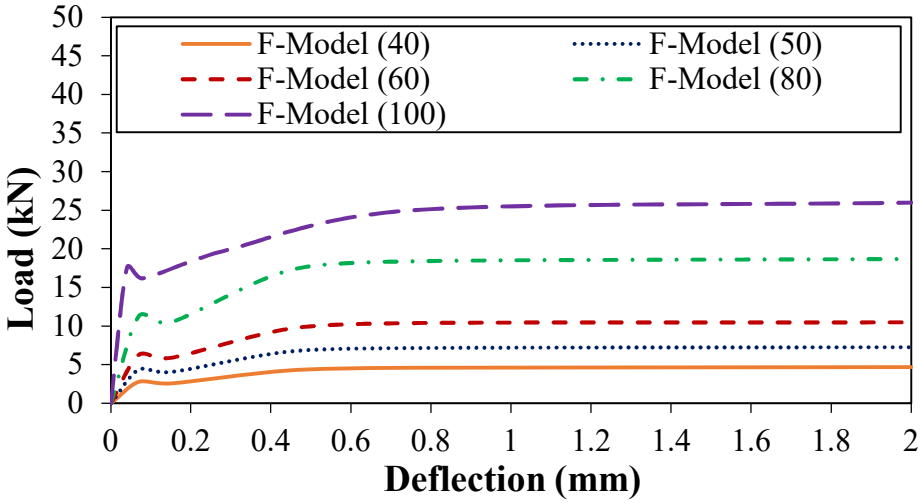

(a)

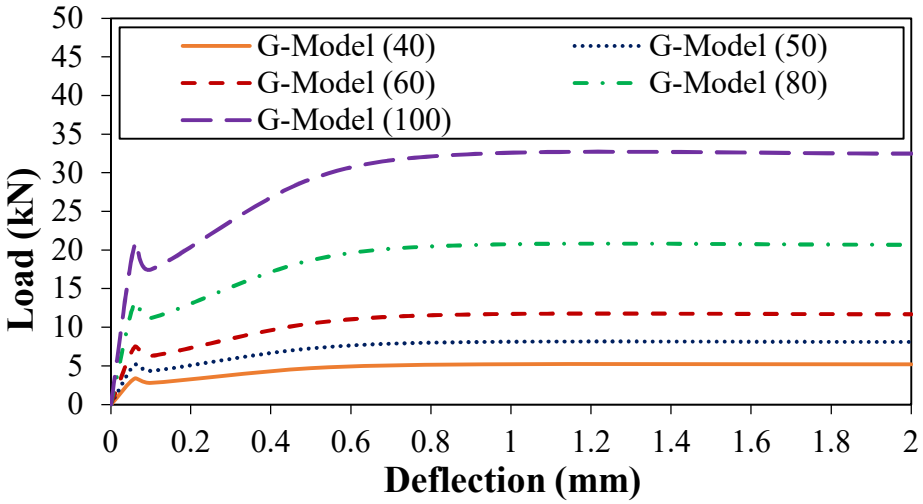

(b)

Figure 7.13: Load-deflection (P-δ) curves for the assemblies with different overlay thicknesses and pre-cracked concrete substrate: (a) N-F-4.5, and (b) N-G-4.5. (Notes: F = N-F-4.5; G = N-G-4.5; the number between parentheses is the overlay thickness in mm).

Table 7.5: Flexural parameters of the overlay assemblies from the FEM parametric analysis

	Intact						Pre-cracked					
	N-F-4.5			N-G-4.5			N-F-4.5			N-G-4.5		
	First-cracking strength (MPa)	Residual strength at *l/150* (MPa)	Toughness (J)	First-cracking strength (MPa)	Residual strength at *l/150* (MPa)	Toughness (J)	First-cracking strength (MPa)	Residual strength at *l/150* (MPa)	Toughness (J)	First-cracking strength (MPa)	Residual strength at *l/150* (MPa)	Toughness (J)
Overlay thickness (mm)												
40	4.7	2.2	13.5	5.1	2.8	17.3	5.2	8.8	8.5	6.2	9.7	9.4
50	4.9	2.7	19.9	5.3	3.6	23.8	5.3	8.8	13.2	6.2	9.7	14.6
60	5.0	3.2	26.3	5.4	4.2	35.6	5.3	8.8	19.1	6.3	9.8	21.0
80	5.2	4.2	45.4	5.7	5.5	61.2	5.3	8.8	34.0	6.3	9.8	37.5
100	5.5	5.0	69.6	6.0	6.5	93.5	5.4	8.8	47.3	6.4	9.8	58.9
Substrate compressive Strength (MPa)												
30	3.8	2.6	19.1	4.0	3.5	23.0	5.1	8.8	13.1	6.0	9.7	14.6
40	4.9	2.7	19.9	5.3	3.6	23.8	5.3	8.8	13.2	6.2	9.7	14.6
50	6.1	2.7	21.4	6.7	3.6	24.8	5.5	8.8	13.2	6.5	9.8	14.7

Note: The strength values of the pre-cracked substrate specimens are calculated based on the depth of the overlay layer above the joint location.

Regarding the assemblies with the intact substrate layer, increasing the overlay thickness did not significantly affect the first-cracking strength of the prisms, while it remarkably affected the ductility of the system. For instance, the increase of the overlay thickness from 50 to 60 mm increased the first-cracking flexural strength for N-F-4.5 and N-G-4.5 by approximately 2%, while it increased the residual strength by 18% and 16% and the toughness by 32% and 50%, respectively. The marginal increase of the first-cracking strength was attributed to the fact that increasing the thickness shifted the neutral axis of the cross-section upward, which would involve more cementitious composite material of the overlay layer (relatively higher strength with respect to the parent concrete) contributing to the flexural capacity of the section. After first-cracking of the assembly, the systematic increase in residual strength (considering the entire cross section of the assembly) and toughness (**Table 7.5**) can be linked to the increase of the ductile material (cementitious composite) portion in the cross-section of the overlay system with increasing the thickness of the topping layer, comprising BFP. Thus, increasing the number of ductile elements would shift the behavior of the assembly towards the behavior of full cementitious composite prisms with significantly improved ductility in terms of residual strength and toughness.

Similar to the experimental trends, the failure of the pre-cracked assemblies took place in the overlay layer above the jointed zone in the substrate concrete layer indicating the dominant role of the overlay/composite layer for depicting the deflection-hardening behavior of the assembly (**Figure 7.13**). Although the first-cracking strength and residual strength of the pre-cracked assemblies are similar to that of the full cementitious composite prisms (as previously discussed), the toughness of the pre-cracked assembly was less (25-46%) than that of the corresponding intact assembly with the same overlay thickness. This

is attributed to the reduction of the load carrying capacity of the assembly in the pre-cracked zone (**Figure 7.13** vs. **Figure 7.12**). Increasing the overlay thickness had marginal influence on the strengths (first-cracking strength and residual strength at *l/150*) of the fly ash- and slag-based composites. Considering the effective cross section of the composite resisting normal tensile stresses (area of the cementitious composite section above the joint), these values remained constant (**Table 7.5**). However, the increase of the topping layer thickness increased the toughness of the composite. For example, the toughness of the fly ash and slag-based overlay systems in the pre-cracked assembly was increased by 45% and 44%, respectively with increasing the thickness of the overlay layer from 50 mm to 60 mm. This could be ascribed to increasing the load carrying capacity of the composite layer and hence the area under load deflection curves (**Figure 7.13**).

7.5.2.2.2 Effect of substrate compressive strength

The influence of variation of compressive strength of the substrate layer, at a fixed overlay layer thickness (50 mm), on the performance of the overlay assemblies at both states is presented in **Figsure 7.14** and **7.15** and **Table 7.5**. Considering the intact substrate system, increasing the compressive strength of the bottom concrete layer significantly influenced the first-cracking strength of the overlay system; however, it had nil to marginal effect on the ductility of the systems (residual strength at *l/150* and toughness). For example, increasing the compressive strength of the substrate concrete from 40 to 50 MPa increased the first-cracking flexural strength for N-F-4.5 and N-G-4.5 by 24% and 26%, respectively, while it had no effect on the residual strength and marginally increased the toughness by 8% and 5%, respectively. This substantiated the dominant effect of the intact substrate layer on the first-cracking strength of the assembly as it is located at the tension side of the cross-

section of the systems, while the top layer is responsible for the ductility of the system after cracking owing to the role of BFP as previously discussed.

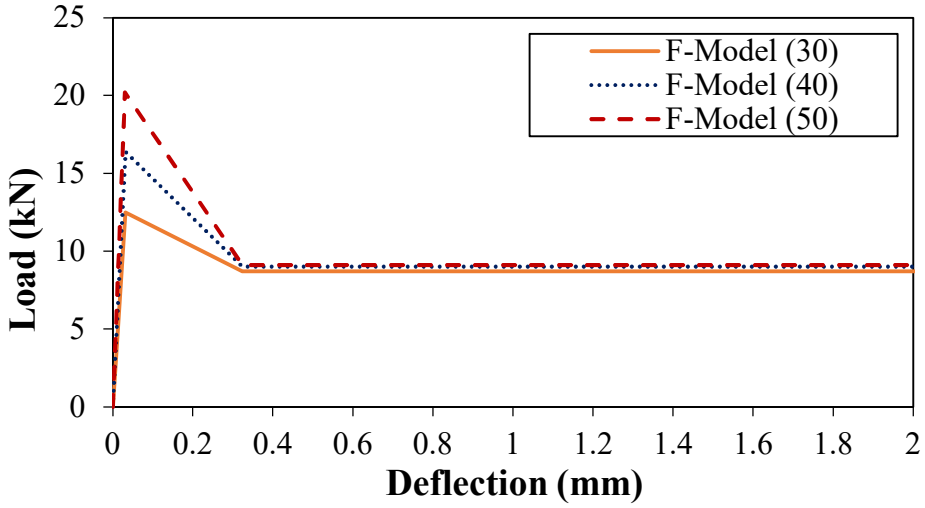

(a)

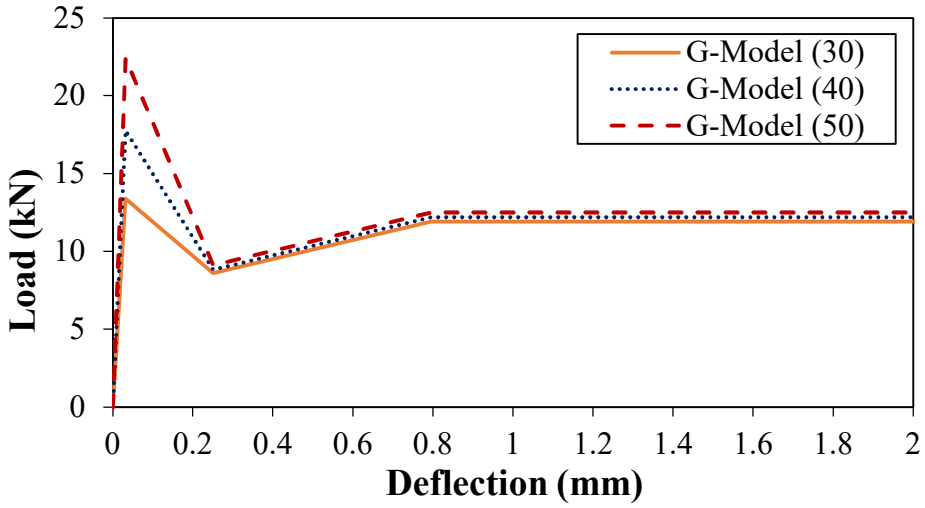

(b)

Figure 7.14: Load-deflection (P-δ) curves for the overlay assemblies with different substrate compressive strengths in the intact state: (a) N-F-4.5, and (b) N-G-4.5. (Notes: F = N-F-4.5; G = N-G-4.5; the number between parentheses is compressive strength of the substrate layer in MPa).

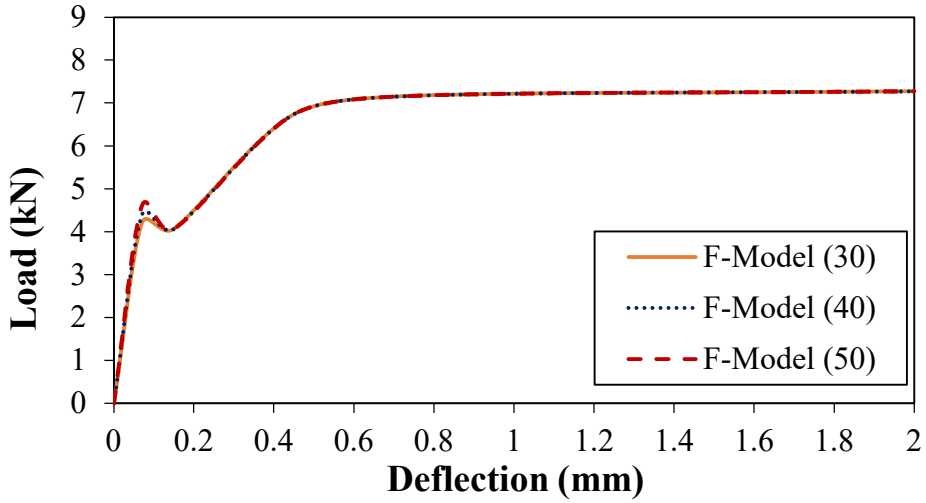

(a)

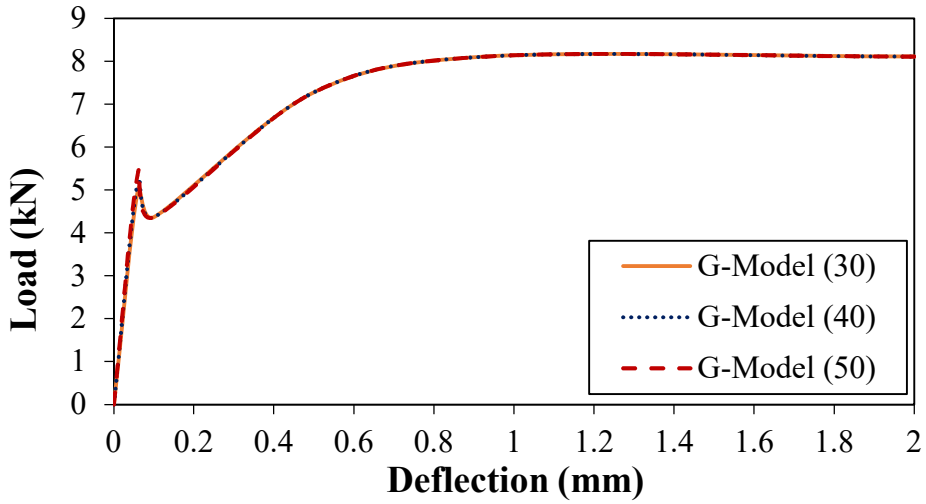

(b)

Figure 7.15: Load-deflection (P-δ) curves for the overlay assemblies with different substrate compressive strengths in the pre-cracked state: (a) N-F-4.5, and (b) N-G-4.5. (Notes: F = N-F-4.5; G = N-G-4.5; the number between parentheses is compressive strength of the substrate layer in MPa).

Similar to the previous trends, the load carrying capacity and consequently toughness of the pre-cracked assemblies were less (31-41%) relative to intact overlay assembly configuration at similar substrate compressive strength (**Figure 7.15** vs. **Figure 7.14**). Increasing the compressive strength of the substrate concrete layer had marginal effect on the flexural properties of the pre-cracked assemblies, regardless the type of the

binder (fly ash- or slag-based). For instance, increasing the compressive strength of the substrate concrete from 40 to 50 MPa only increased the first-cracking flexural strength for N-F-4.5 and N-G-4.5 by 4% and 5%, respectively, while it had almost nil effect on the residual strength and toughness for both systems. This conforms to the key role of the top layer (cementitious composite) at controlling the flexural performance (first-cracking strength, residual strength, toughness) of the pre-cracked assemblies as discussed earlier.

CHAPTER 8: SUMMARY, CONCLUSIONS, AND RECOMMENDATIONS

8.1 Summary

Nano-modified cementitious composites represent a new class of high performance cement-based materials that offers an attractive option for different heavy-duty infrastructure applications such as pavements and bridge decks. In this thesis, experimental work and finite element modeling were conducted in order to comprehend the factors affecting the properties of the cementitious composites (e.g. binder formulation, nano-modifications and pellets' dosage) as well as the durability potentials of the cementitious composites under different environmental and chemical loading schemes, besides identifying the suitability of their employing in different rehabilitation systems.

The experimental program was designed to offer fundamental data on nano-modified cementitious composites incorporating 50% SCM (slag or fly ash) and reinforced with emerging new basalt macro-fiber class termed as BFP. The effect of varying the binder formulation and BFP dosage on the fresh, hardened and durability properties were evaluated. Six different mixtures were cast and tested for mortar flow/mortar flow retention, air content of the fresh mixtures as well as initial and final setting times. The mechanical performance was evaluated through compressive strength at different ages and flexural performance. Furthermore, thermal and microscopy studies were performed to track the hydration evolution and microstructure of the composites. This strategy was adopted to explore the different potentials of the cementitious composite to be employed in specific infrastructure applications.

Based on the outcomes of the aforementioned initial characterization of the cementitious composites, speciality tests pertinent to infrastructure flatwork applications including concrete pavements and bridge decks were evaluated. The behavior of the cementitious composites under low and high strain rate loading schemes were investigated. Ten mixtures were investigated under quasi-static tension/compression and high-speed dynamic compression loading scenarios. In order to have a deeper insight of the material performance under various loading speeds, micro-scale tests were performed additionally, to study the strain-rate dependency of the bonding behavior between the BFP and the developed matrices. These tests comprise the single fiber pull-out test coupled with scanning electron microscopy analysis.

The durability issues confronting infrastructure applications, particularly in severe environmental conditions such as Manitoba, represent a crucial criterion when designing cement-based mixtures for such applications. Thus, a holistic testing approach was adopted to investigate the longevity of the cementitious composites for un-cracked and pre-cracked specimens as well as its self-healing prospect. Salt-frost resistance of the cementitious composites was studied according to ASTM C666 exposure cycles protocol except for using saline solution instead of fresh water. In addition, the resistance of the mixtures to high alkaline solution was assessed as well. The assessment criteria for the mixtures' durability potentials was carried out through determining the physical properties as well as residual flexural strength of un-cracked and pre-cracked prismatic specimens after the exposure regimes. Moreover, the self-healing ability of cracked specimens was investigated, with respect to the effects of the high replacement level of SCM with nano-silica.

Depending on the superb performance of the cementitious composites, the integrity of the mixtures in repair/overlay systems was examined, where the thermal and elastic compatibility between the repair material (cementitious composites) and substrate typical paving concrete in Winnipeg were studied. The bond strength of the cementitious composites was further investigated through pull-off test (pure tensile stresses at the interface) after normal and aggravated exposures. Moreover, the mechanical compatibility of the cementitious composites was investigated through an overlay beam flexural test (combination of shear and compressive stresses at the interface). This was coupled with thermal and microstructure studies to verify the bulk properties' trends. A complementary modeling study using finite element method (FEM) was performed to simulate the overlay beam flexural test assembly using ANSYS software package. The FEM was then calibrated and validated against the obtained experimental data. Thereafter, the model was used to conduct a parametric study on key parameters including overlay thickness and substrate compressive strength.

8.2 Conclusions

8.2.1 Factors affecting properties of cementitious composites (Chapters 3 and 4)

- Combination of nano-silica with a high-volume of fly ash or slag led to adequate initial flow, flow retention, and setting times, making them practical for field operations.
- The early-age and long-term compressive strengths of the nano-modified composites were enhanced, even with increasing the BFP dosage, due to the synergistic effects of nano-silica and fly ash or slag. The strength values obtained herein indicate the suitability of these composites to a suite of construction applications.

- The tensile and impact properties of the developed nano-modified cementitious composites were enhanced relative to the non-modified ones, due to the synergistic effects of nano-silica with high-volume SCMs. Slag-based composites showed higher tensile and impact properties relative to that of the fly ash-based counterparts. This was attributed to the accelerated reactivity of the slag-based binder with nano-silica, leading to enhanced matrix quality, ITZ, and thus bonding with BFP or steel fibers.
- In the direct tension and impact tests, BFP (2.5%, i.e. 1% basalt fibers) was more efficient at improving the post-cracking performance of nano-modified cementitious composites relative to an equivalent volume of steel fibers. The improved interfacial bonding between BFP and matrix enabled the pellets to better resist pull-out from the matrix, due to deposition of the hydration products in the specially designed longitudinal micro-grooves of the BFP.
- BFP, especially at higher dosages, significantly enhanced the flexural performance of the nano-modified composites in terms of post cracking-behavior, owing to the deposition of reaction products in the longitudinal micro-grooves of the pellets.
- Increasing the BFP dosage marginally influenced the pre-cracking behavior of the composites in terms of elastic moduli, but it reduced the ultimate tensile strength due to creation of additional ITZs in the matrix. However, it improved the tensile and dynamic compression post-cracking performance of the nano-modified composites in terms of ductility, due to the abundance of the pellets at failure planes. The 4.5% (i.e. 2% basalt fiber) BFP can be considered an optimal balance between ultimate strength and ductility under the tensile and impact loading schemes.

- Single pellet pullout results confirmed the dependence of BFP interfacial bonding with matrix on the rate of displacement and type of host binder, and the highest results were obtained with the high displacement rate (50 mm/min) and nano-modified slag matrix.
- The nano-modified composites, particularly the slag-based mixtures, exhibited high durability to accelerated slat-frost exposure due to the densified microstructure and efficiency of polyamide resin at protecting basalt fiber strands.
- The compendious results of this study indicate that the nano-modified composites incorporating BFP have high performance; thus, they may present a viable option for a suite of infrastructural applications (e.g. pavements, bridges, repair). Moreover, the slag-based nano-modified cementitious composites incorporating BFP showed promising potential in infrastructural applications subject to tensile and impact stresses (e.g. pavements, bridges, airfield aprons).

8.2.2 Factors affecting long-term durability properties of cementitious composites (Chapter 5)

- The initial properties of nano-modified cementitious composites at 56 days were improved relative to the reference counterparts, due to the synergistic effects of nano-silica with GU cement without/with high-volume SCM. Nano-silica catalyzed the hydration and pozzolanic reactions in the different binder systems, and thus densified the pore structure of the cementitious matrix, especially for nano-modified cement and nano-modified slag based binders.
- Similar to the moist curing (reference) exposure, the alkaline exposure provided favorable conditions for continual reactivity of the binders, as reflected by the improvement of stiffness and maintenance of flexural capacity, as well as autogenous healing and refinement of pore structure of all composites. However, all composites

showed ductility loss of 17% to 25% "un-cracked specimens" and 29% to 46% "pre-cracked specimens" relative to the reference exposure due to degradation of near surface or directly exposed (pre-cracked specimens) BFP. Continuous immersion of the composites in 1N NaOH solution at 38±2°C led to deterioration of the polyamide component, and in turn access of the alkaline medium to the basalt component; hence, the pullout toughening mechanism was limited by rupture of basalt strands.

- All the un-cracked composites remained intact after the salt-frost exposure, where they exhibited expansion as well as loss of flexural strength (25% to 37%) and ductility (24% to 42%); however,the situation was exacerbated for the pre-cracked specimens. The microstructure of all matrices was coarsened after this exposure, although to different extents, due to physical (frost action) and chemical (interaction of high concentration $CaCl_2$ solution with hydration products) attacks, which led to impairing the interfacial bonding with BFP (the pellets remained unaffected though) and/or complete failure of most composites. However, pre-cracked specimens from N-GU-2.5 and N-G-2.5/4.5 composites remained intact after this exposure due to the lower initial penetrability (physical resistance) and/or reduction of initial portlandite contents (chemical resistance) of the matrix.
- The synoptic findings from this study highlighted the promising durability of the nano-modified cement-based (N-GU) and slag-based (N-G) cementitious composites reinforced with 2.5% or 4.5% BFP in harsh exposures similar to the ones implemented herein. The design of BFP can be altered by applying a different resin to enhance protection of basalt strands from prolonged exposure to alkaline media; also, the resistance of such composites to frost action can be further enhanced by air-entrainment.

8.2.3 Cementitious composites for rehabilitation techniques (Chapter 6)

- The nano-modified composites with high content SCM and BFP had high consistency (180%), adequate flow retention (more than 100%) up to 60 min, and normal setting times (4 to 6 h), which make them practical for placement operations in the field.
- The TGA trends captured the catalytic and synergistic effects of NS with fly ash/slag on improving early-age and later-age compressive strength of the composites. Hence, at 1 day, the nano-modified cementitious composites exceeded 30 MPa, and at 56 days, they exceeded 50 MPa with a minimum flexural strength of 5.5 MPa, complying with typical strength requirements for repair/overlay applications in concrete pavements and bridge decks.
- The slag-based composites exhibited higher mechanical properties and resistance to infiltration of fluids, relative to the fly ash-based composites, due their improved reactivity/maturity (TGA) and densified microstructure (MIP). However, all the nano-modified cementitious composites, met the mechanical (strength ranges) and durability (very low penetrability) requirements for repair/overlay applications.
- The cementitious composites showed high thermal compatibility and dimensional stability with substrate concrete, owing to the restraining role of BFP. Thus, no surface cracking was observed during exposure to hot/arid conditions, as the total restrained shrinkage strains for the composites remained low at 416-454 micro-strains. Accordingly, the composites had efficient integrity/continuity (bond strength) with the substrate concrete, without requiring bonding agents, before and after exposure to consecutive freeze-thaw and wetting-drying cycles, where the substrate mode of failure was dominant, which projects long-term durability of the repair/overlay assembly in the field.

- The compendious results show that the nano-modified composites, especially the slag-based, reinforced with BFP can achieve balanced performance in terms of fresh, mechanical and durability properties as well as high compatibility with substrate concrete. Thus, they may present a viable option for high-performance repair/overlay applications at critical and heavy-duty locations in concrete pavements and bridge decks.

8.2.4 Flexural bonded overlay performance and FEM of nano-modified cementitious composites (Chapter 7)

- The synergistic effects of NS with fly ash/slag improved both early-age and later-age strengths of the cementitious composites, with higher reactivity/maturity of the slag-based composite, as elucidated by TGA trends. Accordingly, at 3 and 56 days, the cementitious composites exceeded 35 MPa and 50 MPa, respectively, with a minimum flexural strength of 5 MPa at 56 days, which comply with typical strength requirements for overlay applications in concrete pavements and bridge decks.
- The cementitious composites showed efficient integrity with the intact substrate concrete layer, where the two layers behaved monolithically under the applied flexural loading, without any signs of delamination. The cementitious composite overlay was able to control the propagation of the cracks reflected upwards from the bottom layer without convergence at the interface between the two layers, and the system exhibited a steady and ductile load-deflection plateau instead of the brittle behavior conventional concrete.
- The performance of the overlay system with pre-cracked substrate was governed by the properties of the overlay layer with minimal contribution of the substrate layer, as the failure occurred in the top layer (cementitious composite) over the jointed part in the

parent concrete. No transverse delamination occurred between the two layers at the critical joint zone, which substantiated the efficient bonding between the two layers and the monolithic behavior of the system.

- The developed FEM for the overlay assemblies had matching load-deflection and cracking patterns as well as numerical results (less than 10% error) to that of experimental data. Parametric analysis revealed that the load carrying capacity of the overlay assemblies and consequently toughness increased significantly with increasing the thickness of the composite/ductile layer from 40 to 100 mm, regardless of the substrate condition (intact or pre-cracked). Comparatively, increasing the compressive strength of substrate layer (30 to 50 MPa) significantly influenced the first-cracking strength of the intact overlay system, while it had marginal effect on the ductility of the both overlay assemblies (intact and pre-cracked).
- The compendious results from this study show that the cementitious composites reinforced with BFP can achieve balanced performance in terms of engineering properties and mechanical compatibility with substrate concrete. Hence, they may present a viable performance for high-performance overlay applications in concrete pavements and bridge decks; the choice of a specific overlay thickness is a function of desired ductility and structural design requirements.

8.3 Recommendations

- Based on the results obtained from the characterization of the cementitious composites, complementary research is required to investigate the effect of increasing the portion of SCM in the binder over 50%.

- Further enhancement of the frost-resistance durability properties for the cementitious composites using air-entrainment is recommended for future research.
- The effect of using different polymeric resin (e.g. vinylester) in the encapsulation of basalt fiber strands with different surface groove patterns on the interfacial bonding with cementitious matrix as well as durability of pellets under aggravated exposures is recommended for further investigations.
- The effect of using hybrid fiber system at the micro and nano-scales besides the macro-scale BFP (multi-scale fiber system) on the mechanical performance of the cementitious composites is recommended for further study, particularly ductility relevant properties and multiple cracking phenomenon.
- The effect of different deicing salts with different concentrations at different freeze-thaw cycles frequency on the performance of the cementitious composites is needed for further study, particularly for the mixtures to be employed in severe environmental conditions as in Manitoba.
- The application of nano-modified cementitious composites as a partial depth repair or overlay application in concrete pavements and bridge decks is recommended to confirm the experimental behaviour of the mixtures.
- Supplemental numerical study is required to investigate the influence of increasing the substrate layer thickness as well as variation of BFP dosage in the overlay layer on the flexural overlay performance.
- Laboratory experimental testing is recommended for future research to verify the FEM findings and validate performance expectations.

- Large-scale field trials including realistic cost/performance analysis, especially when producing bulk amounts of BFP, relative to other high-performance fiber reinforced cementitious composites commercially available in the construction sector are recommend for future research.

REFERENCES

AASHTO, 1993. *AASHTO Guide for Design of Pavement Structures,* (Vol. 1). *American Association of State Highway and Transportation Officials,* Washington DC.

AASHTO, 2015. Standard test method for the coefficient of thermal expansion of hydraulic cement concrete. AASHTO T336-15, *American Association of State Highway and Transportation Officials,* Washington DC.

Abbasnia, R., Godossi, P. and Ahmadi, J., 2005. Prediction of restrained shrinkage based on restraint factors in patching repair mortar. *Cement and concrete research*, *35*(10), pp.1909-1913.

ACI, 2010. State-of-the Art Report on Fiber Reinforced Concrete, ACI 544.1R-10, *American Concrete Institute*, Farmington Hills, Michigan.

ACI, 2014. Concrete Repair Guide. *ACI PRC-546R-14*, American Concrete Institute, Farmington Hills, Michigan, USA, 70 p.

ACI, 2016. Guide to Durable Concrete. *ACI 201.2 R*, American Concrete Institute, Farmington Hills, Michigan, USA.

ACI, 2020. Concrete Overlays for Pavement Rehabilitation (Reapproved 2020). *ACI PRC-325.13-06*, American Concrete Institute, Farmington Hills, Michigan, USA, 39 p.

Al-Ostaz, A., Irshidat, M., Tenkhoff, B. and Ponnapalli, P.S., 2010. Deterioration of bond integrity between repair material and concrete due to thermal and mechanical incompatibilities. *Journal of Materials in Civil Engineering*, *22*(2), pp.136-144.

Al-Salloum, Y., Almusallam, T., Ibrahim, S.M., Abbas, H. and Alsayed, S., 2015. Rate dependent behavior and modeling of concrete based on SHPB experiments. *Cement and Concrete Composites*, *55*, pp.34-44.

Antunes, M.D.L., and Nunn, M., 1999. *Development of New Bituminous Pavement Design Method: Final Report of the Action (COST 333). European Commission, Directorate General Transport*, Luxembourg. 375 p. ISBN 92-828-6796-X.

Asala, G., Andersson, J. and Ojo, O.A., 2018. Improved dynamic impact behaviour of wire-arc additive manufactured ATI 718Plus®. *Materials Science and Engineering: A*, *738*, pp.111-124.

ASCE, 2021. Report Card for America's Infrastructure-2021. American Society of Civil Engineers, Restion, Virginia, USA.

ASTM, 2012. Standard Test Method for Scaling Resistance of Concrete Surfaces Exposed to Deicing Chemicals. *ASTM C672/ C672M -12*, American Society for Testing and Materials, West Conshohocken, PA, USA.

ASTM, 2014. Standard test method for sieve analysis of fine and coarse aggregates. *ASTM C136/136M*, American Society for Testing and Materials, West Conshohocken, PA, USA.

ASTM, 2015. Standard Test Method for Obtaining Average Residual-Strength of Fiber-Reinforced Concrete. *ASTM C1399/C1399M*, American Society for Testing and Materials, West Conshohocken, PA, USA.

ASTM, 2015. Standard Test Method for Relative Density (Specific Gravity) and Absorption of Fine Aggregate. *ASTM C128*, American Society for Testing and Materials, West Conshohocken, PA, USA.

ASTM, 2015. Standard test method for resistance of concrete to rapid freezing and thawing.

ASTM C666/C666M, American Society for Testing and Materials, West Conshohocken, PA, USA.

ASTM, 2016. Standard Test Method for Time of Setting of Concrete Mixtures by Penetration Resistance. *ASTM C403/C403M-16*, American Society for Testing and Materials, West Conshohocken, PA, USA.

ASTM, 2017. Standard Specification for Chemical Admixtures for Concrete. *ASTM C494/C494M*, American Society for Testing and Materials, West Conshohocken, PA, USA.

ASTM, 2017. Standard Test Method for Air Content of Freshly Mixed Concrete by the Pressure Method. *ASTM C231/C231M-17a*, American Society for Testing and Materials, West Conshohocken, PA, USA.

ASTM, 2017. Standard Test Method for Length Change of Hardened Hydraulic-Cement Mortar and Concrete. *ASTM C157/C157M*, American Society for Testing and Materials, West Conshohocken, PA, USA.

ASTM, 2019. Standard Test Method for Electrical Indication of Concrete's Ability to Resist Chloride Ion Penetration. *ASTM C1202* American Society for Testing and Materials, West Conshohocken, PA, USA.

ASTM, 2019. Standard Test Method for Flexural Performance of Fiber-Reinforced Concrete (Using Beam With Third-Point Loading). *ASTM C1609/C1609M -19*, American Society for Testing and Materials, West Conshohocken, PA, USA.

ASTM, 2019. Standard Test Method for Fundamental Transverse, Longitudinal, and Torsional Resonant Frequencies of Concrete Specimens. *ASTM C215*, American Society for Testing and Materials, West Conshohocken, PA, USA.

ASTM, 2021. Standard Specification for Flow Table for Use in Tests of Hydraulic Cement. *ASTM C230/C230M-21*, American Society for Testing and Materials, West Conshohocken, PA, USA.

ASTM, 2021. Standard Test Method for Compressive Strength of Cylindrical Concrete Specimens. *ASTM C39/C39M*, American Society for Testing and Materials, West Conshohocken, PA, USA.

Ayub, T., Shafiq, N. and Nuruddin, M.F., 2014. Mechanical properties of high-performance concrete reinforced with basalt fibers. *Procedia Engineering*, *77*, pp.131-139.

Azzam, A., Bassuoni, M.T. and Shalaby, A., 2019. Properties of High-Volume Fly Ash and Slag Cementitious Composites Incorporating Nanosilica and Basalt Fiber Pellets. *Advances in Civil Engineering Materials*, *8*(3), pp.255-274.

Azzam, A., Bassuoni, M.T. and Shalaby, A., 2021. Nanomodified Cementitious Composites Incorporating Basalt Fiber Pellets under Tensile and Impact Loads. *Journal of Materials in Civil Engineering*, In Press.

Barman, M. and Hansen, B., 2018. Comparison of Performances of Structural Fibers and Development of a Specification for Using Them in Thin Concrete Overlays.

Bassuoni, M.T., Nehdi, M.L. and Greenough, T.R., 2005. Enhancing the reliability of evaluating chloride ingress in concrete using the ASTM C 1202 rapid chloride penetrability test. *Journal of ASTM International*, *3*(3), pp.1-13.

Bentur, A., Mindess, S., Routledge., 2006. *Fibre Reinforced Cementitious Composites*. Second Edition. London, UK: CRC Press.

Beushausen, H., Höhlig, B. and Talotti, M., 2017. The influence of substrate moisture preparation on bond strength of concrete overlays and the microstructure of the OTZ. *Cement and Concrete Research*, *92*, pp.84-91.

Birkeland, P.W. and Birkeland, H.W., 1966, March. Connections in precast concrete construction. In *Journal Proceedings* (Vol. 63, No. 3, pp. 345-368).

Bissonnette, B., Courard, L., Fowler, D.W. and Granju, J.L. eds., 2011. *Bonded Cement-based Material Overlays for the Repair, the Lining or the Strengthening of Slabs or Pavements: State-of-the-art Report of the RILEM Technical Committee 193-RLS* (Vol. 3). Springer Science & Business Media.

BNQ, 2002. Determination of the scaling resistance of concrete surfaces exposed to freezing and thawing cycles in the presence of deicing chemicals. *BNQ NQ 2621-900*, Bureau de Normalisation du Québec, Annex A, pp.19-22.

Branston, J., Das, S., Kenno, S.Y. and Taylor, C., 2016. Influence of basalt fibres on free and restrained plastic shrinkage. *Cement and Concrete Composites*, *74*, pp.182-190.

Branston, J., Das, S., Kenno, S.Y. and Taylor, C., 2016. Mechanical behaviour of basalt fibre reinforced concrete. *Construction and Building Materials*, *124*, pp.878-886.

Brown, M. E., 1998. *Handbook of thermal analysis and calorimetry*. Elsevier, Amsterdam, Netherlands.

Burnham, T.R., Johnson, E. and Worel, B.J., 2016. *Performance of Various Partial-Depth Repair Materials at the MnROAD Facility*. Minnesota Department of Transportation, Research Services & Library.

Carlswärd, J., 2006. *Shrinkage cracking of steel fibre reinforced self compacting concrete overlays: test methods and theoretical modelling: test methods and theoretical*

modelling (Doctoral dissertation, Luleå tekniska universitet).

Chabot, A., Hun, M. and Hammoum, F., 2013. Mechanical analysis of a mixed mode debonding test for "composite" pavements. *Construction and Building Materials*, *40*, pp.1076-1087.

Chaichanawong, J., Thongchuea, C. and Areerat, S., 2016. Effect of moisture on the mechanical properties of glass fiber reinforced polyamide composites. *Advanced Powder Technology*, *27*(3), pp.898-902.

Cook, R., Malkus, D., Plesha, M., & Witt, R., 2007. *Concepts and Applications of Finite Element Analysis*. John Wiley & Sons, New York, USA, 537p.

Corinaldesi, V. and Nardinocchi, A., 2016. Influence of type of fibers on the properties of high performance cement-based composites. *Construction and Building Materials*, *107*, pp.321-331.

CSA, 2014. Canadian Highway Bridge design code. *CAN/CSA-S6*, Canadian Standard Association, Mississauga, Ontario, Canada.

CSA, 2018. Cementitious materials for use in concrete. *CSA-A3001-18*. Canadian Standards Association, Mississauga, ON, Canada.

CSA, 2019, Determination of Bond Strength of Bonded Toppings and Overlays and of Direct Tensile Strength of Concrete, Mortar, and Grout. *CSA A23.2-6B*, Canadian Standards Association, Mississauga, ON, Canada.

CSA, 2019. Concrete Materials and Methods of Concrete Construction/ Test Methods and Standard Practices for Concrete. *CSA-A23.1/A23.2:19*, Canadian Standards Association, Mississauga, ON, Canada.

Curosu, I., Mechtcherine, V. and Millon, O., 2016. Effect of fiber properties and matrix composition on the tensile behavior of strain-hardening cement-based composites (SHCCs) subject to impact loading. *Cement and Concrete Research*, *82*, pp.23-35.

CW, 2015. Portland Cement Concrete Pavement Works. *CW3310-R17*, City of Winnipeg Specification, Winnipeg, Manitoba, Canada.

Czarnecki, L., 2008. Adhesion–A challenge for concrete repair. In *Concrete Repair, Rehabilitation and Retrofitting II: 2nd International Conference on Concrete Repair, Rehabilitation and Retrofitting,* ICCRRR-2, Cape Town, South Africa (p. 343). CRC Press.

Detwiler, R.J., Bhatty, J.I. and Battacharja, S., 1996. *Supplementary cementing materials for use in blended cements* (No. R&D Bulletin RD112T,).

Douglas, K.S. and Billington, S.L., 2005, May. Rate dependence in high-performance fiber reinforced cementbased composites for seismic applications. In *Proceedings, HPFRCC-2005 international workshop, Honolulu, Hawaii, USA*.

Du, H., Du, S. and Liu, X., 2014. Durability performances of concrete with nano-silica. *Construction and building materials*, *73*, pp.705-712.

ElBatanouny, M.K., SE, P., Pham, L.T. and Hawkins, K.A., 2020. Late Life Low Cost Deck Overlays.

Emmons, P.H. and Vaysburd, A.M., 1993. Compatibility considerations for durable concrete repairs. *Transportation Research Record*, *1382*, p.13.

FAA. 2004. Concrete Airfield Pavement Surface Evaluation and Rating (PASER) Manual.

Federal Aviation Administration (FAA), Washington, USA.20 p.

Felekoglu, B., Tosun-Felekoglu, K., Ranade, R., Zhang, Q. and Li, V.C., 2014. Influence of matrix flowability, fiber mixing procedure, and curing conditions on the mechanical performance of HTPP-ECC. *Composites Part B: Engineering*, *60*, pp.359-370.

Fick, G., and Harrington, D., 2016. Guide Specifications for Concrete Overlays. National Concrete Pavement Technology Center, Iowa State University, Institute for Transportation, Ames, Iowa, USA.

Fowler, D.W., Zollinger, D.G. and Whitney, D.P., 2008. Implementing best concrete pavement spall repairs (No. FHWA/TX-08/5-5110-01-1).

Frentress, D.P. and Harrington, D.S., 2012. Guide for partial-depth repair of concrete pavements. Iowa State University Institute for Transportation.

Ghazy, A. and Bassuoni, M.T., 2017. Resistance of concrete to different exposures with chloride-based salts. *Cement and Concrete Research*, *101*, pp.144-158.

Ghazy, A. and Bassuoni, M.T., 2017. Shrinkage of Nanomodified Fly Ash Concrete as Repair Material. *ACI Materials Journal*, *114*(6).

Ghazy, A., Bassuoni, M.T. and Islam, A.K.M.R., 2018. Response of Concrete with Blended Binders and Nanosilica to Freezing–Thawing Cycles and Different Concentrations of Deicing Salts. *Journal of Materials in Civil Engineering*, *30*(9), p.04018214.

Ghazy, A., Bassuoni, M.T. and Shalaby, A., 2016. Nano-modified fly ash concrete: a repair option for concrete pavements. *ACI Materials Journal*, *113*(2), pp.231-242.

Ghazy, A., Bassuoni, M.T., Maguire, E. and O'Loan, M., 2016. Properties of fiber-reinforced mortars incorporating nano-silica. *Fibers*, *4*(1), p.6.

Ghazy, A., Bassuoni, M.T., Shehata, E. and Burmey, D., 2019. Comparison of different approaches for determining the residual post-cracking strength index of fiber reinforced concrete for bridges. *Canadian Journal of Civil Engineering*, *46*(5), pp.462-465.

Goldstein, J.I., Newbury, D.E., Michael, J.R., Ritchie, N.W., Scott, J.H.J. and Joy, D.C., 2017. *Scanning electron microscopy and X-ray microanalysis*. Springer.

Granju, J.L., 1996. Thin bonded overlays: about the role of fiber reinforcement on the limitation of their debonding. *Advanced Cement Based Materials*, *4*(1), pp.21-27.

Granju, J.L., 2001. Debonding of thin cement-based overlays. *Journal of materials in civil engineering*, *13*(2), pp.114-120.

Granju, J.L., Sabathier, V., Turatsinze, A. and Toumi, A., 2004. Interface between an old concrete and a bonded overlay: debonding mechanism. *Interface science*, *12*(4), pp.381-388.

Griffiths, G.and Thom, N., 2007. *Concrete Pavement Design Guidance Notes.* London and New York: Taylor and Francis Group. 168 p. CRC Press. ISBN 978-0-203-96206-0.

Halvaei, M., Jamshidi, M. and Latifi, M., 2014. Application of low modulus polymeric fibers in engineered cementitious composites. *Journal of industrial textiles*, *43*(4), pp.511-524.

Hanif, A., Parthasarathy, P., Lu, Z., Sun, M. and Li, Z., 2017. Fiber-reinforced cementitious composites incorporating glass cenospheres–Mechanical properties and microstructure. *Construction and Building Materials*, *154*, pp.529-538.

Hillerborg, A., 1980. Analysis of fracture by means of the fictitious crack model, particularly for fibre reinforced concrete.

Huang, H., Ye, G. and Damidot, D., 2014. Effect of blast furnace slag on self-healing of microcracks in cementitious materials. *Cement and concrete research*, *60*, pp.68-82.

Huang, Y. H., 2004. *Pavement Analysis and Design*. USA, Prentice Hall. 792 p., ISBN 0-13-142473-4.

Isla, F., Luccioni, B., Ruano, G., Torrijos, M.C., Morea, F., Giaccio, G. and Zerbino, R., 2015. Mechanical response of fiber reinforced concrete overlays over asphalt concrete substrate: Experimental results and numerical simulation. *Construction and Building Materials*, *93*, pp.1022-1033.

Iyer, P., Kenno, S.Y. and Das, S., 2015. Mechanical properties of fiber-reinforced concrete made with basalt filament fibers. *Journal of Materials in Civil Engineering*, *27*(11), p.04015015.

Jalasutram, S., Sahoo, D.R. and Matsagar, V., 2017. Experimental investigation of the mechanical properties of basalt fiber-reinforced concrete. *Structural Concrete*, *18*(2), pp.292-302.

Jiang, C., Fan, K., Wu, F. and Chen, D., 2014. Experimental study on the mechanical properties and microstructure of chopped basalt fibre reinforced concrete. *Materials & Design*, *58*, pp.187-193.

Jiang, S., Zhou, D., Zhang, L., Ouyang, J., Yu, X., Cui, X. and Han, B., 2018. Comparison of compressive strength and electrical resistivity of cementitious composites with different nano-and micro-fillers. *Archives of Civil and Mechanical Engineering*, *18*(1), pp.60-68.

Jones, W., Farnam, Y., Imbrock, P., Spiro, J., Villani, C., Golias, M., Olek, J., and Weiss, W. J., 2013. *An Overview of Joint Deterioration in Concrete Pavement: Mechanisms,*

Solution Properties, and Sealers. Report, Purdue University, West Lafayette, Indiana, doi: 10.5703/1288284315339.

Justnes, H., Reyniers, B. and Sellevold, E.J., 1994. An evaluation of methods for measuring chemical shrinkage of cementitious pastes. *Nordic Concrete Research*, *14*(1), pp.45-61.

Kawashima, S. and Shah, S.P., 2011. Early-age autogenous and drying shrinkage behavior of cellulose fiber-reinforced cementitious materials. *Cement and Concrete Composites*, *33*(2), pp.201-208.

Kim, M.O. and Bordelon, A.C., 2017. Age-dependent properties of fiber-reinforced concrete for thin concrete overlays. *Construction and Building Materials*, *137*, pp.288-299.

Kim, M.O., Bordelon, A.C. and Lee, N.K., 2017. Early-age crack widths of thin fiber reinforced concrete overlays subjected to temperature gradients. *Construction and Building Materials*, *148*, pp.492-503.

Kizilkanat, A.B., Kabay, N., Akyüncü, V., Chowdhury, S. and Akça, A.H., 2015. Mechanical properties and fracture behavior of basalt and glass fiber reinforced concrete: An experimental study. *Construction and Building Materials*, *100*, pp.218-224.

Kong, D., Du, X., Wei, S., Zhang, H., Yang, Y. and Shah, S.P., 2012. Influence of nano-silica agglomeration on microstructure and properties of the hardened cement-based materials. *Construction and Building Materials*, *37*, pp.707-715.

Ksouri, I. and Haddar, N., 2018. Long term ageing of polyamide 6 and polyamide 6 reinforced with 30% of glass fibers: temperature effect. *Journal of Polymer*

Research, *25*(7), pp.1-12.

Kuder, K.G., Ozyurt, N., Mu, E.B. and Shah, S.P., 2007. Rheology of fiber-reinforced cementitious materials. *Cement and Concrete Research*, *37*(2), pp.191-199.

Kutz, M., 2012. *Handbook of environmental degradation of materials*, 2nd Edition, NY: William Andrew Publishing, Norwich.

Lee, J.J., Song, J. and Kim, H., 2014. Chemical stability of basalt fiber in alkaline solution. *Fibers and Polymers*, *15*(11), pp.2329-2334.

Lenz, P., 2012. *Concrete-concrete composite potential for shear joints*. PhD Thesis, Technical University of Munich.

Lenz, R. W., 2011. *Pavement Design Guide*. Texas Department of Transportation, Texas, USA, 428 p.

Lepech, M.D., and Li, V.C., 2010. Sustainable pavement overlays using engineered cementitious composites. *International Journal of Pavement Research and Technology*, 3(5), 241-250.

Li, V.C., 1998. *Engineered cementitious composites-tailored composites through micromechanical modeling*. Advanced Civil Engineering Materials Research Laboratory, Department of Civil and Environmental Engineering, University of Michigan, Ann Arbor, MI 48109-2125, USA

Li, V.C., 2004. Strategies for high-performance fiber reinforced cementitious composites development, Fiber Reinforced Concrete: From Theory to Practice. *Proceedings of the North American/European, Workshop on Advances in Fiber Reinforced Concrete*, S. Ahmad, M. di Prisco, C. Meyer, G. A. Plizzari, and S. Shah, eds., Bergamo, Italy; pp. 93-98.

Li, V.C., 2012. Can concrete be bendable?. *American Scientist*, *100*(6), pp.484-493.

Li, V.C., Fischer, G., Kim, Y.Y., Lepech, M., Qian, S., Weimann, M., and Wang, S., 2003. *Durable link slabs for jointless bridge decks based on strain-hardening cementitious composites*. Report for Michigan Department of Transportation, No. Research Report RC-1438.

Li, V.C., Stang, H. and Krenchel, H., 1993. Micromechanics of crack bridging in fibre-reinforced concrete. *Materials and structures*, *26*(8), pp.486-494.

Li, V.C., Wang, S. and Wu, C., 2001. Tensile strain-hardening behavior of polyvinyl alcohol engineered cementitious composite (PVA-ECC). *Materials Journal*, *98*(6), pp.483-492.

Li, V.C., Wang, Y. and Backer, S., 1991. A micromechanical model of tension-softening and bridging toughening of short random fiber reinforced brittle matrix composites. *Journal of the Mechanics and Physics of Solids*, *39*(5), pp.607-625.

Li, W. and Xu, J., 2009. Impact characterization of basalt fiber reinforced geopolymeric concrete using a 100-mm-diameter split Hopkinson pressure bar. *Materials Science and Engineering: A*, *513*, pp.145-153.

Li, W.M. and Xu, J.Y., 2009. Dynamic behavior and constitutive model of basalt fiber reinforced concrete under impact loading. *Engineering Mechanics*, *26*(1), pp.86-91.

Li, W.M., Xu, J.Y., Shen, L.J. and Li, Q., 2008. Dynamic mechanical properties of basalt fiber reinforced concrete using a split Hopkinson pressure bar. *Acta Materiae Compositae Sinica*, *25*(2), pp.135-142.

Lin, Y., Karadelis, J.N. and Xu, Y., 2013. A new mix design method for steel fibre-reinforced, roller compacted and polymer modified bonded concrete

overlays. *Construction and Building Materials*, *48*, pp.333-341.

Lipatov, Y.V., Gutnikov, S.I., Manylov, M.S., Zhukovskaya, E.S. and Lazoryak, B.I., 2015. High alkali-resistant basalt fiber for reinforcing concrete. *Materials & Design*, *73*, pp.60-66.

Liu, A.P., Yin, J., and Song, W.M., 2013. Study on the performance and application of high performance pavement Portland cement concrete. *Advanced Materials Research*, pp. 411-416.

Liu, Z. and Hansen, W., 2015. Freezing characteristics of air-entrained concrete in the presence of deicing salt. *Cement and Concrete Research*, *74*, pp.10-18.

López-Carreño, R.D., Pujadas, P., Cavalaro, S.H. and Aguado, A., 2017. Bond strength of whitetoppings and bonded overlays constructed with self-compacting high-performance concrete. *Construction and Building Materials*, *153*, pp.835-845.

Loser, R., Münch, B. and Lura, P., 2010. A volumetric technique for measuring the coefficient of thermal expansion of hardening cement paste and mortar. *Cement and Concrete Research*, *40*(7), pp.1138-1147.

LS412, M.T.O., 1997. Methods of Test for Scaling Resistance of Concrete Surfaces Exposed to Deicing Chemicals. *MTO Laboratory Testing Manual*.

Ma, H., Qian, S., Zhang, Z., Lin, Z. and Li, V.C., 2015. Tailoring engineered cementitious composites with local ingredients. *Construction and building materials*, *101*, pp.584-595.

MacGregor, J.G., Wight, J.K., Teng, S. and Irawan, P., 1997. *Reinforced concrete: Mechanics and design* (Vol. 3). Upper Saddle River, NJ: Prentice Hall.

Madani, H., Bagheri, A. and Parhizkar, T., 2012. The pozzolanic reactivity of monodispersed nanosilica hydrosols and their influence on the hydration characteristics of Portland cement. *Cement and concrete research*, *42*(12), pp.1563-1570.

Mahmoud, K., Ghazy, A., Bassuoni, M.T. and El-Salakawy, E., 2017. Properties of nanomodified fiber-reinforced cementitious composites. *Journal of materials in civil engineering*, *29*(10), p.04017173.

Malhotra, V.M., Zhang, M.H., Read, P.H. and Ryell, J., 2000. Long-term mechanical properties and durability characteristics of high-strength/high-performance concrete incorporating supplementary cementing materials under outdoor exposure conditions. *Materials Journal*, *97*(5), pp.518-525.

Malvar, L.J. and Ross, C.A., 1998. Review of strain rate effects for concrete in tension. *ACI Materials Journal*, *95*, pp.735-739.

Mattock, A.H. and Hawkins, N.M., 1972. Shear transfer in reinforced concrete—Recent research. *Pci Journal*, *17*(2), pp.55-75.

Mechtcherine, V., 2013. Novel cement-based composites for the strengthening and repair of concrete structures. *Construction and building materials*, *41*, pp.365-373.

Mechtcherine, V., de Andrade Silva, F., Butler, M., Zhu, D., Mobasher, B., Gao, S.L. and Mäder, E., 2011. Behaviour of strain-hardening cement-based composites under high strain rates. *Journal of Advanced Concrete Technology*, *9*(1), pp.51-62.

Mechtcherine, V., de Andrade Silva, F., Müller, S., Jun, P. and Toledo Filho, R.D., 2012. Coupled strain rate and temperature effects on the tensile behavior of strain-hardening cement-based composites (SHCC) with PVA fibers. *Cement and Concrete Research*, *42*(11), pp.1417-1427.

Mechtcherine, V., Millon, O., Butler, M. and Thoma, K., 2011. Mechanical behaviour of strain hardening cement-based composites under impact loading. *Cement and Concrete Composites*, *33*(1), pp.1-11.

Mehta, P.K. and Monteiro, P.J., 2014. *Concrete: microstructure, properties, and materials*. McGraw-Hill Education, USA, 675 p.

Millon, O., Riedel, W., Thoma, K., Fehling, E. and Nöldgen, M., 2009. Fiber-reinforced ultra-high performance concrete under tensile loads. In *9th International Conference on the Mechanical Behaviour of Materials under Dynamic Loading, DYMAT* (pp. 671-677).

Mindess, S., Young, F.J. and Darwin, D., 2003. Concrete 2nd Editio. *Technical Documents*.

Montgomery, D.C., 2017. *Design and analysis of experiments*. John wiley & sons.

Neville, A. M., 2011. *Properties of Concrete*, Prentice Hall, London, UK.

Oertel, T., Hutter, F., Tänzer, R., Helbig, U. and Sextl, G., 2013. Primary particle size and agglomerate size effects of amorphous silica in ultra-high performance concrete. *Cement and Concrete Composites*, *37*, pp.61-67.

Pan, Z., Wu, C., Liu, J., Wang, W. and Liu, J., 2015. Study on mechanical properties of cost-effective polyvinyl alcohol engineered cementitious composites (PVA-ECC). *Construction and Building Materials*, *78*, pp.397-404.

Patel, A.J., Mojab, C.A.G. and Romine, A.R., 1993. *Materials and procedures for rapid repair of partial depth spalls in concrete pavements-Manual of practice*. Strategic

highway research report No. SHRP-H-349, National research council, Washington, D.C.

Peterson, K., Julio-Betancourt, G., Sutter, L., Hooton, R.D. and Johnston, D., 2013. Observations of chloride ingress and calcium oxychloride formation in laboratory concrete and mortar at 5 C. *Cement and Concrete Research*, *45*, pp.79-90.

Powers, T.C. and Helmuth, R.A., 1953. Theory of volume changes in hardened portland-cement paste during freezing. In *Highway research board proceedings* (Vol. 32).

Powers, T.C., 1964. *Topics in Concrete Technology-Mixtures Containing Intentionally Entrained Air* (No. 174).

Powers, T.C., 1975. Freezing effects in concrete. *Special Publication*, *47*, pp.1-12.

Qian, S.Z., Li, V.C., Zhang, H. and Keoleian, G.A., 2013. Life cycle analysis of pavement overlays made with Engineered Cementitious Composites. *Cement and Concrete Composites*, *35*(1), pp.78-88.

Rabinovich, F.N., Zueva, V.N. and Makeeva, L.V., 2001. Stability of basalt fibers in a medium of hydrating cement. *Glass and ceramics*, *58*(11), pp.431-434.

Ramezanianpour, A.A., 2014. Cement replacement materials. *Springer Geochemistry/Mineralogy, DOI*, *10*, pp.978-3.

Ravichandran, G. and Subhash, G., 1994. Critical appraisal of limiting strain rates for compression testing of ceramics in a split Hopkinson pressure bar. *Journal of the American Ceramic Society*, *77*(1), pp.263-267.

Ray, I., Davalos, J.F. and Luo, S., 2005. Interface evaluations of overlay-concrete bi-layer composites by a direct shear test method. *Cement and Concrete Composites*, *27*(3), pp.339-347.

Rokugo, K., Kanda, T., Yokota, H. and Sakata, N., 2009. Applications and recommendations of high performance fiber reinforced cement composites with multiple fine cracking (HPFRCC) in Japan. *Materials and structures*, *42*(9), pp.1197-1208.

Romualdi, J.P. and Batson, G.B., 1963. Mechanics of crack arrest in concrete. *Journal of the Engineering Mechanics Division*, *89*(3), pp.147-168.

Romualdi, J.P. and Mandel, J.A., 1964, June. Tensile strength of concrete affected by uniformly distributed and closely spaced short lengths of wire reinforcement. In *Journal Proceedings* (Vol. 61, No. 6, pp. 657-672).

Rossi, P. and Toutlemonde, F., 1996. Effect of loading rate on the tensile behaviour of concrete: description of the physical mechanisms. *Materials and structures*, *29*(2), pp.116-118.

Şahmaran, M. and Li, V.C., 2007. De-icing salt scaling resistance of mechanically loaded engineered cementitious composites. *Cement and Concrete Research*, *37*(7), pp.1035-1046.

Şahmaran, M. and Li, V.C., 2008. Durability of mechanically loaded engineered cementitious composites under highly alkaline environments. *Cement and Concrete Composites*, *30*(2), pp.72-81.

Şahmaran, M. and Li, V.C., 2009. Durability properties of micro-cracked ECC containing high volumes fly ash. *Cement and Concrete Research*, *39*(11), pp.1033-1043.

Şahmaran, M., Al-Emam, M., Yıldırım, G., Şimşek, Y.E., Erdem, T.K. and Lachemi, M., 2015. High-early-strength ductile cementitious composites with characteristics of low early-age shrinkage for repair of infrastructures. *Materials and Structures*, *48*(5),

pp.1389-1403.

Sahmaran, M., Li, M. and Li, V.C., 2007. Transport properties of engineered cementitious composites under chloride exposure. *ACI Materials Journal*, *104*(6), pp.604-611.

Şahmaran, M., Özbay, E., Yücel, H.E., Lachemi, M. and Li, V.C., 2012. Frost resistance and microstructure of Engineered Cementitious Composites: Influence of fly ash and micro poly-vinyl-alcohol fiber. *Cement and Concrete Composites*, *34*(2), pp.156-165.

Said, A.M., Zeidan, M.S., Bassuoni, M.T. and Tian, Y., 2012. Properties of concrete incorporating nano-silica. *Construction and building materials*, *36*, pp.838-844.

Salemi, N. and Behfarnia, K., 2013. Effect of nano-particles on durability of fiber-reinforced concrete pavement. *Construction and Building Materials*, *48*, pp.934-941.

Savastano Jr, H., Santos, S.F., Radonjic, M. and Soboyejo, W.O., 2009. Fracture and fatigue of natural fiber-reinforced cementitious composites. *Cement and Concrete Composites*, *31*(4), pp.232-243.

Scherer, G.W., 1999. Crystallization in pores. *Cement and Concrete research*, *29*(8), pp.1347-1358.

Sears, G.W., 1956. Determination of specific surface area of colloidal silica by titration with sodium hydroxide. *Analytical Chemistry*, *28*(12), pp.1981-1983.

Shah, S. P., Swartz, S. E. and Ouyang, C., 1995. Fracture mechanics of concrete: applications of fracture mechanics to concrete, rock and other quasi-brittle materials. John Wiley & Sons, Inc., New York, USA, 547 p.

Shah, S.P. and Ouyang, C., 1994. Fracture mechanics for failure of concrete. *Annual review of materials science*, *24*(1), pp.293-320.

Sharma, S.K., Kumar, A.A., Ransinchung, G.D.R.N. and Kumar, P., 2013. Micro fiber reinforced cement paste and mortar overlays-A review. *International Journal of*

Pavement Research and Technology, *6*(6), p.765.

Shi, F.J., 2012. A study on structure and properties of basalt fiber. In *Applied Mechanics and Materials* (Vol. 238, pp. 17-21). Trans Tech Publications Ltd.

Shin, A.H.C. and Lange, D.A., 2012. Effects of overlay thickness on surface cracking and debonding in bonded concrete overlays. *Canadian journal of civil engineering*, *39*(3), pp.304-312.

Sikdar, P.K., Jain, S.S., Bose, S. and Kumar, P., 1999. Premature cracking of flexible pavements. In *Journal of Indian Roads Congress* (Vol. 60, No. 3, pp. 355-398).

Silva, L., Tognana, S. and Salgueiro, W., 2013. Study of the water absorption and its influence on the Young's modulus in a commercial polyamide. *Polymer testing*, *32*(1), pp.158-164.

Sim, J. and Park, C., 2005. Characteristics of basalt fiber as a strengthening material for concrete structures. *Composites Part B: Engineering*, *36*(6-7), pp.504-512.

Smith, K.D., Harrington, D.S., Pierce, L., Ram, P. and Smith, K.L., 2014. *Concrete Pavement Preservation Guide*. No. FHWA-HIF-14-014. Federal Highway Administration, USA.

Smith, K.D., Yu, H.T. and Peshkin, D.G., 2002. *Portland Cement Concrete Overlays*. No. FHWA-IF-02-045, State of the Technology Synthesis.

Smith, T., Eng, P. and Works, P., 2010, September. Concrete Pavement Rehabilitation Techniques and Canadian Based Case Studies. In *paper presentation, Annual Conference of the Transportation Association of Canada, Halifax, Nova Scotia*.

Soliman, H. and Shalaby, A., 2014. Characterizing the performance of cementitious partial-depth repair materials in cold climates. *Construction and Building Materials*, *70*,

pp.148-157.

Szeląg, M., 2018. Development of cracking patterns in modified cement matrix with microsilica. *Materials*, *11*(10), p.1928.

T.I.C., 2002. *Concrete Pavement Surface Evalutaion and Rating (PASER) Manual.* Wisconsin Transportation Information Center (T.I.C.), Madison, Wisconsin. 28 p.

Tada, H., Paris, P. C., and Irwin, G. R., 2000. *The analysis of cracks handbook.* ASME Press, New York, USA, 677 p.

Taktak, R., Guermazi, N., Derbeli, J. and Haddar, N., 2015. Effect of hygrothermal aging on the mechanical properties and ductile fracture of polyamide 6: Experimental and numerical approaches. *Engineering Fracture Mechanics*, *148*, pp.122-133.

Tayeh, B.A., Bakar, B.A. and Johari, M.M., 2013. Characterization of the interfacial bond between old concrete substrate and ultra high performance fiber concrete repair composite. *Materials and structures*, *46*(5), pp.743-753.

Taylor, P.C., Kosmatka, S.H. and Voigt, G.F., 2006. *Integrated materials and construction practices for concrete pavement*. A state-of-the-practice manual, No. FHWA HIF-07-004.

Tran, Q.T., Toumi, A. and Turatsinze, A., 2007. Modelling of debonding between old concrete and overlay: fatigue loading and delayed effects. *Materials and structures*, *40*(10), pp.1045-1059.

Tran, Q.T., Toumi, A. and Turatsinze, A., 2011. Delamination of thin bonded cement-based overlays: analytical analysis. *Materials and structures*, *44*(1), pp.43-51.

Turatsinze, A., Farhat, H. and Granju, J.L., 2003. Influence of autogenous cracking on the durability of repairs by cement-based overlays reinforced with metal fibres. *Materials and structures*, *36*(10), pp.673-677.

Vaitkus, A., Grazulyte, J. and Kleiziene, R., 2014. Influence of static and impact load on pavement performance. In *Environmental Engineering. Proceedings of the International Conference on Environmental Engineering. ICEE* (Vol. 9, p. 1). Vilnius Gediminas Technical University, Department of Construction Economics & Property.

Valenza II, J.J. and Scherer, G.W., 2007. A review of salt scaling: II. Mechanisms. *Cement and Concrete Research*, *37*(7), pp.1022-1034.

Valenza, J.J. and Scherer, G.W., 2006. Mechanism for salt scaling. *Journal of the American Ceramic Society*, *89*(4), pp.1161-1179.

Vaysburd, A.M. and Emmons, P.H., 2006. Concrete repair a composite system: philosophy, engineering and practice. *Restoration of buildings and monuments= Bauinstandsetzen und Baudenkmalpflege*, *12*(5/6), pp.423-436.

Wang, L., 2011. *Foundations of stress waves*. Elsevier, UK, 548 p.

Wang, S. and Li, V.C., 2007. Engineered cementitious composites with high-volume fly ash. *ACI Materials journal*, *104*(3), p.233.

Wang, S., 2005. *Micromechanics based matrix design for engineered cementitious composites*. The University of Michigan, PhD Thesis, Civil Engineering, 222 p.

Weiss, W.J., Yang, W. and Shah, S.P., 1998. Shrinkage cracking of restrained concrete slabs. *Journal of Engineering Mechanics*, *124*(7), pp.765-774.

Wilson, T. P., Smith, K. L., Romine, A.R., 1999. *LTPP pavement maintenance materials: PCC partial-depth spall repair experiment.* Final report, No. FHWA-RD-99-153,

Turner-Fairbank Highway Research Center, U.S. Department of Transportation, Federal Highway Administration, USA, 120 p.

Wilson, T.P., Smith, K.L. and Romine, A.R., 2001. *Materials and Procedures for Rapid Repair of Partial-depth Spalls in Concrete Pavements*. Manual of Practice, No. FHWA-RD-99-152.

Wu, C. L., Tarr, S. M., Refai, T. M., Nagi, M. A., & Sheehan, M. J., 1998. *Development of Ultra-Thin Whitetopping Design Procedure*. Report No. 2124, Portland Cement Association Research and Development, Portland Cement Association, Skokie, Illinois, USA.

Wu, J., Wu, H., Tan, H.W.A. and Chew, S.H., 2018. *Multi-layer Pavement System Under Blast Load*. Singapore: Springer.

Xu, M., Song, S., Feng, L., Zhou, J., Li, H. and Li, V.C., 2021. Development of basalt fiber engineered cementitious composites and its mechanical properties. *Construction and Building Materials*, *266*, p.121173.

Yang, E.H. and Li, V.C., 2012. Tailoring engineered cementitious composites for impact resistance. *Cement and Concrete Research*, *42*(8), pp.1066-1071.

Yang, E.H. and Li, V.C., 2014. Strain-rate effects on the tensile behavior of strain-hardening cementitious composites. *Construction and Building materials*, *52*, pp.96-104.

Yang, E.H., Yang, Y. and Li, V.C., 2007. Use of high volumes of fly ash to improve ECC mechanical properties and material greenness. *ACI materials journal*, *104*(6), pp.620-628.

Yasien, A.M., Bassuoni, M.T., Abayou, A. and Ghazy, A., 2021. Nano-Modified Concrete

as Repair Material in Cold Weather. *ACI Materials Journal*, *118*(2).

Yu, J., Lin, J., Zhang, Z. and Li, V.C., 2015. Mechanical performance of ECC with high-volume fly ash after sub-elevated temperatures. *Construction and Building Materials*, *99*, pp.82-89.

Yu, K.Q., Dai, J.G., Lu, Z.D. and Poon, C.S., 2018. Rate-dependent tensile properties of ultra-high performance engineered cementitious composites (UHP-ECC). *Cement and Concrete Composites*, *93*, pp.218-234.

Yucel, H.E., Jashami, H., Sahmaran, M., Guler, M. and Yaman, I.O., 2013. Thin ECC overlay systems for rehabilitation of rigid concrete pavements. *Magazine of Concrete Research*, *65*(2), pp.108-120.

Zhang, H., Wang, B., Xie, A. and Qi, Y., 2017. Experimental study on dynamic mechanical properties and constitutive model of basalt fiber reinforced concrete. *Construction and Building Materials*, *152*, pp.154-167.

Zhang, H., Wang, L., Zheng, K., Bakura, T.J. and Totakhil, P.G., 2018. Research on compressive impact dynamic behavior and constitutive model of polypropylene fiber reinforced concrete. *Construction and Building Materials*, *187*, pp.584-595.

Zhang, J. and Li, V.C., 2002. Monotonic and fatigue performance in bending of fiber-reinforced engineered cementitious composite in overlay system. *Cement and Concrete Research*, *32*(3), pp.415-423.

Zhang, J., Gong, C., Guo, Z. and Zhang, M., 2009. Engineered cementitious composite with characteristic of low drying shrinkage. *Cement and Concrete Research*, *39*(4), pp.303-312.

Zhang, M.H. and Islam, J., 2012. Use of nano-silica to reduce setting time and increase

early strength of concretes with high volumes of fly ash or slag. *Construction and Building Materials*, *29*, pp.573-580.

Zhang, M.H., Islam, J. and Peethamparan, S., 2012. Use of nano-silica to increase early strength and reduce setting time of concretes with high volumes of slag. *Cement and Concrete Composites*, *34*(5), pp.650-662.

Zhao, Y.R., Wang, L., Lei, Z.K., Han, X.F. and Xing, Y.M., 2017. Experimental study on dynamic mechanical properties of the basalt fiber reinforced concrete after the freeze-thaw based on the digital image correlation method. *Construction and Building Materials*, *147*, pp.194-202.

Zhishen, W., Xin, W. and Gang, W., 2012. Advancement of structural safety and sustainability with basalt fiber reinforced polymers. *CICE2012, Rome*, *13*, pp.15-29.

Zhou, J., Qian, S., Ye, G., Copuroglu, O., van Breugel, K. and Li, V.C., 2012. Improved fiber distribution and mechanical properties of engineered cementitious composites by adjusting the mixing sequence. *Cement and Concrete Composites*, *34*(3), pp.342-348.

Zhou, Z. and Qiao, P., 2020. Direct tension test for characterization of tensile behavior of ultra-high performance concrete. *Journal of Testing and Evaluation*, *48*(4).

Zhu, Y., Yang, Y. and Yao, Y., 2012. Autogenous self-healing of engineered cementitious composites under freeze–thaw cycles. *Construction and Building Materials*, *34*, pp.522-530.

Zhu, Y., Yang, Y. and Yao, Y., 2012. Use of slag to improve mechanical properties of engineered cementitious composites (ECCs) with high volumes of fly ash. *Construction and building materials*, *36*, pp.1076-1081.

Zhu, Y., Yang, Y. and Yao, Y., 2012. Use of slag to improve mechanical properties of engineered cementitious composites (ECCs) with high volumes of fly ash. *Construction and building materials*, *36*, pp.1076-1081.

APPENDIX A: SUPPLEMENTAL RESULTS FOR CHAPTER 3

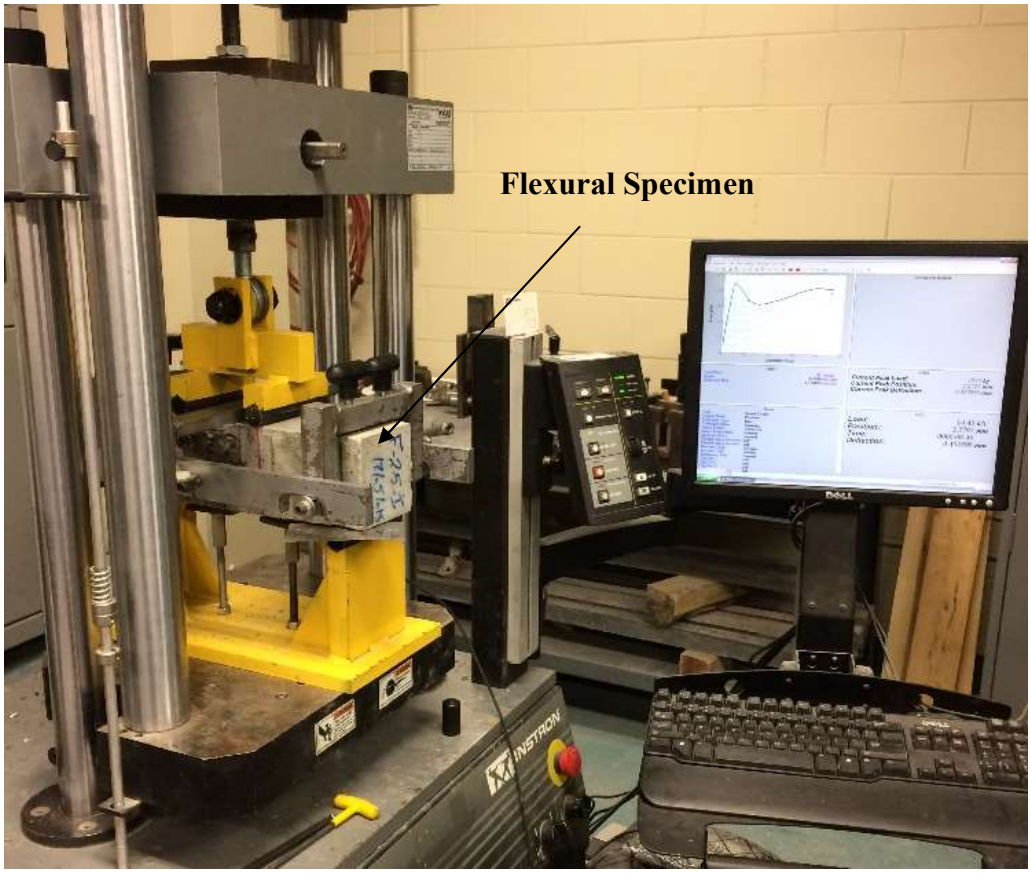

Figure A.1: Flexural test setup.

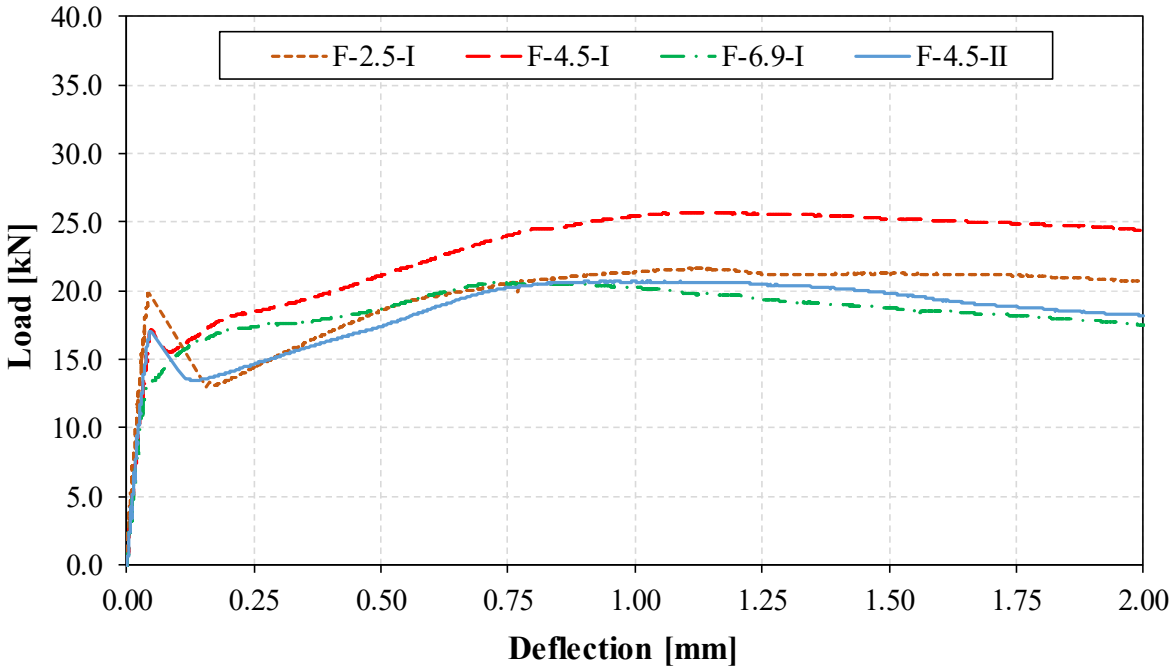

Figure A.2: Load-deflection (P-δ) curves for F-mixtures.

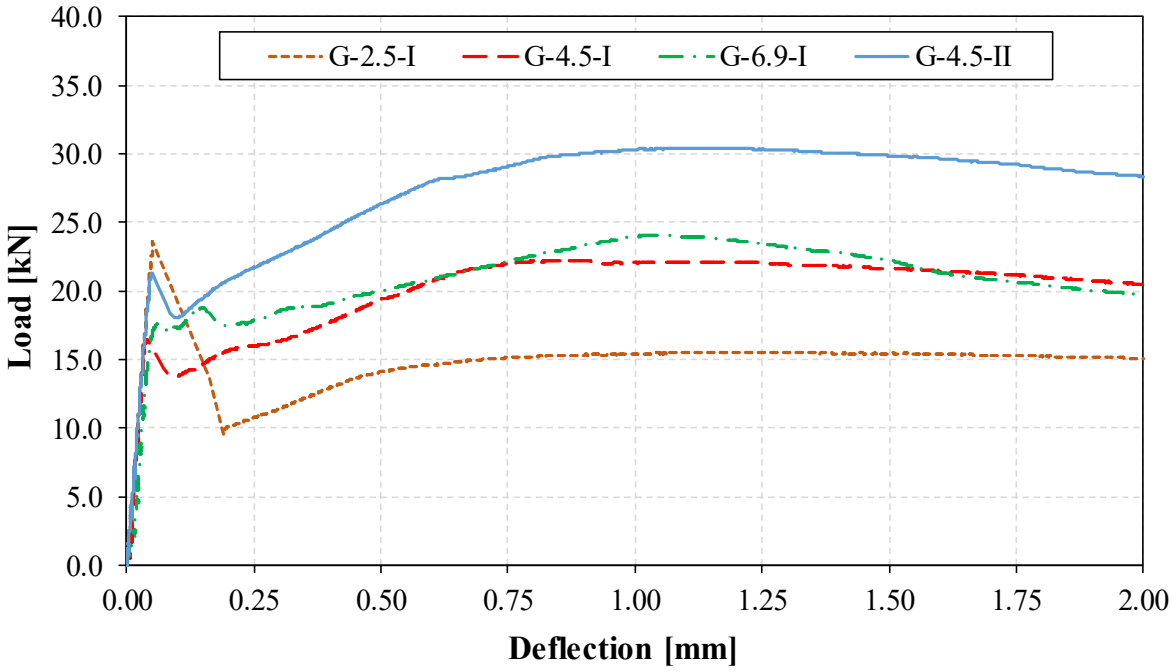

Figure A.3: Load-deflection (P-δ) curves for G-mixtures

Figure A.4: Walk-in Environmental Chamber.

Figure A.5: Whitish precipitates show the average penetration depth of chloride ions for the developed composites

Table A.1: ANOVA for the Results of Compressive Strength at 28 Days

Parameter	Compressive Strength		
	F	**P value**	**F_{cr}**
Effect of Matrix			
F-4.5-I versus G-4.5-I	344.99	4.94E-05	7.70
Effect of Dosage			
F-2.5-I versus F-4.5-I versus F-6.9-I	24.19	0.00134	5.14
G-2.5-I versus G-4.5-I versus G-6.9-I	163.54	5.84E-06	5.14
Effect of Mixing Procedure			
F-4.5-I versus F-4.5-II	1.14	0.344	7.70
G-4.5-I versus G-4.5-II	0.29	0.617	7.70
Dual Effect of Dosage and Matrix			
Matrix	885.62	1.29E-12	4.74
Dosage	154.39	2.74E-09	3.88
Interaction	47.90	1.90E-06	3.88
Dual Effect of Mixing Procedure and Matrix			
Matrix	1278.81	4.09E-10	5.31
Mixing Procedure	0.95	0.357	5.31
Interaction	0.00047	0.983	5.31

APPENDIX B: SUPPLEMENTAL RESULTS FOR CHAPTER 4

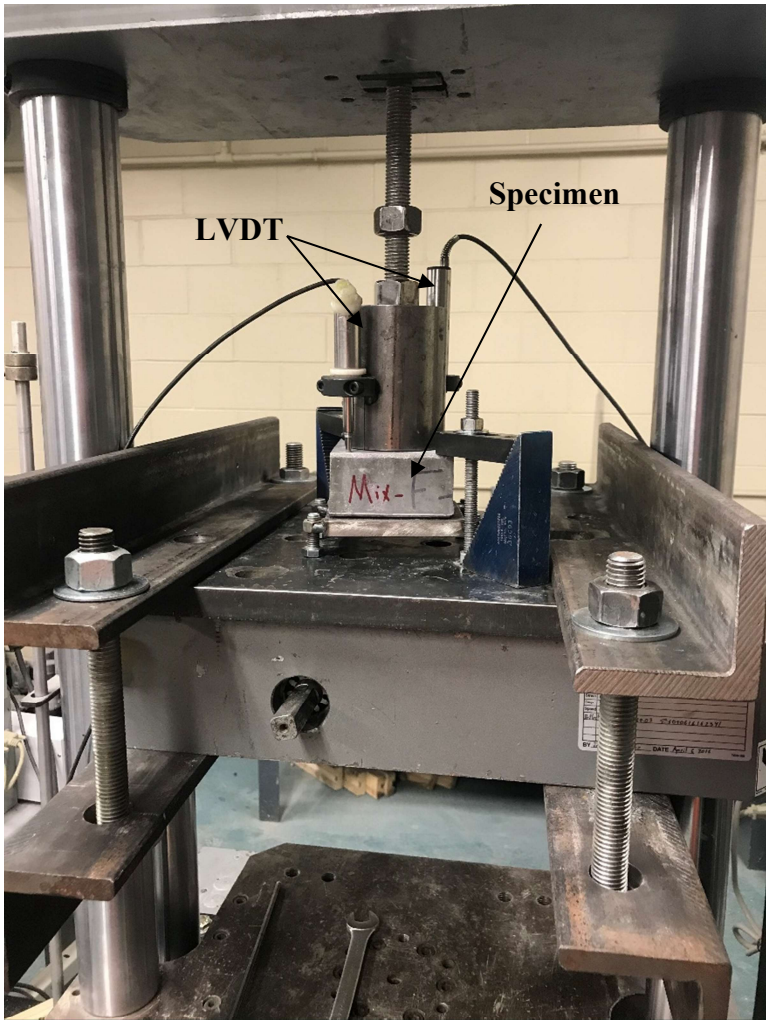

Figure B.1: Single pellet pull-out test setup.

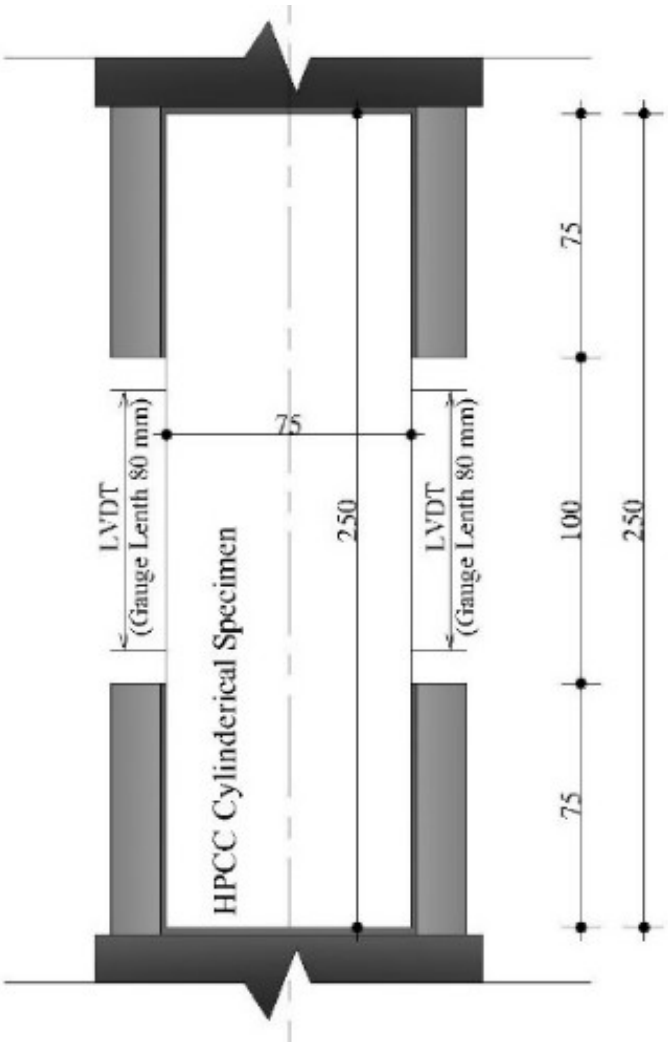

Figure B.2: Quasi-static tensile test setup (dimensions in mm).

Figure B.3: Quasi-static tensile test specimen failure in the middle.

APPENDIX C: SUPPLEMENTAL RESULTS FOR CHAPTER 5

Figure C.1: Preparations and molds for the prismatic specimens of the different exposures.

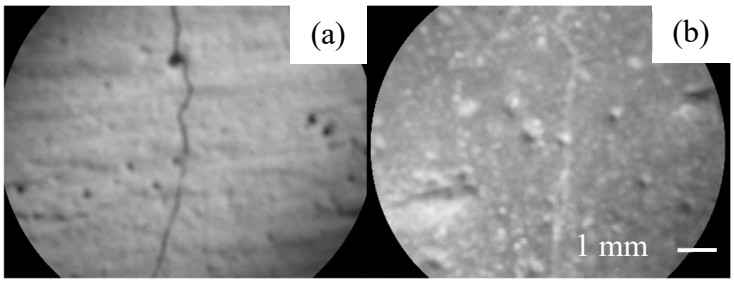

N-GU-2.5 for reference exposure

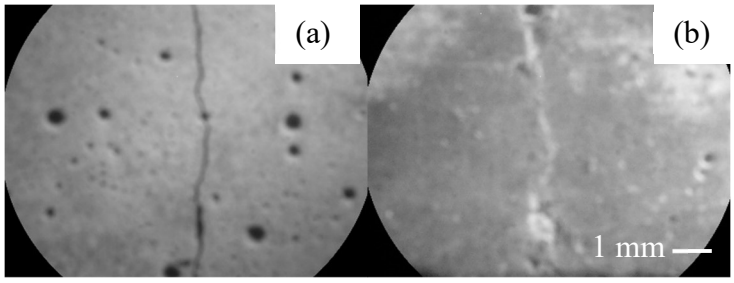

N-GU-2.5 for alkaline exposure

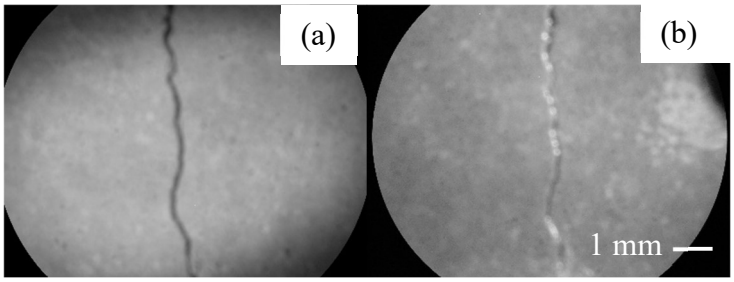

N-F-2.5 for reference exposure

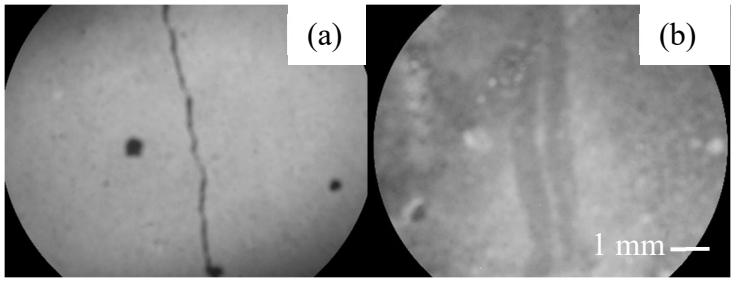

N-F-2.5 for alkaline exposure

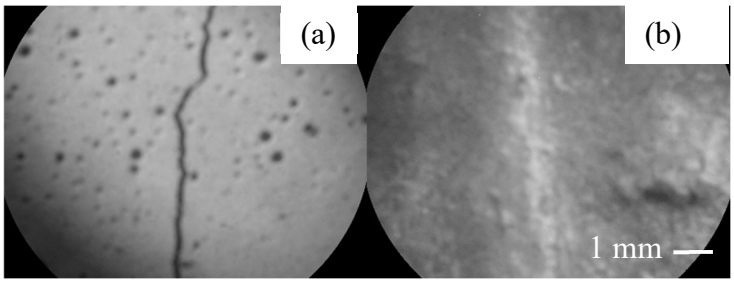

N-G-2.5 for reference exposure

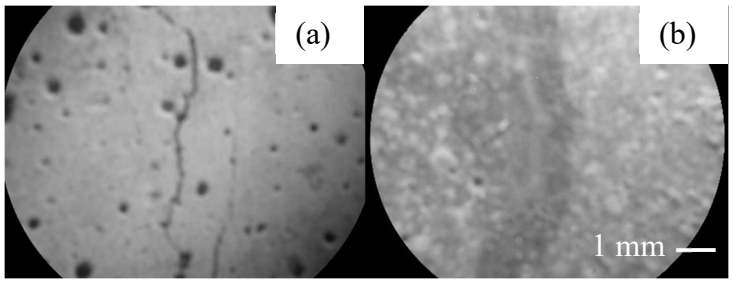

N-G-2.5 for alkaline exposure

Figure C.2: Exemplar induced cracks: (a) before exposure and (b) after exposure showing significant self-healing.

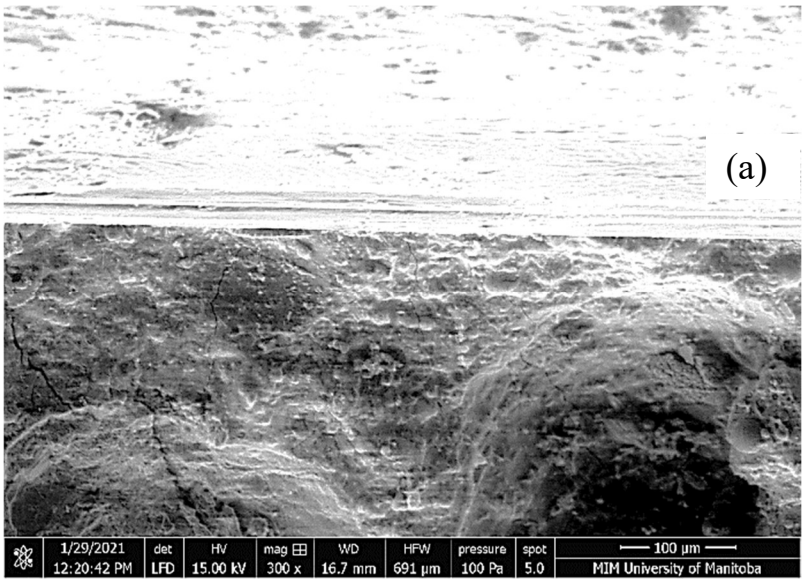

Figure C.3: Exemplar SEM micrograph after freezing-thawing exposure showing ITZ with BFP for nano-modified cement-based composite N-GU-2.5.

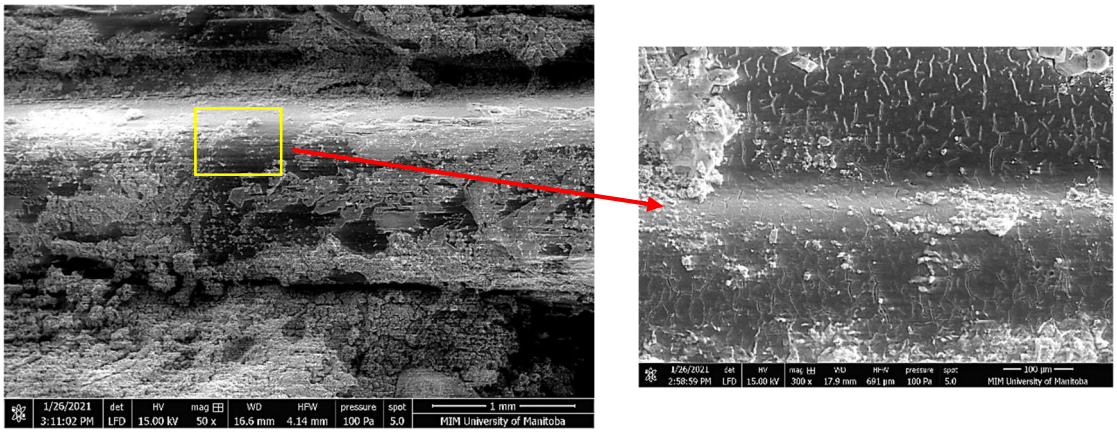

Figure C.4: Exemplar SEM micrographs for the surface of BFP in N-G-2.5 subjected to alkaline exposure after flexural testing showing discrete micro-cracks on the surface of the pellet.

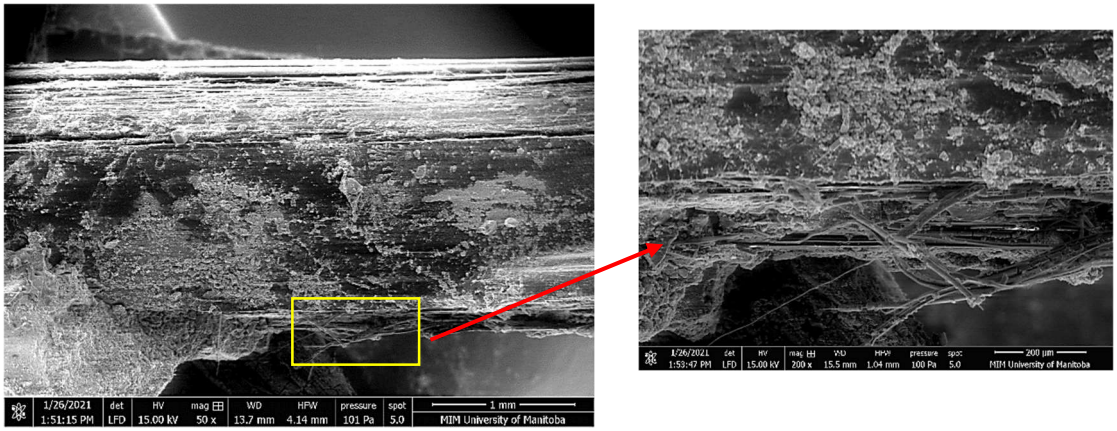

Figure C.5: Exemplar SEM micrographs for the surface of BFP in N-G-2.5 subjected to alkaline exposure after flexural testing showing evidence of tearing of the polyamide encapsulation layer

APPENDIX D: SUPPLEMENTAL RESULTS FOR CHAPTER 6 AND 7

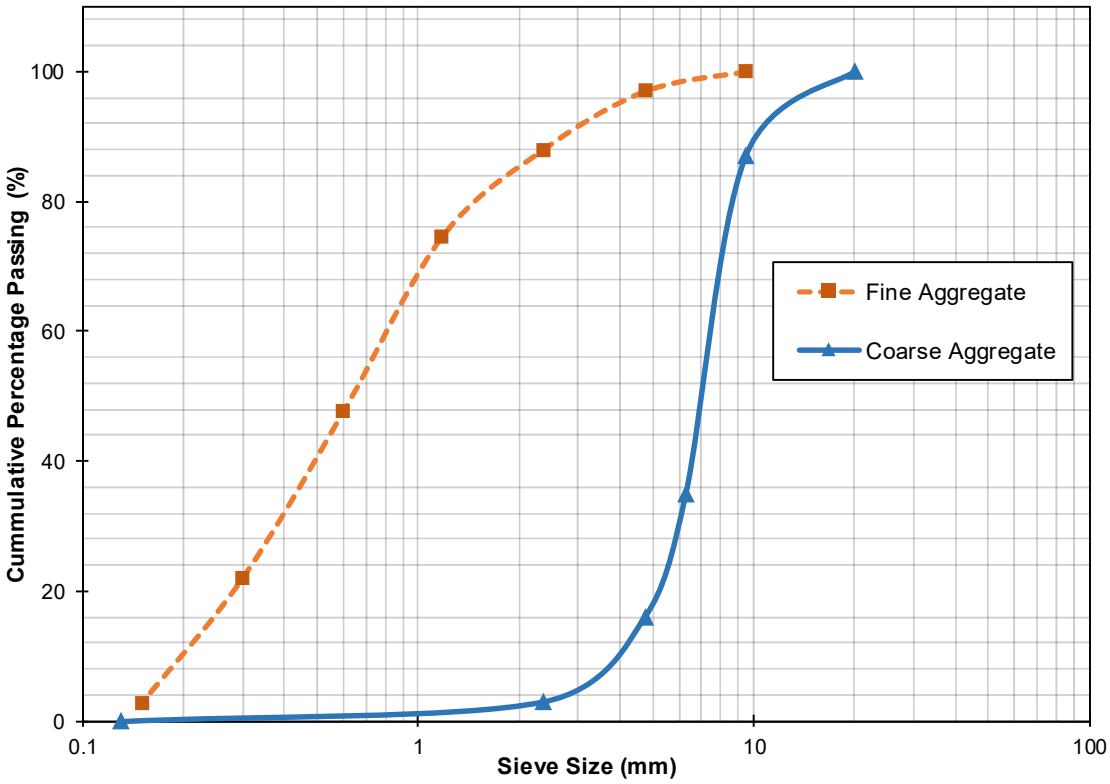

Figure D.1: Fine and coarse aggregates particle size distribution used for parent concrete.

Figure D.2: Parent concrete surface before and after roughening

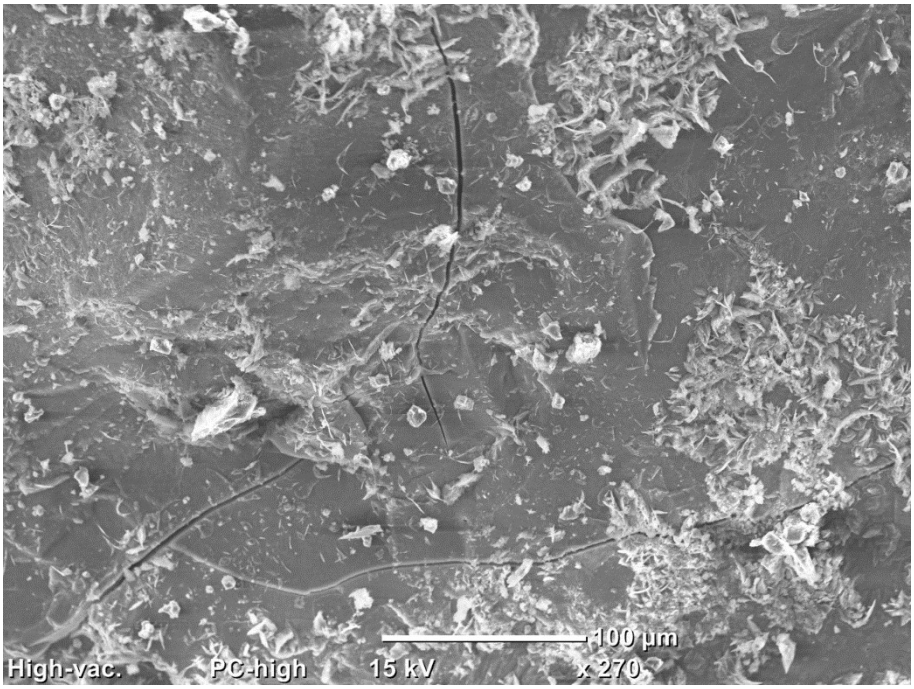

Figure D.3: Nano-silica separating layer at the interface between the substrate and the applied topping layer.

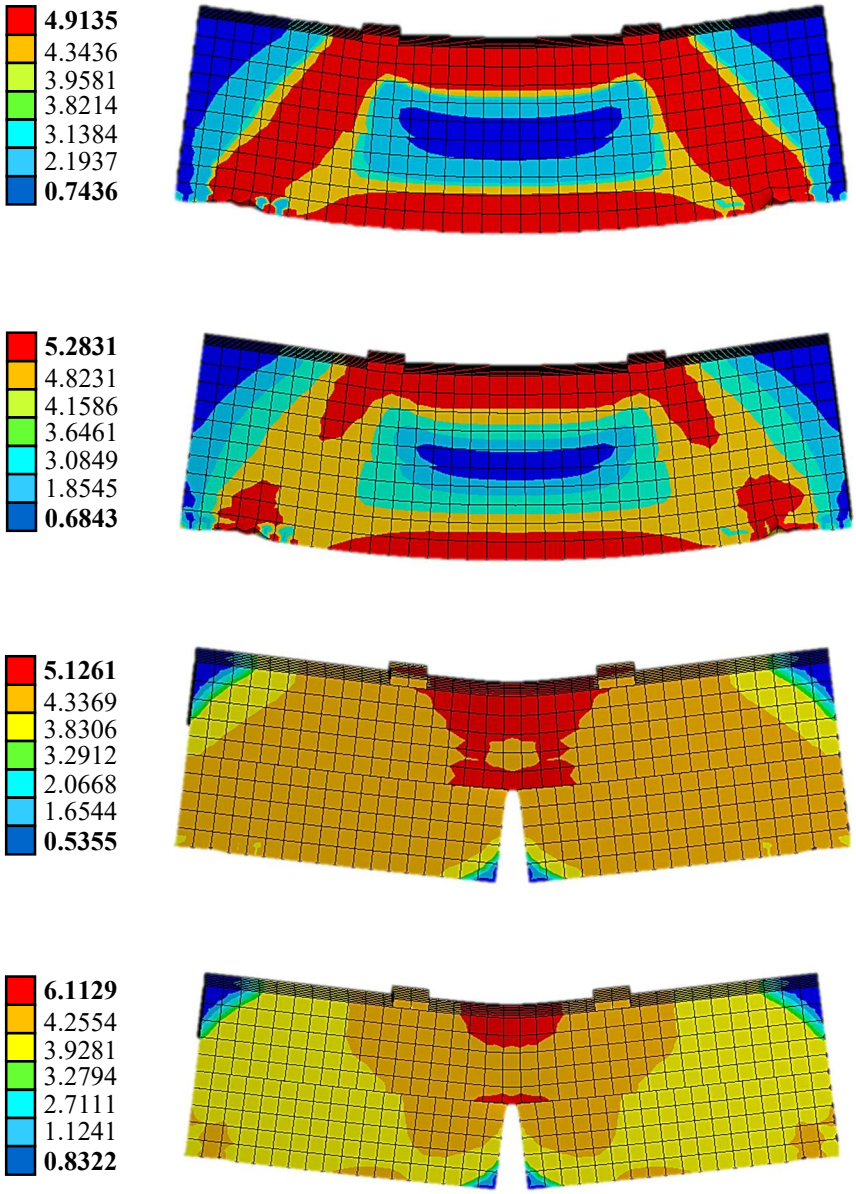

Figure D.4: Stress distribution in the overlay systems in both intact and pre-cracked substrate conditions at first-cracking stage

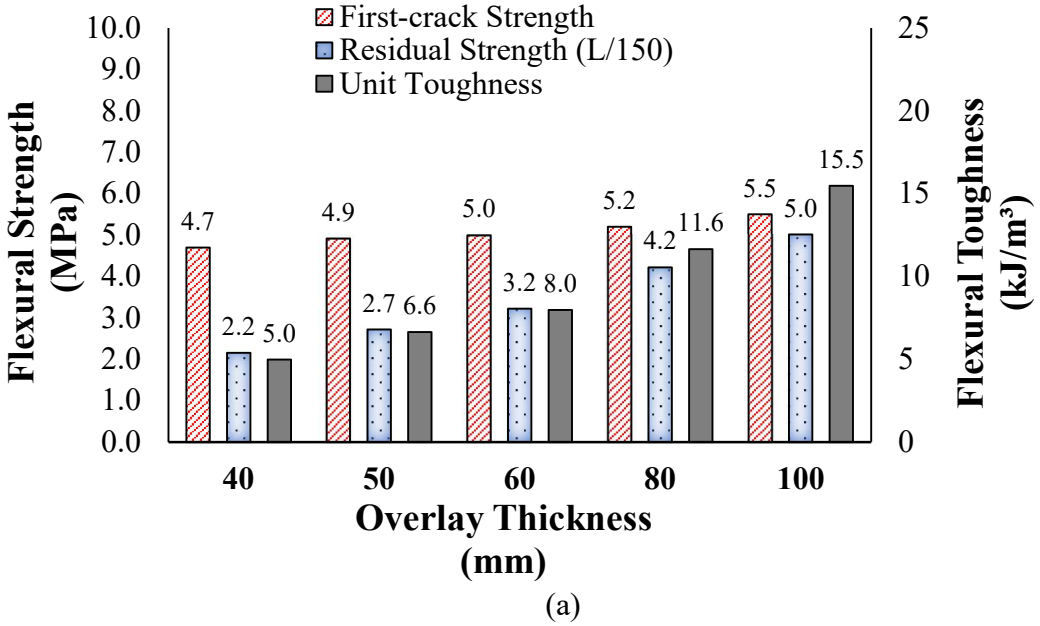

(a)

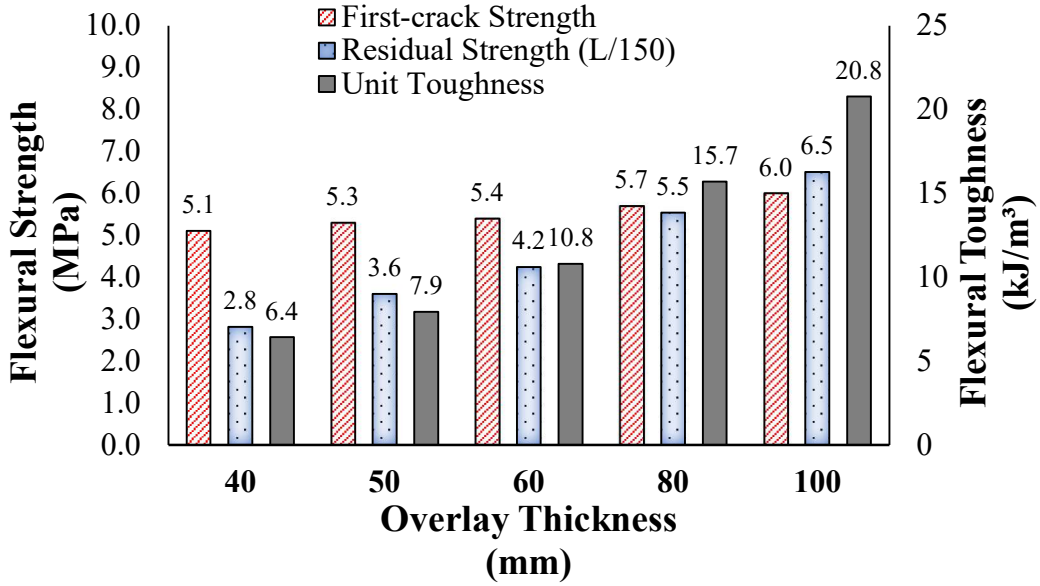

(b)

Figure D.5: Flexural properties for the overlay systems with different overlay thicknesses and intact parent concrete substrate layer; (a) N-F-4.5, and (b) N-G-4.5

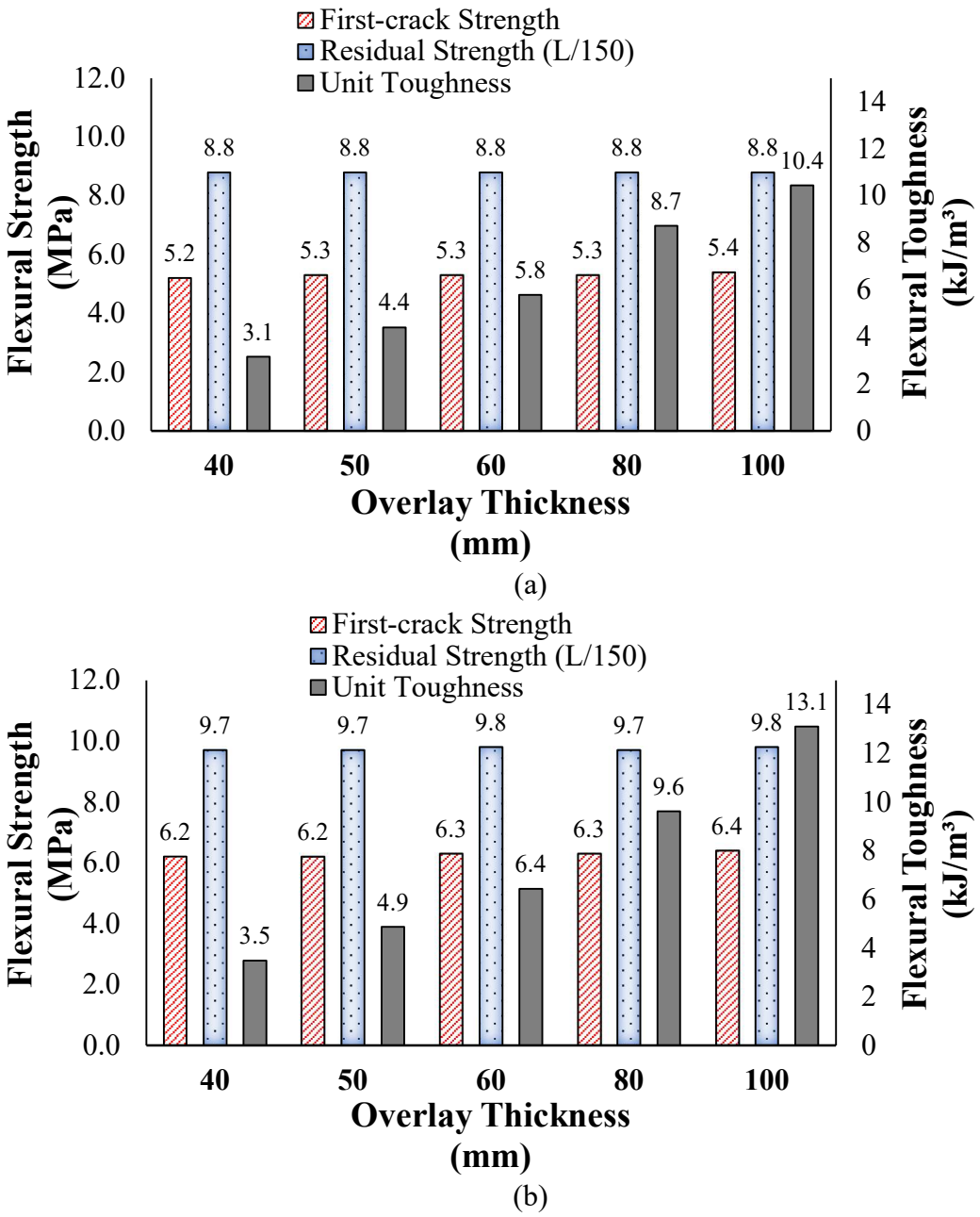

Figure D.6: Flexural properties for the overlay systems with different overlay thicknesses and pre-cracked parent concrete substrate layer; (a) N-F-4.5, and (b) N-G-4.5

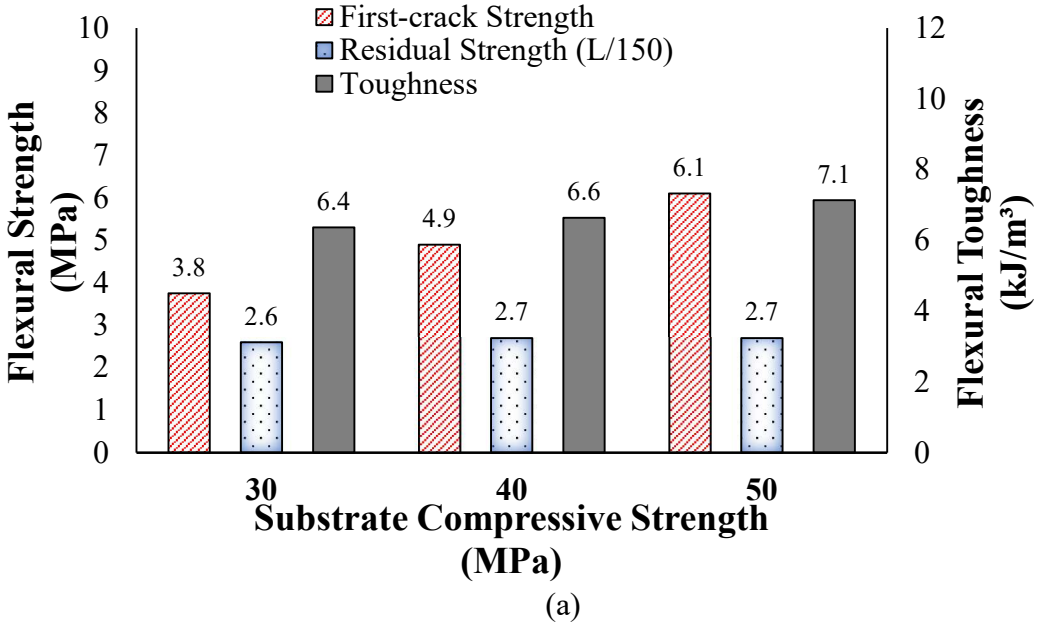

(a)

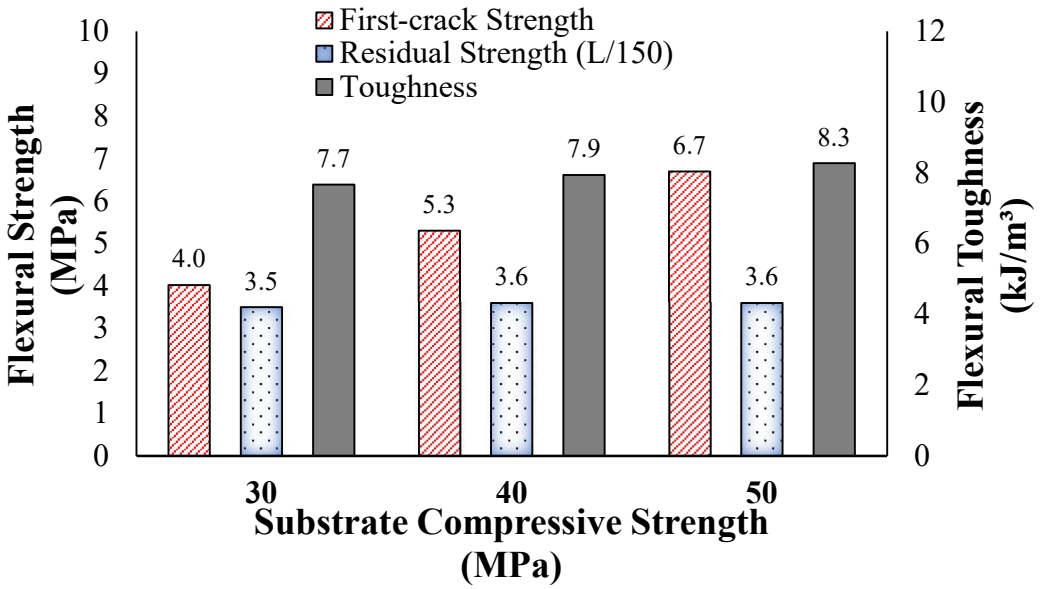

(b)

Figure D.7: Flexural properties for the overlay systems with different compressive strength of parent concrete substrate layer in the intact condition; (a) N-F-4.5, and (b) N-G-4.5

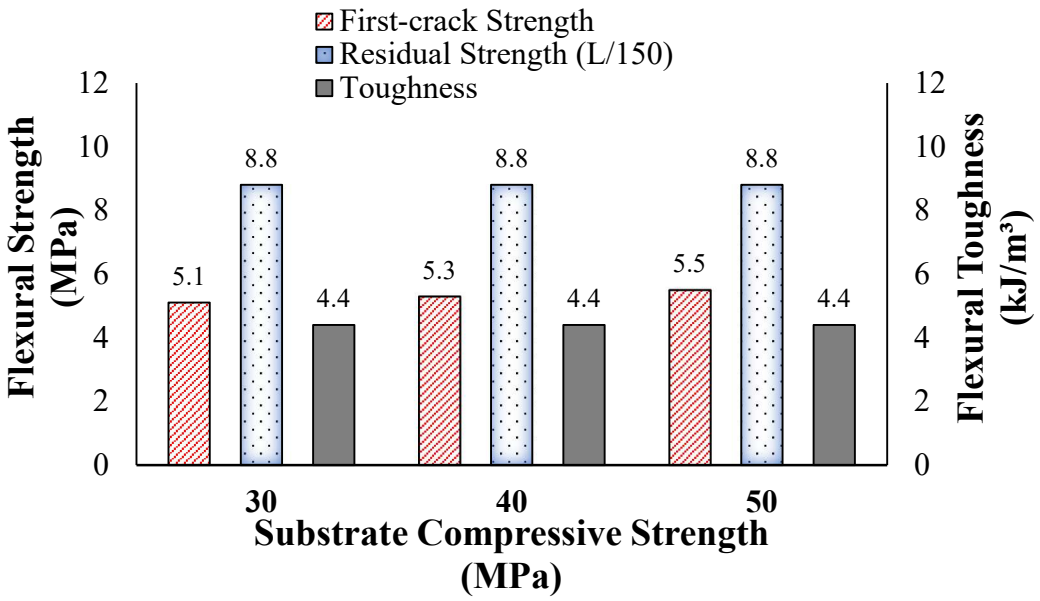

(a)

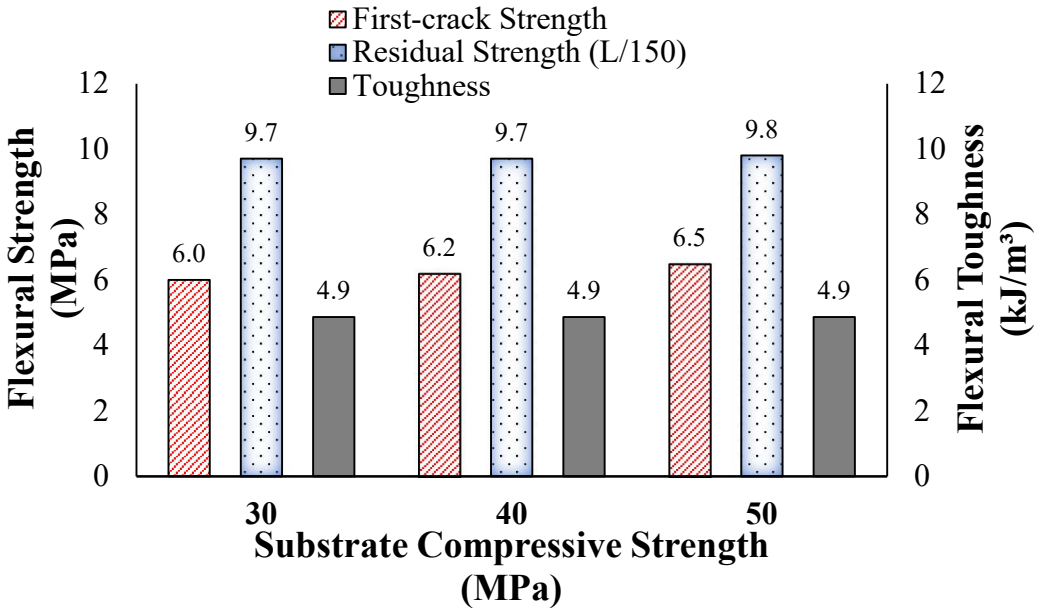

(b)

Figure D.8: Flexural properties for the overlay systems with different compressive strength of parent concrete substrate layer in the pre-cracked condition; (a) N-F-4.5, and (b) N-G-4.5